Crustal Deformation Associated with Great Subduction Earthquakes

by

Tianhaozhe Sun
B.Sc., Tongji University, 2011

A Dissertation Submitted in Partial Fulfillment
of the Requirements for the Degree of

DOCTOR OF PHILOSOPHY

in the School of Earth and Ocean Sciences

Supervisory Committee

Crustal Deformation Associated with Great Subduction Earthquakes

by

Tianhaozhe Sun
B.Sc., Tongji University, 2011

Supervisory Committee

Dr. Kelin Wang (School of Earth and Ocean Sciences)
Co-Supervisor

Dr. George Spence (School of Earth and Ocean Sciences)
Co-Supervisor

Dr. Stan Dosso (School of Earth and Ocean Sciences)
Departmental Member

Dr. Michel Lefebvre (Department of Physics and Astronomy)
Outside Member

Dr. Earl Davis (Pacific Geoscience Centre, Geological Survey of Canada)
Additional Member

Abstract

Supervisory Committee
Dr. Kelin Wang (School of Earth and Ocean Sciences)
Co-Supervisor
Dr. George Spence (School of Earth and Ocean Sciences)
Co-Supervisor
Dr. Stan Dosso (School of Earth and Ocean Sciences)
Departmental Member
Dr. Michel Lefebvre (Department of Physics and Astronomy)
Outside Member
Dr. Earl Davis (Pacific Geoscience Centre, Geological Survey of Canada)
Additional Member

The slip behaviour of subduction faults and the viscoelastic rheology of Earth's mantle govern crustal deformation throughout the subduction earthquake cycle. This Ph.D. dissertation presents research results on two topics: (1) coseismic and postseismic slip of the shallowest segment of subduction faults and (2) postseismic deformation following great subduction earthquakes controlled by mantle viscoelasticity.

Topic 1: Slip behaviour of the shallowest subduction faults. By modelling high-resolution cross-trench bathymetry surveys before and after the 2011 M_w 9.0 Tohoku-oki earthquake, we determine the magnitude and distribution of coseismic slip over the most near-trench 40 km of the Japan Trench megathrust. The inferred > 60 m average slip and a gentle increase by 5 m towards the trench over this distance indicate moderate degree of net coseismic weakening of the shallow fault. Using near-trench seafloor and sub-seafloor fluid pressure variations as strain indicators in conjunction with land-based geodetic measurements, we determine coseismic-slip and afterslip distributions of the 2012 M_w 7.6 Costa Rica earthquake. Here, trench-breaching slip similar to the Tohoku-oki rupture did not occur during the earthquake, but afterslip extended to the trench axis and reached ~0.7 m over 1.3 years after the earthquake, exhibiting a velocity-strengthening behaviour. These two contrasting examples bracket a possibly wide range of slip behaviour of the shallow megathrust. They help us understand why large tsunamis are generated by some but not all subduction earthquakes.

Topic 2: Postseismic deformation following great subduction earthquakes. Due to the asymmetry of megathrust rupture, with the upper plate undergoing greater coseismic tension than the incoming plate, viscoelastic stress relaxation causes the trench and land areas to move in opposite, opposing directions immediately after the earthquake. Seafloor geodetic measurements following the 2011 Tohoku-oki earthquake, modelled in this work, provided the first direct observational evidence for this effect. Systematic modelling studies in this work suggest that such viscoelastic opposing motion should be common to all $M_w \geq 8$ subduction earthquakes. As the effect of viscoelastic relaxation decays with time and the effect of fault relocking becomes increasingly dominant, the dividing boundary of the opposing motion continues to migrate away from the rupture area. Comparative studies of ten $8 \leq M_w \leq 9.5$ subduction earthquakes in this dissertation quantifies the primary role of earthquake size in controlling the "speed" of the evolution of this deformation. Larger earthquakes are followed by longer-lived opposing motion that affects a broader region of the upper plate.

Table of Contents

List of Tables

List of Figures

Acknowledgments

First of all, I would like to express my sincere gratitude to my supervisor, Dr. Kelin Wang, for his invaluable guidance and continuous support during my study. His immense knowledge and dedication for science always and will continue to inspire me.

Besides my supervisor, I would like to thank the rest of my Ph.D. supervisory committee: Drs. Earl Davis, George Spence, Stan Dosso, and Michel Lefebvre, for their stimulating advice and encouragement, and for helping me widen my research from various perspectives. I would like to thank my external examiner, Dr. David Schmidt, for his helpful comments.

Many scientists and staff members at the Pacific Geoscience Centre, Geological Survey of Canada helped me during my study. They create a great work and study environment that I benefit a lot from. Among them, my special thanks go to Dr. Jiangheng He, for developing the numerical modelling codes used in this research and for his help throughout my study, and Robert Meldrum, for offering technical training in borehole fluid pressure monitoring and for being a great friend.

I would also like to thank the faculty and staff members in the School of Earth and Ocean Sciences, University of Victoria, for their help and support. Among them, I give special thanks to the Graduate Program Secretary, Allison Rose, for always cheerfully helping me throughout my Ph.D. program.

I appreciate the opportunities to work with many collaborators and colleagues from various institutes or research teams. Among them, I give special thanks to the IODP Expedition JFAST participants, Drs. Ryota Hino and Takeshi Iinuma and other colleagues at the Tohoku University (TU), and Drs. Shuichi Kodaira and Toshiya Fujiwara and other colleagues at the Japan Agency for Marine-Earth Science and Technology (JAMSTEC). The world-class geophysical observations made by the TU and JAMSTEC colleagues provided the data used in Chapters 2 and 4 of this dissertation.

I would like to thank my friends and fellow graduate students, for their support and understanding, and for making my Ph.D. study a happy journey.

Last but not least, I would like to thank my family, especially my parents, Hongxia Ding and Zonghua Sun, for their love and boundless support.

Dedication

This Ph.D. dissertation is dedicated to the victims of the March 11th, 2011 M_w 9.0 Tohoku-oki earthquake and its tsunami and also victims of other great earthquakes.

Chapter 1. Introduction

The 2004 moment magnitude (M_w) 9.2 Sumatra earthquake marked the beginning of a surge of great earthquakes worldwide [Lay et al., 2015]. The majority of these earthquakes are due to the rupture of subduction interface faults, referred to as megathrusts. Since 2004, twelve $M_w \geq 8$ earthquakes of this type have occurred, some accompanied with devastating tsunamis, such as the 2004 Sumatra and the 2011 M_w 9.0 Tohoku-oki earthquakes. These earthquakes and their tsunamis have taken hundreds of thousands of lives and caused severe property damage and economic disruptions. On the other hand, because of rapidly advancing observation technology, these earthquakes have also yielded a wealth of geophysical data [e.g., Bürgmann and Chadwell, 2014; Kanamori, 2014]. These data enable us to study the geodynamic processes responsible for these great earthquakes. Some of the new observations have led to paradigm-shifting findings that challenge conventional theories [Wang, 2013]. Improved understanding of the geodynamic processes will continue to help society assess seismic and tsunami hazards for the purpose of risk mitigation.

Less than six months after the March 11th, 2011 M_w 9.0 Tohoku-oki earthquake and its tsunami, I started my graduate study in the School of Earth and Ocean Sciences, University of Victoria. This was the time when the global scientific community was just beginning to come to grips with the many scientific surprises presented by this devastating event. In the following year, I participated in the deep-sea drilling expedition JFAST (Japan Trench Fast Drilling Project), an international project designed to study why the shallowest portion of the Japan Trench megathrust underwent very large slip during the M_w 9.0 earthquake to generate the huge tsunami. In the meantime, colleagues at the Japan Coast Guard and Tohoku University had been frequently revisiting several seafloor geodetic stations not far from our drilling site to monitor postseismic deformation. Their measurements soon provided breathtaking yet intriguing data that

show motion in opposing directions between the trench and land areas. With this background, the slip behaviour of the shallowest portion of the megathrust and postseismic deformation controlled by Earth rheology became the two primary topics of my Ph.D. research.

With regard to the shallow fault behaviour, whether, how much, and why the shallowest part of a megathrust slips during an earthquake are key questions to address in understanding rupture propagation and tsunami generation. However, compared to the deeper part of the subduction fault which is closer to onshore monitoring networks, the behaviour of the shallow megathrust is poorly observed and understood, due to the lack of offshore near-trench deformation observations. This situation has been improved by observations for the 2011 Tohoku-oki and 2012 M_w 7.6 Costa Rica earthquakes. The two events exhibited contrasting slip behaviour: Large slip breached the trench during the Tohoku-oki earthquake at the seismic slip rate, but slip extended to the trench only after the Costa Rica earthquake with much lower slip rates. In my Ph.D. study, using high-resolution bathymetry measurements before and after the Tohoku-oki earthquake across the trench, I determined the magnitude and distribution of the coseismic slip of the shallow megathrust in the main rupture area. Using seafloor and sub-seafloor fluid pressure measurements at two closely located sites at the trench as strain indicators during and after the Costa Rica earthquake, I studied the postseismic slip of the shallowest megathrust updip of the rupture area. The results of studying these end-member slip behaviours contribute to our understanding of fault mechanics and tsunami generation.

With regard to the postseismic crustal deformation, how the deformation evolves with time and how the evolution is controlled by the viscoelastic Earth rheology, continuing slip of different parts of the fault after the earthquake, and the relocking of the fault are important questions. Addressing these questions allows us to put the study of subduction fault behaviour (the first topic discussed above) in proper geodynamic context. It also allows us to understand the very different deformation patterns presently observed at different subduction margins in terms of a common geodynamic process. Using seafloor geodetic observations following the Tohoku-oki earthquake, I studied the

contribution of mantle viscoelasticity right after the rupture, with a focus on explaining the postseismic motion in opposing directions in the near-trench area. By conducting systematic modelling tests, I studied how this short-term (months to years) opposing motion is affected by various rheological and structural factors, and showed that it is a common feature for megathrust earthquakes. By conducting a comparative study of postseismic deformation of ten great ($M_w \geq 8$) subduction earthquakes, I studied why the evolution of deformation governed by a common geodynamic process takes place at very different rates after earthquakes of different sizes, with more prolonged postseismic deformation following larger earthquakes. The results presented in this dissertation offer a rather complete synthesis of geodetically constrained postseismic deformation of $M_w \geq 8$ earthquakes, and they shall provide guidance for making future observations.

Besides the Introduction (Chapter 1) and Conclusions (Chapter 7), this dissertation consists of five standalone scientific journal papers that are either already published or nearly ready for submission. The author of the dissertation is the lead author for all these papers. Each paper forms a chapter of the dissertation. Chapters 2 and 3 address the topic of the shallow megathrust behaviour, and the other three chapters address the topic of postseismic deformation. Chapter 2 is a paper published in Nature Communications in 2017 on the coseismic trench-breaching slip during the Tohoku-oki earthquake. Chapter 3 is a manuscript in preparation on the trench-breaching afterslip following the Costa Rica earthquake. Chapter 4 is a paper published in Nature in 2014 on the short-term (months to years) postseismic deformation following the 2011 Tohoku-oki earthquake. Chapter 5 is a paper published in Journal of Geophysical Research in 2015 which built on the results of Chapter 4 to present a systematic examination of the influences of various rheological and structural factors on short-term postseismic deformation. Chapter 6 is a manuscript in preparation which greatly expands the materials of Chapters 4 and 5 and systematically studies ten subduction earthquakes worldwide to investigate the effects of earthquake size and other factors on the duration of postseismic deformation. References cited in all the five papers (chapters) are given together at the end of the dissertation.

Some of the five papers have multiple co-authors from various institutions, because much of this dissertation is the result of international scientific collaboration. Researchers

at the Japan Agency for Marine-Earth Science and Technology collected and processed the high-resolution bathymetry data for the work in Chapter 2. Researchers at the Tohoku University conducted seafloor geodetic surveys and provided the data for the most critical site used in Chapter 4, although many of the seafloor geodetic data published by the Japan Coast Guard were also used in this chapter.

Chapter 2. Shallow Rupture During the 2011 Tohoku-oki Earthquake

This chapter is the first of the two chapters addressing the kinematics and mechanics of the shallowest part of subduction faults. The main body of this chapter consists of a published journal article [Sun et al., 2017] on using near-trench deformation observations to constrain the rupture behaviour of the shallowest portion of the subduction fault during the 2011 Tohoku-oki earthquake. Section 2.1 describes basic article information. Section 2.2 presents the article itself. Supplementary material that accompanied the published article is presented as section 2.3.

2.1. Article Information

2.1.1. Author and Coauthor Contributions

Section 2.2 consists of an article published in journal Nature Communications but reformatted for the dissertation. The author of this dissertation T.S. carried out most of the deformation modelling of this study. Coauthor K.W. and T.S. jointly designed the study and did most of the writing. Coauthors T.F. and S.K. contributed to the collection and processing of the high-resolution bathymetry data used in the study. Coauthor J.H. developed the computer code used for, and participated in, the deformation modelling.

2.1.2. Citation

Sun, T., K. Wang, T. Fujiwara, S. Kodaira, and J. He (2017), Large fault slip peaking at trench in the 2011 Tohoku-oki earthquake, *Nature Communications, 8*, 14044, doi:10.1038/ncomms14044.

2.1.3. Author's Names and Affiliations

Tianhaozhe Sun[1], Kelin Wang[1,2*], Toshiya Fujiwara[3], Shuichi Kodaira[4], Jiangheng He[2]

[1] School of Earth and Ocean Sciences, University of Victoria, Victoria, British Columbia, Canada V8P 5C2

[2] Pacific Geoscience Centre, Geological Survey of Canada, Natural Resources Canada, 9860West Saanich Road, Sidney, British Columbia, Canada V8L 4B2

[3] R&D Center for Earthquake and Tsunami (CEAT), Japan Agency for Marine-Earth Science and Technology (JAMSTEC), Natsushima-cho 2-15, Yokosuka 237-0061, Japan

[4] R&D CEAT, JAMSTEC, Showamachi 3173-25, Kanazawa-ku, Yokohama 236-0001, Japan

[*] Corresponding author: kelin.wang@canada.ca

2.1.4. Article Format

The text and figures included in Section 2.2 are taken directly from the Nature Communications article. Articles published in this journal all have a standard but special structure in which the Results section directly follows the Introduction section, with Methods described after Discussion. The supplementary material for the article is given in Section 2.3. Sections, figures, and tables in the original article have been renumbered to be compatible with the chapter format of the dissertation. References cited in the article are included in the bibliography of this dissertation.

2.2. Large Fault Slip Peaking at Trench in the 2011 Tohoku-oki Earthquake

2.2.1. Abstract

During the 2011 magnitude 9 Tohoku-oki earthquake, very large slip occurred on the shallowest part of the subduction megathrust. Quantitative information on the shallow slip is of critical importance to distinguishing between different rupture mechanics and understanding the generation of the ensuing devastating tsunami. However, the magnitude and distribution of the shallow slip are essentially unknown due primarily to

the lack of near-trench constraints, as demonstrated by a compilation of 45 rupture models derived from a large range of data sets. To quantify the shallow slip, here we model high-resolution bathymetry differences before and after the earthquake across the trench axis. The slip is determined to be about 62 m over the most near-trench 40 km of the fault with a gentle increase towards the trench. This slip distribution indicates that dramatic net weakening or strengthening of the shallow fault did not occur during the Tohoku-oki earthquake.

2.2.2. Introduction

The occurrence of very large slip on the shallowest part of the megathrust during the 2011 moment magnitude (M_w) 9.0 Tohoku-oki earthquake [Fujiwara et al., 2011; Kodaira et al., 2012] is considered to be of paradigm-shifting importance in understanding tsunami generation and rupture mechanics [Wang, 2013]. Clear definition of the actual near-trench slip during the earthquake is critically needed for distinguishing between different trench-breaching slip scenarios that reflect fundamentally different fault mechanics [Wang and Kinoshita, 2013]. If the most near-trench segment of the megathrust is not only an integral part of the seismogenic zone but also underwent the greatest stress drop (coseismic weakening), the resultant slip distribution should feature a large increase towards the trench. If the shallow segment strengthens with increasing slip rate (velocity-strengthening) but is unable to fully resist a large rupture propagated from the deeper seismogenic zone [Wang and Hu, 2006], the resultant slip distribution should feature a distinct decrease towards the trench. If the shallow megathrust exhibits velocity strengthening to resist slip at low slip rates but weakens to facilitate slip once a sufficiently high slip rate (~1 m s^{-1}) is attained, a phenomenon known as dynamic weakening [Noda and Lapusta, 2013; Di Toro et al., 2011], the slip distribution may feature neither large increase nor large decrease towards the trench. All proposed models remain untested until we know the actual shallow slip.

However, despite the Tohoku-oki earthquake being by far the best instrumentally recorded subduction earthquake, the actual magnitude and distribution of the slip on the

shallow megathrust are essentially unknown. A compilation of 45 published slip models, including those constrained by seafloor geodetic [Sato et al., 2011; Kido et al., 2011] and tsunami wave data [Saito et al., 2011; Satake et al., 2013] (Tables 2.1 and 2.2), shows vastly different slip patterns in the most trenchward 100 km of the fault (Figure 2.1 and Figure 2.9). The differences are due partly to various simplifications in inverting coseismic observations to determine fault slip. For example, many of the finite fault models, especially those used for inverting tsunami data, assume a planar fault and/or consist of rather large subfaults of rectangular shape [Brown et al., 2015]. Depending on how fault slip is constrained at the trench, the peak slip determined by the inversion may be located at the trench or some distance away from the trench. However, the primary reason for the poor state of knowledge is the lack of near-field observations of horizontal seafloor displacements: all seafloor global positioning system (GPS) measurements were made more than 50 km away from the trench [Sato et al., 2011; Kido et al., 2011].

Displacement observations nearest to the trench are the differential bathymetry measured before and after the Tohoku-oki earthquake by Japan Agency for Marine-Earth Science and Technology [Fujiwara et al., 2011], which were not used by any of the 45 slip models in Figure 2.1. By modelling these data using a finite-element deformation model, we are able to estimate the near-trench slip distribution along the main corridor (Figure 2.1, inset). The inferred slip is of a very large average value (> 60 m) for the most seaward 40 km of the fault but with only a very small increase (~5 m) over this distance, indicating neither large net weakening nor large net strengthening of this fault segment during the earthquake.

2.2.3. Results

Differential bathymetry before and after the earthquake

During the earthquake, seafloors on the two sides of the trench moved in opposite directions, with the motion of the landward side much larger than that of the seaward side [Sun and Wang, 2015]. For each point of the seafloor with fixed geographic coordinates (longitude and latitude), water depth is changed because of the motion and deformation

of the sloping seafloor. The differential bathymetry is this change in water depth (Figure 2.2).

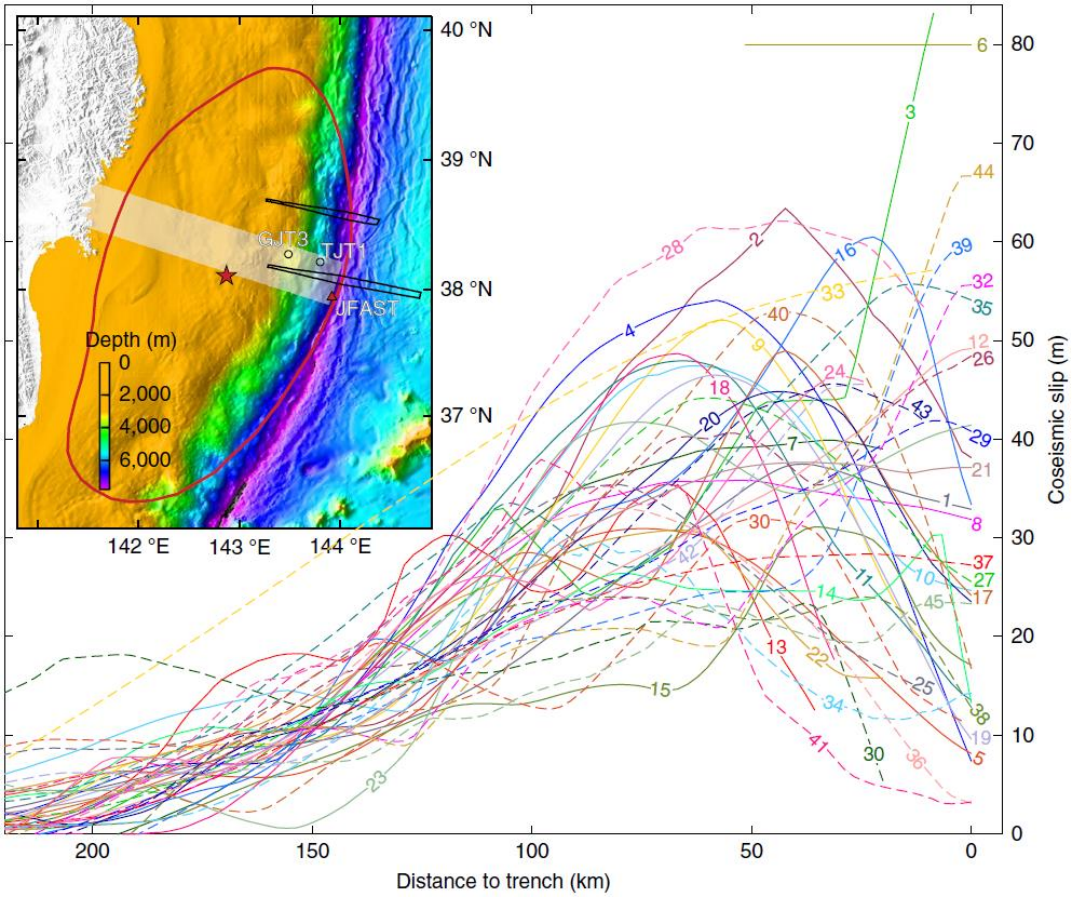

Figure 2.1. Compilation of 45 published slip models along a central corridor through the main rupture area. The white band in inset shows the corridor. Each curve is labelled with its model number as in Tables 2.1 and 2.2. Solid and dashed lines show models with and without, respectively, using seafloor GPS data as constraints. The subset of models that used tsunami data shows similar scatter of results near the trench (see Figure 2.9). In inset, red outline shows the 2-m contour of coseismic slip of the 2011 M_w Tohoku-oki earthquake from Wang and Bilek [2014], and star shows the epicentre. The two differential bathymetry tracks studied in this work are outlined in black. Track MY102 along the central corridor is the main focus of this study. Track MY101, ~50 km to the north, is discussed in Discussion. GJT3 is a nearby seafloor GPS site [Kido et al., 2011], and TJT1 is a nearby ocean bottom pressure (OBP) gauge site [Ito et al., 2011]. Red triangle shows the JFAST drilling location [Chester et al., 2013] where samples of the subduction fault zone were retrieved.

A SeaBeam 2112 multibeam sonar system with a frequency of 12 kHz and a beam width of 2° × 2° was used to collect bathymetry data along track MY102 (Figure 2.1, inset) in 1999, 2004 and in 2011 about 10 days after the earthquake [Fujiwara et al., 2011]. Using the seaward side of the track as the reference, Fujiwara et al. [2011] derived differential bathymetry of the landward side (Figure 2.3d), hereafter referred to as the observed differential bathymetry (ODB). In deriving the ODB, only the inner beam soundings within a 45° swath width among the total available 120° swath width were used, because uncertainties in water sound speed affect the inner beam to a lesser degree than the outer beam. By cross correlating the bathymetries before and after the earthquake, Fujiwara et al. [2011] estimated about 50 m horizontal and 10 m vertical motion of the landward side relative to the seaward side. This rough estimate did not invoke deformation modelling.

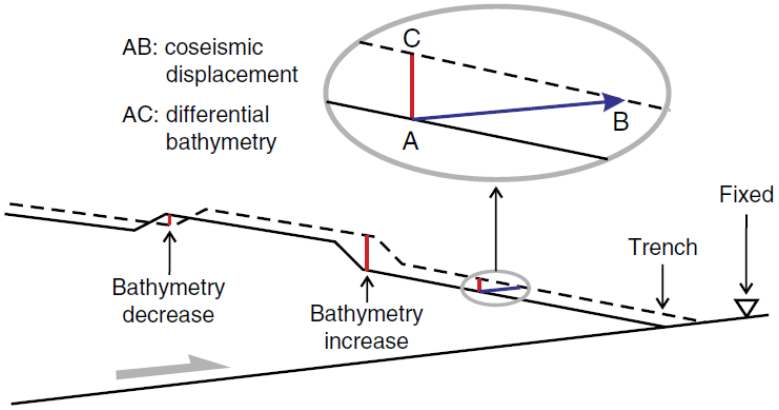

Figure 2.2. Cartoon illustration of the generation of differential bathymetry by a trench-breaching subduction earthquake. Solid and dashed lines show the bathymetry before and after the earthquake, respectively. While coseismic deformation is of long wavelength, local seafloor slope variations can lead to coherent short-wavelength features of bathymetry decrease or increase.

In this work, we model the 1999–2011 bathymetry differences for track MY102 reported by Fujiwara et al. [2011] and quantitatively determine the near-trench slip in the main rupture area of the Tohoku-oki earthquake. The 2004 bathymetry data are not

modelled except for testing purpose. The very short length of the seaward portion of the 2004 survey corridor, being only 1/5 of the 1999 survey, causes great difficulty in using it as the reference for ODB. Therefore the ODB based on the 2004 data is considered less reliable. Because seafloor displacement between 1999 and 2004 is expected to be very small, if not negligible, bathymetry differences between 1999 and 2004 provide an error estimate for ODB. The error thus estimated by Fujiwara et al. [2011] in terms of inferred total horizontal seafloor displacement is about 20 m, or about 10 m if resolved to the trench normal direction. This error to a large part is due to the inadequate length of the seaward section of the 2004 data. When applied to the 1999–2011 ODB, the actual error should be much less but difficult to quantify. Nonetheless, we do not expect the 1999–2011 error in the trench-normal direction to be much larger than 5 m. Bathymetry data for track MY101 (Figure 2.1, inset) [Kodaira et al., 2012], with poorer quality than the MY102 data, will be discussed in Section 2.2.4.

Because the pre-event bathymetry data were collected 12 years before the Tohoku-oki earthquake and the post-event data were collected 10 days after, there is a question to what degree the deformation reflected in the ODB is truly coseismic. We think it is extremely unlikely that a large part of the 1999–2011 ODB could be due to fault creep before the earthquake. To produce tens of metres of coseismic slip, the shallow megathrust must have accumulated sufficient slip deficit prior to the 2011 earthquake, due to either actual fault locking by itself or the stress-shadowing effect of a locked patch immediately downdip. Large afterslip of the shallow megathrust in this area during the 10 days after the earthquake is also extremely unlikely, given the absence of interplate aftershocks along the main rupture zone which underwent large stress drop [Nakamura et al., 2016]. Modelling of post-seismic seafloor GPS measurements does not indicate afterslip in this area, although it does suggest large near-trench afterslip to the south of the main rupture zone [Sun and Wang, 2015].

Synthetic differential bathymetry from deformation modelling

We use a three-dimensional elastic finite element model that includes actual fault

geometry and long-wavelength bathymetry (Figure 2.10). We add the model-predicted three-component coseismic displacements to the pre-earthquake bathymetry to produce synthetic differential bathymetry (SDB), in the manner illustrated in Figure 2.2. This model allows us to study the role of internal deformation of the upper plate as well as its rigid-body translation along the megathrust in generating the ODB. For example, a trenchward decrease in slip causes horizontal shortening and enhances seafloor uplift, and vice versa. We have tested hundreds of SDB models. Those subsequently discussed in this article are summarized in Table 2.3.

The SDB models for this small area are essentially two-dimensional, for lack of adequate constraints on along-strike variations of near-trench slip. For modelling convenience, we assign the same slip distribution over a wide along-strike range (> 400 km) that is much wider than the actual rupture area of the Tohoku-oki earthquake. Because the studied near-trench fault segment is quite shallow (< 10 km below sea surface), seafloor displacement is sensitive mainly to the fault slip right beneath the track and very insensitive to assigned slip more than 20 km away to the north and south.

We determine three parameters by comparing our SDB models with the ODB. The first two parameters are the average slip and the slip gradient over the most near-trench 40 km of the megathrust. The third parameter, a depth adjustment to the SDB of the landward side, is to account for a remnant depth bias in the acoustically derived ODB. Although temporal and spatial variations in water temperature, especially at shallow depths (< 2,000 m below sea surface), have been accounted for in deriving sound speed structure of ocean water for ODB determination, remaining uncertainties still lead to some remnant depth bias in the bathymetry data, even after maximizing cross correlations of the seaward (reference) side of different surveys. This is reflected in the ratio of the vertical to horizontal motion (~10 to 50 m) of the landward-side seafloor relative to the seaward side estimated by Fujiwara et al. [2011]. This ratio would require a fault dip > 10° near the trench that is much higher than the actual dip of ~5°.

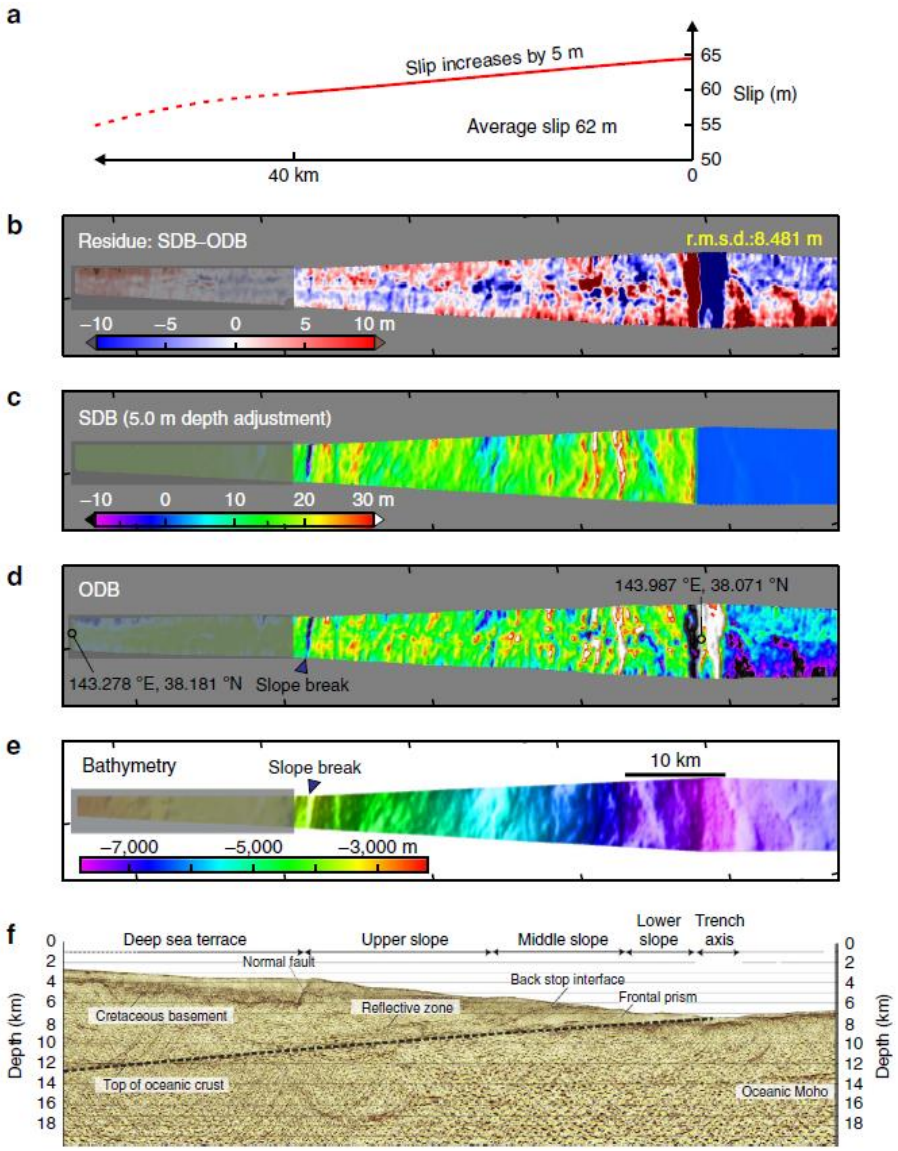

Figure 2.3. The optimal SDB model along the central corridor. The location of the corridor is shown in Figure 2.1 inset. (a) Fault slip distribution over the most seaward 40 km. (b) Residue between the SDB (c) and 1999–2011 ODB (d). (c) SDB produced using the slip distribution shown in Figure 2.3a. (d) 1999–2011 ODB. (e) Bathymetry acquired in 1999. The deep sea terrace segment (< 3,500 m; shadowed in Figures 2.3b–e) has large uncertainties in water sound speed and the interpreted seafloor depth. Possible submarine landslides at the trench axis are not modelled in the SDB. Therefore, these segments as well as that seaward of the trench are not included for calculating the r.m.s.d. (f) Seismic reflection section along the same track [Kodaira et al., 2012]. Thick dashed line shows the megathrust fault.

Optimal slip model along the main track

We search the model space defined by the three parameters described above to find the optimal SDB (Figure 2.3c) that best matches the 1999–2011 ODB (Figure 2.3d) and hence minimizes the root mean square deviation (r.m.s.d.) from the ODB (Figure 2.4). We have also done the search by minimizing the mean absolute deviation of SDB from ODB and obtained the same results as with the r.m.s.d. Incoherent short-wavelength fluctuations in the ODB associated with sea and seafloor conditions, stability of the acoustic and navigation systems, and errors in local water temperature and salinity profiles [Fujiwara et al., 2011] are not minimized, and are partly responsible for the relatively large r.m.s.d. For our study, the useful information is from long-wavelength coseismic deformation and coherent short-wavelength differential bathymetry due to topographic shift as shown in Figure 2.2. The useful information is reflected in the r.m.s.d. differences between different models that are based on the same data set.

The optimal model for the main corridor (Figure 2.3) requires an average fault slip of ~62 m in the most seaward 40 km of the megathrust with the slip increasing towards the trench by 5 m over this distance. The resultant bathymetry change is due to a combination of the updip motion of the overriding plate along the megathrust, seaward motion of the sloping seafloor and internal deformation of the upper plate. On the background of an overall uplift, coherent short-wavelength uplift and subsidence features are generated by local seafloor slope variations (Figure 2.2), such as at the slope break between the deep sea terrace and the upper slope (Figure 2.3e,f). Some of the differences between the optimal SDB and the ODB, especially in the amplitude of the short-wavelength features near the trench, may be due to inelastic deformation during or shortly after the earthquake [Tsuji et al., 2013] that are not modelled in this work. They also contribute to the relatively large r.m.s. In addition, for comparison, the optimal SDB based on the less reliable 2004–2011 ODB is shown in Figure 2.11.

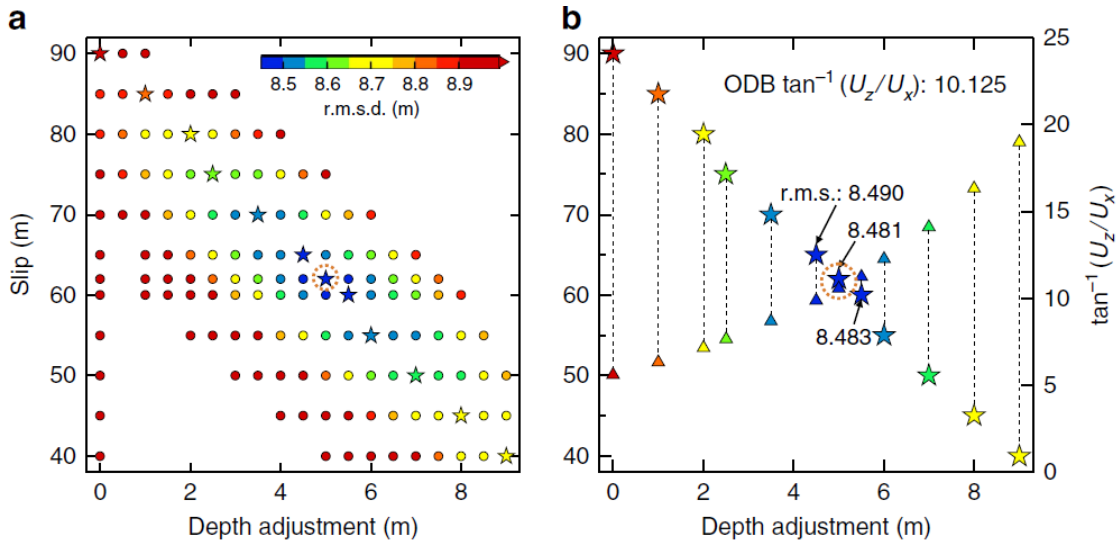

Figure 2.4. Search for optimal SDB in the parameter space for the central corridor. (a) R.m.s.d.'s of SDB models as a function of average slip and depth adjustment. Slip gradient is fixed at the optimal value (5 m increase over 40 km) for all the models. Stars represent the best models (lowest r.m.s.d.'s) given slip value. The maximum r.m.s.d. is 12.5 m (for 40-m slip and 0-m depth adjustment), but the colour scale saturates at 8.9 m. (b) Ratio of average vertical to horizontal motion (U_z/U_x) of the seafloor as a function of slip magnitude and depth adjustment. Each star-triangle pair represents one model, with the star being the same as in Figure 2.4a (same r.m.s.d. colour scale) and the triangle showing the corresponding arctangent value of (U_z/U_x). The $\tan^{-1}(U_z/U_x)$ of the optimal SDB agrees with the interpretation of the ODB (~10.125°) through cross correlation [Fujiwara et al., 2011]. In both panels, the orange dashed circle marks the optimal SDB model shown in Figure 2.3.

In deriving the SDB, there is a trade-off between the average slip and the depth adjustment, as shown in Figure 2.4 where the slip gradient is fixed at the optimal value of 5 m over the most seaward 40 km. For example, a model with a near-trench slip of ~90 m but with no depth adjustment can also produce ~10–20 m water depth decrease as in the ODB, but the resultant seafloor displacement poorly explains short-wavelength features in the ODB and results in a larger r.m.s.d. (Figure 2.12). The 5 m adjustment for the remnant depth bias required by the optimal average slip of 62 m accounts for the problematic fault dip (> 10°) mentioned above (Figure 2.4b).

Slip gradient

The frictional behaviour of the shallow megathrust during the earthquake is reflected not only in the magnitude of the slip but also in how the slip changes towards the trench. The sensitivity of SDB models to the slip gradient is illustrated by Figure 2.5, where the average slip is fixed at the optimal 62 m. These tests indicate that the SDB is not very sensitive to small changes in the slip gradient, such that assuming 0 or 10 m increase (over 40 km) will not produce a very different SDB from using the optimal value of 5 m. However, using the SDB results, we can confidently reject some larger slip gradient values that are more diagnostic in reflecting fault frictional behaviour. For example, increasing (Figure 2.6) or decreasing (Figure 2.7) the gradient by 20 m from the optimal value of 5 m over the most seaward 40 km obviously degrades the SDB's fit to the long-wavelength ODB. In other words, to explain the ODB in the main rupture area, the required coseismic slip exhibits neither large increase nor large decrease towards the trench.

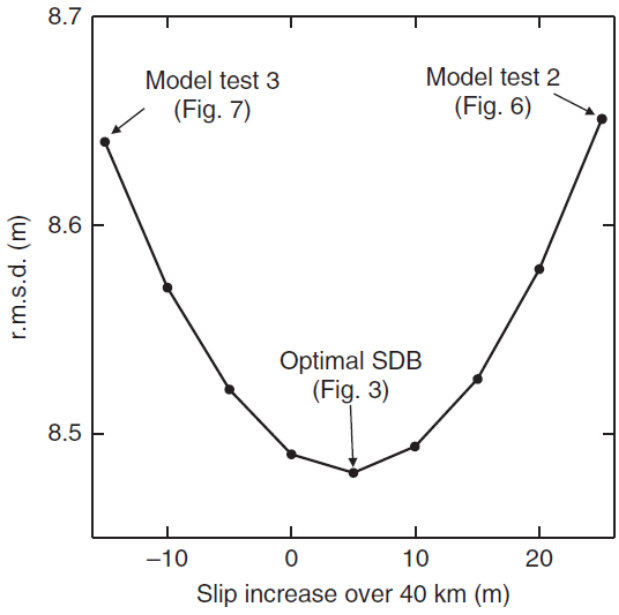

Figure 2.5. Sensitivity of SDB to slip gradient for the central corridor in terms of increase over the most near-trench 40 km. Trenchward increase (as in Figure 2.3a) is positive. Average slip is fixed at the optimal value of 62 m; the optimal depth adjustment varies with the slip gradient (not displayed). Note that "Fig. 3", "Fig. 6", and "Fig. 7" refer to the figure numbering in the published article. For this dissertation, they should be interpreted as "Figure 2.3", "Figure 2.6", and "Figure 2.7".

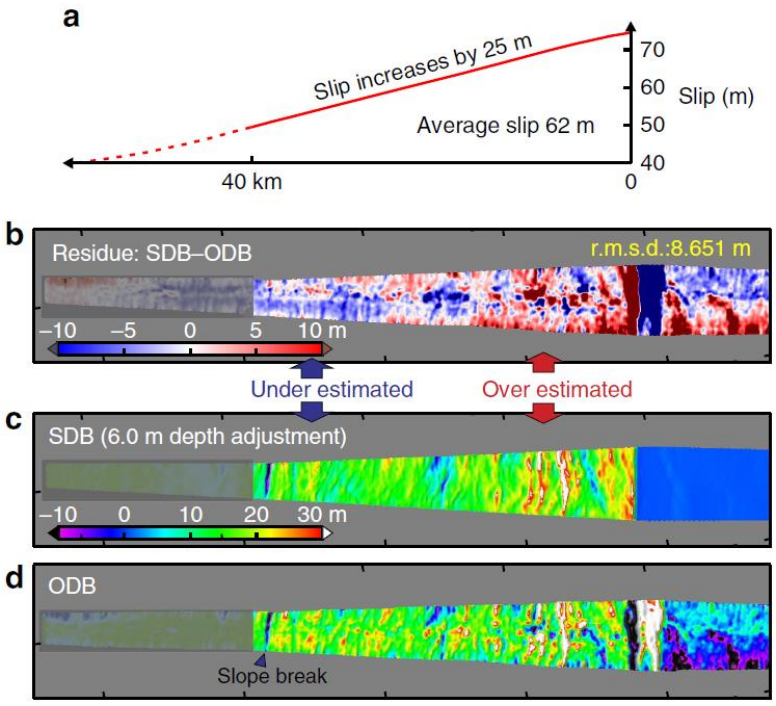

Figure 2.6. Testing SDB model for the central corridor with large trenchward increase in fault slip. Otherwise the figure is similar to Figure 2.3. (a) Fault slip distribution over the most seaward 40 km. (b) Residue between the SDB (c) and 1999–2011 ODB (d) showing overestimate of differential bathymetry near the trench but underestimate away from the trench. (c) SDB produced using the slip distribution shown in Figure 2.6a and optimal depth adjustment 6.0 m. (d) 1999–2011 ODB.

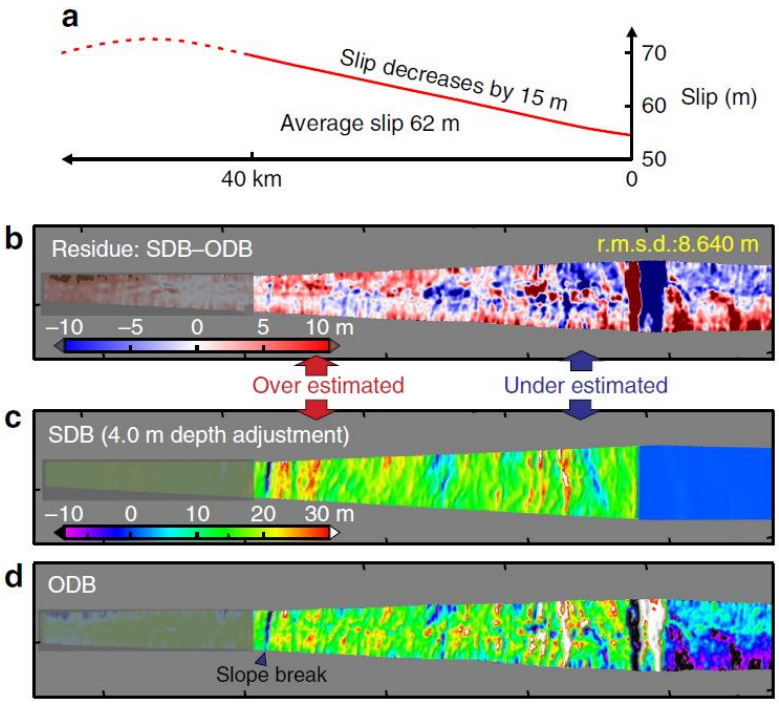

Figure 2.7. Testing SDB model for the central corridor with large trenchward decrease in fault slip. Otherwise the figure is similar to Figure 2.3. (a) Fault slip distribution over the most seaward 40 km. (b) Residue between the SDB (c) and 1999–2011 ODB (d) showing underestimate of differential bathymetry near the trench but overestimate away from the trench. (c) SDB produced using the slip distribution shown in Figure 2.7a and optimal depth adjustment 4.0 m. (d) 1999–2011 ODB.

2.2.4. Discussion

The large (> 60 m) slip with a gentle updip increase (~5 m) on the shallow megathrust shows a pattern different from nearly all the published rupture models in the main rupture area (Figure 2.8a). Uncertainties in this slip distribution are reflected in the sensitivity plots of Figures 2.4 and 2.5. This result allows us to narrow the range of possible slip behaviour scenarios as outlined in the opening paragraph. On the basis of the results shown in Figure 2.6, we can reject the scenario that the shallowest megathrust underwent greater coseismic weakening than the deeper part, which would cause a large slip increase towards the trench and extreme stress drop on the shallowest megathrust (green curve in Figure 2.8b). On the basis of the results shown in Figure 2.7, we can also reject the scenario that the shallow megathrust persistently exhibited velocity strengthening during the rupture process, which would lead to slip decrease towards the trench and stress increase on the shallowest megathrust (red curve in Figure 2.8b).

The optimal slip distribution (Figure 2.3a) suggests that the shallowest segment of the megathrust along the central corridor must have weakened to a degree similar to the deeper epicentral area. This can be accomplished in two ways: (1) the shallowest segment shares the same frictional behaviour as the deeper seismogenic zone (blue curve 1 in Figure 2.8b), or (2) the shallow segment exhibits velocity strengthening in the early phase of the rupture but dynamically weakens only when the slip accelerates to an adequately high rate (> 1 m s^{-1}) [Noda and Lapusta, 2013] (blue curve 2 in Figure 2.8b).

Based on the information from drill core samples retrieved during the JFAST expedition from the shallowest part of the fault zone 7 km landward of the trench axis (Figure 1) [Chester et al., 2013], the scenario represented by blue curve 2 in Figure 2.8b is more likely. The core samples show both distributed (pervasive scaly fabrics) and localized (millimetre-scale slip zones) shear deformation within the plate boundary fault zone [Chester et al., 2013; Kirkpatrick et al., 2015]. Co-existence of structures reflecting distinctly different modes of deformation is understood to imply rate-dependent frictional behaviour: the distributed deformation suggests low-rate velocity strengthening, while the

localized slip zones may suggest high-rate (> 1 m s^{-1}) dynamic weakening [Kirkpatrick et al., 2015]. The rate-dependent behaviour is observed also in laboratory friction experiments on these core samples [Ikari et al., 2015; Ujiie et al., 2013].

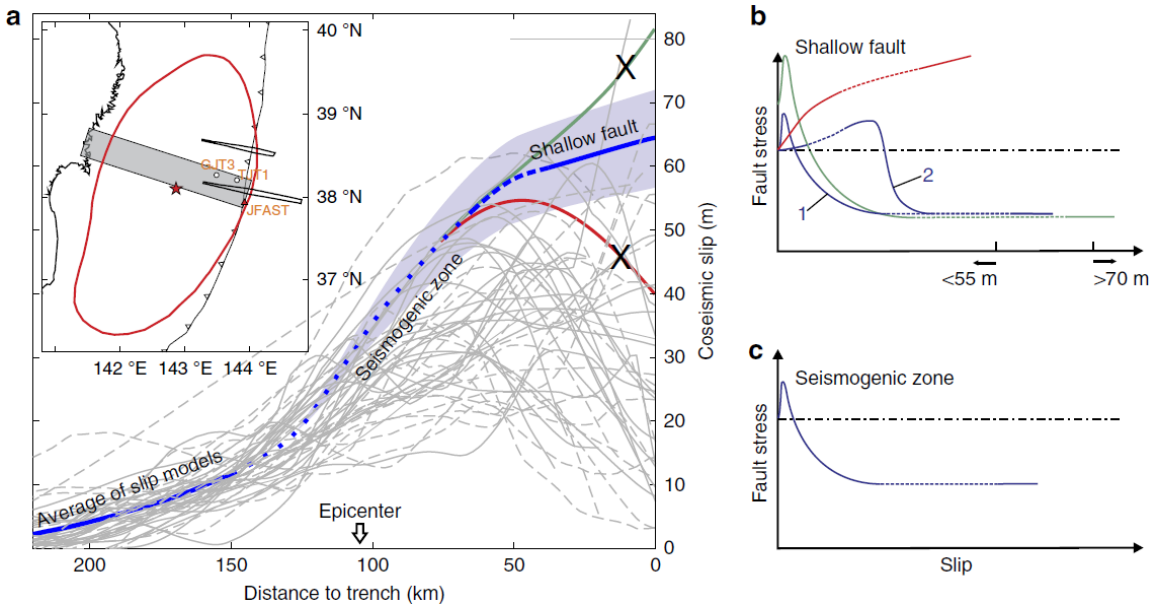

Figure 2.8. Illustrations of different mechanical behaviours of the shallow fault and their resultant slip distributions along the main corridor rejected and supported by SDB modelling. (a) Comparison between the optimal shallow fault slip of this work (blue line) and the 45 published slip models shown in Figure 2.1 (grey lines). The error range (blue shading) is based on models with r.m.s.d.'s < 8.55 m (Figure 2.4a). Dotted part of the blue line is a hand-drawn, poorly constrained smooth connection between the near-trench slip determined in this work and the slip further downdip based on an average of the 45 slip models. Slip scenarios represented by the green and red lines are not supported by the SDB analysis. (b) Schematic illustration of stress evolution of the shallowest fault segment. Red, green and the two blue curves represent mechanically different shallow fault behaviours, corresponding to lines of same colours in Figure 2.8a. Blue curve 2 represents a more likely scenario in which delayed dynamic weakening [Noda and Lapusta, 2013; Smith et al., 2015] of the shallow fault occurred during the earthquake. (c) Similar to Figure 2.8b but for the deeper seismogenic zone.

The ODB studied in this work allows us to determine shallow coseismic slip of the Tohoku-oki earthquake only in the main rupture area (Figure 2.8a). The slip must have

varied along the Japan Trench as controlled by heterogeneous fault properties and stress conditions. For example, SDB modelling for bathymetry track MY101 (near 38.6° N), about 50 km north of our central corridor (Figure 2.1, inset), shows a smaller average value (~40 m) but a larger increase (20 m) of slip to the trench, suggesting a higher degree of coseismic weakening of the shallow fault (Figure 2.13). The SDB results from both the central and northern tracks, together with the coseismic displacements recorded at nearby seafloor geodetic stations [Sato et al., 2011; Kido et al., 2011; Ito et al., 2011] can provide a much improved view of the trench-breaching slip of the Tohoku-oki earthquake as demonstrated by the slip distribution shown in Supplementary Figure 2.6, which is obtained by hand-extrapolating the results shown in Figures 2.3a and 2.13a.

2.2.5. Methods

Deformation model

We used the spherical-Earth finite-element code PGCviscl-3D developed by one of us (J.H.). The code uses 27-node isoparametric elements throughout the model domain. The effect of gravitation is incorporated using the stress-advection approach [Peltier et al., 1981]. Coseismic rupture is simulated using the split-node method [Melosh and Raefsky, 1981]. The code has been extensively benchmarked against analytical deformation solutions [Okada, 1985] and was applied to many subduction zone earthquake cycle modelling studies [Wang et al., 2012; Sun et al., 2014]. For modelling the coseismic deformation, the entire model domain is an elastic body. Other computer codes that can model elastic deformation, fault dislocation, and realistic fault and surface geometry will also suffice, although details of the model results could slightly differ if a Cartesian (as opposed to spherical) coordinate system is used and/or the effect of gravity is ignored or simulated in a different way. It can be readily shown that given the slip distribution, the effect of spatial variations in rock mechanical properties on affecting elastic coseismic deformation directly above the thrust fault is negligibly small, although the effect can be larger for deformation farther away or if stress drop instead of slip distribution is prescribed to the fault. Therefore, we use uniform values for the rigidity

(40 GPa), Poisson's ratio (0.25), and rock density (3,300 kg m^{-3}). We build a very large finite element mesh for the Japan Trench subduction zone to minimize the effect of the fixed lateral and bottom boundaries. The lateral boundaries are more than 1,000 km away from the rupture area, and the bottom boundary is set at 2,000 km depth (Figure 2.10). Subduction fault geometry is the same as in Sun et al. [2014] and is constrained by earthquake relocation results and seismic reflection profiles [Nakajima and Hasegawa, 2006; Kita et al., 2010; Zhao et al., 2009], except that we have fine-tuned the dip of the shallowest part of the megathrust to 5° in accordance with the seismic imaging results in Kodaira et al. [2012].

2.2.6. Acknowledgements

We thank the authors of the 45 published rupture models of the Tohoku-oki earthquake for providing the digital values of their slip models. T.S. was a member of the onboard Science Party of IODP Expedition 343 (JFAST). T.S. was supported by a University of Victoria PhD Fellowship, an Alexander and Helen Stafford MacCathy Muir Graduate Scholarship, a Bob Wright Graduate Scholarship and a Natural Sciences and Engineering Research Council of Canada discovery grant to K.W. This is Geological Survey of Canada contribution 20160230.

2.3. Supplementary Material

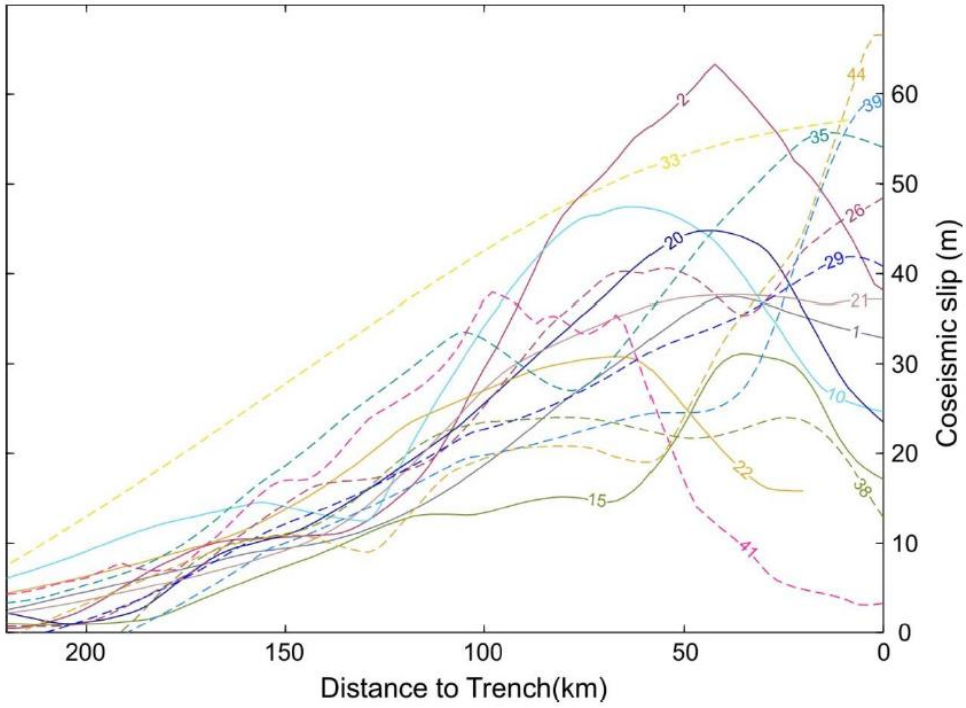

Figure 2.9. Published rupture models of the Tohoku-oki earthquake that included tsunami data as constraints. Each curve is labelled with its model number as in Tables 3.1 and 3.2. This is a subset of the models shown in Figure 2.1. The use of tsunami data in some of the recent models helped improve near-trench resolution of slip models such as models 26 and 35, but not in all the recent models.

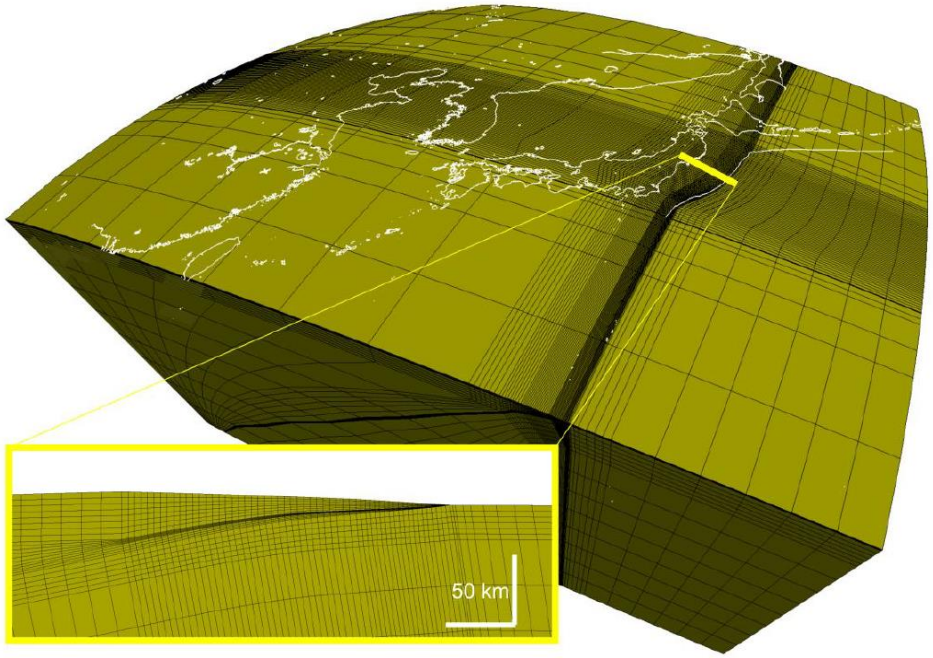

Figure 2.10. Finite element mesh used in this work for modelling coseismic deformation of the Tohoku-oki earthquake. Inset: cross-section view of the mesh along the central corridor for SDB calculation.

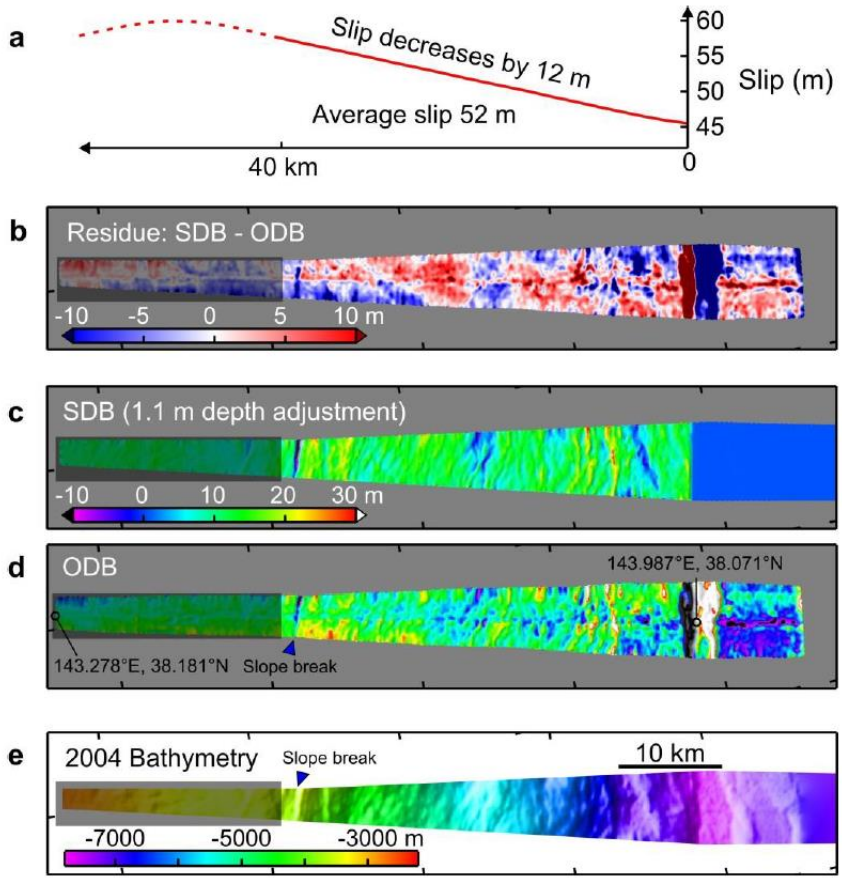

Figure 2.11. Optimal SDB model for the central corridor using 2004–2011 ODB. (a) Fault slip distribution over the most seaward 40 km. (b) Residue between the SDB and 2004–2011 ODB. (c) SDB produced using the slip distribution shown in (a). (d) 2004–2011 ODB. The limited coverage seaward of the trench renders the ODB image much less reliable than the 1999–2011 image (Figure 2.3d). (e) Bathymetry acquired in 2004.

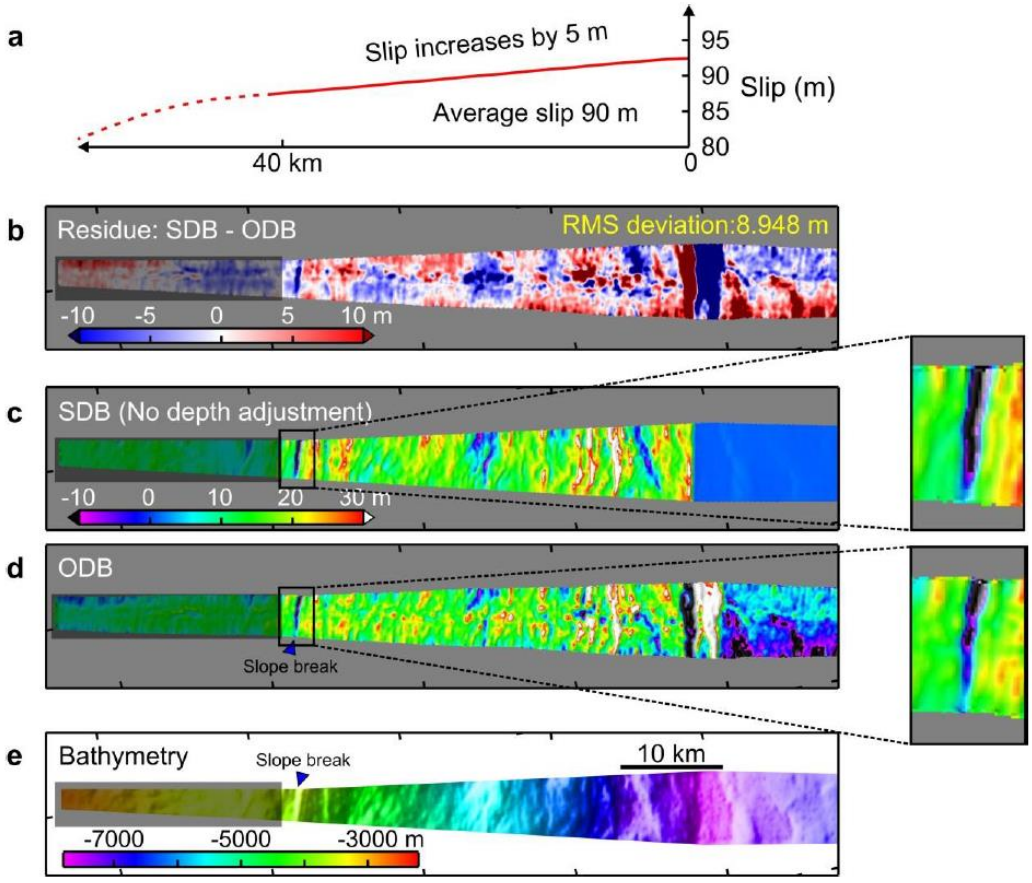

Figure 2.12. SDB model for the central corridor with an average fault slip of 90 m and zero optimal depth adjustment. Otherwise the figure is similar to Figure 2.3. (a) Fault slip distribution over the most seaward 40 km. (b) Residue between the SDB and 1999–2011 ODB. (c) SDB produced using the slip distribution shown in (a). (d) 1999–2011 ODB. (e) Bathymetry acquired in 1999. The zoom-in area in (c) and (d) shows that the SDB incorrectly predicts a wider area of local bathymetry decrease than in the ODB.

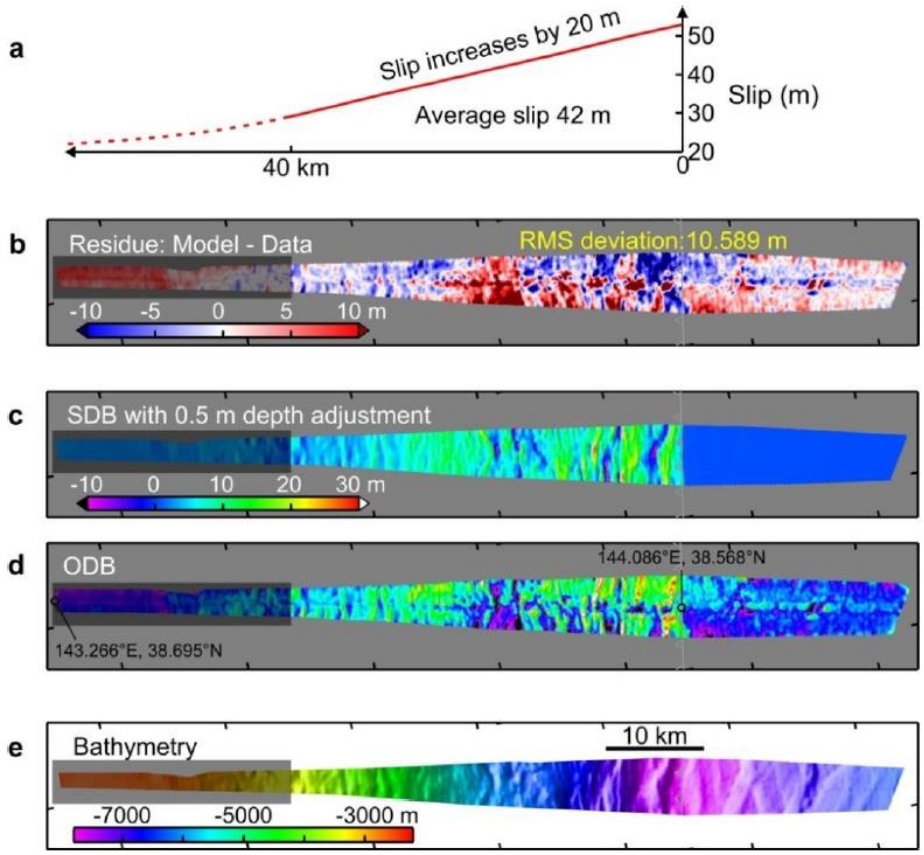

Figure 2.13. Optimal SDB model along bathymetry track MY101 about 50 km north of the central corridor. Otherwise the figure is similar to Figure 2.3. (a) Fault slip distribution. (b) Residue between the SDB and ODB. (c) SDB produced using the slip distribution shown in (a). (d) ODB from data collected in 1999 and May 2011. (e) Bathymetry acquired in 1999.

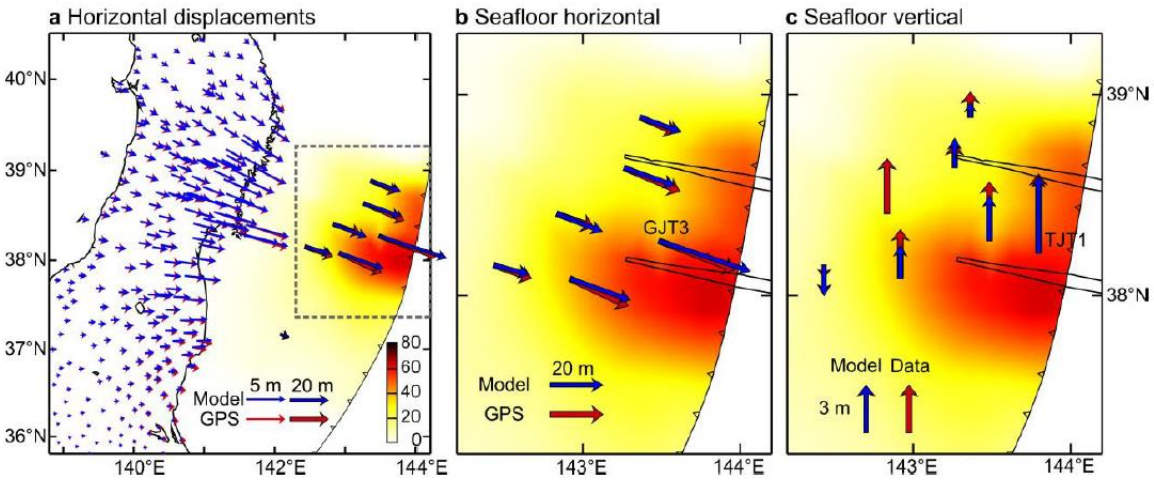

Figure 2.14. A slip distribution of the Tohoku-oki earthquake that can satisfy differential bathymetry and is also compatible with other geodetic data. (a) Broad-scale view of the model slip distribution (in metres) and model-predicted horizontal displacements in comparison with land-based [Ozawa et al., 2012] and seafloor [Sato et al., 2011; Kido et al., 2011] GPS measurements. (b) Enlarged view of the main rupture area (dashed box in (a)) with the two bathymetry tracks shown. (c) View of the main rupture area showing model-predicted uplift in comparison with coseismic uplift inferred from seafloor GPS [Sato et al., 2011; Kido et al., 2011] or OBP [Ito et al., 2011] data. The slip model shown in this figure represents an earthquake of M_W=9.02 if rigidity is assumed to be 40 GPa. The slip distribution is not obtained by inversion but is based on hand-extrapolating the slip distribution shown in Figure 2.3a and Figure 3.5a. The forward modelling of surface displacements is done with the same mesh as shown in Figure 3.2. The purpose is not to fit all the geodetic data, but to show that the magnitude of seafloor displacements is consistent with most data, especially the ODB data at site TJT1. A more complete understanding of the heterogeneous shallow slip distribution would require more near-trench observations.

Table 2.1. Rupture models of the Tohoku-oki earthquake obtained by including seafloor GPS data.

Model No.	Reference	Data used	Seafloor GPS sites used	Peak slip* (m)	Peak slip along the corridor (m)
1	Gusman et al., 2012	Tsunami (seafloor pressure and tide gauge), land and seafloor GPS	5 sites	42.0	37.5
2	Hooper et al., 2013	Land and seafloor GPS, tsunami (seafloor pressure gauges), satellite altimetry	5 sites	78.7	63.4
3	Iinuma et al., 2012	Land and seafloor GPS, seafloor pressure sensors	7 sites	87.9	83.0
4	Imakiire and Koarai, 2012	Land and seafloor GPS	≤5 sites	59.2	54.1
5	T. Ito et al., 2011	Land and seafloor GPS	3 sites	59.8	31.0
6	Y. Ito et al., 2011	Seafloor pressure and acoustic ranging records	1 site	80.0	80.0
7	Kubo and Kakehi, 2013	Teleseismic body waves, land and seafloor GPS	5 sites	42.9	39.9
8	Kyriakopoulos et al., 2013	Land and seafloor GPS (FEM inversion)	5 sites	39.2	35.9
9	Lee et al., 2011	Teleseismic waves, land and seafloor GPS, strong motion	5 sites	56.1	52.0
10	Minson et al., 2014	High-rate GPS, land and seafloor GPS, tsunami	7 sites	73.8	47.4
11	Ozawa et al., 2012	Land and seafloor GPS	7 sites	64.0	48.0
12	Perfettini and Avouac, 2014	Land and seafloor GPS	6 sites	53.6	49.2
13	Pollitz et al., 2011	Land (including very far field) and seafloor GPS	5 sites	38.5	35.5
14	Pulvirenti et al., 2014	Land and seafloor GPS	5 sites	35.1	30.3
15	Romano et al., 2014	Land and seafloor GPS, tsunami (DART, coastal wave, seafloor pressure gauges) (FEM inversion)	7 sites	44.7	31.1

16	Shao et al., 2012	Teleseismic, local strong motion, land & seafloor GPS	5 sites	63.5	60.5
17	Silverii et al., 2014	Land and seafloor GPS	7 sites	57.7	49.0
18	Wang et al., 2012	Land and seafloor GPS, InSAR	5 sites	49.9	48.7
19	Wang et al., 2013	Strong motion (K & KiK nets), land and seafloor GPS	5 sites	47.6	46.5
20	Wei et al., 2012	Strong motion, land and seafloor GPS, DART data	5 sites	48.0	44.8
21	Wei et al., 2014	Tsunami (open ocean GPS buoy), land and seafloor GPS	5 sites	48.7	37.7
22	Yokota et al., 2011	Strong motion, teleseismic, land and seafloor GPS, tsunami	5 sites	35.3	30.8
23	Yue and Lay, 2013**	High-rate GPS, teleseismic P wave, Rayleigh wave, seafloor GPS	5 sites	70.4	41.7
24	Zhou et al., 2014	Land and seafloor GPS	7 sites	53.0	46.5

* The peak values were obtained from the original finite fault slip models.

** Updated version of this model available on SRCMOD website is used in this work.

Table 2.2. Rupture models of the Tohoku-oki earthquake obtained without using seafloor GPS data.

Model No.	Rupture model	Data used	Peak slip* (m)	Peak slip along the corridor (m)
25	Ammon et al., 2011	Teleseismic P wave, Rayleigh wave, high-rate GPS	40.0	35.4
26	Bletery et al., 2014**	High-rate GPS, strong motion, teleseismic waves, tsunami, land GPS	64.0	48.4
27	Diao et al., 2013	Land GPS	45.8	44.2
28	Frankel et al., 2013	Strong motion and High-rate GPS	65.6	62.1
29	Fujii et al., 2011	Tsunami (coastal tide gauge, offshore GPS wave, pressure gauge, open ocean buoy)	47.9	41.9
30	Hayes, 2011	Teleseismic body and surface waves	33.5	31.9
31	Ide et al., 2011	Teleseismic waves (empirical Green's function)	30.7	23.4
32	Lay et al., 2011	Teleseismic P wave	58.1	55.6
33	Maeda et al., 2011	Tsunami (coastal tide gauge, seafloor pressure gauge)	57.0	57.1
34	Maercklin et al., 2012	Accelerometer (strong motion) (back projection)	54.8	29.5
35	Melgar and Bock, 2015	High-rate GPS, strong motion, tsunami (wave gauge)	61.7	55.7
36	Miyazaki et al., 2011	Land GPS	34.2	33.0
37	Ozawa and Fujita, 2013	InSAR, land GPS	28.7	28.4
38	Saito et al., 2011	Tsunami (pressure gauge, GPS wave gauge)	33.4	24.0
39	Satake et al., 2013	Tsunami (open ocean buoy, coastal tide gauge, pressure gauge)	69.1	58.9
40	Satriano et al., 2014	Teleseismic P wave (back projection technique)	56.5	52.9

41	Simons et al., 2011	Land GPS, tsunami (open ocean buoy)	59.7	38.0
42	Suzuki et al., 2011	Low frequency (0.01–0.125 Hz) strong motion	48.3	45.5
43	Yagi and Fukahata, 2011	Teleseismic P wave	51.2	45.6
44	Yamazaki et al., 2011	Teleseismic P wave, Tsunami (GPS buoy, wave gauges, open ocean Buoy)	70.3	66.7
45	Yoshida et al., 2011	Strong motion	46.9	23.5

* The peak values were obtained from the original finite fault slip models.

** Seafloor GPS data were testing purpose only, not used in the predicted model.

Table 2.3. SDB models presented in this paper*.

SDB Model	ODB to fit	Average slip	Slip gradient**	Depth adjustment***	RMS deviation	Figure Number
Optimal	1999–2011 central	62.0	5.0	5.0	8.481	2.3
Huge slip	1999–2011 central	90.0	5.0	0.0	8.948	A.4
Slip increase	1999–2011 central	62.0	25.0	6.0	8.651	2.6
Slip decrease	1999–2011 central	62.0	-15.0	4.0	8.731	2.7
2004	2004–2011 central	52.0	-12.0	1.1	8.116	A.3
North track	1999–2011 northern	42.0	20.0	0.5	10.589	A.5

* Slip, depth adjustment, and RMS deviation are all in metres.

** Slip gradient is given as linear change (m) over the most near-trench 40 km. Positive values indicate increase towards the trench.

*** Given the average slip and slip gradient in each model, the listed depth adjustment is the optimal value (for obtaining the lowest RMS deviation).

Chapter 3. Afterslip Following the 2012 Costa Rica Earthquake

This chapter is the second of the two chapters addressing the kinematics and mechanics of the shallowest part of subduction faults. The main body of this chapter consists of a manuscript in preparation for journal submission, investigating the trench-breaching afterslip following the 2012 M_w 7.6 Costa Rica earthquake. This trench-breaching afterslip represents a fault behaviour very different from the trench-breaching coseismic slip of the 2011 M_w 9.0 Tohoku-oki earthquake discussed in the preceding chapter. Section 3.1 describes basic manuscript information. Section 3.2 presents the manuscript itself. Supplementary material that accompanies the manuscript is presented as section 3.3.

3.1. Manuscript Information

3.1.1. Author, Coauthor, and Outside Contributions

Section 3.2 consists of a manuscript in preparation. The author of this dissertation T.S. carried out most of the forward and inverse modelling of this study. Coauthor E.D. and T.S. jointly designed the study. Coauthor K.W. developed the slip distribution inversion and stress modelling codes used in this study, and participated in the modelling. T.S., E.D., and K.W. together did most of the writing. Coauthor J.Y. processed the GNSS data used in the study. Deep-ocean borehole observatories that provided the pressure data used in this chapter were established by coauthor E.D. and H. Villinger (University of Bremen).

3.1.2. Citation

Sun, T., E. E. Davis, K. Wang, and Y. Jiang, Trench-breaching afterslip following the 2012 M_w 7.6 Costa Rica earthquake, in preparation.

3.1.3. Authors' Names and Affiliations

Tianhaozhe Sun[1], Earl E. Davis[2], Kelin Wang[2,1*], Yan Jiang[2]

[1] School of Earth and Ocean Sciences, University of Victoria, Victoria, British Columbia, Canada V8P 5C2

[2] Pacific Geoscience Centre, Geological Survey of Canada, Natural Resources Canada, 9860West Saanich Road, Sidney, British Columbia, Canada V8L 4B2

[*] Corresponding author: kelin.wang@canada.ca

3.1.4. Manuscript Format

The figures included in Section 3.2 have been numbered to maintain consistency with the rest of the dissertation. References cited in the manuscript are included in the bibliography of this dissertation.

3.2. Trench-Breaching Afterslip Following the 2012 M_w 7.6 Costa Rica Earthquake

3.2.1. Abstract

Large rupture of the shallowest portion of subduction thrust faults (megathrusts), such as in the 2011 moment magnitude (M_w) 9.0 Tohoku-oki earthquake [Fujiwara et al., 2011; Sun et al., 2017; Kodaira et al., 2012], can generate the most devastating tsunamis. However, it remains unclear whether such trench-breaching rupture is typical of other subduction earthquakes [Wang, 2013; Lay, 2015]. The main difficulty in answering this question is the lack of geodetic monitoring at the trench in all the subduction zones of the world. Seafloor and sub-seafloor fluid pressure measurements at two closely located borehole observatories in the Middle America trench have provided clear evidence for the absence of trench-breaching rupture during the 2012 M_w 7.6 Costa Rica earthquake, and for the presence of substantial trench-breaching afterslip at slow rates after the rupture [Davis et al., 2015]. Here we compare postseismic seafloor pressure change at the

outermost subduction prism and coastal Global Navigation Satellite System (GNSS) displacements. The same temporal characteristics of the deformation at the two disparate sites indicate a common afterslip process over a wide spatial range updip of the rupture. By determining the co- and post-seismic slip distributions and inferring the associated shear stress changes on the megathrust, we show that the mechanical behaviour varies in the dip direction. The slip behaviour of the shallow megathrust at Costa Rica is consistent with conventional conceptual models [Moore and Saffer, 2001; Scholz, 1998; Wang and He, 2008], and opposite to the behaviour of the shallowest megathrust during the Tohoku-oki event.

3.2.2. Manuscript Main Body

Whether subduction megathrusts slip to trenches during or after large earthquakes is an important question for understanding tsunami generation and fault dynamics. Traditionally, the shallow part of the fault is assumed to strengthen during earthquakes to resist rupture propagation but slip aseismically afterwards, but the dramatic trench-breaching coseismic slip during the 2011 moment magnitude (M_w) 9 Tohoku-oki earthquake [Sun et al., 2017] seriously challenges the conventional thinking. However, because of the paucity of near-trench geodetic monitoring, there is little observational information to tell whether trench-breaching rupture is common or rare. The conventional view is based on inferences from the mechanical properties of the fault zone materials at shallow depths [Moore and Saffer, 2001; Scholz, 1998; Wang and He, 2008], not on direct observations. Fluid pressure monitoring by two borehole observatories off Costa Rica during and after a M_w 7.6 subduction earthquake in 2012 has now provided unconventional geodetic information directly from the trench [Davis et al., 2015].

At Nicoya Peninsula, Costa Rica, the Cocos plate subducts beneath the Caribbean Sea plate at a rate of 8 cm/yr [DeMets et al., 2010]. In addition to land-based seismic and geodetic networks, which are already monitoring the megathrust seismogenic zone at an unusually close range owing to the small (~70 km) trench-coast distance [Dixon et al., 2013], there are two ODP CORK (Ocean Drilling Program, Circulation Obviation

Retrofit Kit) borehole hydrologic observatories near the seafloor outcrop of the megathrust, one (Hole 1253A) roughly 175 m seaward drilled into the subducting Cocos plate, and the second (Hole 1255A) drilled into the outermost subduction prism roughly 745 m landward of the fault outcrop (Figures 3.1 and 3.2c). They have been recording fluid pressures at and below the seafloor at intervals of 10 min since December 2003 [Davis et al., 2015; Morris et al., 2003; Davis and Villinger, 2006; Davis et al., 2011] (see Section 3.2.3).

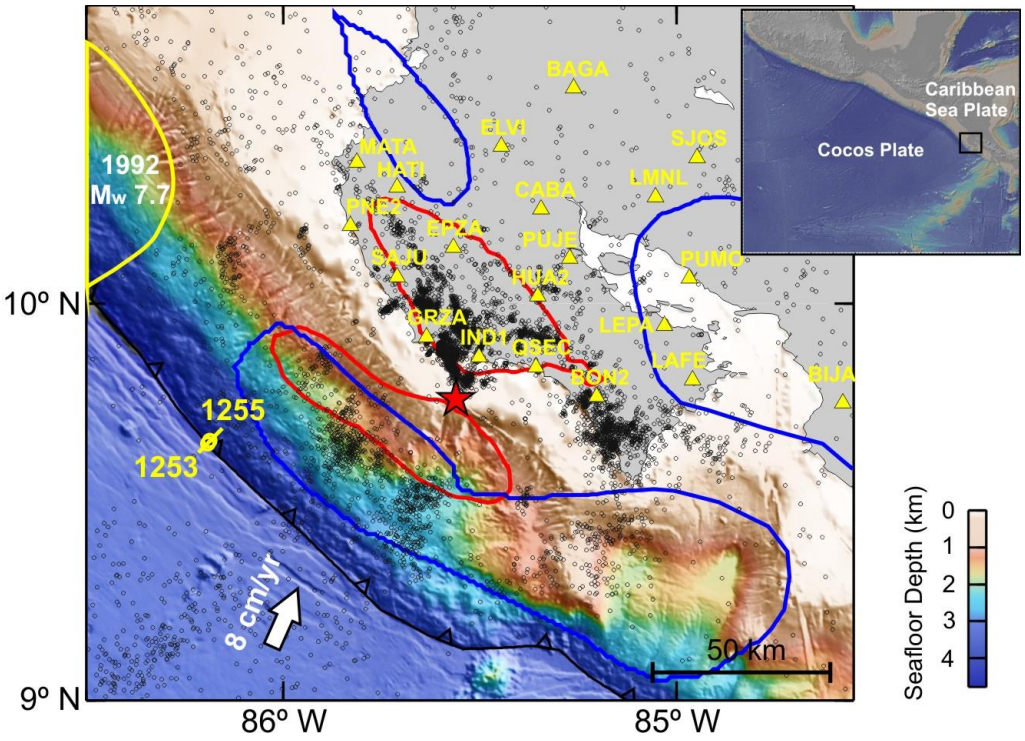

Figure 3.1. 1-m coseismic slip contour (red) of the 2012 Costa Rica earthquake estimated in this work. Red star shows the epicentre of this earthquake [Yue et al., 2013]. Yellow line shows the southern part of the rupture area of a M_w 7.7 tsunami earthquake in 1992. Blue lines encompass areas of ≥ 0.1 m cumulative megathrust slow slip over 5 years before the 2012 earthquake [Dixon et al., 2014]. Black circles show relocated aftershocks before the end of 2012 [Yao et al., 2017]. Name-labelled yellow triangles are continuous GNSS sites; their postseismic time series are shown in Figure 3.6. Locations of the two near-trench borehole CORK pressure observatories are marked using yellow circles, and the location of the seismic profile in Figure 3.2c using a yellow line. White arrow shows the convergence between the subducting Cocos plate and the overriding Caribbean Sea plate. Inset: Box outlines the study area.

These pressure measurements provide critical information on crustal deformation at the trench. Seafloor pressure reflects water depth. It is influenced by oceanographic phenomena such as tides, waves, and wind-forced sea-level changes but is also sensitive to vertical seafloor deformation. Because of the proximity of the two observatories, long-wavelength oceanographic signals in their measurements are common, and the oceanographic "noise" can be mostly removed by subtracting the record of Hole 1253A (the incoming plate "reference") from the record of 1255A (Figure 3.2a lower panel and Figure 3.5). Any change in this differential seafloor pressure reflects a temporal change in the depth difference between the two sites. Sub-seafloor fluid pressure also responds to oceanographic loading, along with hydrologic diffusion within the formation, but it is also sensitive to volumetric strain. To remove the effect of oceanographic loading, we subtract the seafloor pressure scaled by the accurately defined tidal loading efficiency [Davis and Villinger, 2006] from the sub-seafloor record. We further suppress the unaccounted for tidal residuals arising from earth tides and hydrologic diffusion by applying a 12.5-hour-moving-average filter (Figure 3.2a upper and middle panels). Any change in the processed sub-seafloor pressure reflects primarily volumetric strain of the rock formation, with a pressure increase indicating contraction and a pressure decrease indicating dilatation.

At the time of the 5 September 2012 M_w 7.6 Costa Rica earthquake, GNSS stations on the Nicoya Peninsula detected trenchward horizontal motion up to 68 cm and uplift up to 53 cm (Figure 3.3a, red arrows), delineating substantial coseismic slip beneath the peninsula [Protti et al., 2014]. At this time there was no change in differential seafloor pressure between the two observatories across the trench, indicating no trench-breaching rupture directly updip of the hypocentral area (Figure 3.2a lower panel). Coseismic sub-seafloor-pressure drops were recorded at both sides, however, suggesting that some near-trench crustal dilatation was induced by fault slip in the epicentral area [Davis et al., 2015].

After the earthquake, while GNSS sites continued to move trenchward [Malservisi et al., 2015], several episodes of seafloor pressure changes were detected at the trench over

the first month, with the first episode starting ~1.5 days after the earthquake and each episode lasting 2–3 days (Figure 3.2a). Within each episode, seafloor pressure of the prism site (1255A) decreased relative to the incoming-plate site (1253A), indicating stepwise uplift of the prism toe. Concurrent with the seafloor pressure changes, sub-seafloor pressures dropped at Hole 1253A, indicating dilatation in the incoming plate, and increased at Hole 1255A, indicating contraction of the outer prism or in the outer thrust fault zone. These strain signals are consistent with the passing by of an updip-propagating slip front along the megathrust [Davis et al., 2011; LaBonte et al., 2009]. The observed prism toe uplift and the concurrent contrasting volumetric strains on different sides of the trench thus indicate trench-breaching afterslip.

Over a longer time (> 1 year), the seafloor pressure change (prism toe uplift) at the trench and the postseismic GNSS displacements on land (see Section 3.2.3) share the same temporal characteristics (Figure 3.2b and Figure 3.6). For this and other earthquakes with $M_w < 8$, crustal deformation caused by viscoelastic relaxation of the coseismically induced stresses in the mantle is small [Sun and Wang, 2015]. We conclude that the relative seafloor pressure change between the two sites mainly reflects deformation caused by the trench-breaching afterslip of the megathrust; the erratic pressure variations in the early half of 2013 appear to be associated with disturbances of the incoming plate reference site signal, probably instrumental in origin (Figure 3.5). The overall similarity of the temporal characteristics of the onshore and offshore displacements suggests a common driving function of the afterslip over a wide updip range.

We use both the GNSS displacements and the seafloor pressure changes to determine the coseismic slip and afterslip (cumulative to the end of 2014) of this earthquake. For each slip mode, we iteratively use two types of model (see Section 3.2.3). Nonlinear Bayesian inversion of GNSS data is performed using a standard uniform elastic half-space model (Figure 3.7a), in which point-source dislocation solutions [Okada, 1992] (or Green's functions) can be efficiently derived. Because the half-space model cannot accommodate seafloor slope at the trench, a finite element model (FEM) (Figure 3.7c) with actual long-wavelength seafloor topography is used for forward modelling near-

trench deformation. Fault slip distribution from one model is updated with the other model, and only two complete iterations are needed to obtain the final, FEM-based slip distribution shown in Figure 3.3. An example of intermediate results, i.e., of the first round of half-space inversion of the GNSS data, is shown in Figure 3.8.

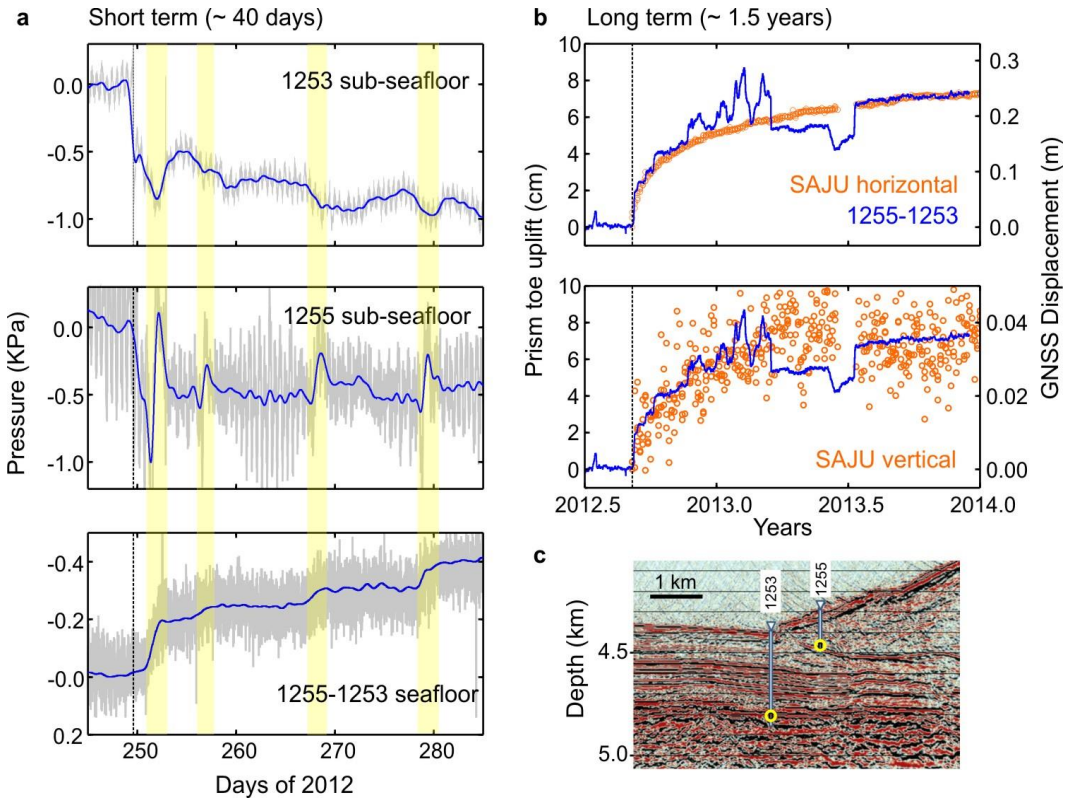

Figure 3.2. Seafloor and sub-seafloor (formation) fluid pressure measurements during and after the 2012 Costa Rica earthquake. The locations of CORK pressure observatories are shown in Figure 3.1. Vertical dashed line indicates the time of the earthquake. (a) Grey curves show the original pressure records, and blue curves show the time series after a 12.5-hour-moving-average filter is applied (see Section 3.2.3). Yellow bars highlight slow slip episodes, during which seafloor and sub-seafloor pressures show concurrent anomalies. (b) Comparison between the uplift of the prism toe (reflected by seafloor pressure change) and postseismic displacements (orange dots) of on-land GNSS site SAJU. (c) Cross-trench seismic reflection profile through the CORK observatories (location shown in Figure 3.1). Yellow circles indicate depths of sub-seafloor pressure monitoring (see Section 3.2.3).

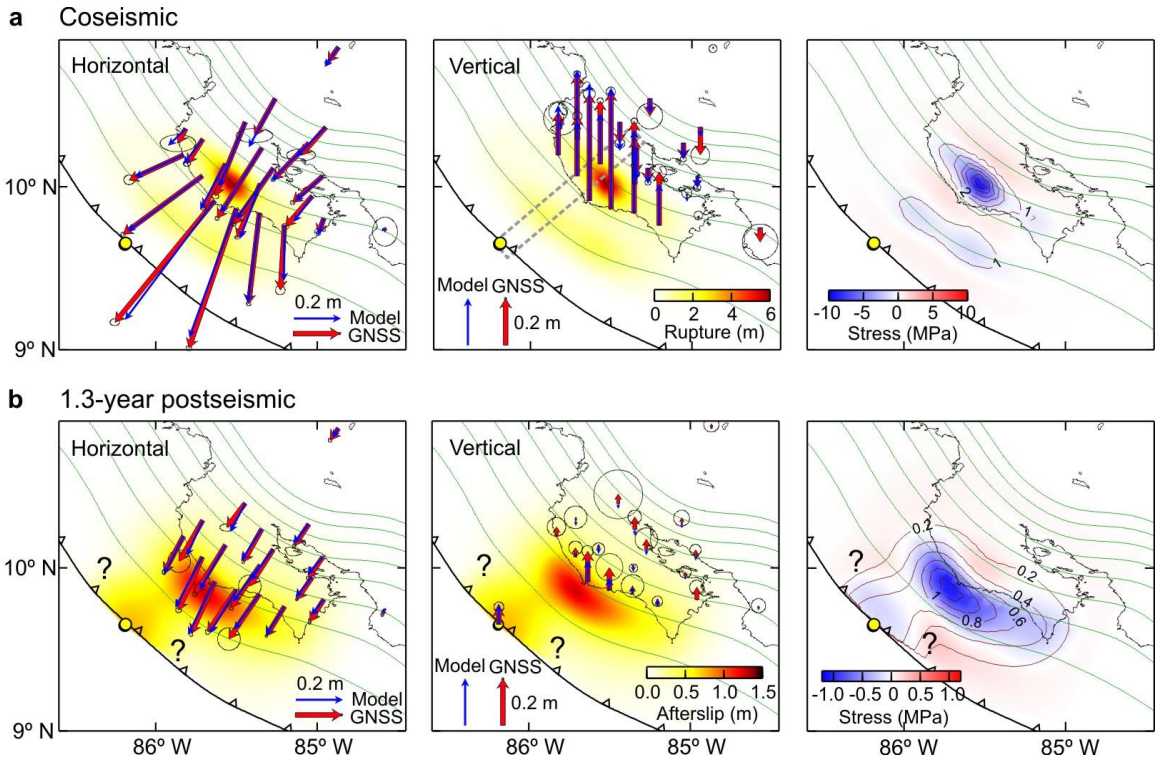

Figure 3.3. Co- and post-seismic (1.3-year) slip distributions of the 2012 Costa Rica earthquake and their associated stress changes on the megathrust. Depth below sea level of the megathrust is contoured at 10 km intervals (green curves). For each row, the left and middle panels show horizontal and vertical displacements, respectively, and coseismic or postseismic slip distribution determined in this work. Observed cumulative postseismic displacements over the first 1.3 years after the earthquake are listed in Table 3.1. Model displacements are calculated using a finite element mesh (shown in Figure 3.7c) from the shown slip distributions with actual fault geometry and long-wavelength surface topography. The right panel shows the associated shear stress changes on the megathrust. Contours show slip distributions (same as in the left and middle panels) in m. (a) Coseismic deformation. Dashed box shows location of the profile used in Figure 3.4a. (b) 1.3-year postseismic deformation. A correlation scale of 25 km is used in the inversion (see Section 3.2.3). Question marks near the trench indicate the regions where afterslip cannot be constrained by the existing GNSS and pressure observations (Figure 3.9). Using a different correlation scale (50 km) does not change the main characteristics of the results (Figure 3.10).

Our preferred coseismic slip model shows a primary rupture zone with a peak slip > 5 m at depths of 25-30 km beneath the Nicoya Peninsula, downdip of the earthquake hypocentre beneath the coast [Yue et al., 2013], and a secondary rupture area of much less slip offshore at shallower depths (~ 10 km). For the trench-breaching afterslip, the two existing observatories do not allow any estimates of slip variation along the trench (Figure 3.3b and Figure 3.9), but the data do provide strong constraints in the trench-normal direction. Afterslip distributed fully from the hypocentral region to the trench is required to explain both the onshore and offshore deformation. Details of the slip distribution are affected by smoothing constraints used in the inversion (see Section 3.2.3), but very different degrees of smoothing do not change the main characteristics of the results (Figure 3.10). Above all, our model tests confirm that without the pressure observations at the trench, the land-based GNSS observations alone would not be able to resolve the trench-breaching afterslip (Figure 3.8b).

Using the slip distribution shown in Figure 3.3, we then calculate the static shear stress changes on the megathrust associated with the above determined coseismic slip and afterslip (Figure 3.3). The method of stress calculation is exactly the same as in Brown et al. [2015]. With an assumed Poisson's ratio of 0.25 and rigidity of 40 GPa, we determine a peak static coseismic stress drop > 8 MPa on the fault in the main rupture zone. Using a lower rigidity will lead to a proportionally lower magnitude of the stress drop but does not change its distribution. Fault areas updip and downdip of the main rupture underwent stress increase during the earthquake, except within the shallow secondary rupture area. After the earthquake, afterslip of the shallow megathrust is accompanied with small stress drop over a wide spatial range updip of the rupture (~1 MPa).

Our model of the slips and stress changes suggests substantial variations in the mechanical behaviour of the subduction fault in the dip direction (Figure 3.4). The main rupture zone underwent large coseismic weakening (stress drop). At a shallower depth just offshore, the fault underwent coseismic strengthening (stress increase), allowing a sharp updip decrease of coseismic slip (from 5 m to 0.5 m). The coseismically increased stress in the offshore region then drove slow afterslip all the way to the trench. We speculate that the shallowest part of the fault underwent brief episodes of minor

strengthening in response to "jerky" afterslip motion of its neighbouring segment immediately downdip. Because of the low rigidity of the unconsolidated sediments at the shallowest depths, stress variations can only be small, although they cannot be estimated by our uniform-rigidity model (Figure 3.4c).

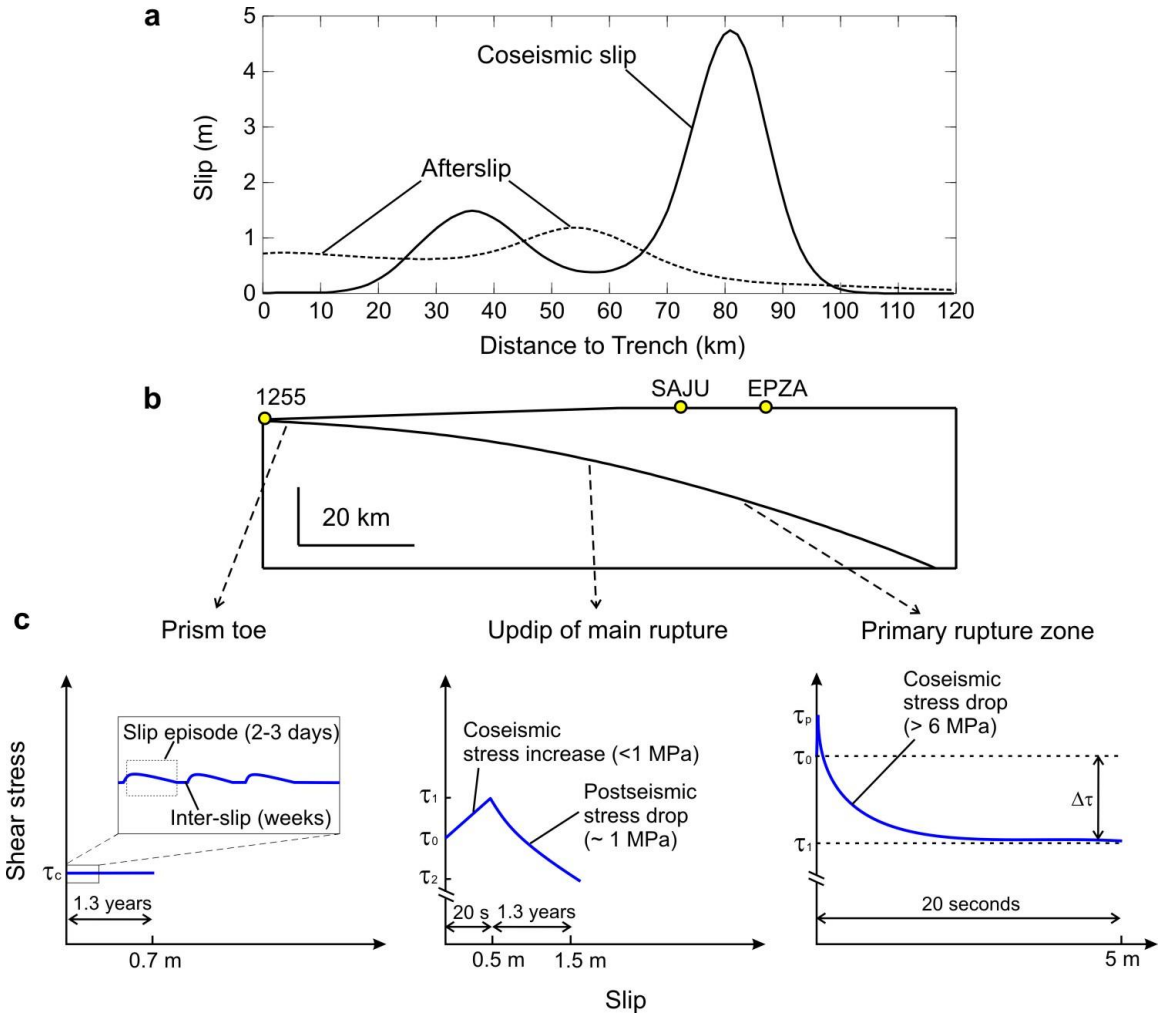

Figure 3.4. Illustration of different mechanical behaviours of three segments of the megathrust in the dip direction. (a) Magnitudes of coseismic slip and afterslip along a trench-normal corridor (shown as the dashed grey box in Figure 3.3a middle panel) that covers the CORK observatories and on-land GNSS stations SAJU and EPZA. (b) Geometry of the megathrust along this corridor. (c) Stress-slip evolution during and after the 2012 Costa Rica earthquake. $\boldsymbol{\tau}_0$ and $\boldsymbol{\tau}_1$ represent pre-earthquake stress and stress at the end the dynamic rupture, respectively, $\boldsymbol{\tau}_p$ the peak stress during rupture, $\Delta\boldsymbol{\tau}$ the static stress drop, and, $\boldsymbol{\tau}_2$ the stress updip of the main rupture at the end of 2013 (end of the modelling period). Beneath the prism toe, $\boldsymbol{\tau}_c$ represents the yield stress of the weak megathrust at the shallowest depth.

Seafloor and sub-seafloor pressure observations indicate that similar trench-breaching slow slip, which induced pressure changes of the same pattern as during the postseismic slip episodes, also occurred before the 2012 earthquake and cumulated about 0.26 m slip during 2007–2012 [Davis et al., 2015]. This slip followed slow slip events at greater depths [Davis et al., 2015; Dixon et al., 2014; Jiang et al., 2012; Jiang et al., 2017], indicating that slip of the shallowest megathrust is likely driven by stress stored downdip away from the outermost prism. If the behaviour of the shallow fault segment over these 5 years is typical of the entire interseismic period, these slow slip events plus the afterslip determined in this work can roughly accommodate plate convergence over the ~50 year earthquake cycle at the shallowest depth.

The trench-breaching afterslip studied here represents one type of slip-to-trench that is in sharp contrast to that which occurred during the 2011 Tohoku-oki earthquake. Near-trench geodetic observations that have been and/or will soon be conducted, such as at Nankai, Hikurangi, and northern Cascadia [Wallace et al., 2016; Wallace et al., 2016; Saffer et al., 2016; Davis et al., 2010; Yao et al., 2017], promise opportunities to deepen our understanding of various slip modes of shallow megathrusts, and improve assessments of the associated hazards.

3.2.3. Methods

CORK borehole observatories

The two borehole hydrologic observatories were installed during ODP Leg 205 in late 2002. Hole 1253A was drilled through ~400 m of hemipelagic and pelagic sediments, ~31 m of gabbroic sill, ~30 m of sediments underlying the sill, and ~140 m of igneous rocks as a part of the oceanic basement. Hole 1255A was drilled into the toe of the subduction prism to a depth of 153 m below the seafloor (mbsf), across the base of the decollement at ~144 mbsf. For each site, seafloor fluid pressures are measured by a pressure sensor on the borehole wellhead, and formation fluid pressures are measured by pressure sensors at the wellheads connected to two formation screens at different depth intervals through hydraulic lines. In Hole 1253A, the upper and lower screens are centred

at 453 and 500 mbsf, respectively. Because formation pressures recorded at the two intervals are almost identical, here we show only the measurements from the upper interval. In Hole 1255A, the upper and lower screens are centred at 127 and 140 mbsf, respectively. Because formation pressures recorded at the lower interval suffered from leakage at the bottom of the hole since September 2004, here we also show only the measurements from the upper interval. More complete descriptions of the observatories and the pressure sensors can be found in Morris et al. [2003].

Obtaining postseismic GNSS displacements

We used continuous GNSS data collected from 2002-2016 to derive pre- and post-earthquake deformation fields. Raw observations downloaded from the UNAVCO data archive (www.unavco.org/data/data.html) were smoothed and resampled at 5-minute intervals. Daily site positions were then determined using the procedure described in Jiang et al. [2012]. We excluded observations with less than 4 hours of observations. The daily positions were first placed in a loosely constrained terrestrial reference frame, and then were aligned to the IGb08 reference frame [Rebischung et al., 2012] through a 7-parameter transformation. To obtain postseismic GNSS displacements, we removed the interseismic trend of GNSS time series using the pre-earthquake portion of the data and an offset due to a M_w 6.6 aftershock (Figure 3.6). All the GNSS time series can be fit by the following logarithmic function with characteristic time (τ) of 5 days (Figure 3.6).

$$f(t) = c \times \log\left(1 + \frac{t}{\tau}\right)$$

Using this function, we derived cumulative GNSS site displacements and their errors (as standard deviation of displacement residues) through the end 2014 (Table 3.1).

Inversion of GNSS displacements

The nonlinear Bayesian inversion algorithm used this work was developed by one of the authors (KW) based on the theory of Tarantola [1982] and was used to determine slip

distributions of Cascadia slow slip events [Dragert and Wang, 2011] and the 2012 M_w 7.8 Haida Gwaii earthquake [Nykolaishen et al., 2015]. Nonlinearity arises because each slip vector is represented by the logarithm of its magnitude and its rake. See Dragert and Wang [2011] for a description of the inversion method. The Green's functions are derived using the point-source dislocation solution [Okada, 1992] along the three-dimensionally curved megathrust in a uniform elastic half-space. The Poisson's ratio is assigned to be 0.25; no other moduli are needed for an elastic half-space. For the megathrust geometry, we use the model of slab1.0 [Hayes et al., 2012], except that a correction is made to the shallow part of the fault so that the depth of the fault below seafloor, instead of depth below sea level, is used as the fault depth in our flat-surface model [Wang et al., 2003]. We divide the fault area into 555 triangular elements of about 8 km size (Figure 3.7a), each assigned a slip vector. The inversion involves the use of correlation scales in the dip and strike directions to describe probabilistically the smoothness of the slip vector distribution [Dragert and Wang, 2011]. In this work, we use the same correlation scale for the two directions. For both the coseismic slip and afterslip, the preferred correlation scale is 25 km, similar to the depth of the fault below the GNSS network. A correlation scale much smaller than the fault depth does not yield useful or even convergent results. A larger correlation scale such as 50 km leads to a smoother slip distribution but does not change the main characteristics of the results (Figure 3.10).

Finite element modelling

We use a spherical-Earth finite-element model that includes actual fault geometry and long-wavelength surface topography for forward modelling both on-land and near-trench deformation. The finite-element code is the same as used in Sun et al. [2017], Wang et al. [2012], and Sun et al. [2014] for studying crustal deformation at other subduction margins. It employs 27-node isoparametric elements throughout the model domain, with the effect of gravitation incorporated using the stress advection approach [Peltier et al., 1981] and fault slip simulated using the split-node method [Melosh and Raefsky, 1981]. Very fine elements are used near the trench and close to the subduction fault (Figure 3.7c). For modelling both coseismic and postseismic deformation, we use

uniform rock rigidity (40 GPa), Poisson's ratio (0.25), and rock density (3,300 kg/m^3) to be compatible with the companion uniform half-space model used for the inversion. Any other numerical codes will produce similar results, with minor differences depending on whether and how the effect of gravity is simulated and whether a spherical or Cartesian coordinate system is used.

3.2.4. Acknowledgements

We thank Bob Meldrum, Bob Macdonald, Heinrich Villinger, Martin Heesemann and others for providing technical expertise throughout this ODP CORK installation and monitoring project. Other teams and companies such as remotely operated vehicle Jason, R/V Atlantis, Richard Brancker Research, Ltd., Paroscientific, Inc., SeaCon/Brantner and Associates, Inc., Mecco, Inc., and Tadiran, Ltd. have provided support for either ship time or instrument components. Funding for instruments and site visits has been provided through U.S. National Science Foundation Grants OCE-25145 and -1130146. We thank Jiangheng He for developing the finite element code used in this work. T.S. was supported by a University of Victoria PhD Fellowship, an Alexander and Helen Stafford MacCathy Muir Graduate Scholarship, a Bob Wright Graduate Scholarship and a Natural Sciences and Engineering Research Council of Canada discovery grant to K.W.

3.3. Supplementary Material

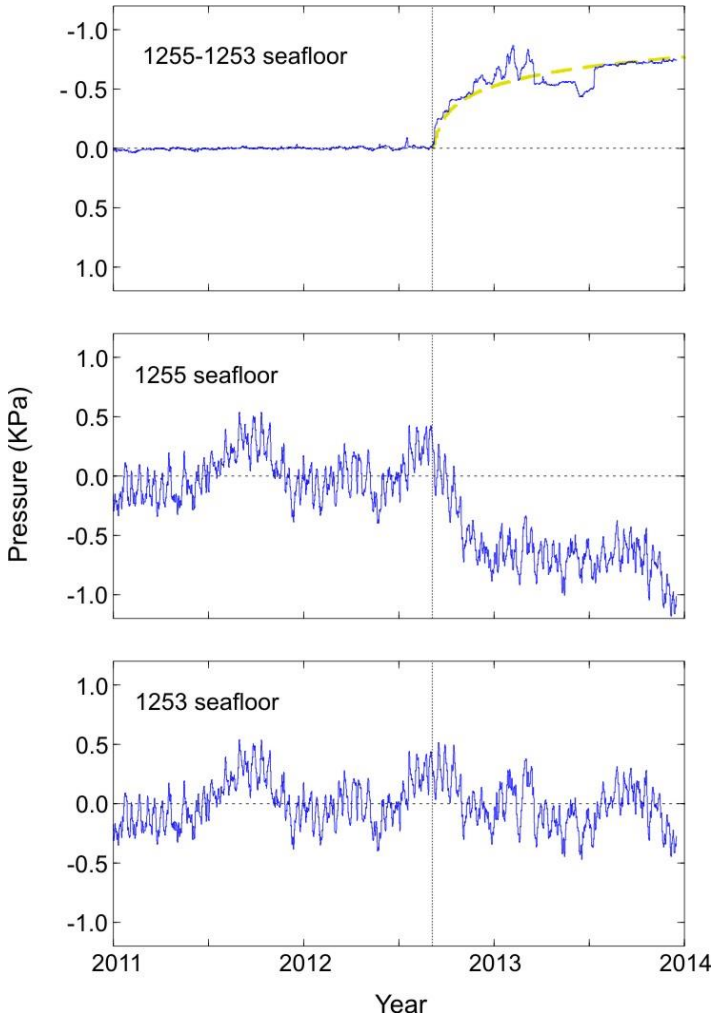

Figure 3.5. Seafloor pressure measurements at 1253 (incoming plate site) and 1255 (prism toe site) and their difference. For the differential seafloor pressure (1255-1253), the yellow dashed line shows a logarithmic function fit (see Section 3.2.3), with the same characteristic time (5 days) as used for fitting land-based GNSS displacements (Figure 3.6).

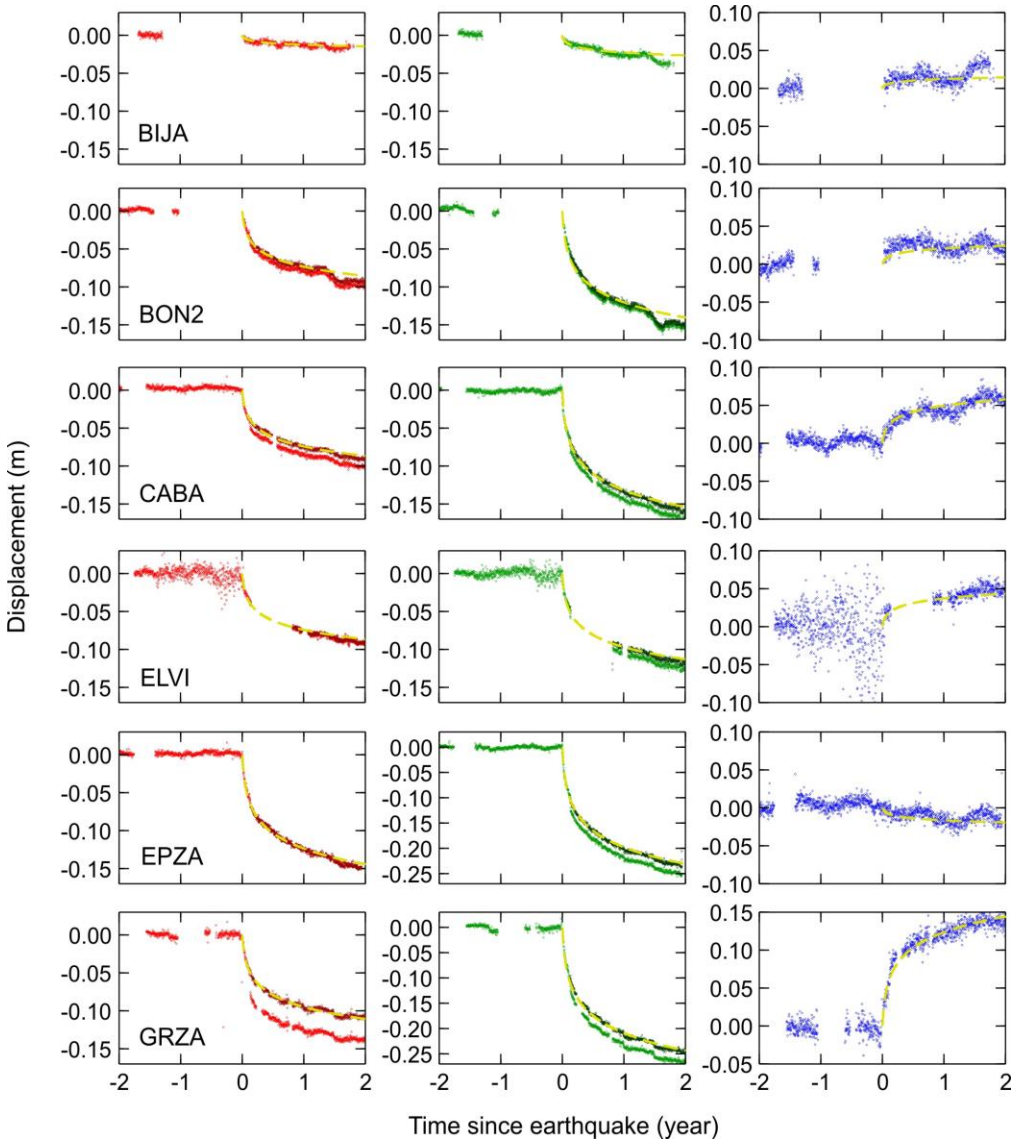

Figure 3.6. Displacements of GNSS stations. Each row is for one site (site name given in the left panel) and from left to right shows the east, north, and vertical components. Coseismic offset of the 2012 M_w 7.6 earthquake [Protti et al., 2014] and interseismic trend due to megathrust locking [Feng et al., 2012] have been removed. Dots in deeper red and green show GNSS displacements after correcting for an offset caused by a M_w 6.6 aftershock [Malservisi et al., 2015]. Yellow dashed curves show a logarithmic function fit to the corrected time series (see Section 3.2.3).

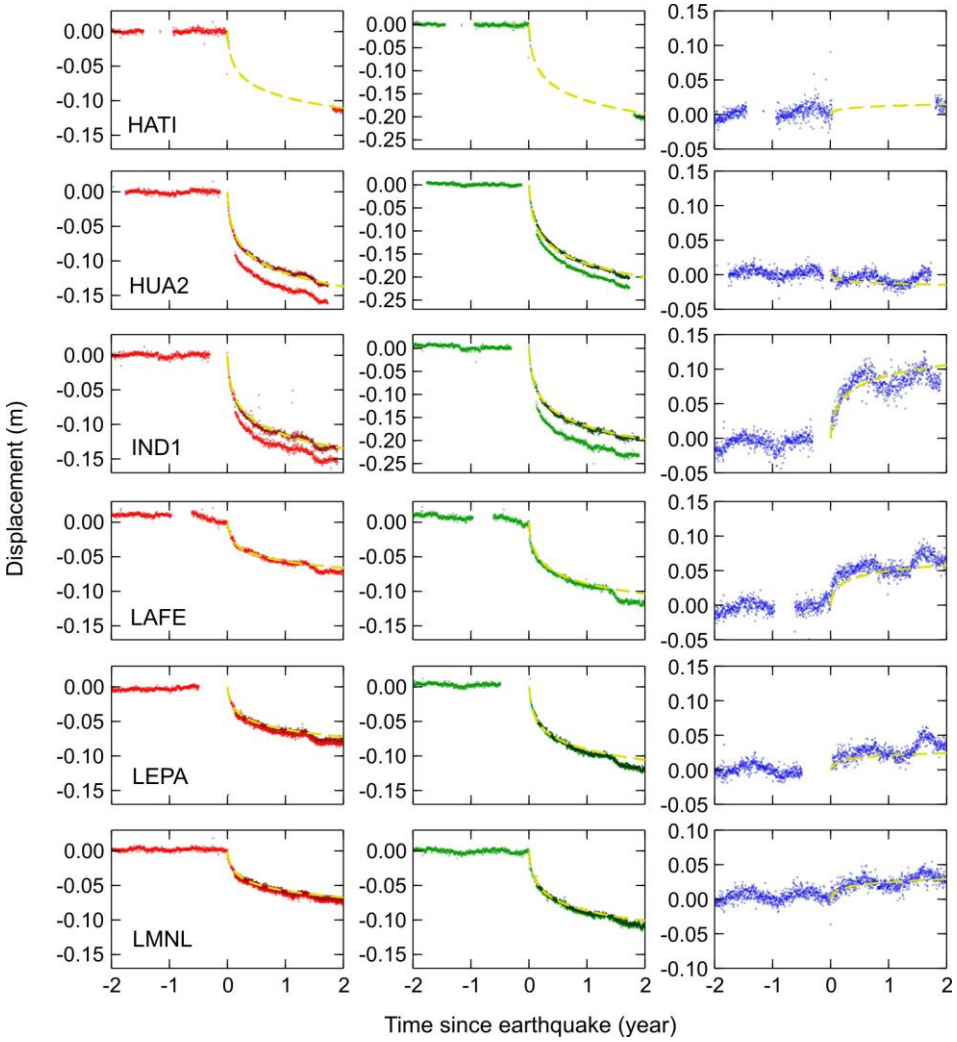

Figure 3.6. continued

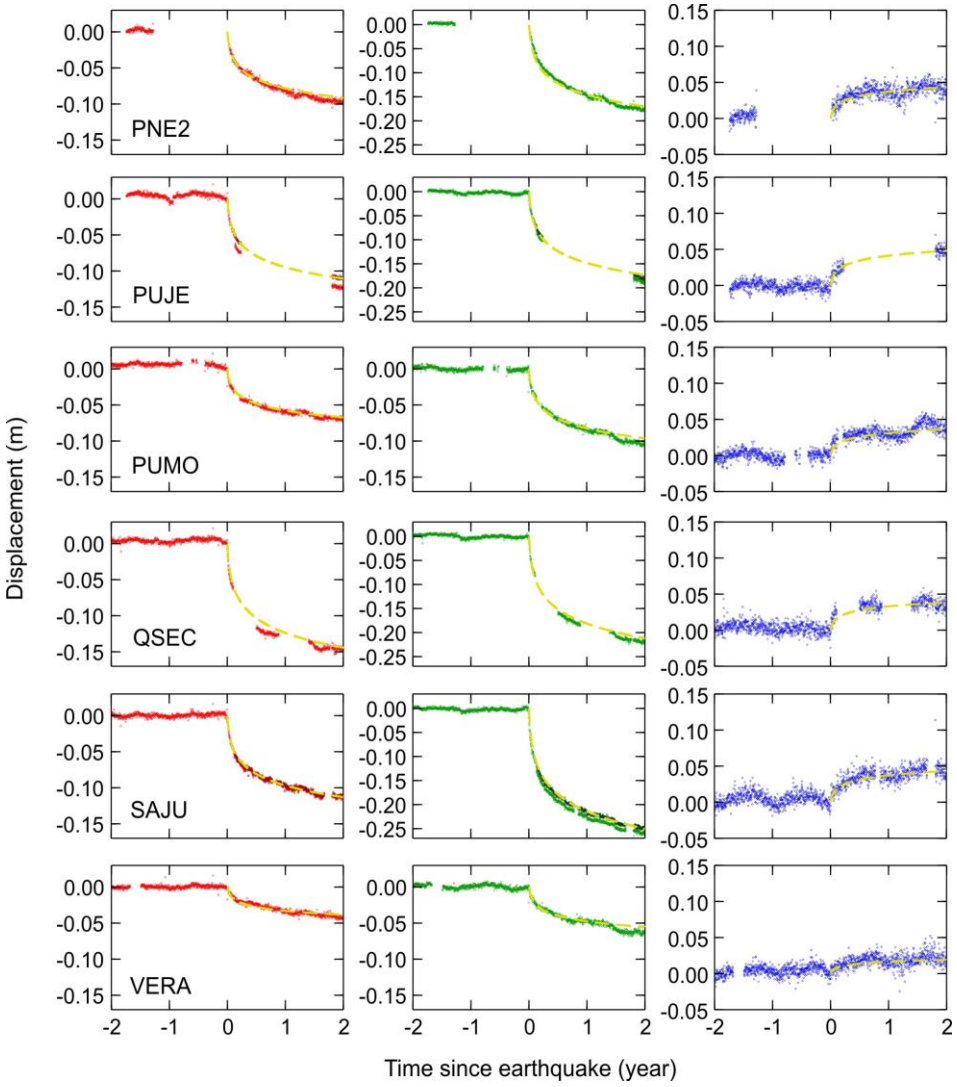

Figure 3.6. continued

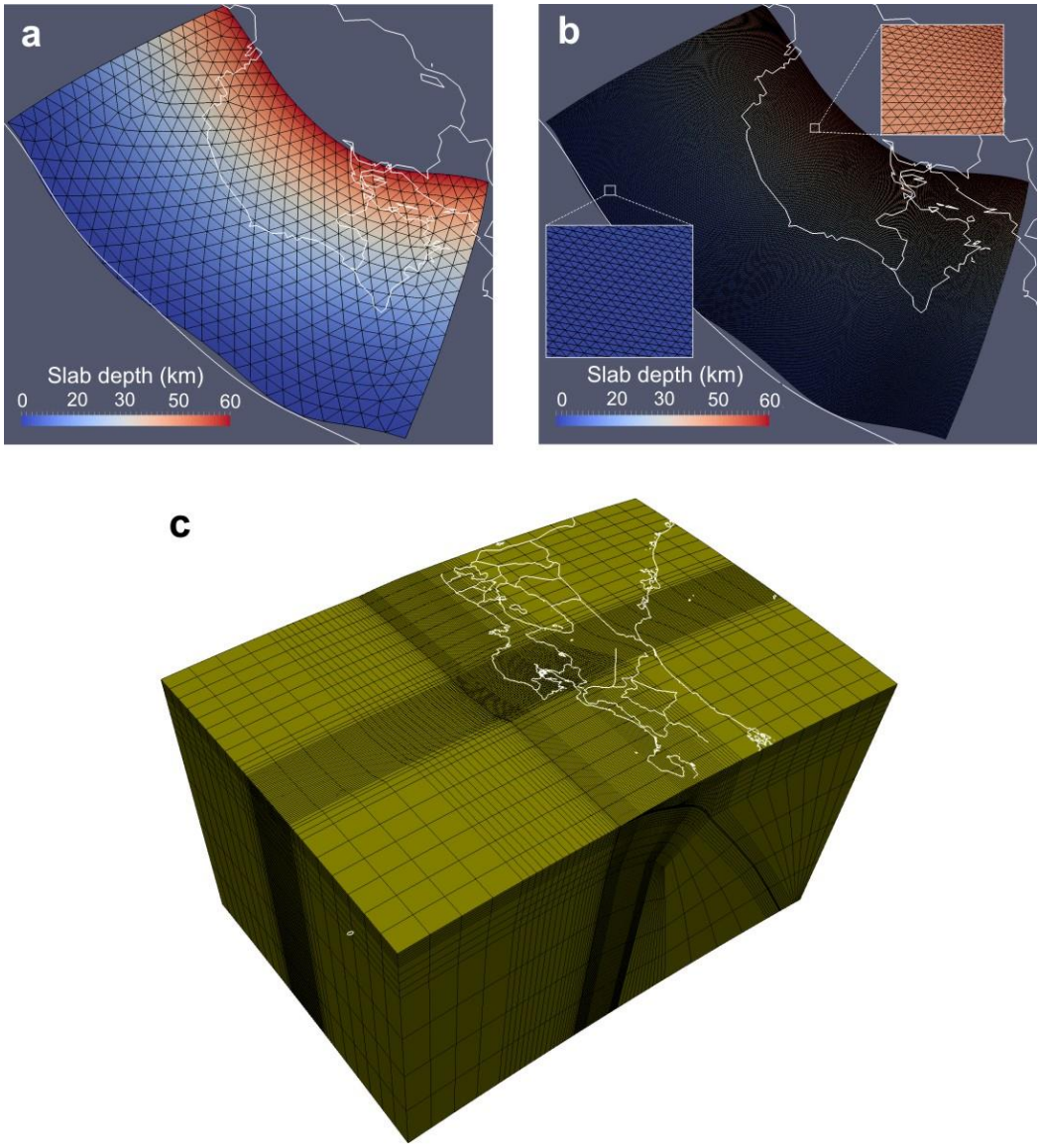

Figure 3.7. Meshes used in this work for determining slip distributions and stress changes. (a) Fault mesh for inverting land-based GNSS observations with a uniform elastic half-space model. Size of each triangular sub-fault is ~8 km. (b) Similar to Figure 3.7a but with a much denser mesh density for calculating stress changes on the megathrust. Size of each triangular sub-fault is ~500 m. (c) Central part of the finite element mesh for forward modelling both near-trench and on-land deformation. Each quadratic element has 27 nodal points.

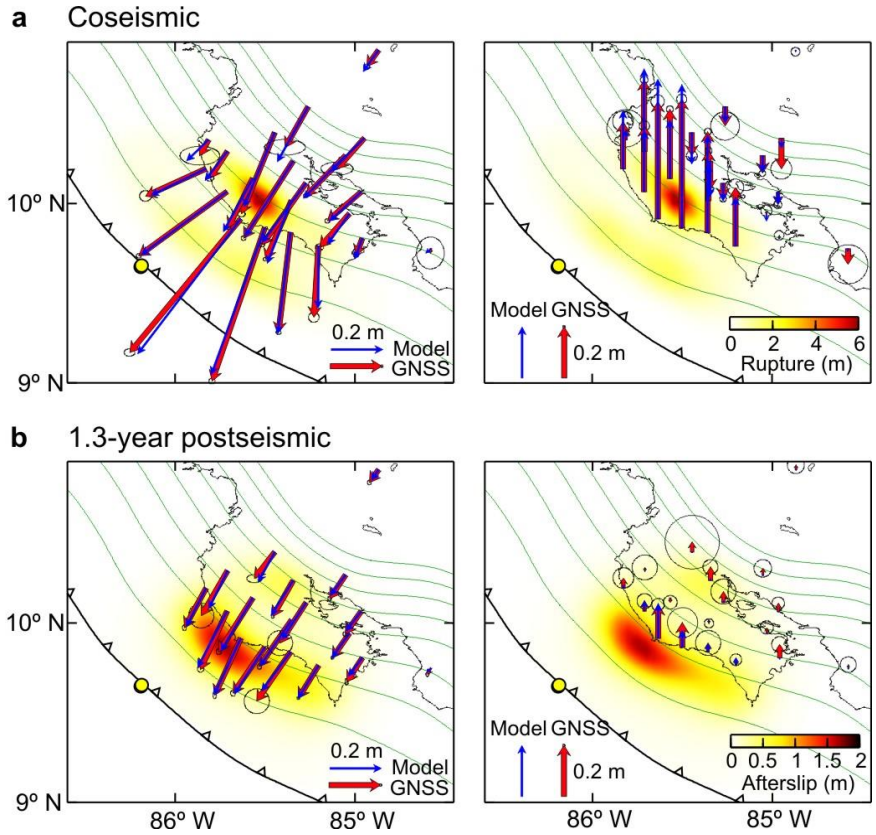

Figure 3.8. Fault slip determined by inverting GNSS displacements using an elastic half space model without fluid pressure data from the trench and comparison of model prediction with data. Fault mesh is shown in Figure 3.7a.

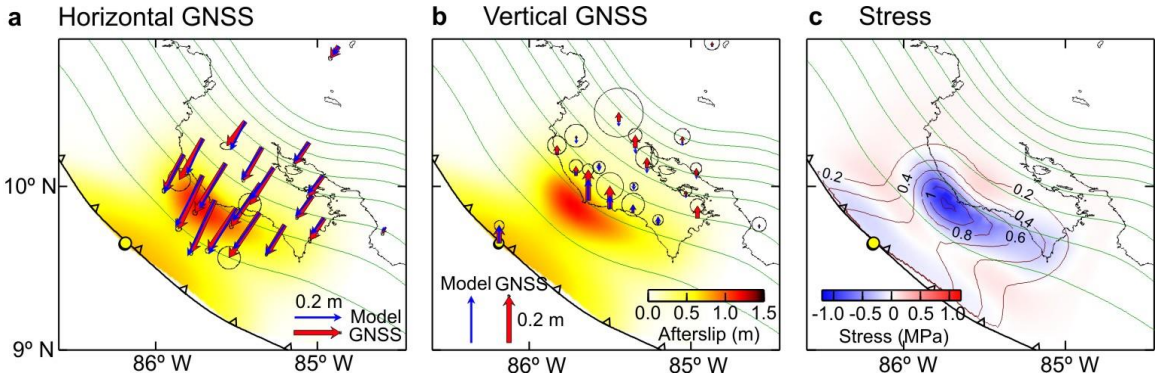

Figure 3.9. 1.3-year afterslip distribution and the associated stress changes on the megathrust assuming a wider along-strike distribution of trench-breaching afterslip. Same as Figure 3.3b, except that a wider patch along the trench is imposed.

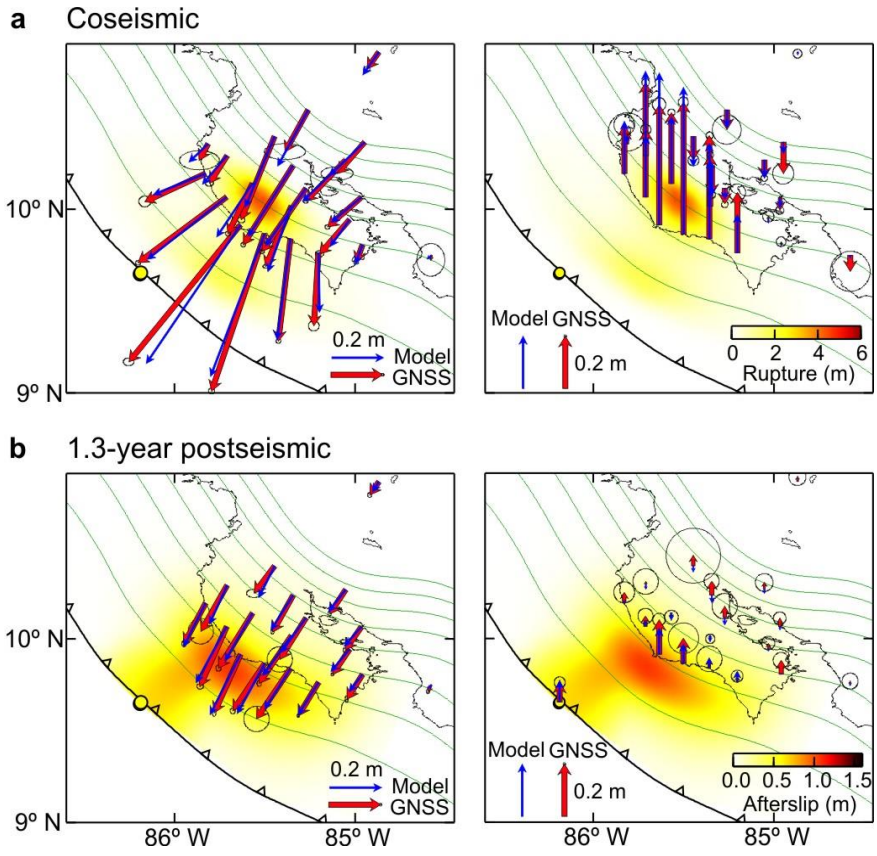

Figure 3.10. Results of using a larger correlation scale for the slip inversion. Same as in Figure 3.3, except for the use of a correlation scale of 50 km (instead of 25 km) in both the strike and dip directions. Model predicted displacements are calculated using the finite element mesh shown in Figure 3.7c.

Table 3.1. Cumulative postseismic GNSS and seafloor displacements from right after the 2012 earthquake to the end of 2013. Errors are determined as the standard deviations of the residue between the observed displacements and the logarithmic function for fitting the time series (Figure 3.6), except for HATI, PUJE, and QSEC. For these three sites, because of the missing observation around the end of 2013, a larger error (10 mm) is set for all displacement components. NA = Not available.

Site	Long. [º]	Lat. [º]	Elev. [m]	Displacement [cm]			Error [mm]		
				E	N	V	E	N	V
BIJA	-84.577	9.750	555.6	-1.31	-2.41	1.32	1.23	1.79	6.30
BON2	-85.203	9.765	28.0	-7.83	-12.84	2.20	1.09	1.09	4.62
CABA	-85.344	10.238	27.0	-7.91	-14.07	5.28	1.22	1.73	5.97
ELVI	-85.446	10.395	81.9	-7.91	-10.33	3.96	6.08	3.22	21.48
EPZA	-85.568	10.141	668.4	-13.19	-21.10	-1.76	2.04	2.41	5.46
GRZA	-85.636	9.916	39.3	-10.11	-22.29	13.19	1.33	2.98	4.94
HATI	-85.710	10.292	58.6	-10.11	-17.59	1.32	10.0	10.0	10.0
HUA2	-85.352	10.018	593.9	-12.53	-18.25	-1.32	1.66	2.35	3.69
IND1	-85.502	9.865	75.3	-12.31	-18.03	9.67	2.00	2.32	12.56
LAFE	-84.960	9.807	65.2	-6.02	-9.45	5.28	1.18	2.66	6.18
LEPA	-85.031	9.945	20.9	-6.59	-9.67	2.20	1.19	1.10	5.23
LMNL	-85.053	10.268	103.0	-6.16	-9.23	2.64	1.33	1.78	6.98
PNE2	-85.829	10.196	19.5	-8.35	-15.56	3.96	1.57	2.31	8.20
PUJE	-85.272	10.114	30.1	-10.11	-15.83	4.40	10.0	10.0	10.0
PUMO	-84.967	10.064	18.0	-6.16	-8.79	3.30	1.53	1.84	4.94
QSEC	-85.357	9.840	17.4	-13.19	-19.34	3.52	10.0	10.0	10.0
SAJU	-85.711	10.067	73.4	-10.33	-22.86	3.96	2.57	2.21	6.00
VERA	-84.869	10.854	64.3	-3.52	-5.06	1.76	1.48	1.91	6.72
1255	-86.186	9.655	-4312	NA	NA	7.52	NA	NA	4.35

Chapter 4. Crustal Deformation Following the 2011 Tohoku-oki Earthquake

This chapter is the first of three chapters addressing how Earth rheology and fault behaviour control time-dependent crustal deformation following great subduction earthquakes. The main body of this chapter consists of a published journal paper [Sun et al., 2014] on the effect of viscoelastic relaxation on postseismic deformation immediately following the Tohoku-oki earthquake. Section 4.1 describes basic paper information. Section 4.2 presents the paper itself. Supplementary material that accompanied the published paper is presented as section 4.3.

4.1. Paper Information

4.1.1. Author and Coauthor Contributions

Section 4.2 consists of a paper published in journal Nature as a Letter but reformatted for the dissertation. The author of this dissertation T.S. carried out the deformation modelling of this study. Coauthor K.W. designed the study, and K.W. and T.S. did most of the writing. Coauthor T.I. processed land GPS data. Coauthors R.H., H.F., M.K., Y. Osada, S.M., and Y. Ohta collected and processed GJT3 seafloor GPS data. Coauthor J.H. wrote the modelling code and contributed to the deformation modelling. Coauthor Y.H. constructed geometry of the Japan Trench subduction fault and initiated the modelling.

4.1.2. Citation

Sun, T., K. Wang, T. Iinuma, R. Hino, J. He, H. Fujimoto, M. Kido, Y. Osada, S. Miura, Y. Ohta, and Y. Hu (2014), Prevalence of viscoelastic relaxation after the 2011 Tohoku-oki earthquake, *Nature, 514*, 84–87, doi: 10.1038/nature13778.

4.1.3. Authors' Names and Affiliations

Tianhaozhe Sun[1], Kelin Wang[1,2*], Takeshi Iinuma[3], Ryota Hino[3], Jiangheng He[2], Hiromi Fujimoto[3], Motoyuki Kido[3], Yukihito Osada[3], Satoshi Miura[3], Yusaku Ohta[4], Yan Hu[5]

[1] School of Earth and Ocean Sciences, University of Victoria, Victoria, British Columbia, Canada V8P 5C2

[2] Pacific Geoscience Centre, Geological Survey of Canada, Natural Resources Canada, 9860West Saanich Road, Sidney, British Columbia, Canada V8L 4B2

[3] International Research Institute of Disaster Science, Tohoku University, Sendai 980-0845, Japan

[4] Research Center for Prediction of Earthquakes and Volcanic Eruptions, Graduate School of Science, Tohoku University, Sendai 980-8578, Japan

[5] Berkeley Seismological Laboratory and Department of Earth and Planetary Sciences, University of California, Berkeley, California, California 94720, USA

[*] Corresponding author: kelin.wang@canada.ca

4.1.4. Article Format

The text and figures included in Section 4.2 are taken directly from the Nature Letter. The supplementary material for the Letter is given in Section 4.3. Sections, figures, and tables have been renumbered to fit the dissertation format. References cited in the Letter are included in the bibliography of this dissertation.

4.2. Prevalence of Viscoelastic Relaxation After the 2011 Tohoku-oki Earthquake

4.2.1. Abstract

After a large subduction earthquake, crustal deformation continues to occur, with a complex pattern of evolution [Wang et al., 2012]. This postseismic deformation is due primarily to viscoelastic relaxation of stresses induced by the earthquake rupture and continuing slip (afterslip) or relocking of different parts of the fault [Hu et al., 2004; Pollitz et al., 2006; Suito and Freymueller, 2009; Kogan et al., 2013; Pritchard and Simons, 2006]. When postseismic geodetic observations are used to study Earth's rheology and fault behaviour, it is commonly assumed that short-term (a few years) deformation near the rupture zone is caused mainly by afterslip, and that viscoelasticity is important only for longer-term deformation [Pritchard and Simons, 2006; Hsu et al., 2006]. However, it is difficult to test the validity of this assumption against conventional geodetic data. Here we show that new seafloor GPS (Global Positioning System) observations immediately after the great Tohoku-oki earthquake provide unambiguous evidence for the dominant role of viscoelastic relaxation in short-term postseismic deformation. These data reveal fast landward motion of the trench area, opposing the seaward motion of GPS sites on land. Using numerical models of transient viscoelastic mantle rheology, we demonstrate that the landward motion is a consequence of relaxation of stresses induced by the asymmetric rupture of the thrust earthquake, a process previously unknown because of the lack of near-field observations. Our findings indicate that previous models assuming an elastic Earth will have substantially overestimated afterslip downdip of the rupture zone, and underestimated afterslip updip of the rupture zone; our knowledge of fault friction based on these estimates therefore needs to be revised.

4.2.2. Nature Letter Main Body

Land-based GPS observations from multiple subduction zones delineate three stages of postseismic deformation following a great megathrust earthquake: wholesale seaward

motion, opposing motion of the coastal and inland areas, and wholesale landward motion [Wang et al., 2012]. This progressive motion reversal contains important information on Earth's viscoelastic rheology and the slip behaviour of subduction megathrusts [Wang et al., 2012; Hu et al., 2004; Pollitz et al., 2006; Suito and Freymueller, 2009; Kogan et al., 2013]. However, we know surprisingly little about the mechanism of postseismic deformation at the timescale of a few years.

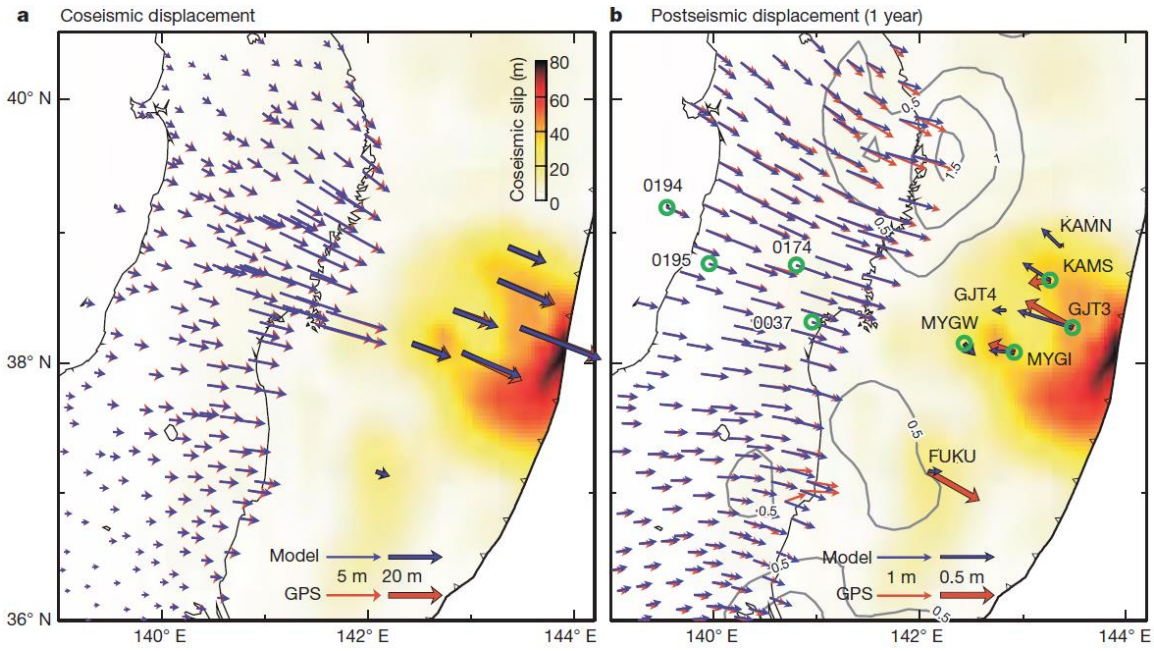

Figure 4.1. Coseismic and postseismic deformation of the 2011 Tohoku-oki earthquake. (a) Coseismic displacements of land [Ozawa et al., 2011] and seafloor [Sato et al., 2011; Kido et al., 2011] GPS sites and model predicted displacements based on the fault slip model shown (see Section 4.2.3). (b) One-year postseismic displacements of land [Ozawa et al., 2012] and seafloor [Japan Coast Guard and Tohoku University, 2013; Watanabe et al., 2014] GPS sites and model predicted values based on the viscoelastic model of this work. Seafloor GPS vectors were obtained through fitting campaign data with logarithmic functions as in Figure 4.9. Site GJT4 failed shortly after the earthquake. Black contours (m) are the afterslip distribution used in our modelling (see Section 4.2.3). Observed and model time series at sites marked with a green circle in the main corridor of interest are shown in Figure 4.3.

During the Tohoku-oki earthquake, seven seafloor GPS stations operated by the Japan Coast Guard (JCG) [Sato et al., 2011] and Tohoku University (TU) [Kido et al.,

2011] detected seaward displacements of up to 31 m, much larger than the largest coseismic motion of coastal GPS sites (~5 m) [Ozawa et al., 2011] (Figure 4.1). Many rupture models, in particular those involving tsunami data and seafloor geodetic observations, feature peak slip exceeding 50 m at rather shallow depths and breaching the trench [Fujii et al., 2011; Iinuma et al., 2012; Shao et al., 2012; Tajima et al., 2013].

After the earthquake, the terrestrial GPS network in northeast Japan continued to show wholesale seaward motion as expected (Figure 4.1b). These terrestrial observations can be adequately explained by an afterslip model [Ozawa et al., 2012] similar to those developed for most other subduction earthquakes and also based only on terrestrial observations [Pritchard and Simons, 2006]. However, seafloor GPS observations near the trench present a fundamental challenge to the validity of ignoring viscoelastic stress relaxation in short-term postseismic deformation. Whereas some of the seafloor sites also exhibited seaward motion, sites nearest to the peak rupture area immediately reversed their direction from coseismic seaward to postseismic landward (Figure 4.1b). These data demonstrate that opposing motion begins immediately after the earthquake, a phenomenon previously unknown because of the lack of seafloor observations. The motion of these sites (Figure 4.1b), ~50 cm at TU site GJT3 (Figures 4.8 and 4.9) and, ~20–25 cm at JGC sites KAMS and MYGI in the first year [Japan Coast Guard and Tohoku University, 2013; Watanabe et al., 2014], is much faster than the subduction rate (8.3 cm yr^{-1}) at the Japan Trench [DeMets et al., 2010] and thus cannot be explained by the relocking of the subduction fault. Neither can it be explained by afterslip, which would cause the surface to move in the opposite (seaward) direction [Pritchard and Simons, 2006; Ozawa et al., 2012]. The effect of poroelastic rebound after the earthquake is far too small to explain the observed motion, even in a model that maximizes such an effect [Hu et al., 2014]. Therefore, the primary process responsible for this motion must be viscoelastic relaxation [Sun et al., 2013].

We explain the immediate landward motion of the trench area, represented by sites GJT3, KAMS and MYGI, as a manifestation of viscoelastic relaxation of stresses induced by the asymmetric rupture of the Tohoku-oki earthquake. We first use a simple two-dimensional (2D) model (Figure 4.2a) to elucidate the physical process. This simple

model captures the essence of viscoelastic deformation in earthquake cycles [Wang et al., 2012; Pollitz et al., 2006]: the tectonic plates exhibit elastic behaviour, and the asthenospheric mantle deforms elastically at the time of the earthquake but increasingly exhibits viscous behaviour afterwards (Figure 4.4).

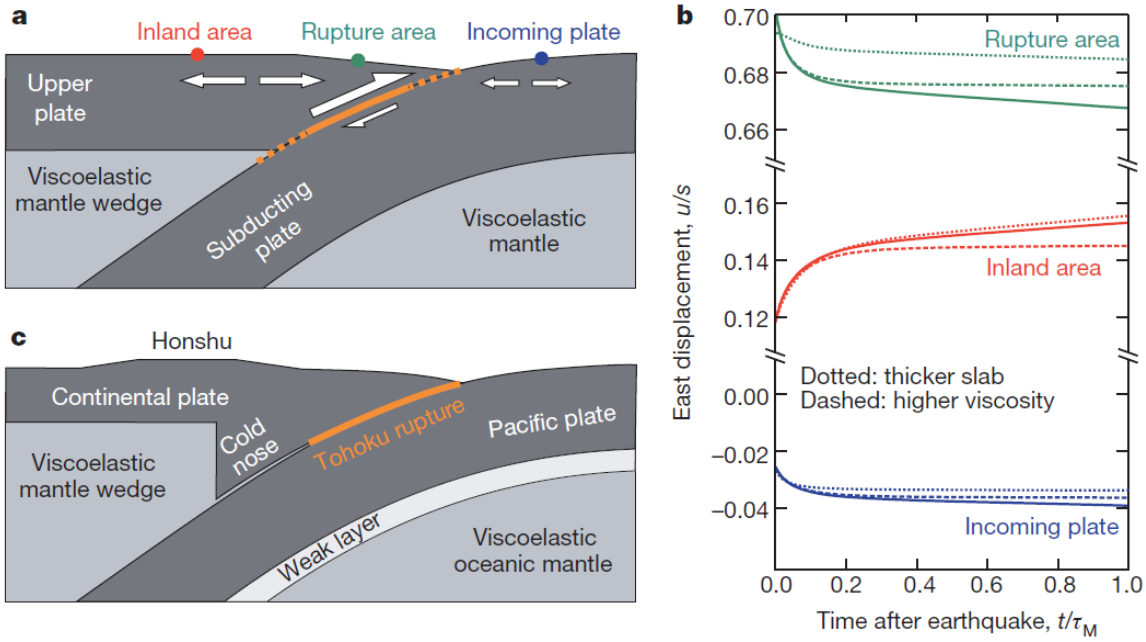

Figure 4.2. Numerical models of short-term viscoelastic relaxation. (a) A 2D generic subduction earthquake model used to illustrate the consequence of asymmetric rupture. Fault slip, *s*, is denoted by a solid orange line, and tapers to zero over dashed portions. Greater tensile stress is coseismically induced in the upper plate than in the incoming plate (diverging arrows). (b) Horizontal coseismic ($t = 0$) and postseismic ($t > 0$) displacements (u) of the three colour coded sites in Figure 4.2a in response to the earthquake. τ_M is the Maxwell time of the mantle wedge (Figure 4.4). Solid lines show results based on a model with 30-km-thick upper and lower plates and a rigidity and viscosity structure similar to previous subduction earthquake cycle models [Wang et al., 2012; Pollitz et al., 2006; Hu and Wang, 2012] and identical to model B in Table 4.1. In the 'thicker slab' model, the lower plate is twice as thick; in the 'higher viscosity' model, the steady-state mantle wedge viscosity is an order of magnitude higher (10^{20} Pa s). (c) Schematic illustration of the structure of the 3D model for the 2011 Tohoku-oki earthquake, with results shown in Figures 4.1 and 4.3.

Asymmetric coseismic elastic deformation is a fundamental outcome of any thrust

rupture that is not deeply buried. Because of the presence of the free surface (seafloor), the hanging wall overlying the rupture is less stiff than the foot wall beneath. Consequently, even though the double-couple source mechanism is symmetric, the hanging wall undergoes greater coseismic motion than does the foot wall. In subduction earthquakes, the asymmetry is very pronounced owing to the shallow dip and depth of the megathrust (Figure 4.2a). The maximum seaward motion of the upper plate is larger than the maximum landward motion of the incoming plate often by an order of magnitude. Systematic spatial variations in rock rigidity or plastic yielding in parts of the system can only slightly modify the relative magnitude of the motion but cannot reduce the asymmetry in any substantive fashion.

The asymmetric rupture induces greater tension in the upper plate than in the incoming plate (Figure 4.2a). The stress asymmetry around the rupture zone is accompanied by heterogeneous incremental stresses in the rest of the coseismically elastic system that, for static deformation, balance the net force and torque. As the underlying mantle undergoes viscoelastic relaxation after the earthquake [Wang et al., 2012; Pollitz et al., 2006], the greater tension in the upper plate pulls the trench area landward (Figure 4.2b). The site in the rupture area reverses its direction of motion immediately after the earthquake in all the models, irrespective of the vastly different parameters used. For example, a very thick subducting plate or highly viscous mantle can slow down the motion but cannot prevent it from occurring (Figure 4.2b).

In the real Earth, the only process that may offset or even reverse this motion in limited areas is fast afterslip, especially at very shallow depths such as that observed after the 2005 moment magnitude M_w=8.7 Sumatra earthquake [Hsu et al., 2006]. At the Japan Trench, the very fast seaward motion of JCG site FUKU, outside the main rupture area (Figure 4.1b), is undoubtedly caused by shallow afterslip. We think that the lack of landward motion of JCG site KAMN is probably because the motion was offset by local afterslip, an issue that we do not have adequate information to explore in our modelling.

To apply the conceptual model illustrated in Figures 4.2a and 4.2b to the seafloor GPS observations after the Tohoku-oki earthquake, we developed a three-dimensional (3D) spherical-Earth finite element model (see Section 4.2.3) involving the Burgers

mantle rheology (Figure 4.4) and the actual fault geometry (Figure 4.5). Our main region of interest is the broad margin-normal corridor including the peak rupture area and sites GJT3, MYGI, KAMS and MYGW. To focus on the first-order physical process, we purposely simplified the model by using uniform material properties for each of the major structural units (model A in Table 4.1). Elastic modulus values are the same as in Wang et al. [2012] except for those required by the transient rheology (Figure 4.4), for which larger values better reproduce postseismic motion of all the land GPS sites in the first few weeks. The most seaward part of the mantle wedge overlying the shallower-than-70-km part of the slab is an elastic 'cold nose' (Figure 4.2c), representing the stagnant and cold part of the mantle wedge [Wada and Wang, 2009] and consistent with the results of seismic tomography in this region [Yamamoto et al., 2011]. Between the cold nose and the slab, the plate interface changes from a distinct fault at shallow depths to a thin viscoelastic shear zone at greater depths (see Section 4.2.3). Differently from previous models, we included a weak layer (Table 4.1) below the oceanic plate, approximately accounting for the recently but widely reported mechanical decoupling of the oceanic lithosphere from the underlying mantle material (see Section 4.2.3). All the viscosity values were optimized to fit observations via a trial-and-error approach.

We used a coseismic rupture model slightly modified (see Section 4.2.3) from Iinuma et al. [2012] (Figure 4.1a). Our tests show that different choices of coseismic slip models [Tajima et al., 2013] may lead to slightly different estimates of viscosity values but do not change the physical process demonstrated by the model. Because postseismic GPS observations reflect both viscoelastic relaxation and afterslip, we must consider both processes to allow meaningful comparisons with data [Hu and Wang, 2012]. We opted to revise the afterslip model of Ozawa et al. [2012] and combine it into our 3D viscoelastic model in a trial-and-error fashion. The introduction of viscoelasticity as required by seafloor observations greatly reduced the amount of afterslip required to explain the land GPS data. The afterslip values shown in Figure 4.1b have been reduced from those of Ozawa et al. [2012] by as much as 95% directly downdip of the main rupture area and by about 30% farther away (see Section 4.2.3). Our model does not include shallow and/or trench-breaching afterslip and therefore is not designed to explain the motion of site FUKU (see Section 4.2.3). If significant shallow afterslip did occur in our main corridor

of interest, the landward motion of seafloor GPS sites due to viscoelastic relaxation should be even faster than shown in Figure 4.1b, further strengthening the main argument of this chapter.

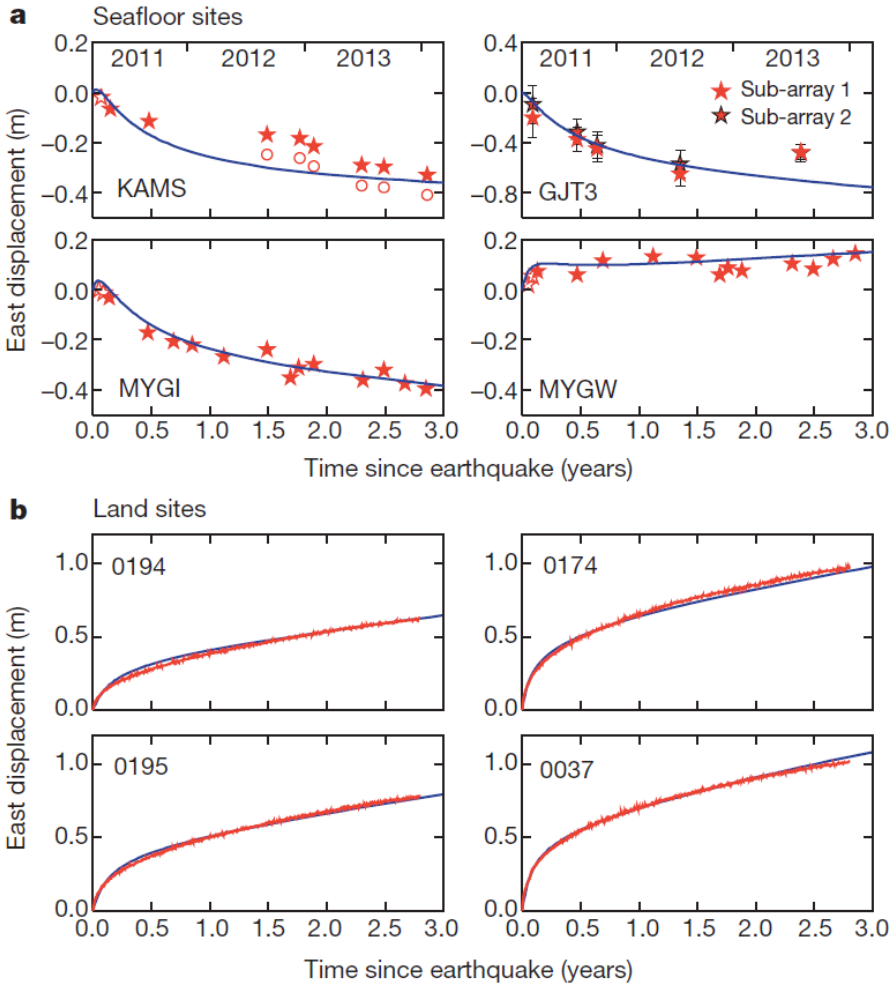

Figure 4.3. Observed (red) and model-predicted (blue) time series of the east component of postseismic displacements. The locations of the GPS sites are shown in Figure 4.1b. (a) Seafloor sites. For TU site GJT3, error bars (standard error) are based on error analysis, and sub-arrays are formed by different combinations of seafloor transponders, both as explained in Section 4.2.3. For the JCG sites [Japan Coast Guard and Tohoku University, 2013; Watanabe et al., 2014], error estimates were not provided but are estimated to be smaller than those of GJT3 (see Section 4.2.3) except for the first one or two less reliable measurements at each site (open stars). Circles for KAMS represent position data after a manual correction for an assumed delayed local afterslip during 2012. The one-year vector for this site shown in Figure 4.1b is based on the corrected data. (b) Randomly selected land sites in the main corridor of interest. Other sites in this corridor have similar results.

Our 3D model adequately explains the spatial (Figure 4.1b) and temporal (Figure 4.3) patterns of postseismic deformation. Even in areas away from the main corridor of interest, the model fits GPS observations to a considerable degree of fidelity. Second-order temporal variations in the GPS time series, such as the brief slowing down of KAMS during 2012 and the motion reversal of GJT3 in 2013, may be due to local adjustment of the megathrust (delayed afterslip) and cannot be explained by viscoelastic relaxation (Figure 4.3a). Steady-state viscosities in this model (model A in Table 4.1) are lower than in previous models [Wang et al., 2012] that were based mostly on longer-term postseismic and interseismic observations (see also Figures 4.6 and 4.7). The reason is most probably that transient mantle rheology is more complex than described by the Burgers model (Figure 4.4) and our steady-state viscosity based on the ~3 years of postseismic observations may still be affected by transient creep.

Our numerous testing runs using both 2D and 3D models (not all displayed here) show that landward trench motion does not occur in any purely elastic model but always occurs in viscoelastic models irrespective of the details of the viscoelastic mantle rheology, afterslip and model structure. Therefore, in elastic models for any large subduction earthquakes, afterslip downdip of the rupture zone will have been overestimated, and afterslip at shallower depths, if present and resolvable by observations [Hsu et al., 2006], will have been underestimated. Reassessing afterslip using viscoelastic models will lead to a revision of our knowledge of the slip behaviour and physics of subduction megathrusts.

4.2.3. Methods

Finite element model

We assume that the mantle obeys the bi-viscous Burgers rheology [Wang et al., 2012; Pollitz et al., 2006]. The Kelvin solid of viscosity η_K and rigidity μ_K and the Maxwell fluid of viscosity η_M and rigidity μ_M in the Burgers body (Figure 4.4) are the

simplest parameterizations of the transient and steady-state rheology, respectively [Peltier et al., 1981]. The characteristic timescales of the transient and steady-state rheology are thus represented by the Kelvin relaxation time $\tau_K = \eta_K/\mu_K$ and Maxwell relaxation time $\tau_M = \eta_M/\mu_M$, respectively. Note that μ_K is not a real physical property but a parameter introduced to control the initial rate of transient creep of mantle material without invoking more parameters.

Secular mantle wedge flow maintains high temperatures in the arc and back arc region [Wada and Wang, 2009]. The different thermal states of the two sides can result in not only different thicknesses of the elastic plates, but also differences in the viscosities of the mantle below. Following the arguments of Wang et al. [2012], we required the viscosities of the mantle wedge to be about one order of magnitude lower than those of the oceanic mantle (Table 4.1).

We used the spherical-Earth finite-element code PGCviscl-3D developed by J.H. The code uses 27-node isoparametric elements throughout the model domain. The effect of gravitation is incorporated using the stress-advection approach [Peltier, 1974]. Coseismic rupture and afterslip are simulated using the split-node method [Melosh and Raefsky, 1981]. Time (t) integration is performed using a fully implicit algorithm, with time steps no greater than $0.01\,\tau_k$ for $t < \tau_k$ and no greater than $0.01\,\tau_M$ for $t < 0.5\,\tau_M$. The parallel code has been extensively benchmarked against analytical deformation solutions for elastic, Maxwell and Burgers materials and applied to subduction zone earthquake cycle modelling [Wang et al., 2012; Hu and Wang, 2012].

The central part of the element mesh for the Tohoku-oki model is shown in Figure 4.5. The subduction fault geometry was constrained by earthquake relocation results and seismic reflection profiles [Nakajima and Hasegawa, 2006; Kita et al., 2010; Zhao et al., 2009] and is similar to what was used in Iinuma et al. [2012]. We accounted for the presence of a cold and stagnant nose of the mantle wedge [Wada and Wang, 2009; Yamamoto et al., 2011] and its sharp landward termination [Wada et al., 2011] by adding a triangular region to the elastic upper plate in the forearc (Figure 4.2c and Figure 4.5).

Studies of fault processes indicate that the distinction between shear along a thin fault plane and within a broader shear zone becomes blurry at large depths [Noda and Shimamoto, 2012]. Much of the afterslip is actually shear deformation that gradually spreads over a shear zone that thickens with increasing depth. In our model, between the elastic cold nose and the elastic slab is a layer of viscoelastic mantle material that thickens with increasing depth (Figure 4.2c and Figure 4.5). This layer approximates the deeper fault zone to a depth of 70 km. Deeper than 70–80 km, the mantle wedge is fully coupled with the slab, that is, there is no longer a fault zone that accommodates localized shear such as afterslip [Wada and Wang, 2009].

Recent studies suggest mechanical decoupling at the lithosphere-asthenosphere boundary (LAB) [Kawakatsu et al., 2009; Rychert and Shearer, 2009; Fischer et al., 2010], due to the presence of either fluids [Karato, 2012] or partial melts [Sakamaki et al., 2013; Schmerr, 2012]. We thus introduced a thin layer of low viscosity underlying the elastic oceanic plate to approximate this effect (Figure 4.2c and Table 4.1). This approximate LAB layer decreases the ratio of vertical to horizontal postseismic displacements at the seafloor. Compared to models without this layer, our model predicts smaller postseismic subsidence in the rupture area and is generally more consistent with observations. However, because of the much larger errors in observed vertical deformation, we did not try to fit the vertical data precisely.

Assigning coseismic slip and afterslip

In Iinuma et al. [2012], terrestrial and seafloor GPS and ocean bottom pressure data were inverted using a model of a planar fault to determine the coseismic slip distribution. We mapped the slip vectors onto our 3D curved fault surface. The original slip model used a straight line to represent the trench, resulting in a gap between the model rupture zone and the actual curved trench or some slip seaward of the trench. We filled the artificial trench gap by extrapolating slip values from the model rupture zone (Figure 4.1a), and the additional slip resulted in a larger seismic moment and surface displacements. We scaled the fault slip to 92% of its original values in order to match the GPS observations (Figure 4.1a). We have developed postseismic deformation models

using other published rupture models. Different coseismic slip distributions require slightly different mantle viscosity values in order to fit the GPS data, but all lead to the same main conclusions.

The afterslip model shown in Figure 4.1b (contours) was revised from the model of afterslip 8 months after the earthquake developed in Ozawa et al. [2012]. Because the model of Ozawa et al. [2012] assumed a purely elastic Earth, postseismic deformation caused by viscoelastic relaxation was also attributed to afterslip, resulting in over-estimated afterslip. Therefore, we scaled down the afterslip values when assigning them to our finite element mesh. Unlike the uniform scaling ratio used for coseismic slip, we needed to use a smoothly variable function for the afterslip scaling. With trial-and-error, the scaling factor was determined to be ~0.05 downdip of the main rupture zone at ~60–70 km depth, ~0.35 to the north of the main rupture zone, and ~0.7 to the south of the main rupture zone. For the temporal evolution of the afterslip, we used the power-law function reported in Hu and Wang [2012] with a characteristic timescale of 1.5 years.

Our model does not include any shallow afterslip near or breaching the trench. For our main corridor of interest, the assumption of no shallow afterslip is supported by the fact that a postseismic thermal-sensor monitoring string deployed in a near-trench borehole was retrieved intact [Fulton et al., 2013], indicating no trench-breaching afterslip at this site during the monitoring period (16–24 months after the Tohoku-oki earthquake). If there is significant shallow afterslip before the monitoring period or in other parts of our main corridor of interest, the actual landward motion of sites GJT3, MYGI and KAMS due to viscoelastic relaxation should be even faster than shown by the GPS data. For this reason, our model represents a minimum estimate of the effect of viscoelastic relaxation.

Model using the viscosity values of Wang et al. [2012]

Testing model B (Table 4.1) shows why we cannot use the viscosity structure and values used in Wang et al. [2012]. A mantle wedge Maxwell viscosity of 10^{19} Pa s was used in Wang et al. [2012] for a study of longer-term postseismic deformation. If the

same value is used in our model, it is possible to explain cumulative GPS displacements observed at a specific time (Figure 4.6) but very difficult to explain the time-dependent evolution of the deformation field (Figure 4.7).

Seafloor/acoustic observation at GJT3

GJT3 operated by Tohoku University is the most important seafloor GPS site in this study because it is the nearest to the trench. The basic concept of the GPS/acoustic technique used by Tohoku University to make seafloor geodetic measurements was developed originally by the Scripps Institution of Oceanography [Spiess, 1985; Fujimoto, 2014]. The technique measures the horizontal displacement of the virtual seafloor benchmark, the centre of an array of at least three seafloor precision transducers (PXPs), by repeated surveys using a sea surface platform equipped with GPS antennas and an acoustic transducer [Kido et al., 2006]. Two survey methods can be used. In the fixed-point survey method, routinely used by Tohoku University, the surface platform is placed above the centre of the PXP array. If the array geometry does not change with time, the fixed-point survey method can be used to monitor the horizontal motion of the virtual benchmark. In the moving survey method, routinely used by JCG [Sato et al., 2013], the platform moves around each individual PXP to determine its absolute position. This procedure is more robust because no assumptions on PXP array geometry are required, but it is very time consuming.

Given precise position of the surface platform, two-way travel times between the platform and the PXPs, and knowledge of temporal variations in underwater sound speed, the horizontal position of the array is determined by simultaneous ranging of a single acoustic ping to all the transponders [Kido et al., 2008]. If the sound speed structure is horizontally stratified, this method is expected to give reliable estimates of the array position. However, temporal changes and three-dimensional heterogeneities of the sound speed structure often cause the position measurements to fluctuate. During a campaign, we take an ensemble mean of many measurements to estimate the array position, such that much of the effects of the sound speed anomalies are averaged out.

Within the first two years after the Tohoku-oki earthquake, Tohoku University conducted four campaign surveys at GPS/acoustic station GJT3, located above the main rupture area (Figure 4.1). The first measurement, made in April 2011, showed a displacement of about 31 m due mainly to coseismic motion [Kido et al., 2011]. This and the two subsequent surveys in 2012 used only the fixed-point method because of limited ship time allocation. In 2013, we used the moving survey method to reassess the array geometry at this site while continuing to use the fixed-point method to determine the position of the virtual seafloor benchmark. The moving survey results indicated that the PXP array geometry had changed, most likely during the earthquake. Given the proximity of the site to the peak rupture area (Figure 4.1), this finding is not surprising. For the very large coseismic displacement [Kido et al., 2011], errors due to incorrectly assuming rigid array geometry are negligibly small. For the much smaller postseismic displacements, however, this assumption leads to significant errors. We conclude that the postseismic motion of GJT3 based on the fixed-point survey results of 2012 alone [Osada et al., 2012] had yielded an incorrect direction of motion. There is no obvious reason why the array geometry would have suffered further significant distortion after the earthquake. Therefore, in the present study, we reprocessed all the postseismic data using the PXP geometry newly determined in 2013.

The JCG array positions shown in Figures 4.1 and 4.3 were determined by averaging the positions of individual PXPs. Without invoking fixed-point survey, a large amount of ship time is required in order to minimize errors caused by the uncertainties of individual PXP locations. However, because no assumptions about array geometry are involved, the locations of the seafloor benchmark estimated by JCG are minimally affected by potential coseismic distortion of array geometry.

Regardless of the survey method, uncertainties in the position of individual PXPs can be a source of error in estimating the array position. When a fixed-point survey is made near the array centre, uncertainties in PXP positions do not affect the estimation of the array position. However, the estimation error rapidly increases with the offset of the surface platform from the array centre. Keeping the platform at the centre was especially

difficult during the survey in April 2011 when large amounts of tsunami debris drifted around the site and prevented the research vessel from staying at the optimum location.

Another factor we have to take into account is site displacement caused by nearby major aftershocks. An M_w 7 intraslab earthquake occurred on 10 July 2011, and had a strike-slip mechanism. The epicentre is only about 20 km from GJT3 and induced coseismic displacement that cannot be ignored. Its fault location was defined by the aftershock distribution precisely determined with an ocean bottom seismic network [Obana et al., 2013], and its slip model was estimated from near-field tsunami waveforms [Kubota et al., 2012]). Using this information, we estimated that the displacement of GJT3 due to this event was 2.0 cm westward and 6.6 cm southward.

Figure 4.8 shows the PXP array configuration at GJT3. Excluding PXPs EJ16 and EJ23, which were installed for testing purposes, the PXPs form an equilateral triangle with side length of ~2.5 km. Two PXPs (EJ15 andEJ22) are collocated at one of the apexes. Since the array position can be determined using the fixed-point observation with three seafloor PXPs, we can have two different sub-arrays: subarray 1, composed of PXPs EJ15, EJ12 and EJ13, and sub-array 2, composed of PXPs EJ22, EJ12 and EJ13. Figure 4.9 shows the time series of the array positions of the two sub-arrays after a correction for the effect of the 2011 M_w 7 earthquake discussed above. Position error in each campaign is estimated from the root-mean-squares of position measurements around the mean position and uncertainties in PXP positioning. Here, we assumed that the PXP positions determined by the moving survey method contain 1 m uncertainties, based on uncertainties in the sound speed of the order of 0.01% and the slant ranges from the surface platform to PXPs at ~4,000 m. Consistency between the two sub-arrays suggests the robustness of the results.

4.2.4. Acknowledgements

We thank the Japan Coast Guard for making available digital values of published data. Comments from M. Sato improved the manuscript. K.W. was supported by Geological Survey of Canada core funding and a Natural Sciences and Engineering

Research Council of Canada Discovery Grant through the University of Victoria. T.S. was supported by a University of Victoria PhD Fellowship and a Howard E. Petch Scholarship. The Tohoku University seafloor observation study was supported by the Ministry of Education, Culture, Sports, Science and Technology of Japan under its Earthquake and Volcano Hazards Observation and Research Program. This is Geological Survey of Canada contribution 20140167.

4.3. Supplementary Material

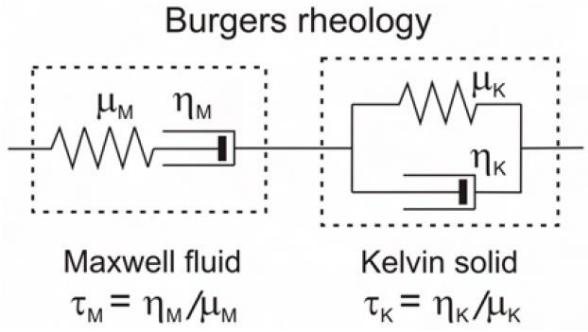

Figure 4.4. Illustration of the Burgers rheology used in this work. The Burgers rheology is represented by a serial connection of a Maxwell fluid of viscosity η_M and rigidity μ_M and a Kelvin solid of viscosity η_K and rigidity μ_K. τ_M and τ_K are Maxwell and Kelvin relaxation times, respectively.

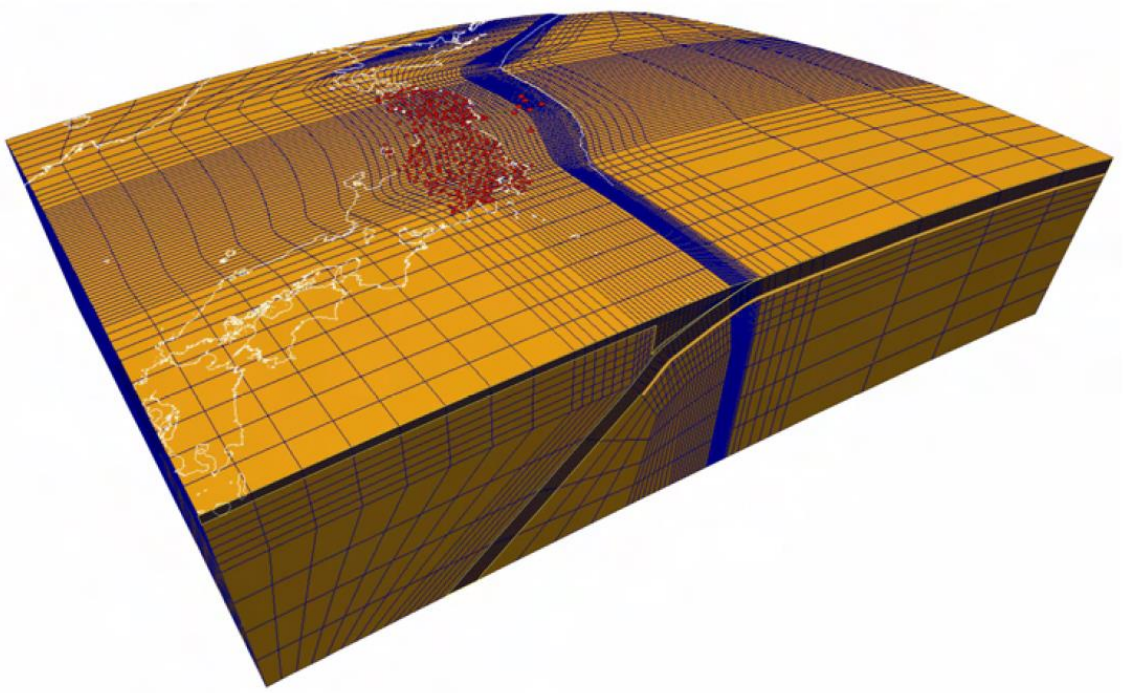

Figure 4.5. Central part of the finite element mesh for modelling deformation associated with the Tohoku-oki earthquake. Darker layers represent elastic plates. The LAB layer is highlighted in yellow. Structural details are shown in Figure 4.2c. GPS sites used to constrain the model in this work are shown in red. Elements near the trench are too fine to be discerned at this plotting scale and hence collectively appear as a blue region.

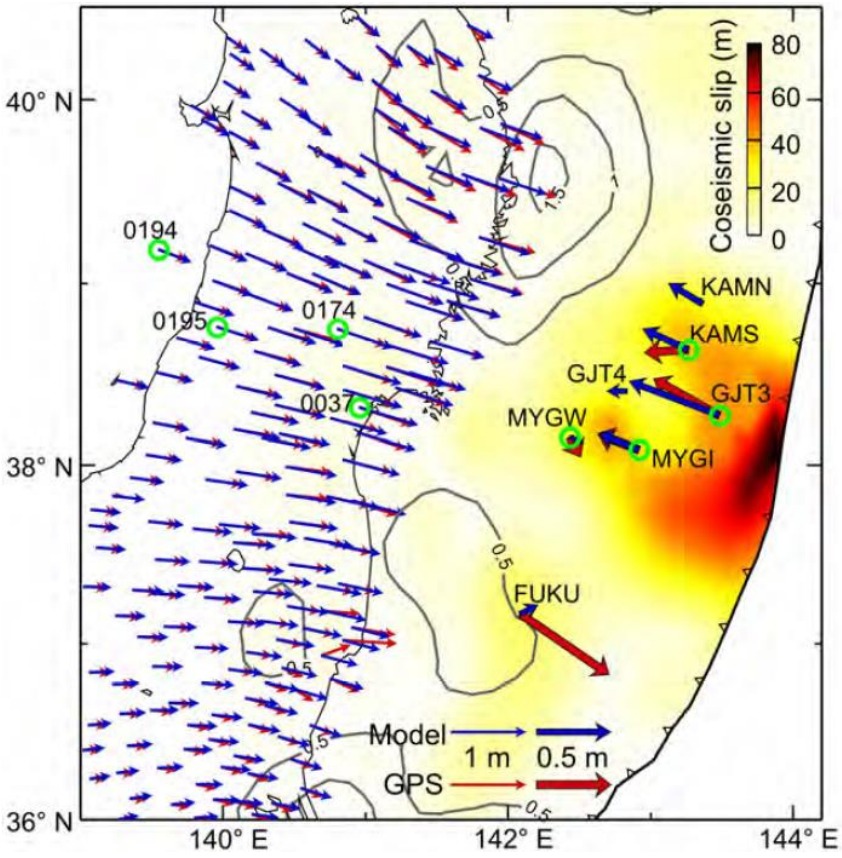

Figure 4.6. Postseismic (1 year) deformation results of model B in Table 4.1. Otherwise the figure is the same as Figure 4.1b. Time series at sites marked with a green circle are shown in Figure 4.7.

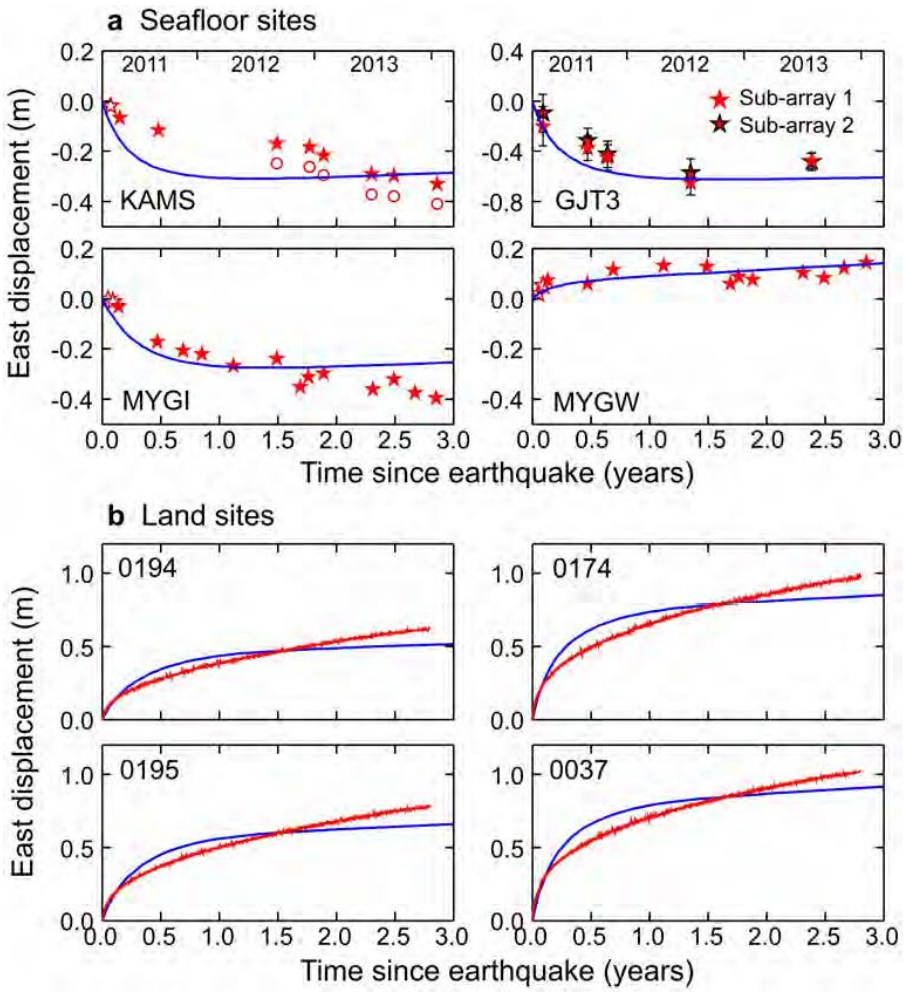

Figure 4.7. East component of postseismic displacements of model B in Table 4.1. Otherwise the figure is the same as Figure 4.3. Locations of the GPS sites are shown in Figure 4.6.

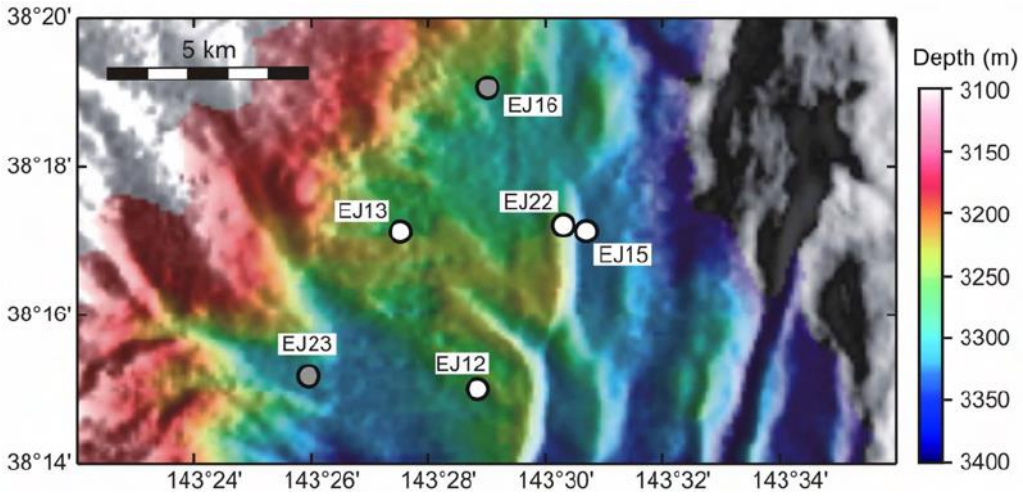

Figure 4.8. Layout of PXPs (precision transponders) at seafloor GPS site GJT3. Grey filled circles are PXPs installed for testing purposes [Kido et al., 2011], not used in this work.

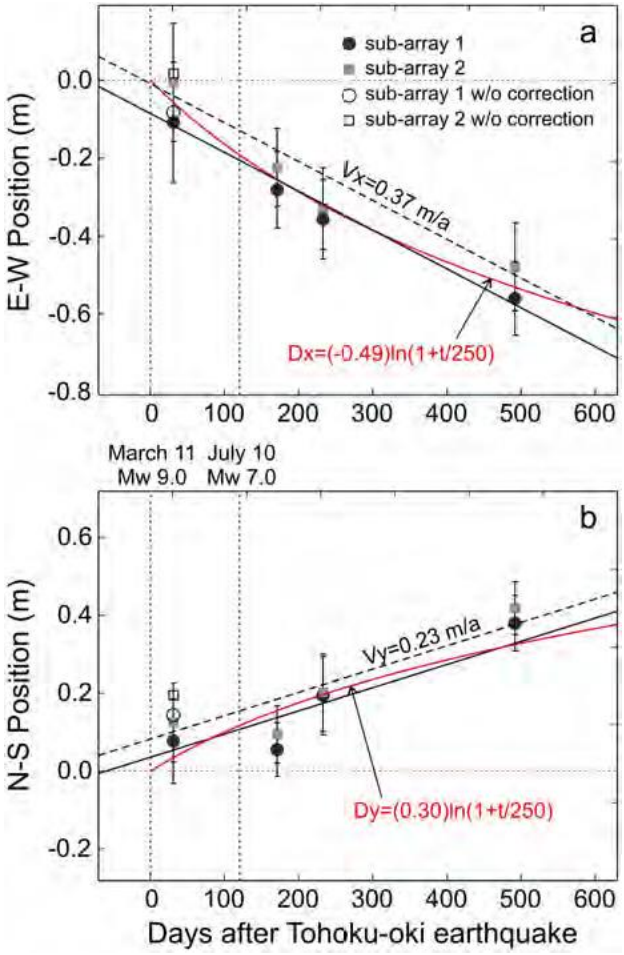

Figure 4.9. Postseismic survey results for seafloor GPS site GJT3. (a) East component Dx. (b) North component Dy. Open symbols for the first measurement show array position before the effect of the M_w 7.0 intraslab earthquake on 10 July 2011 was removed. Sub-array 1 includes PXP EJ12, EJ13 and EJ15, and sub-array 2 includes PXP EJ12, EJ13 and EJ22 (Figure 4.8). The straight solid and dashed lines show linear trends of survey results of sub-array 1 and sub-array 2, respectively, with resultant average velocities Vx and Vy for the east and north components, respectively. The red curves show a logarithmic function fit to the survey results.

Table 4.1. 3D model parameters

Model	Mantle wedge viscosity (Pa s)		Oceanic mantle viscosity (Pa s)		LAB layer viscosity (Pa s)	
	η_K	η_M	η_K	η_M	η_K	η_M
A	2.5×10^{17}	1.8×10^{18}	2.0×10^{18}	1.0×10^{20}	2.5×10^{17}	2.5×10^{17}
B	5.0×10^{17}	1.0×10^{19}	5.0×10^{17}	1.0×10^{20}	Not applicable	

Here η_K and η_M are transient (Kelvin) and steady-state (Maxwell) viscosities, respectively. In both models, the elastic upper plate landward of the cold nose (Figure 4.2c) and the lower plate are of thicknesses 25 km and 45 km, respectively, both with rigidity 48 GPa. Rigidity of the Maxwell body of the viscoelastic mantle is 64 GPa. Rigidity of the Kelvin body is 136 GPa in model A and 64 GPa in model B (the same as Wang et al. [2012]). The Poisson's ratio and rock density are 0.25 and 3,300 kg m^{-3}, respectively. LAB, lithosphere-asthenosphere boundary.

Chapter 5. Effects of Viscoelastic Relaxation on Afterslip Determination

This chapter is the second of three chapters addressing how Earth rheology and fault behaviour control time-dependent crustal deformation following great subduction earthquakes. The main body of this chapter consists of a published journal article [Sun and Wang, 2015] that systematically examines the effect of viscoelastic relaxation on the short-term postseismic deformation of great subduction earthquakes. Special attention is paid to how the incorporation of mantle viscoelasticity, when compared to using purely elastic models, improves the estimate of afterslip at shallow depths near the trench. Section 5.1 describes basic article information. Section 5.2 presents the article itself.

5.1. Article Information

5.1.1. Author and Coauthor Contributions

Section 5.2 consists of an article published in Journal of Geophysical Research: Solid Earth but reformatted for the dissertation. The author of this dissertation T.S. carried out all the 2-D and 3-D deformation modelling of this study. Coauthor K.W. and T.S. together designed the study and did the writing.

5.1.2. Citation

Sun, T., and K. Wang (2015), Viscoelastic relaxation following subduction earthquakes and its effects on afterslip determination, *Journal of Geophysical Research: Solid Earth, 120*, doi:10.1002/2014JB011707.

5.1.3. Author's Names and Affiliations

Tianhaozhe Sun[1*], Kelin Wang[1,2]

[1] School of Earth and Ocean Sciences, University of Victoria, Victoria, British Columbia, Canada V8P 5C2

[2] Pacific Geoscience Centre, Geological Survey of Canada, Natural Resources Canada, 9860West Saanich Road, Sidney, British Columbia, Canada V8L 4B2

[*] Corresponding author: thzsun@uvic.ca

5.1.4. Article Format

The text and figures included in Section 5.2 are taken directly from the article published in Journal of Geophysical Research: Solid Earth. Sections, figures, and tables have been renumbered to fit the dissertation format. The original article used American spelling as required by the journal. To be compatible with the rest of the dissertation, all affected words have been changed to Canadian spelling here. References cited in the article are included in the bibliography of this dissertation.

5.2. Viscoelastic Relaxation Following Subduction Earthquakes and its Effects on Afterslip Determination

5.2.1. Abstract

Afterslip is commonly thought to be the controlling process in postseismic deformation immediately following a great megathrust earthquake and is usually inferred from geodetic observations using purely elastic models. However, observed motion reversal of the near-trench area right after the 2011 M_w 9 Tohoku-oki earthquake demonstrates the dominance of viscoelastic relaxation of coseismically induced stresses. To understand the importance of incorporating viscoelasticity in afterslip determination, we employ biviscous Burgers mantle rheology and use finite element models to explore how viscoelastic relaxation in short-term postseismic deformation is controlled by various geometrical and rheological factors. Our results indicate that immediately after

large megathrust earthquakes ($M_w > 8.0$), viscoelastic deformation should always cause opposing motion of inland and trench areas and subsidence around landward termination of the rupture, although the rate of such postseismic motion depends on local conditions such as the age and hence thickness of the slab and transient mantle viscosity values. While elastic models may be adequate for afterslip estimation for earthquakes of $M_w <$ 7.5, neglect of viscoelasticity for larger events leads to overestimate of afterslip downdip of the rupture and underestimate of afterslip at shallower depths. Reassessing shallow afterslip following the 2005 M_w 8.7 Nias earthquake using 2-D viscoelastic models suggests that the actual afterslip may be greater than that estimated using an elastic model by more than 50%. Similarly, interpreting trenchward motion of some seafloor GPS sites following the Tohoku-oki earthquake using a viscoelastic model suggests large shallow afterslip outside of the main rupture area.

5.2.2. Introduction

Following a great megathrust earthquake, continuing slip (afterslip) or relocking of different parts of the subduction fault and relaxation of coseismicially induced stresses in the viscoelastic mantle (viscoelastic relaxation) continue to drive crustal deformation [Wang et al., 2012]. Properly assessing these processes helps us understand fault mechanics and Earth rheology. In particular, afterslip immediately after coseismic rupture provides important information on the frictional properties and slip behavior of the fault zone. However, the relative importance of afterslip and viscoelastic relaxation in the short-term postseismic deformation remains poorly understood, due mainly to the paucity of observations in the near field, preventing us from correctly characterizing either process. In this work, we investigate how viscoelastic relaxation occurs in short-term postseismic deformation, in order to define the appropriate rheological setting for the study of afterslip.

Afterslip can be understood as velocity-strengthening stable sliding of the fault areas that may have undergone coseismic stress increase [Scholz, 1998; Marone et al., 1991]. In previous studies of afterslip, it is common to employ purely elastic Earth models,

based on the assumption that viscoelastic relaxation becomes important only a longer time after the earthquake, such as several years to decades [e.g., Pritchard and Simons, 2006; Hsu et al., 2006; Ozawa et al., 2012; Bedford et al., 2013; Lin et al., 2013]. Recent seafloor observations of postseismic motion after the 2011 M_w 9 Tohoku-oki earthquake require that this assumption be reevaluated. Seafloor Global Positioning System (GPS) sites in the main rupture area were observed to have reversed their direction of motion from coseismic seaward to postseismic landward immediately after the earthquake [Japan Coast Guard and Tohoku University, 2013; Watanabe et al., 2014], opposing the continuing seaward motion of land-based GPS sites [Ozawa et al., 2012]. Sun et al. [2014] showed that this observation can be explained only by considering viscoelastic relaxation. They proposed that the neglect of short-term viscoelastic relaxation in previous studies of afterslip may have led to substantial overestimate of afterslip downdip of the rupture zone and underestimate of afterslip at shallower depths.

To understand whether the viscoelastic deformation as observed immediately after the 2011 Tohoku-oki earthquake is commonly prevalent after other megathrust earthquakes and to what extent previous afterslip estimates need to be revised, in this work we explore the effects of various geometrical and rheological factors in this process. We are particularly interested in how the incorporation of viscoelastic effects improves the estimate of shallow afterslip near the trench, where the fault behavior can be quite different between different earthquakes and/or between different subduction zones [e.g., Fujiwara et al., 2011; Kodaira et al., 2012; Hsu et al., 2006; Hill et al., 2012].

This chapter is structured as follows. In Section 5.2.3, we investigate how the asymmetry of megathrust rupture, that is, the coseismic motion of the hanging wall being larger than that of the footwall, controls the evolution of stresses and deformation rates in the ensuing process of viscoelastic relaxation. In Section 5.2.4, we use simple models to explore the effects of various controlling factors on the relaxation process, such as viscosities, thicknesses of oceanic slab and continental lithosphere, coseismic slip distribution, and earthquake size. In Section 5.2.5, we provide two examples for applying the knowledge learned to the estimation of near-trench shallow afterslip from GPS observations. The first example is a simple reassessment of shallow afterslip following

the 2005 M_w 8.7 Nias earthquake at the Sumatra margin. We demonstrate that the afterslip estimated using a viscoelastic model is much larger than previously estimated from GPS observations using an elastic model. The second example is a preliminary assessment of shallow afterslip following the 2011 M_w 9 Tohoku-oki earthquake. In an earlier model for this earthquake [Sun et al., 2014], we used seafloor GPS measurements in the main rupture area to show how including the effect of viscoelastic relaxation led to much smaller afterslip estimates downdip of the rupture zone. Here we provide an estimate of the amount of shallow afterslip north and south of the main rupture area on the basis of observed fast trenchward motion of some seafloor GPS sites [Watanabe et al., 2014]. Main conclusions are summarized in Section 5.2.6.

5.2.3. Mechanics of Near-Field Viscoelastic Postseismic Deformation

Rupture asymmetry of thrust earthquakes

As qualitatively explained by Sun et al. [2014], rupture asymmetry is the core element of the physical process of short-term viscoelastic postseismic deformation following a subduction earthquake. For any shallowly positioned thrust fault, the coseismic motion of the hanging wall is much larger than that of the footwall. The rupture asymmetry is due to the presence of the free surface and the consequent stiffness contrast between the footwall and hanging wall. The lower stiffness of the hanging wall leads to larger coseismic deformation and is well known to be responsible for greater seismic damage on the hanging wall side of thrust earthquakes in continental settings. This rupture asymmetry is an integral component of the theory of edge dislocation in an elastic half-space.

In Figure 5.1, we further demonstrate the asymmetry of thrust ruptures in a quantitative manner. For a shallowly positioned thrust fault, regardless of whether the rupture tapers to zero at the surface (Figure 5.1a) or breaches the surface (Figure 5.1b), the maximum seaward motion of the hanging wall above the fault is 2–3 times as large as the maximum landward motion of the footwall beneath the fault. The maximum surface motion of the hanging wall side can be larger than the footwall side by an order of

magnitude (Figure 5.1a). A much lower rigidity (50%) of the frontal portion of the hanging wall, which may represent a more compliant accretionary prism in a subduction zone [e.g., Kopp, 2013], only slightly amplifies the rupture asymmetry near the trench (Figure 5.1c). For a hypothetically very deeply buried thrust fault, the free surface has much less influence on the rupture behavior, and the coseismic deformation is more symmetric (Figure 5.1d). In some sense, the deeply buried thrust rupture is like a strike-slip rupture turned sideways, with the two fault walls having a similar stiffness. As long as the thrust fault is shallow, our tests show that rupture asymmetry is a persistent behavior even if the strike length of the rupture zone is relatively small.

Mantle Rheology and Finite Element Models

To model viscoelastic stress relaxation following the above described asymmetric rupture, we employ a biviscous Burgers mantle rheology, as did Wang et al. [2012] and Sun et al. [2014]. The Burgers body (Figure 5.2), represented by a Kelvin solid in series with a Maxwell fluid, is a simple parameterization of the transient and steady state rheology [Peltier et al., 1981; Pollitz et al., 2006; Bürgmann and Dresen, 2008; Wang et al., 2012]. The transient rheology is widely observed in laboratory experiments and can explain rapid decrease in deformation rates in the first few days to years after an earthquake. It has been increasingly widely used to describe short-term viscoelastic relaxation [Pollitz, 2003; Pollitz et al., 2006; Karato, 2010; Bürgmann and Dresen, 2008; Wang et al., 2012; Hu and Wang, 2012; Trubienko et al., 2013; Sun et al., 2014].

The Kelvin solid, with rigidity μ_K and viscosity η_K (Figure 5.2), describes the initial transient phase of viscoelastic relaxation. Upon sudden loading, it deforms as a Newtonian fluid at the beginning but as an elastic Hooke solid sometime after, and the transition is characterized by the Kelvin time $\tau_K = \eta_K/\mu_K$. The Maxwell fluid, with rigidity μ_M and viscosity η_M, describes the steady state phase and has the opposite time-dependent behavior. Its transition from the initial elastic behavior to the eventual viscous behavior is characterized by the Maxwell time $\tau_M = \eta_M/\mu_M$.

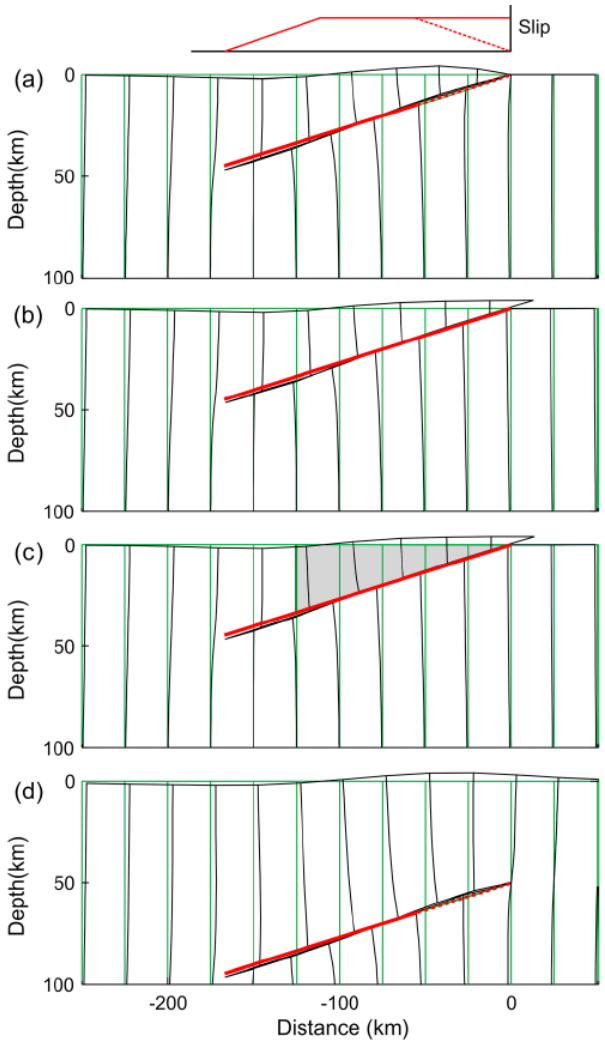

Figure 5.1. Two-dimensional illustrations of asymmetric rupture of thrust earthquakes using a finite element elastic half-space model. Dipping red and black lines indicate fault geometry before and after coseismic slip, with slip distribution shown at the top. Green and black line markers track medium geometry before and after the rupture. (a) Rupture in a uniform half-space with fault slip tapering to zero at surface (dashed segment in the top part). (b) Same as Figure 5.1a except for a surface-breaching fault slip (solid line in the top part). (c) Same as Figure 5.1b except for a lower (50%) rigidity of the shaded portion. (d) Same as Figure 5.1a except for a hypothetically large depth designed to illustrate the smaller influence of the free surface.

For numerical simulation, we use a finite element model that consists of two elastic converging plates and a viscoelastic mantle (Figure 5.2). Based on numerous studies as

reviewed by Wang et al. [2012], the steady state viscosity of the mantle wedge is about 10^{19} Pa s. The transient viscosity is much lower, and a value of 5×10^{17} Pa s has been used by different researchers to model observations for the 2004 Sumatra earthquake [Pollitz et al., 2006; Panet et al., 2010; Hu and Wang, 2012]. We use these values for our reference (REF) model (Table 5.1) in this section, but we will use other values for testing purposes in Section 5.2.4. Because of the presence of aqueous fluids from the dehydrating slab and high temperatures associated with mantle flow, the continental mantle wedge is expected to be less viscous than the oceanic mantle [Hu et al., 2004; Wang et al., 2012]. However, for simplicity, here we use a uniform value for the entire mantle in our REF model. In this model, the thickness of both the upper plate and slab is 30 km. Rigidity is 48 GPa for the elastic plates and 64 GPa for the mantle. Poisson's ratio and rock density are assumed to be uniformly 0.25 and 3300 kg/m^3, respectively. The mantle Maxwell time $\tau_M = \eta_M/\mu_M \approx 5$ years.

Our models are developed in a spherical Earth coordinate system, so it is convenient to use degrees to measure length. The models in this section and Section 5.2.4 are centred at the equator, and 1° is approximately 111km. The trench is oriented in the north-south direction, and subduction is from east to west. Similar to Hu et al. [2004] and Wang et al. [2012], the lower boundary of all our models is at 500 km depth, within the mantle transition zone, and all the lateral boundaries are more than 500 km from the rupture zone. The top boundary is free, and the basal boundary is fixed. For each lateral boundary, displacements are fixed to zero in the normal direction but unconstrained in tangential directions. In a spherical Earth, there is no such thing as a plane strain or plane stress two-dimensional (2-D) model. When we refer to a model as being 2-D in this paper, we mean that the structure, material properties, and earthquake rupture are all uniform in the strike direction so that the problem is axisymmetric to allow a thin wedge to be used to represent the spherical Earth.

Viscoelastic Opposing Motion Induced by Asymmetric Stresses

The asymmetric coseismic deformation (Figure 5.1) is elastic except for the brittle failure of rocks immediately around the fault, but it has a first-order control on subsequent viscoelastic postseismic deformation, particularly in the short term and in the near field. As qualitatively discussed in Sun et al. [2014], greater tension is induced in the hanging wall than in the incoming plate seaward of the trench by the asymmetric rupture (white arrows in Figure 5.2). After the earthquake, relaxation of the viscoelastic mantle allows the great tension in the elastic upper plate to drive the trench and inland areas to move toward each other.

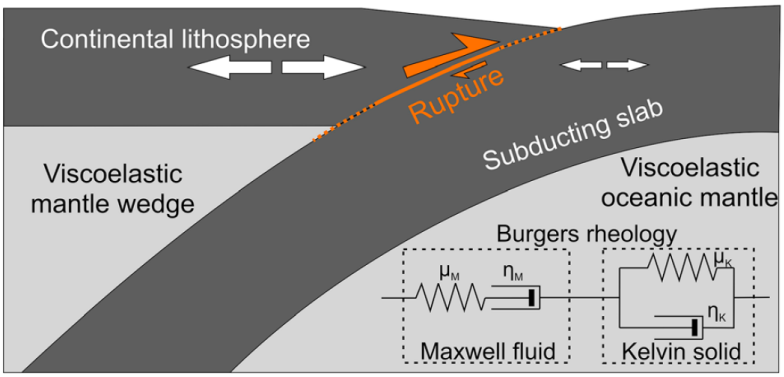

Figure 5.2. Model structure and rheology of the 2-D reference model REF (Table 5.1). Assigned coseismic fault slip is uniform (Us) in the solid segment of the shown rupture zone and linearly tapers to zero over the dashed segments. Orange arrows illustrate the asymmetric coseismic motion of the two fault walls (see Figure 5.1 and Section 5.2.3). Larger and smaller diverging white arrows represent different degrees of tension induced by the thrust rupture. The Burgers rheology applies to both the mantle wedge and the oceanic mantle. Symbols μ and η denote rigidity and viscosity, respectively, and subscripts M and K indicates Maxwell and Kelvin components, respectively.

To provide a more quantitative description of the above process, we show in Figure 5.3 the change of deformation rates and deviatoric stresses with time in the REF model. Similar to the model in Figure 5.1a, the REF model uses an idealized coseismic slip distribution that is uniform in the middle portion of the rupture zone but tapers linearly to zero in both the updip and downdip directions (orange dashed lines in Figure 5.2). Although unimportant for the purpose of demonstrating the physical mechanism in this section, details of the slip distribution have a first-order effect on near-field postseismic

deformation and will be discussed in section 5.2.4. Here we only consider viscoelastic relaxation of the earthquake-induced stresses without the influence of afterslip and fault relocking.

In Figure 5.3, the velocity fields at different times after the rupture illustrate viscous mantle flow as a result of stress relaxation, and the stress field (of selected sections) shows the much greater tension of the upper plate than the incoming plate due to the rupture asymmetry discussed in Section 5.2.3. The velocities form two convective cells sharing a sinking limb. Far-field inland sites move seaward with the clockwise cell, but the trench area moves landward with the counterclockwise cell. The velocities decrease with time, but the same flow pattern is sustained. As the mantle continues to relax, the stresses above the landward end of the rupture become less tensile, albeit very slowly (Figure 5.3c).

The model also shows that the dividing boundary between the opposing seaward and landward motion discussed in Sun et al. [2014] is over the above mentioned sinking limb. Over time, the effect of viscoelastic relaxation of earthquake-induced stresses will diminish, and the effect of relocking the megathrust will become increasingly dominant, so that this dividing boundary will migrate landward until the entire upper plate is in wholesale landward motion [Wang et al., 2012].

In this model, the viscoelastic landward motion of the above-rupture site 50 τ_M after the earthquake exceeds 20% of its coseismic motion. After a real earthquake, shallow afterslip [Hsu et al., 2006] may offset the effect of viscoelastic relaxation, modify the position of the dividing boundary of landward and seaward motion, and make the landward motion of the trench area less obvious or even make it move the other way. This also means that for a meaningful study of afterslip distribution, near-field effects of short-term viscoelastic relaxation must be understood and accounted for. This is the central issue of the present study and will be further discussed in Section 5.2.5.

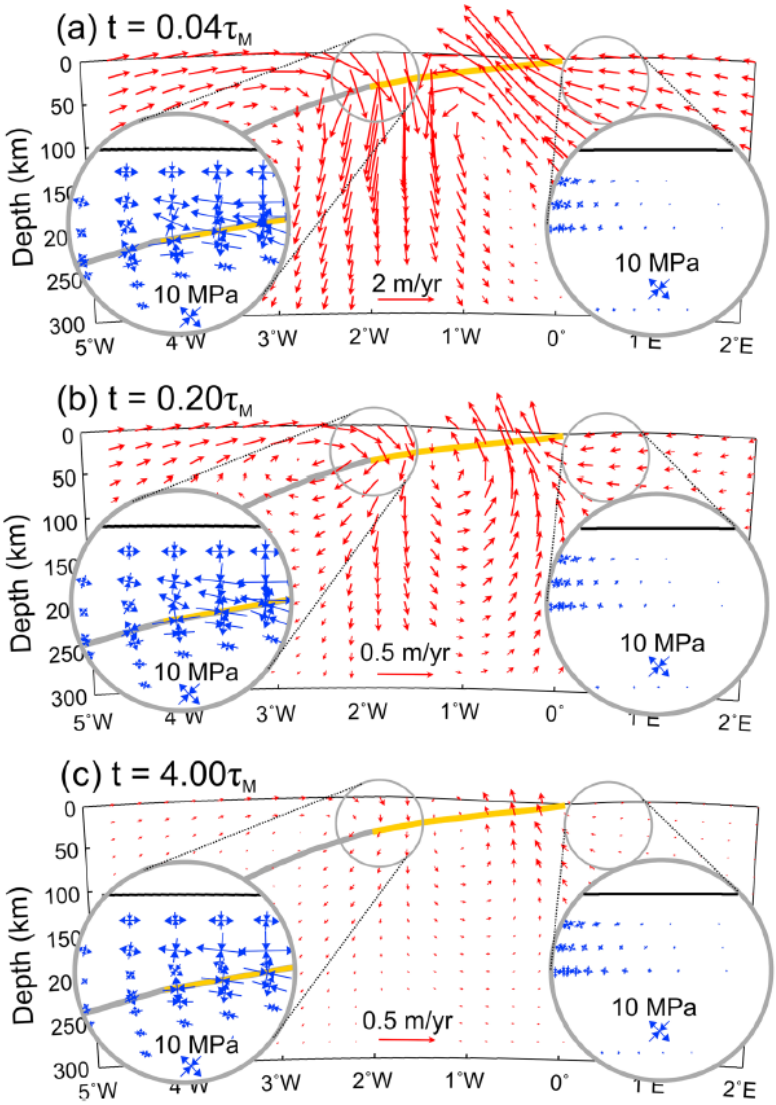

Figure 5.3. Results of model REF (Table 5.1). Postseismic velocities (red arrows) in response to earthquake alone, without afterslip and fault relocking. Orange part of the subduction interface is the rupture zone, in which slip tapers to zero at both the updip and downdip edges as shown in the top part of Figure 5.1. Deviatoric stresses are shown in the two zoom-in areas. For the material properties used in REF, τ_M is ~5 years.

5.2.4. Factors controlling viscoelastic opposing motion

Because megathrust rupture is always asymmetric in the sense explained in Section 5.2.3, the immediate viscoelastic opposing motion between the trench and land areas must commonly occur following subduction earthquakes. Important questions to be

answered include how the prevalence of this opposing motion is affected by various geological conditions and earthquake size and under what circumstances afterslip modelling can be adequately performed without including viscoelastic rheology. Models described in this section (Table 5.1) are designed to address these questions. For each model, except for the parameters being examined, all the other parameters are set to the same values as in REF. We will show that none of the parameter changes can change the fundamental behavior shown in Figures 5.3, but they affect the rates of motion in different parts of the system. Similar to Figure 5.3, deformation caused only by the viscoelastic relaxation of earthquake induced stresses is shown, without the effect of afterslip and fault relocking.

Mantle viscosities

Mantle viscosities strongly control the rate of postseismic motion. Variations in the thermal state and fluid contents and other factors may affect mantle viscosity thus can cause the rate of postseismic motion to differ among different subduction boundaries. Out of the numerous testing models, we use three of them to illustrate the viscosity effects (Table 5.1).

Models VK and VM1 both employ uniform mantle viscosities. In VK, the transient viscosity is higher than REF, so the landward motion of the trench area is slower than in REF right after the earthquake ($t < 0.2\,\tau_M$). In VM1, the steady state viscosity is higher than REF, so the landward motion is slower than in REF a longer time after the earthquake ($t > 0.4\,\tau_M$) (Figure 5.4).

In model VM2, the steady state viscosity of the oceanic mantle (1×10^{20} Pa s) is higher than that of the mantle wedge (1×10^{19} Pa s). In this case, the above-rupture site (green curve in Figure 5.4d) reverses its motion direction from landward to seaward at $\sim0.2\,\tau_M$. In comparison to VM1, the less viscous mantle wedge in VM2 results in a faster seaward flow of the shallow mantle wedge and hence a tendency for surface sites to move seaward.

Table 5.1. Model parameters[a]

Model	Mantle wedge η_K	Mantle wedge η_M	Oceanic mantle η_K	Oceanic mantle η_M	Slab thickness	Upper plate thickness	M_w	Figure No.
REF	5×10^{17}	1×10^{19}	5×10^{17}	1×10^{19}	30	30	N.A.	5.3
VK	1×10^{18}	1×10^{19}	1×10^{18}	1×10^{19}	30	30	N.A.	5.4
VM1	5×10^{17}	1×10^{20}	5×10^{17}	1×10^{20}	30	30	N.A.	5.4
VM2	5×10^{17}	1×10^{19}	5×10^{17}	1×10^{20}	30	30	NA	5.4
ST	5×10^{17}	1×10^{19}	5×10^{17}	1×10^{19}	60	30	NA	5.5
PT	5×10^{17}	1×10^{19}	5×10^{17}	1×10^{19}	30	40	NA	5.5
SLIP	5×10^{17}	1×10^{19}	5×10^{17}	1×10^{19}	30	30	NA	5.6
RL1	5×10^{17}	1×10^{19}	5×10^{17}	1×10^{19}	30	30	9.5	5.7
RL2	5×10^{17}	1×10^{19}	5×10^{17}	1×10^{19}	30	30	9.1	5.7
ME1	5×10^{17}	1×10^{19}	5×10^{17}	1×10^{19}	30	30	8.3	5.8
ME2	5×10^{17}	1×10^{19}	5×10^{17}	1×10^{19}	30	30	7.9	5.8
ME3	5×10^{17}	1×10^{19}	5×10^{17}	1×10^{19}	30	30	8.3	5.8
SE1	5×10^{17}	1×10^{19}	5×10^{17}	1×10^{19}	30	30	7.5	5.8
SE2	5×10^{17}	1×10^{19}	5×10^{17}	1×10^{19}	30	30	7.5	5.8
Nias1	5×10^{17}	1×10^{19}	5×10^{17}	1×10^{20}	30	30	NA	5.9 & 5.10
Nias2	2.5×10^{17}	1.8×10^{18}	2×10^{18}	1×10^{20}	30	30	NA	5.9 & 5.10
Tohoku1	2.5×10^{17}	1.8×10^{18}	2×10^{18}	1×10^{20}	45	25	9.09	5.11
Tohoku2	2.5×10^{17}	1.8×10^{18}	2×10^{18}	1×10^{20}	45	25	9.09	5.11

[a] η_K and η_M are the transient (Kelvin) and steady-state (Maxwell) viscosities (Pa s). Slab and upper plate thicknesses are in km. Upper plate thicknesses in Nias1, Nias2, Tohoku1, and Tohoku2 are those apart from the cold nose (see Figure 5.9b). Rigidity of the elastic plate is 48 G Pa, and rigidity of the viscoelastic mantle is 64 G Pa, except in Nias2, Tohoku1, and Tohoku2 in which rigidity of the Kelvin body is 136 G Pa [Sun et al., 2014]. Poisson's ratio and density in all the models are 0.25 and 3300 kg/m^3, respectively. NA = not available.

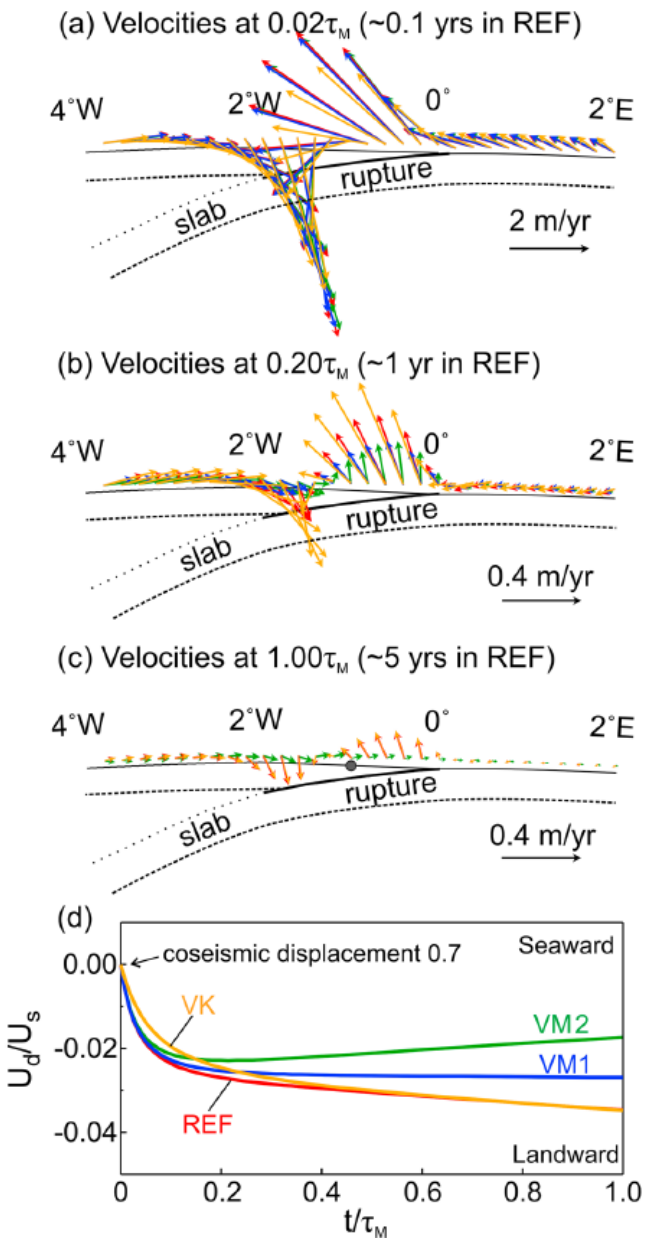

Figure 5.4. Results of four models with different viscosities but identical fault slip: REF, VK, VM1, and VM2 (Table 5.1). (a–c) Surface velocities at different times after the earthquake. Here τ_M is that of the REF model (~5 years). (d) Time-dependent postseismic east displacement Ud, normalized by fault slip Us, of a surface site above the rupture zone (location shown as the solid circle in Figure 5.4c). Results for different models are color coded as their names in Figure 5.4d.

Thicknesses of elastic plates

The thickness of the oceanic lithosphere varies with its age. An older lithosphere is cooler and hence thicker. A thicker elastic slab tends to retard the process of viscoelastic relaxation and thus slows the landward motion of the trench area. To demonstrate this "anchoring" effect, we use a model (ST) with a slab twice as thick as in REF (Table 5.1). Trench-normal profiles of viscoelastic east-west (E-W) surface displacements at two selected time points ($0.2\,\tau_M$ and $4\,\tau_M$ after the earthquake) are shown in Figure 5.5a. The anchoring effect of the 60 km slab is so large that several near-trench sites undergo slight seaward motion at $4\,\tau_M$ (~20 years for $\eta_M = 10^{19}$ Pa s) (blue curve in Figure 5.5a).

Another effect of the thicker slab (not displayed) is that its greater flexural rigidity increases the wavelength of the spatial variations of postseismic vertical deformation. Compared to REF, the area of surface uplift extends much farther seaward and the area of subsidence extends much farther landward. However, as will be discussed in the next sub-section, the vertical deformation is controlled more strongly by coseismic fault slip distribution.

The thickness of the lithospheric upper plate is controlled by the thermal state of the back-arc region. For simplicity, here we ignore the contrast between the cold fore arc and warm arc and back arc [Wada and Wang, 2009]. To illustrate the general role of upper plate thickness, we use a model (PT) with an upper plate thicker than in REF by 10 km (Table 5.1). The effect of a thinner upper plate is the opposite (not shown).

In coseismic deformation, because the upper plate has a lower rigidity than the mantle, its larger thickness decreases the stiffness of the upper wall of the thrust system. Therefore, the same prescribed coseismic fault slip induces less stresses and hence smaller far-field displacements (not displayed here). For postseismic deformation, the role of the thicker upper plate is reversed. As the mantle wedge relaxes, the thicker upper plate results in a stiffer upper wall of the thrust system than in REF. It thus dampens the seaward mantle wedge flow beneath the inland area (Figure 5.3), resulting in a faster landward motion of the trench area (Figure 5.5b).

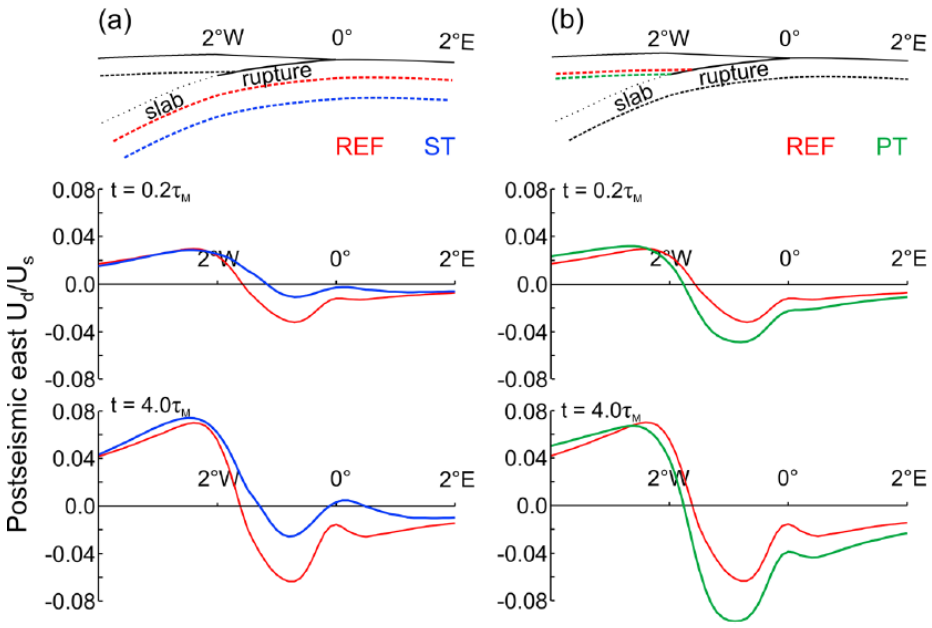

Figure 5.5. Results of models ST (blue) and PT (green) (Table 5.1) in comparison with REF (red) showing the effects of varying the thicknesses the slab and the upper plate on postseismic viscoelastic relaxation. (a) Surface displacements normalized by fault slip at two labelled times for slab thicknesses 30 (red) and 60 (blue) km. (b) Surface displacements normalized by fault slip at two labelled times for upper plate thicknesses 30 (red) and 40 (green) km. In these models τ_M is ~5 years.

Downdip distribution of coseismic slip

Subduction earthquakes exhibit a wide variety of slip distributions. The examples in Figure 5.6 illustrate how the slip distribution affects near-field postseismic deformation. Figure 5.6a reproduces the t = 0.2 τ_M velocity field of REF (Figure 5.3b), with coseismic fault slip peaking at some 50–150 km from the trench. The results shown in Figure 5.6b are also based on the REF model but with a different slip distribution in which the slip peaks within 50 km of the trench. The two model earthquakes have the same average slip (and hence moment), but the main slip area in Figure 5.6b is shallower, similar to most published rupture scenarios of the 2011 Tohoku-oki earthquake [Tajima et al., 2013].

Coseismic slip distribution determines the dividing boundary between seaward and landward motion, that is, the location of the sinking limb of the velocities field (Figure 5.3). Therefore, the slip distribution strongly controls the spatial pattern of postseismic

subsidence (Figure 5.6). In comparison, changes in other parameters have little effect on the location of the dividing boundary and vertical deformation pattern (Figures 5.4 and 5.5), although they do affect deformation rates and, in the case of slab thickness, the size of the areas of uplift and subsidence.

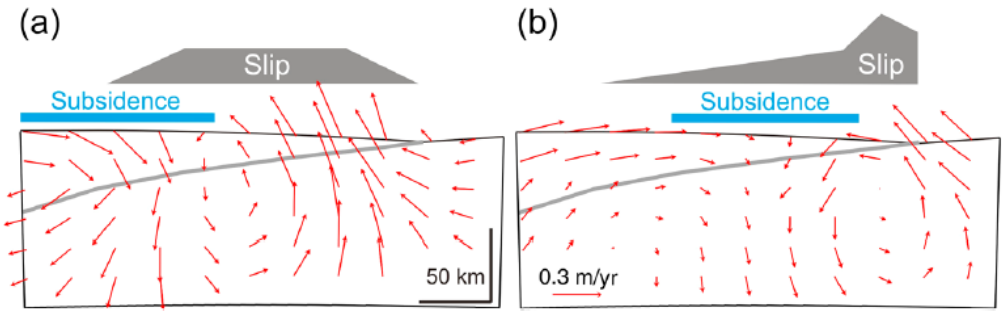

Figure 5.6. Velocity field at t = 0.2 τ_M (~1 year) to illustrate the effect of coseismic slip distribution on postseismic relaxation. Coseismic slip distribution along the megathrust and area of surface subsidence at t = 0.2 τ_M are shown at the top. (a) Part of the REF model shown in Figure 5.3b. (b) Model with a seaward skewed slip distribution but otherwise the same as REF.

Rupture length and earthquake size

The above 2-D models, implying extremely long rupture length in the strike direction, allow us to investigate the physical process in a simple manner. However, real earthquakes have finite along-strike rupture lengths and different along-dip rupture widths that control earthquake size, distribution of the cosesimic stress perturbation, and thus evolution speed of postseismic deformation characterized by the progressive motion reversal away from the rupture zone [Wang et al., 2012]. In this section, we use three-dimensional (3-D) models to illustrate the effects of finite rupture lengths and different earthquake sizes. These models have uniform structure and material properties along strike, the same as REF, but variable rupture zone geometries (Figures 5.7 and 5.8).

Results of two models with rupture lengths 6° (RL1) and 2° (RL2) are shown in Figure 5.7. The two models share some common features. Immediately after the earthquake (t = 0.004 τ_M), all surface sites along the line of symmetry (the equator) behave in the same way as in the 2-D models. In map view, sites in the rupture area show

a pattern of landward divergent flow, while inland sites show a pattern of seaward convergent flow toward the downdip edge of the rupture. The area of landward motion shortly after the earthquake is broader than the rupture zone along strike but shrinks toward the rupture edge with time (dashed curves in Figures 5.7a and 5.7c).

Figures 5.7b and 5.7d show velocities as a function of time for five upper plate sites, all at the same distance (1°) from the trench (green dots in Figures 5.7a and 5.7c). With the shrinking of the area of landward motion, sites not within the rectangular rupture area eventually reverses their motion direction from landward to seaward, and the time of motion reversal is inversely related to the distance from the rupture. The different rupture lengths of RL1 and RL2 give rise to differences in their viscoelastic deformation. The area of near-field landward motion following a longer rupture shrinks faster.

Our tests (not all shown) indicate that shorter rupture lengths result in slower viscoelastic seaward motion of inland sites in both the transient and steady state phases and slower landward motion of the rupture area in the transient phase. The systematic increase in the tendency for seaward motion in the inland area with increasing rupture length is due to the faster seaward mantle wedge flow (Figure 5.3) as a result of the larger coseismic stress perturbation.

Figure 5.8 shows 1 year ($t = 0.2\,\tau_M$) viscoelastic postseismic surface displacements for four earthquakes with different sizes and/or depths. Larger events ($M_w > \sim 8$) induce large asymmetric stresses and thus faster landward motion of the rupture area (Figures 5.8a–5.8d). A shallower rupture (closer to the trench) (Figure 5.8d) induces greater postseismic landward motion of the trench and the incoming plate. For smaller earthquakes ($M_w \sim 7.5$), the viscoelastic effects are much less pronounced. For example, in the models of Figures 5.8e and 5.8f, 4 year postseismic landward motion of the rupture area is less than 1% of the peak coseismic slip, regardless of the rupture depth. Our tests using the same small earthquake rupture but with other reasonable values of mantle viscosities show similarly small surface motion (results not displayed). In this situation, a purely elastic model is acceptable in the determination of afterslip from geodetic observations.

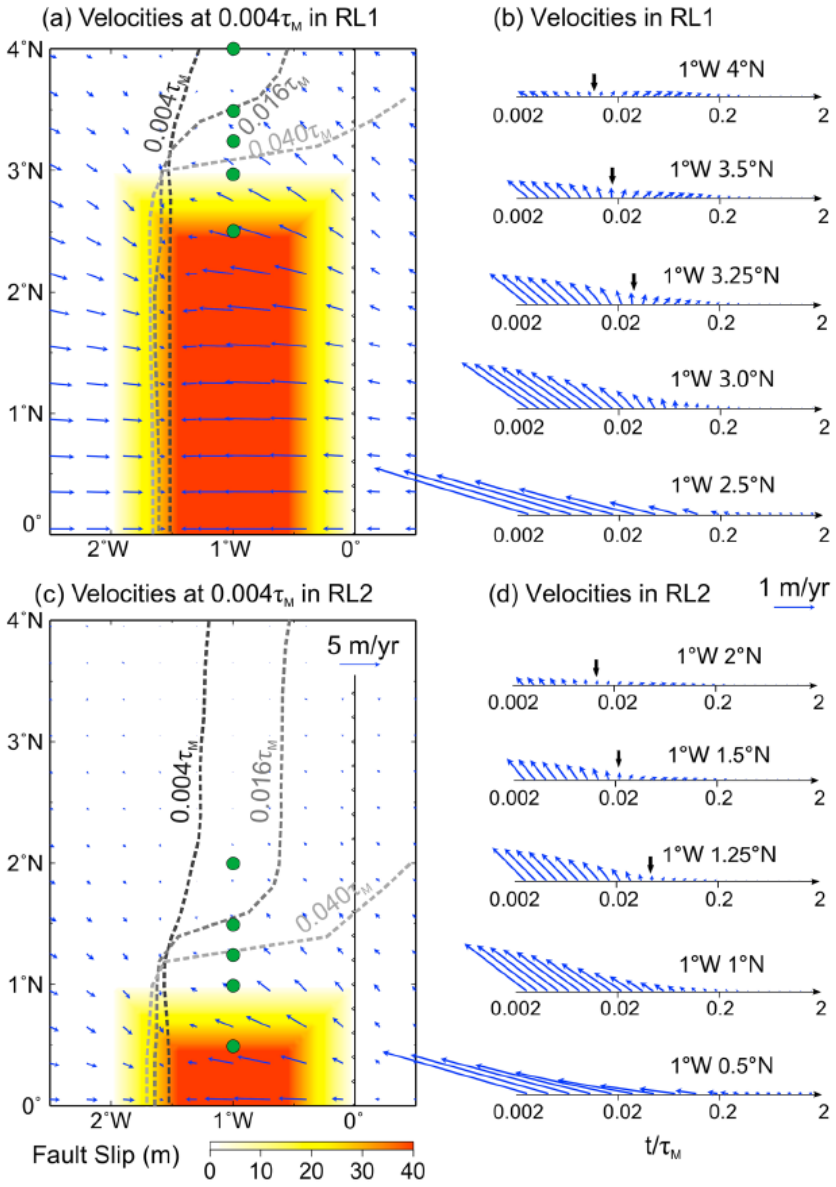

Figure 5.7. Velocities of two models (RL1 and RL2, Table 5.1) with finite rupture lengths in strike direction. The models are symmetric with respect to the equator, so only the northern half is shown. (a and c) Velocities of surface points at $0.004\,\tau_M$. Dashed lines depict the dividing boundary of landward and seaward motion at different times after the earthquake; surface sites east of the boundary move landward, and sites west of it move seaward. (b and d) Time-dependent velocities at five sites marked by green circles in Figures 5.7a and 5.7c, respectively. Vertical black arrow marks the time of reversal of motion from landward to seaward.

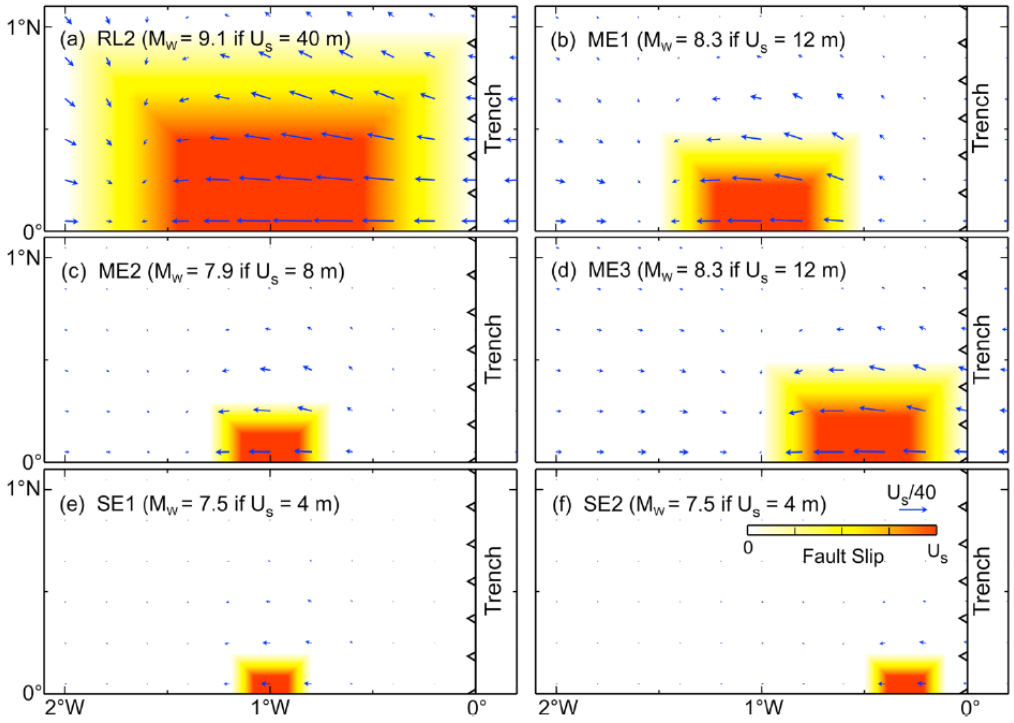

Figure 5.8. One year (~0.2 τ_M) postseismic displacements due to viscoelastic relaxation in six models with different rupture sizes and/or depths (Table 5.1). Slab depth at 1°W is about 22.5 km. The models are symmetric with respect to the equator, so only the northern half is shown. Magnitudes of earthquakes are based on a rigidity of 48 GPa. The depths of the centre of the rupture are (a–c and e) ~22.5 km, (d) ~15.5 km, and (f) ~13 km.

5.2.5. Assessing shallow afterslip in a viscoelastic Earth

Viscoelastic mantle relaxation and afterslip downdip of the rupture zone both cause postseismic seaward motion of areas landward of the rupture zone [Hu and Wang, 2012]. If viscoelastic relaxation is neglected, observed postseismic motion of these areas will be incorrectly attributed to the deep afterslip alone, and the afterslip will be overestimated from geodetic observations [Sun et al., 2014].

Closer to the trench, the effect is reversed. Here viscoelastic relaxation causes landward postseismic motion, as shown by Sun et al. [2014] and the tests discussed in Sections 5.2.3 and 5.2.4 above, but shallow afterslip still causes seaward motion. In this situation, if viscoelastic relaxation is neglected, the afterslip will be underestimated from

geodetic observations. In this section, we use two real-world examples to show how the incorporation of viscoelasticity affects the estimates of shallow afterslip. In the first example, the 2005 Nias earthquake, shallow afterslip occurred updip of the main rupture zone. In the second example, the 2011 Tohoku-oki earthquake, shallow afterslip occurred in the same depth range as the main rupture but outside of the main rupture area.

Shallow Afterslip Following the 2005 Nias Earthquake

The 28 March 2005 M_w 8.7 Nias earthquake ruptured a ~350 km segment of the subduction fault offshore of Sumatra (Figure 5.9a). The rupture terminated to the north near the southern edge of the 2004 M_w 9.2 Sumatra-Andaman earthquake rupture [Briggs et al., 2006] and to the south at a creeping segment of the megathrust [Konca et al., 2008; Chlieh et al., 2008].

At the time of the earthquake, three continuous GPS sites located on fore-arc islands recorded up to ~4.5 m seaward displacement right above the rupture [Hsu et al., 2006; Briggs et al., 2006]. After the earthquake, these and additional new sites continued to move seaward and accrued up to 0.8 m horizontal displacement (site LHWA) over 9 months (Figure 5.9a) [Hsu et al., 2006]. This pattern of postseismic deformation is well explained by shallow afterslip updip of the rupture, and the amount of afterslip was estimated from the GPS data using an elastic model [Hsu et al., 2006] (Figure 5.9a). The inferred shallow afterslip is evidence for the velocity-strengthening behavior of the shallow megathrust in this area [Wang and Hu, 2006; Hu and Wang, 2008], and the Nias model is a classic example for the traditional seismogenic zone model in which the shallow segment of the megathrust resists coseismic rupture but slips aseismically afterward [Wang, 2013].

Here using a 2-D model profile crossing site LHWA (Figure 5.9b), we illustrate that the argument of Hsu et al. [2006] for the presence of large shallow afterslip is further strengthened if we incorporate the effects of viscoelastic relaxation. For the purpose of this paper, it suffices to provide an order of magnitude estimate of the contribution of viscoelastic relaxation to surface deformation over the 9 month observation period

considered by Hsu et al. [2006]. A full-blown model that inverts GPS time series for the temporal evolution of the afterslip using Green's functions derived in a 3-D viscoelastic subduction system awaits future studies.

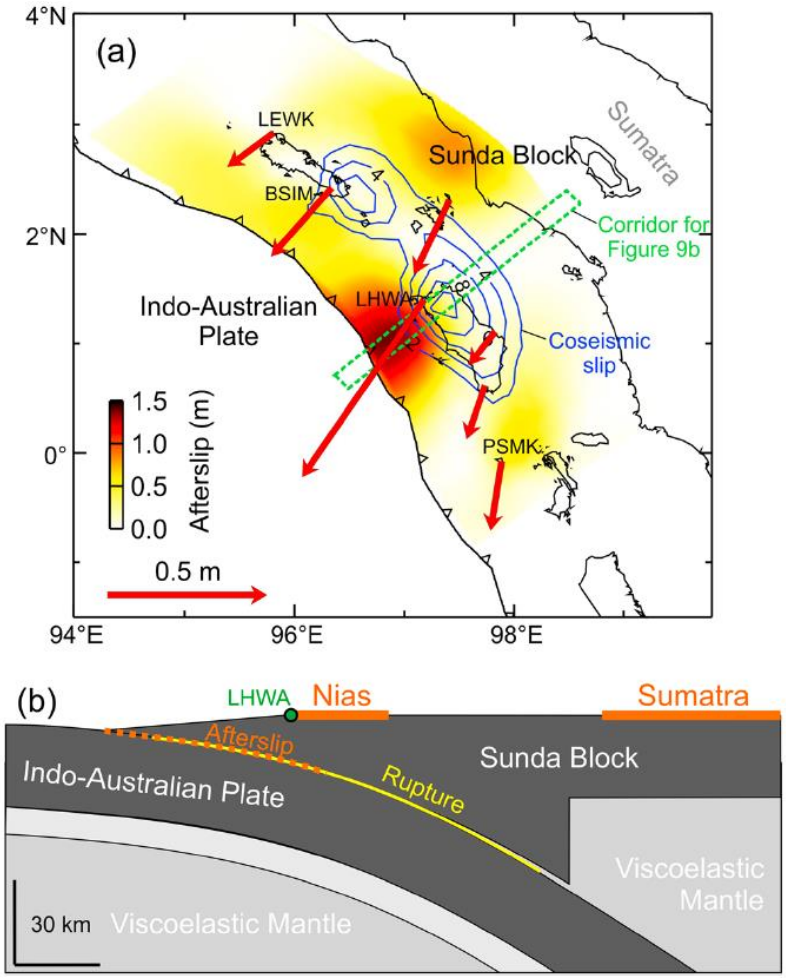

Figure 5.9. (a) Coseismic slip of the 2005 M_w 8.6 Nias earthquake, observed postseismic GPS displacements (red arrows) over the first 9 months, and afterslip inferred from these observations using an elastic model [Hsu et al., 2006]. (b) Structure of 2-D viscoelastic models (Nias1 and Nias2 in Table 5.1) along the green dashed corridor used to derive results shown in Figure 5.10. A weak layer below the slab (light shading), the same as in the Tohoku-oki model of Sun et al. [2014], is used only in Nias2. Note that "Figure 9b" in (a) refers to the figure numbering in the published article. For this dissertation, it should be interpreted as "Figure 5.9b".

For our 2-D model profile, we employ the fault geometry compiled by Chlieh et al. [2008] using relocated earthquakes and megathrust earthquake focal mechanisms (Figure

5.9b). Following Sun et al. [2014], we use a thickened elastic upper plate in the fore arc to account for the mechanical effect of a cold nose of the fore-arc mantle wedge (Figure 5.9b) [Wada and Wang, 2009]. Similar to the finite element model of postseismic deformation of the 2004 M_w 9.2 Sumatra-Andaman earthquake by Hu and Wang [2012], we set the thickness of the subducting slab at 30 km. Hu and Wang [2012] used a 40 km thick upper plate, but we use a smaller thickness of 30 km in conjunction with the much thicker portion that represents the cold nose of the mantle wedge.

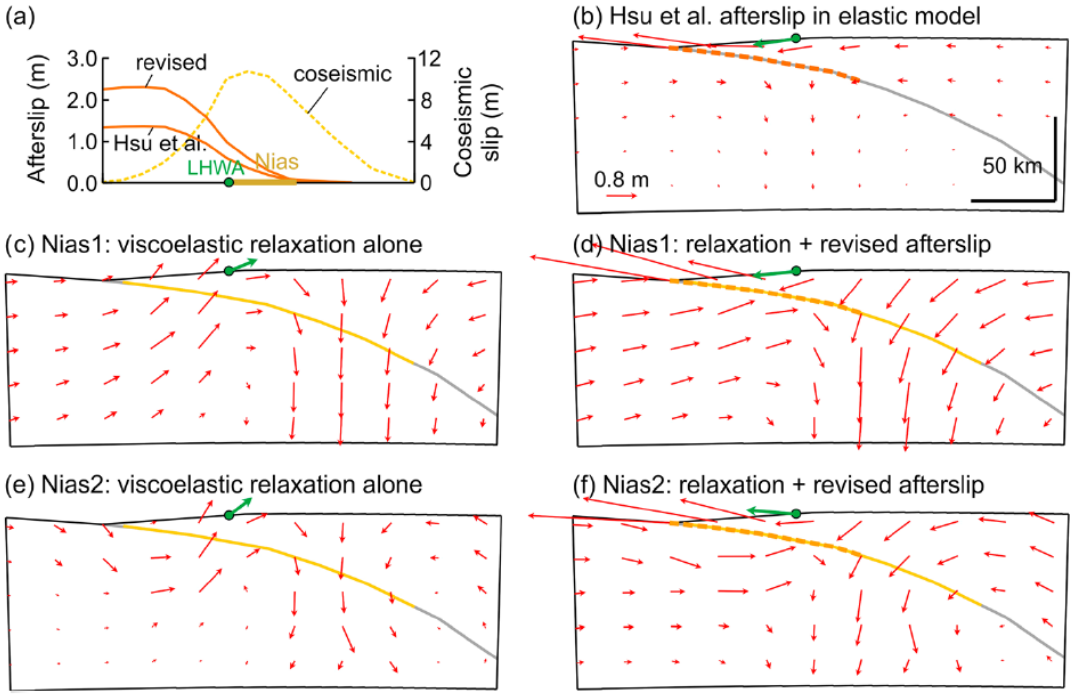

Figure 5.10. Two-dimensional models to illustrate the effects of including and not including viscoelasticity in estimating afterslip for the 2005 Nias earthquake. Arrows show model-predicted postseismic displacements over the first 9 months (same period as for the GPS observations shown in Figure 5.9a). (a) Downdip distributions of coseismic slip and afterslip of Hsu et al. [2006] along the model corridor shown in Figure 5.9a and revised afterslip (1.7 times the original) after including viscoelastic relaxation. (b) Deformation caused by Hsu et al.'s [2006] afterslip in an elastic model. The 2-D model prediction at site LHWA (green) is in agreement with GPS observation except for some exaggeration due to the neglect of 3-D effects. (c and e) Deformation caused by viscoelastic relaxation alone in two viscoelastic models (Table 5.1). (d and f) Deformation in the same models as in Figures 5.10c and 5.10e, respectively, but also including the revised afterslip.

We test two viscoelastic models (Table 5.1). Model Nias1 is based on the Sumatra model of Hu and Wang [2012] in which the Kelvin mantle viscosity is 5.0×10^{17} Pa s and the Maxwell viscosities of the mantle wedge and oceanic mantle are 10^{19} Pa s and 10^{20} Pa s, respectively. Model Nias2 is similar to the Tohoku-oki model of Sun et al. [2014] and features much lower viscosities, with the Kelvin and Maxwell viscosities of the mantle wedge being 2.5×10^{17} Pa s and 1.8×10^{18} Pa s, respectively, and a low-viscosity (2.5×10^{17} Pa s) layer below of the slab. As discussed in Sun et al. [2014], the lower viscosity values required by the Tohoku-oki model, especially that of the steady state viscosity, imply that the transient phase of postseismic viscoelastic relaxation may be more complex than can be described by the biviscous Burgers' rheology and may last longer than previously thought. Other material property parameters are the same as in the REF model (Table 5.1).

We apply the coseismic slip and afterslip values of Hsu et al. [2006] along the corridor shown in Figure 5.9a to our 2-D model (Figure 5.10a) and compare resultant deformation fields obtained using a purely elastic model (Figure 5.10b) and using the two viscoelastic models (Figures 5.10c–5.10f). Because we neglect 3-D effects in this exercise, we should not compare model results directly with observed displacement of site LHWA but should only examine how including or not including viscoelastic relaxation affects model displacement at this site (green arrow in Figures 5.10b, 5.10d, and 5.10f), as well as in the rest of the model domain.

A purely elastic model (Figure 5.10b) produces larger displacement at LHWA than that of Hsu et al. [2006] (Figure 5.9a) because of the neglect of 3-D effects as discussed above. In both the viscoelastic models, the effect of viscoelastic relaxation alone without afterslip (Figures 5.10c and 5.10e) results in the same pattern of opposing motion as shown by models in Sections 5.2.3 and 5.2.4 and causes site LHWA to move landward, opposite of its observed seaward motion. In order to explain the observed seaward motion of LHWA using these viscoelastic models, we need to apply an afterslip much larger than required by the elastic model of Figure 5.10b. By using afterslip values 1.7 times those of Hsu et al. [2006] (Figure 5.10a), we have obtained the results shown in Figures 5.10d and

5.10e. With the greater afterslip, these models predict essentially the same amount of seaward motion of LHWA as in the elastic model of Figure 5.10b. In a more complete 3-D model, the incorporation of viscoelastic relaxation will have the same effect, and afterslip values required to explain all the GPS observations will need to be scaled up in this fashion from those based on the original 3-D elastic model. The resultant much greater shallow afterslip lends stronger support for the argument of Hsu et al. [2006] regarding the velocity-strengthening behavior of the shallow segment of the megathrust.

Shallow Afterslip Following the 2011 Tohoku-Oki Earthquake

The 2011 M_w 9.0 Tohoku-oki earthquake occurred offshore of northeast Japan with a very large coseismic fault slip (> 50 m) at shallow depths that breached the trench [e.g., Tajima et al., 2013; Iinuma et al., 2012; Fujiwara et al., 2011; Kodaira et al., 2012; Kido et al., 2011; Sato et al., 2011]. After the earthquake, seafloor GPS sites in the main rupture area and near the trench quickly reversed their motion to move landward, opposing the continuing seaward motion of land-based GPS sites [Japan Coast Guard and Tohoku University, 2013; Watanabe et al., 2014]. The landward motion of the seafloor sites provides unambiguous evidence for the prevalence of viscoelastic relaxation in short-term postseismic deformation [Sun et al., 2014]. The viscoelastic model of Sun et al. [2014] (Figure 5.11a) requires much less deep afterslip than estimated from land-based GPS data using elastic models [Ozawa et al., 2012; Silverii et al., 2014]. The lack of deep afterslip is complementary to the accelerated fault creep downdip of the rupture zone prior to the Tohoku-oki earthquake inferred from decade-long land-based GPS observations [Mavrommatis et al., 2014; Yokota and Koketsu, 2015].

The study of Sun et al. [2014] was focused mainly on a margin-normal corridor crossing the main rupture area. The behavior of the shallow megathrust seen here, that is, very large trench-breaching coseismic slip followed by little or no afterslip, is in sharp contrast with that of Nias in 2005 discussed in the preceding section, and it demonstrates that the traditional seismogenic zone model is not universally applicable [Wang, 2013]. However, Sun et al. [2014] also pointed out that the large seaward motion of site FUKU to the south and the lack of significant seaward motion of site KAMN to the north (Figure

5.11a) might be due to shallow afterslip. In this section, we modify the model of Sun et al. [2014] to address this issue. The results are shown in Figure 5.11b.

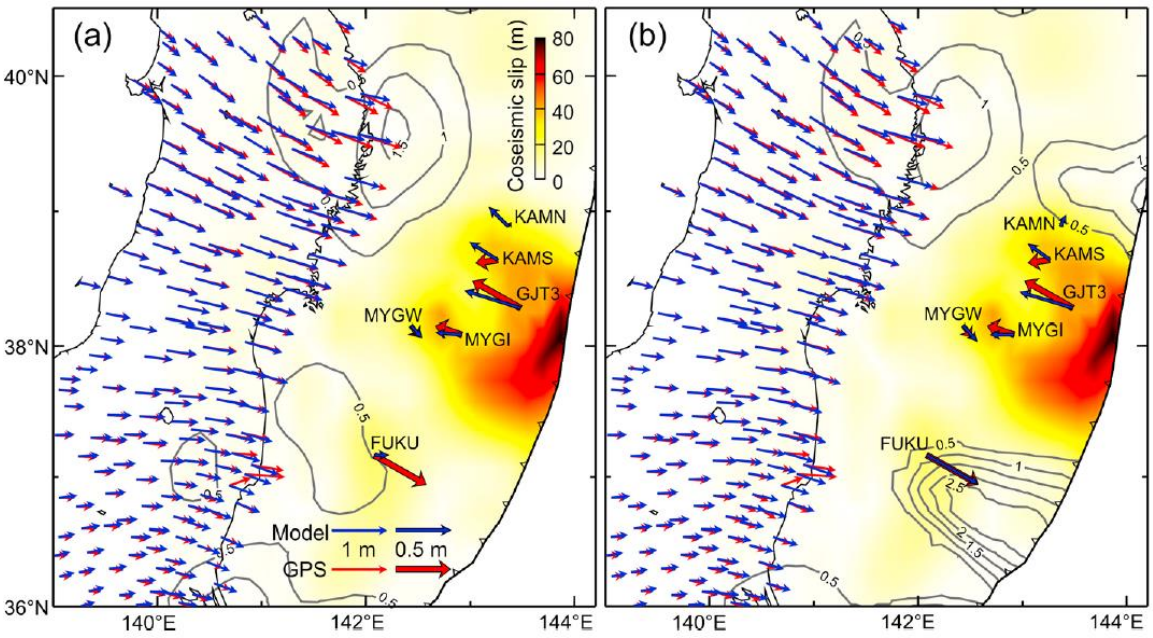

Figure 5.11. One year postseismic displacements of land and seafloor GPS stations following the 2011 M_w 9.0 Tohoku-oki earthquake. (a) Results of the 3-D finite element model of the Japan Trench subduction zone of Sun et al. [2014] (figure modified from Sun et al. [2014]). Afterslip is contoured in metres. No shallow afterslip is included in this model. (b) Results obtained using the same 3-D finite element model as in Sun et al. [2014], but with the addition of shallow afterslip near seafloor GPS sites FUKU and KAMN (contours in metres) and correspondingly smaller deep afterslip.

Besides afterslip, there is no other logical way to explain the very fast seaward motion of site FUKU, but the location of the fault patch that undergoes afterslip in this part of the margin is difficult to constrain because of the lack of a dense seafloor geodetic network nearby. Therefore, we do not attempt to pursue a unique solution but only to provide a representative scenario that demonstrates the importance of shallow afterslip (Figure 5.11b). In the dip direction, we infer that it is more likely that the afterslip occurs mostly seaward of the site, based on the observed postseismic subsidence over the first year at this location [Watanabe et al., 2014]. Our modelling indicates that viscoelastic

relaxation causes very little vertical displacement of this site, and deep afterslip can only lead to uplift here. The updip edge of the afterslip patch cannot be determined. For simplicity, we assume that it extends all the way to the trench. The northern termination of the afterslip patch is expected to be south of the main rupture area. To the south, the afterslip may extend much farther than depicted by the slip patch shown in Figure 5.11b and may even merge into a creeping segment of the megathrust around 36°S, where a seamount chain is subducting [Mochizuki et al., 2008; Wang and Bilek, 2014]. Within the creeping segment, a near-trench seafloor GPS site is observed to be moving seaward also at a relatively fast rate [Bürgmann and Chadwell, 2014].

The model of Sun et al. [2014] predicts landward motion of site KAMN due to viscoelastic relaxation (Figure 5.11a). Because mantle relaxation affects surface deformation at rather large wavelengths as compared with the dimension of coseismic rupture, it cannot produce large postseismic motion at sites GJT3 and KAMS without also producing significant motion at KAMN. The lack of observed large motion at KAMN is therefore best explained by the effect of shallow afterslip (Figure 5.11b). In fact, second-order temporal variations of the GPS time series at site KAMS and the faster than observed motion of that site predicted by the model (Figure 5.11a) were also attributed to local fault motion [Sun et al., 2014]. Similar to the FUKU area, the assumed afterslip patch near KAMN shown in Figure 5.11b only serves as one candidate among many possible afterslip scenarios. The current sparse seafloor geodetic observations do not offer adequate resolution to constrain afterslip distribution at shallow depths. Better understanding of shallow megathrust behavior requires more near-field observations. Nonetheless, the model shown in Figure 5.11b illustrates the importance of including viscoelasticity, as an elastic model would predict no afterslip at KAMN and unphysical normal-faulting-type afterslip at GJT3, KAMS, and MYGW.

5.2.6. Conclusions

Among all the processes controlling short-term postseismic deformation following great subduction earthquakes, afterslip and viscoelastic relaxation are of first-order

importance but their relative contribution remains unclear. Afterslip is determined from geodetic observations commonly by using a purely elastic Earth model, assuming viscoelasticity is less important in the short-term postseismic deformation. But recent seafloor geodetic observations following the 2011 M_w 9 Tohoku-oki earthquake provided unambiguous evidence for the dominant role of viscoelastic relaxation [Sun et al., 2014]. To understand whether viscoelastic relaxation is universally prevalent after subduction earthquakes and how it influences afterslip determination, we have conducted a systematic numerical study of postseismic viscoelastic deformation as controlled by various geometrical and rheological factors and earthquake sizes. We have also investigated shallow afterslip processes after the great 2005 Nias and 2011 Tohoku-oki earthquakes using viscoelastic models. Here we draw the following conclusions.

1. Earthquake size is among the most important factors for determining whether viscoelastic relaxation can be ignored in afterslip determination. In our model tests with different mantle viscosities and earthquake rupture depths, viscoelastic deformation following events of $M_w > \sim 8$ is always large and cannot be ignored. However, viscoelastic deformation following earthquakes of $M_w < 7.5$ is usually small, such that afterslip determined in a purely elastic model can be a reasonable approximation.

2. Postseismic deformation due to viscoelastic relaxation shows a characteristic pattern (Figure 5.3). Above the area of downdip rupture termination, the surface (seafloor) undergoes postseismic subsidence, and the inland and trench areas at the two sides move toward each other, such as observed after the 2011 M_w 9 Tohoku-oki earthquake. Postseismic deformation not showing the landward motion of the rupture area, such as after the 2005 M_w 8.7 Nias earthquake and in some part of the Japan Trench after the 2011 M_w 9 Tohoku-oki earthquake, indicates large afterslip at shallow depths that locally offsets the effect of the viscoelastic relaxation.

3. Various rheological and geometrical factors affect the rates and spatial wavelengths of short-term viscoelastic deformation. A lower transient mantle viscosity, a thinner slab, and a thicker upper plate all lead to faster landward motion of the rupture area, although a low value of steady state viscosity for the mantle wedge and/or a high value for that of the oceanic mantle may retard the landward motion at some later time.

Lower mantle viscosities cause faster postseismic subsidence near the landward edge of the rupture, and a thicker slab can cause the subsidence to occur over a wider area. It is important to emphasize that both the rate and spatial wavelength of postseismic subsidence are strongly controlled by the pattern of coseismic slip distribution (Figure 5.6). The different effects of various factors reflect the complexity of the physical process and hence difficulty in precisely constraining mantle rheology using current geodetic observations. More offshore geodetic observations near the trench and the megathrust seismogenic zone at different margins are urgently needed. The numerical results of this work may provide some guidance for the development of future observation strategies.

4. Afterslip, whether deep or shallow, always causes seaward motion of the surface, whereas viscoelastic relaxation causes opposing motion of the trench area and the area landward of the rupture zone. Therefore, compared to purely elastic models, afterslip determined using viscoelastic models should be smaller downdip of the rupture zone but larger at shallower depths. Our reassessment of the postseismic deformation following the Nias earthquake using simple 2-D viscoelastic models suggests that the actual afterslip may be greater than previously estimated using an elastic model by > 50%, further strengthening the dominance of shallow afterslip after this earthquake as argued by Hsu et al. [2006].

5.2.7. Acknowledgements

We thank J. He for developing the finite element code used in this work and Y. Hu, R. Hino, and T. Iinuma for fruitful discussions. T.S. was supported by a University of Victoria PhD Fellowship, an Alexander and Helen Stafford MacCathy Muir Graduate Scholarship, and Bob Wright Graduate Scholarships and a Natural Sciences and Engineering Research Council of Canada discovery grant to K.W. This is Geological Survey of Canada contribution 20140354.

Chapter 6. Crustal Deformation Following Global Great Subduction Earthquakes

This chapter is the third and final one of three chapters addressing how Earth rheology and fault behaviour control time-dependent crustal deformation following great subduction earthquakes. The main body of this chapter consists of the first draft of a manuscript in preparation for submitting to a journal. By comparatively studying ten M_w 8-9.5 earthquakes around the world, this work systematically examines the evolution of postseismic opposing crustal motion due primarily to viscoelastic relaxation and fault relocking. Special attention is paid to the effect of earthquake size on the duration of the opposing motion, but effects of other site-specific factors are also investigated. Section 6.1 describes basic manuscript information. Section 6.2 presents the manuscript itself.

6.1. Manuscript Information

6.1.1. Author, Coauthor, and Outside Contributions

Section 6.2 consists of the first draft of a manuscript in preparation. The author of this dissertation T.S. carried out most of the deformation modelling. Coauthors T.S. and K.W. designed the study and together did the writing. Coauthor J.H. wrote the computer code used for this study and provided assistance in the modelling. GNSS observations used in this study have all been previously published by other researchers, as referenced in the paper. The data were made available to us by Drs. J. Freymueller, T. Iinuma, R. Hino, M. Moreno, L. Feng, G. Khazaradze, J. Klotz, D. Remy, H. Perfettini, C. DeMets, W. Hutton, T. Nishimura, and M. Bevis, and Y. Itoh, F. Tomita, Shanshan Li, and Shaoyang Li.

6.1.2. Citation

Sun, T., K. Wang, and J. He, Crustal deformation following great subduction earthquakes controlled by earthquake size and mantle rheology, in preparation.

6.1.3. Authors' Names and Affiliations

Tianhaozhe Sun[1], Kelin Wang[2,1], Jiangheng He[2]

[1] School of Earth and Ocean Sciences, University of Victoria, Victoria, British Columbia, Canada V8P 5C2

[2] Pacific Geoscience Centre, Geological Survey of Canada, Natural Resources Canada, 9860West Saanich Road, Sidney, British Columbia, Canada V8L 4B2

6.1.4. Manuscript Format

The figures included in Section 6.2 have been numbered to maintain consistency with the rest of the dissertation. References cited in the manuscript are included in the bibliography of this dissertation.

6.2. Crustal deformation following great subduction earthquakes controlled by earthquake size and mantle rheology

6.2.1. Abstract

After a great subduction earthquake, while afterslip continues to cause seaward motion of surface sites, viscoelastic stress relaxation causes opposing motion, with the dividing boundary located roughly above the downdip termination of the rupture. As the effect of the viscoelastic relaxation decays with time, the effect of the relocking of the megathrust becomes increasingly dominant to cause the dividing boundary to migrate away from the rupture zone, eventually leading to wholesale landward motion of the surface. A higher mantle viscosity generally leads to slower viscoelastic relaxation which is manifested as longer-lived opposing motion and slower landward migration of its dividing boundary. A larger earthquake also leads to slower relaxation, because it induces

a greater coseismic stress perturbation, and its typical longer rupture length results in inefficient postseismic viscous mantle flow in the strike direction. As end-member examples, the geodetically observed opposing motion following the 1960 M_w 9.5 Chile earthquake is long-lived and is still continuing today, but that of the 1995 M_w 8.0 Antofagasta earthquake was short-lived and lasted for only one year. To understand the contributions from the different processes, we employ 3-D spherical-Earth finite element models of Burgers rheology to study ten $8.0 \leq M_w \leq 9.5$ subduction earthquakes. Using geodetic data of limited spatial and temporal coverages as constraints, we develop spatiotemporally continuous evolution of postseismic deformation for each earthquake. The continuous patterns enable comparisons of deformation processes among different earthquakes at common reference location. Using a reference location landward of the rupture and 175 km from the trench, we examine the "reference time" when the dividing boundary of opposing motion migrates through this location. The model results demonstrate the first-order dependence of the reference time on earthquake size, with a longer reference time following a larger earthquake. Our models suggest that other site-specific factors, such as subduction rate, locking state of the megathrust, and afterslip, can also affect postseismic deformation. Upper mantle viscosities constrained by available geodetic observations show somewhat different values between subduction zones far from each other.

6.2.2. Introduction

Following a great subduction earthquake, crustal deformation continues to evolve, due to continuing slip (afterslip) of various parts of the subduction fault, relocking of the fault, and relaxation of the coseismically induced stresses in the viscoelastic upper mantle (viscoelastic relaxation). Each of these processes plays a dominant role at a given time, and their combination gives rise to different deformation patterns at subduction zones that are presently at different times after a great earthquake. From these different patterns, each representing a different stage of the earthquake deformation cycle, a common evolution history can be pieced together, at least for very large earthquakes [Wang et al., 2012]. This deformation cycle starts with opposing motion of the land and trench areas

immediately after the earthquake [Sun et al., 2014]. The dividing boundary of the opposing motion then gradually migrates landward, eventually leading to wholesale landward motion, similar to the interseismic situation before the earthquake [Wang et al., 2012]. Over the past two decades, the Global Navigation Satellite Systems (GNSS), especially the Global Positioning System (GPS), have yielded geodetic observations of crustal deformation associated with a number of subduction earthquakes and thus enable us to examine this issue in a systematic manner.

In this work, we conduct a comparative study of postseismic deformation following great to giant (M_w 8-9.5) earthquakes. Building on the study of Wang et al. [2012] which examined three $M_w \geq 9$ earthquakes, we include seven $8 \leq M_w < 9$ events and two additional $M_w \geq 9$ events, thus providing a rather complete documentation to date of geodetically constrained postseismic deformation of $M_w \geq 8$ subduction earthquakes. For each earthquake, we review critical postseismic geodetic observations and construct three-dimensional (3-D) finite element models to simulate the postseismic deformation process. Compared to most previous studies that are usually focused on individual earthquakes, a global study of this type will better illuminate the common physical process. It may also help understand what and how site-specific factors in terms of rheology, structure, and plate kinematics affect the earthquake deformation cycle.

The aforementioned opposing motion begins immediately after the earthquake. While most of the upper plate adjacent to the rupture zone moves seaward, the near-trench area just above the rupture zone moves backwards in the opposite direction. The primary cause for this opposing motion is viscoelastic relaxation of the stresses asymmetrically induced by the megathrust earthquake; that is, the earthquake induces much greater tension landward than seaward of the rupture zone [Sun and Wang, 2015]. Seafloor GNSS observations following the 2011 M_w 9 Tohoku-oki earthquake show the dividing boundary of the opposing motion to be located roughly above the downdip termination of the rupture zone [Watanabe et al., 2014; Sun et al., 2014], where the greatest incremental tension was generated by the earthquake [Sun and Wang, 2015]. Because the effect of megathrust relocking becomes increasingly dominant as the effect of viscoelastic relaxation decays with time, landward motion gradually prevails. The

dividing boundary thus migrates landward, which can be observed as progressive reversal of GNSS sites away from the trench [Wang et al., 2012]. Geodetic observations at Southern Chile and Alaska, nearly half a century after the 1960 M_w 9.5 Chile and 1964 M_w 9.2 Alaska earthquakes, show that the dividing boundary of the opposing motion has migrated to some 200 – 300 km from the trench [Hu et al., 2004; Wang et al., 2007; Freymueller, 2008; Li et al., 2016]. In time, the dividing boundary in these regions will continue to migrate farther inland until there is no opposing motion (Figure 6.1). An example of the eventual wholesale landward motion is given by observations at the Cascadia margin today, more than 300 years after a M_w ~9 earthquake in 1700, after a correction for the secular motion of upper-plate crustal blocks is made [Wang et al., 2003; McCaffrey et al., 2013].

We are particularly interested in the migration of the dividing boundary of the opposing motion. The "speed" of this migration and the spatial extent of the opposing motion are theoretically inferred to be associated with not only mantle rheology, but also the size of the earthquake [Wang et al., 2012]. Because a larger earthquake causes a larger stress perturbation, the ensuing viscoelastic relaxation takes longer, and the opposing motion involves a large area and is longer-lived [Wang et al., 2012]. Another reason is that a larger earthquake usually features a longer rupture along strike, so that the flow of mantle material during relaxation is geometrically constrained to occur dominantly in the dip direction [Wang et al., 2012]. For a smaller earthquake, it is easier for mantle materials to flow in from both ends of the rupture, and the additional along-strike flow helps to speed up the relaxation. By synthesizing postseismic observations and modelling the process of opposing motion for a range of earthquake magnitudes, we are able to investigate systematically the effects of earthquake size, mantle rheology, afterslip, and megathrust locking on the evolution of the deformation.

Besides Introduction and Conclusions, this paper is organized as follows. In Section 6.2.3, we discuss the mantle rheology employed in our models and describe our modelling method and strategy. In Sections 6.2.4–6.2.6, we present model results, with $M_w \geq 9$ earthquakes discussed in Section 6.2.4, $8.5 < M_w < 9$ events in Section 6.2.5, and $M_w < 8.5$ events in Section 6.2.6. In Section 6.2.7, we investigate the relation between

earthquake size and duration of postseismic deformation by comparing observations and modelling results of all the earthquakes studied here and discuss contributions of other factors.

6.2.3. Mantle rheology and modelling strategy

Bi-viscous Burgers rheology

Following our previous work [Wang et al., 2012; Hu and Wang, 2012; Sun et al., 2014; Sun and Wang, 2015], we employ a bi-viscous Burgers rheology for the upper mantle in our models. The Burgers rheology is the simplest approximation of the time-dependent mantle rheology. It can be envisioned to be serially connected Kelvin solid and Maxwell fluid that represent the transient rheology and steady-state rheology, respectively (Figure 6.1) [Peltier et al., 1981; Pollitz et al., 2006; Bürgmann and Dresen, 2008; Wang et al., 2012]. For the purpose of identifying the first-order physical process, it is deemed unnecessary to invoke more complex rheologies that may involve multiple Kelvin components or a nonlinear relationship between stress and strain rate.

Upon sudden loading, the Kelvin solid deforms initially as a Newtonian fluid with the deformation rate controlled by the transient viscosity η_K but eventually transitions to a Hooke solid with the deformation determined by its rigidity μ_K. The Maxwell fluid exhibits an opposite time-dependent behaviour, that is, initial elastic deformation controlled by its rigidity μ_M transitioning to eventual viscous deformation controlled by the steady-state viscosity η_M. The steady-state (or Maxwell) viscosity is higher than the transient (or Kelvin) viscosity. Accordingly, the Burgers rheology features two material relaxation times, with a smaller Kelvin time $\tau_K = \eta_K/\mu_K$ and a larger Maxwell time $\tau_M = \eta_M/\mu_M$.

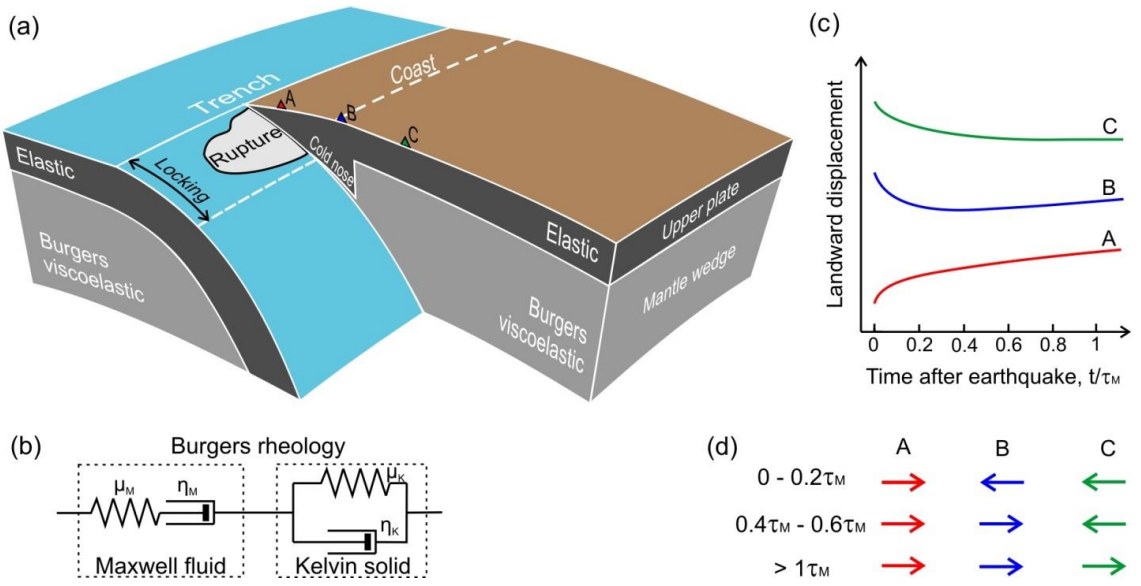

Figure 6.1. Model structure, upper mantle rheology, and schematic illustration of postseismic deformation. (a) Model structure. An elastic "cold nose" beneath the forearc crust is to represent the stagnant mantle wedge [Wada and Wang, 2009]. (b) Mantle rheology. The Burgers rheology that can be envisioned as serially connected Maxwell fluid and Kelvin solid. (c) Hand-drawn illustration of horizontal motion of three sites (colour coded in Figure 6.1a) after an earthquake (t=0). $\boldsymbol{\tau_M}$ is the Maxwell time of the mantle wedge (Section 6.2.3). (d) Time-dependent sense of horizontal motion of the three sites. The dividing boundary of opposing motion migrates away from the trench, leading to eventual wholesale landward motion. Time (in $\boldsymbol{\tau_M}$) shown in (c) and (d) is approximate.

Because the subduction zone system consists of geological units of different material properties, the timescale of its viscoelastic stress relaxation cannot be characterized by the material relaxation time of the upper mantle alone. Besides, the relaxation process is strongly dependent on the size of the preceding earthquake. Therefore, it is convenient to define a system relaxation time that scales with the earthquake size [Wang et al., 2012]. For example, for the steady-state component, the system relaxation time is

$$T_M = (M_o/M_o^0)\tau_M \qquad (1)$$

where M_o is the seismic moment of the earthquake, and M_o^0 is a reference moment. M_o and M_W are related by $\log(M_o/M_o^0) = 1.5(M_W - M_W^0)$, where M_W^0 corresponds to M_o^0. A

lower-magnitude subduction earthquake has a smaller system relaxation time and thus is expected to be followed by a shorter-lived opposing motion.

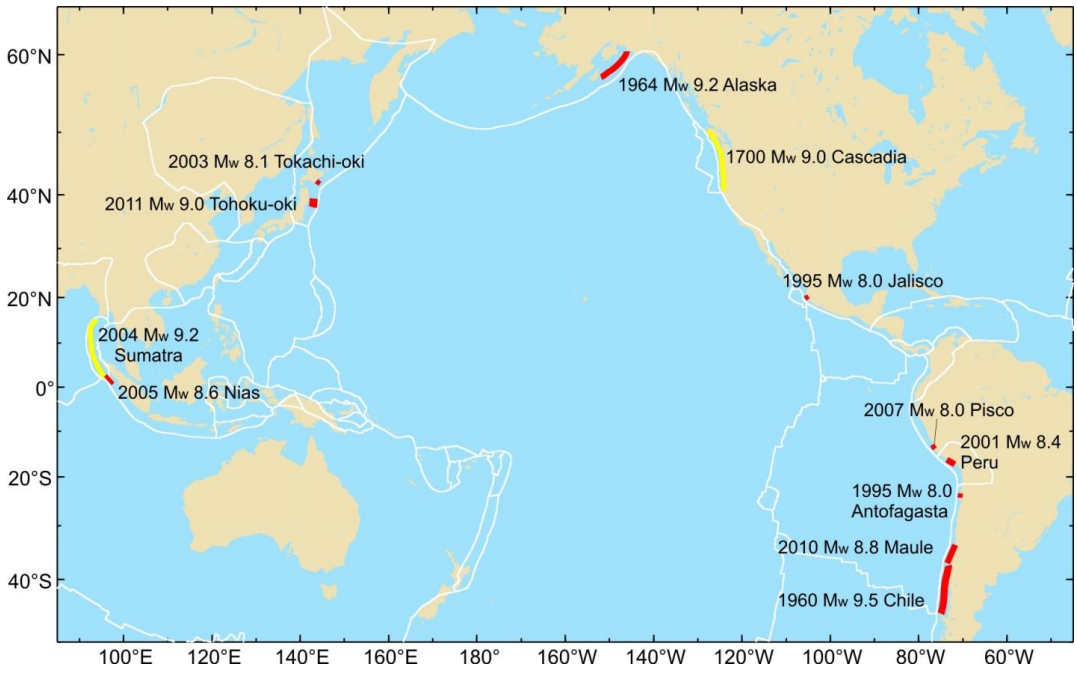

Figure 6.2. Map showing the locations and approximate rupture areas of the ten $8.0 \leq M_w \leq 9.5$ subduction earthquakes (red) studied in this work and the two $M_w \geq 9.0$ events studied by Wang et al. [2012]. See Tables 6.1 and 6.2 for further details.

3-D spherical-Earth finite element model

For numerical simulation, we use a 3-D spherical-Earth finite element model which employs 27-node isoparametric elements throughout the model domain. The effect of the gravitational force is approximately incorporated using the stress-advection approach [Peltier, 1974]. Fault slip, including thrust-faulting coseismic slip, afterslip, and the normal-faulting type backslip used for simulating the effect of megathrust locking (see the next sub-section), are incorporated using the split-node method [Melosh and Raefsky, 1981]. We use small time steps ($< 0.1\tau_K$) immediately after the earthquake to model the postseismic deformation in the transient phase and increasingly larger steps for later deformation.

Our models include actual subduction fault geometry and long-wavelength surface topography. For all the studied areas, we use the global Slab1.0 model [Hayes et al., 2012] for the fault geometry, except for Japan Trench, Eastern Alaska, and the northernmost part of the Middle America Trench subduction zones, where fault geometries are considered to be better constrained by earthquake relocation results, seismic reflection profiles, or receiver function analyses of local studies (see Table 6.1 for references). We use constant thicknesses for the elastic oceanic plate and the arc and backarc parts of the elastic upper plate. Similar to Sun et al. [2014], we include an elastic mantle wedge corner beneath the forearc crust to represent the stagnant "cold nose" of the mantle wedge (Figure 6.1) [Wada and Wang, 2009].

For the convenience of finite element mesh construction, we wish to have distant model boundaries to be roughly parallel or perpendicular to the average strike direction of the subduction zone, and we wish to have more or less parallel meridians. We therefore conduct a coordinate transformation for some subduction zones to have the new "equator" approximately normal to the trench crossing the rupture area, such as in Eastern Alaska, Southern Kuril, Southern Peru, and Northern Sumatra. This new coordinate system also makes it convenient to partition GNSS displacements and their time series into trench-normal and trench-parallel directions (see figures in Sections 6.2.5-6.2.6).

The bottom boundary of our models is at 500 km depth. The lateral boundaries are more than 1000 km from the rupture area and have minimal effects on model results. At the four lateral boundaries, the displacement is fixed in the normal direction but free in the tangential directions. The bottom boundary is fixed, and the top boundary is free in all directions.

Modelling strategy

Following Wang et al. [2001] and Hu et al. [2004], we separately model the "earthquake effect" and the "fault locking effect" and then combine the results to have the total deformation field.

The earthquake effect includes seismic rupture followed by viscoelastic stress relaxation and afterslip. Assigning a well determined static coseismic slip distribution is an important first step. For each earthquake, we use a published coseismic slip model if applying it to our finite element mesh yields surface deformation in good agreement with coseismic observations. For some earthquakes, we need to modify the original slip models by scaling up or down slip values in order to better match observations. Such modifications are necessitated by differences in fault geometry and/or rigidity values between the original models and ours. If the adaptation of published slip models cannot fit coseismic observations, we construct our own slip distributions using single or multiple elliptical patches. The spatial distribution of slip magnitude within each elliptical patch is assigned using the method of Wang et al. [2013], assuming a peak slip value at the centre of the patch and a smooth decrease of the slip value in all directions.

Properly assessing afterslip in the viscoelastic Earth is challenging, because geodetic observations reflect both viscoelastic relaxation and afterslip [Sun and Wang, 2015]. Most published afterslip distributions for the earthquakes studied here were derived using purely elastic models. Studies that did consider viscoelastic relaxation, such as for the 1964 Alaska, 2011 Tohoku-oki, 2010 Maule, and 2003 Tokachi-oki earthquakes, typically did not include the transient rheology and sometimes did not include a subducting slab. Therefore, we do not directly apply the published afterslip models. Instead, we determine the spatiotemporal distribution of afterslip, together with other key model parameters such as viscosities, via trial-and-error by visually comparing model results and observations. For the afterslip distribution of most earthquakes, we use elliptical patches as described in the previous paragraph. For the 1964 Alaska, 1995 Jalisco, and 2001 Peru earthquakes, afterslip is not assigned because the effect of viscoelastic relaxation alone is adequate in explaining the basic pattern of postseismic observations. To define the temporal evolution, we use the cubic function described in Hu and Wang [2012]. The duration of the afterslip following each earthquake is reported in Table 6.2.

In modelling the locking effect, we assign a constant rate of slip deficit (or backslip) [Savage, 1983] to the fault nodes. Full locking is simulated using a rate equal to the

subduction rate, and incomplete locking using a lower rate. The assigned slip deficit rate may change along strike as required by GNSS observations. Initially (decades to 1-2 centuries), surface velocities change with time in response to the suddenly imposed slip deficit rate, but the system will eventually stabilize to a steady state. We wait until the surface velocities become constant, typically after more than 300 years for a Maxwell mantle viscosity of the order of 10^{19} Pa s. For different subduction zones, we refer to published locking distributions obtained by inverting interseismic GNSS velocities (see Table 6.1 for references), mainly for along-strike variations. Because these studies assumed an elastic Earth, they usually overestimate the downdip width of the locked zone [Wang and Tréhu, 2016; Li et al., 2015]. We use narrower locked zones in our models, with the slip deficit rate tapering to zero in the downdip direction to a depth no greater than 30-50 km. Except for the Tohoku-oki earthquake, all our GNSS observations were from land stations, and they usually have no sensitivity to megathrust locking or creep near the trench [Wang and Tréhu, 2016]. We thus use a very simple distribution of slip deficit rate in the dip direction and focus on studying the effect of along-strike variations.

The campaign and continuous GNSS data included in this work have all been published by other researchers. We obtained digital values from the original publications or from their authors (see ensuing sections for individual earthquakes). Where a dense network of continuous GNSS sites was available, we only selected a subset of the sites optimally distributed to represent the spatiotemporal pattern of postseismic deformation. The GNSS motion is always with respect to the stable part of the upper plate. For the subduction zones featuring secular motion of upper-plate crustal blocks, such as northern Sumatra [Bradley et al., 2016] and eastern Alaska [Li et al., 2016], we applied an appropriate correction as will be detailed in later sections.

To compare the observations and models of different earthquakes, we define a reference location landward of the rupture zone and 175 km from the trench. Our models constrained by available geodetic observations allow us to predict a continuous spatiotemporal postseismic deformation pattern. We thus can find the time after each earthquake when the dividing boundary of the opposing motion passes through this reference location. For earthquakes with very long ruptures in the strike direction, such as

the M_w 9.5 Chile and M_w 9.2 Alaska earthquakes, we take an average over several of these reference locations along strike.

Table 6.1. Summary of subduction zone segments hosting the earthquakes studied in this work.

Figure No.	Subduction zone	Fault geometry references	Subduction azimuth (°) /rate (mm/yr)*	Locking distribution references	Upper-plate block motion references
6.3	S. Chile (1960 M_w 9.5)	Hayes et al. [2012]	72/66	Moreno et al. [2010], Metois et al.[2012]	Wang et al. [2007]
6.4	E. Alaska (1964 M_w 9.2)	Li et al. [2013] Kim et al. [2014]	337/54	Li et al. [2016]	Li et al. [2016]
6.5	Japan Trench (2011 M_w 9.0)	Nakajima & Hasegawa [2006], Kita et al. [2010], Zhao et al. [2009]	290/80	Suwa et al. [2006], Hashimoto et al. [2009]	NA
6.6, 6.7	Chile (2010 M_w 8.8)	Hayes et al. [2012]	72/68	Chileh et al. [2008], Moreno et al. [2010]	NA
6.8, 6.9	C. Sumatra (2005 M_w 8.6)	Hayes et al. [2012]	34/45	Chileh et al. [2008], Prawirodirdjo et al. [2010]	Bradley et al. [2016]
6.10	N. Chile (1995 M_w 8.0)	Hayes et al. [2012]	75/65	Chileh et al. [2011], Li et al. [2015]	NA
6.11, 6.12	C. Peru (2007 M_w 8.0)	Hayes et al. [2012]	70/62	Chileh et al. [2011], Villegas-Lanza et al. [2016]	Villegas-Lanza et al. [2016]
6.13	N. Mexico (1995 M_w 8.0)	Pardo & Suarez [1995], Suhardja et al. [2015]	48/25**	NA***	NA
6.14, 6.15	S. Kuril (2003 M_w 8.1)	Hayes et al. [2012]	291/80	Suwa et al. [2006], Hashimoto et al. [2009]	NA
6.16	S. Peru (2001 M_w 8.4)	Hayes et al. [2012]	70/62	Chileh et al. [2011]	Villegas-Lanza et al. [2016]

* Relative to the forearc where upper-plate block motion exists.
** Large variations in subduction rate along strike [DeMets and Wilson, 1997]. Shown is the average.
*** Uniform locking assumed.

Table 6.2. Summary of earthquakes and model parameters

Figure No.	Earthquake	Mw	Coseismic slip model	Afterslip duration (year)	Peak afterslip amount (m)	Mantle wedge viscosity (Pa s)		Oceanic mantle viscosity (Pa s)	
						η_K	η_M	η_K	η_M
6.3	1960 Chile	9.5	Moreno et al. [2009]	NA	0	1×10^{18}	2×10^{19}	1×10^{19}	1×10^{20}
6.4	1964 Alaska	9.2	This work	NA	0	1×10^{18}	7×10^{18}	1×10^{19}	1×10^{20}
6.5	2011 Tohoku-oki	9.0	Iinuma et al. [2012]*	10.0***	3.8***	5×10^{17}	2×10^{18}	2.0×10^{18}	1×10^{20}
6.6, 6.7	2010 Maule	8.8	Moreno et al. [2012]	4.5	2.2	1×10^{18}	3×10^{18}	6.7×10^{18}	1×10^{20}
6.8, 6.9	2005 Nias	8.6	Konca et al. [2007]**	7.5	3.9	5×10^{17}	2×10^{18}	5.0×10^{18}	1×10^{20}
6.10	1995 Antofagasta	8.0	This work	1.0	0.2	1×10^{18}	3×10^{18}	1×10^{19}	1×10^{20}
6.11, 6.12	2007 Pisco	8.0	Remy et al. [2016]	2.0	0.7	1×10^{18}	3×10^{18}	1×10^{19}	1×10^{20}
6.13	1995 Jalisco	8.0	This work	NA	0	2.5×10^{17}	1×10^{18}	2.5×10^{18}	1×10^{20}
6.14, 6.15	2001 Tokachi-oki	8.1	This work	12.0	2.8	2.5×10^{17}	7×10^{17}	2.0×10^{18}	1×10^{20}
6.16	2001 Peru	8.4	This work	NA	0	2×10^{18}	5×10^{18}	1×10^{19}	1×10^{20}

* Original slip values are scaled down by a factor of 0.92.

** Original slip values are scaled up by a factor of 1.3.

*** The values listed here are for the deep afterslip north of the coseismic slip. For other afterslip patches, see Wang et al. [2017].

6.2.4. Crustal motion following $M_w \geq 9$ subduction earthquakes

The 1700 M_w 9.0 Cascadia, 1960 M_w 9.5 Chile, and 2004 M_w 9.2 Sumatra earthquakes

Synthesizing present-day deformation patterns at Sumatra, Southern Chile, and Cascadia, Wang et al. [2012] demonstrate a common evolution process of the deformation cycle of great subduction earthquakes. For these giant ($M_w \geq 9$) earthquakes, the process of viscoelastic relaxation is very long. At the Chile margin, ~ 40-50 years after the 1960 M_w 9.5 earthquake, opposing motion of the coastal and inland areas can still be observed [Khazaradze et al., 2002] and may last for ~70 years as predicted by Hu et al. [2004] using a Maxwell viscoelastic model.

In this work, we do not re-construct models for Sumatra and Cascadia, where modern land-based GNSS observations show wholesale seaward motion and wholesale

landward motion, respectively. For our purpose, further modelling will not add much to what has been learned by Wang et al. [2012] (and references therein) for these end-member cases. However, for Chile, where opposing motion of the coastal and inland GNSS sites is going on, we made an effort to slightly refine the previous model. In particular, to improve the prediction of GPS velocities, we allow the degree of locking of the subduction fault to vary along the strike (Figure 6.3). We have also added the "cold nose" mentioned in section 6.2.3 to the new Chile model. To the first order, the new results are very similar to those in Wang et al. [2012], so the results will not be further discussed.

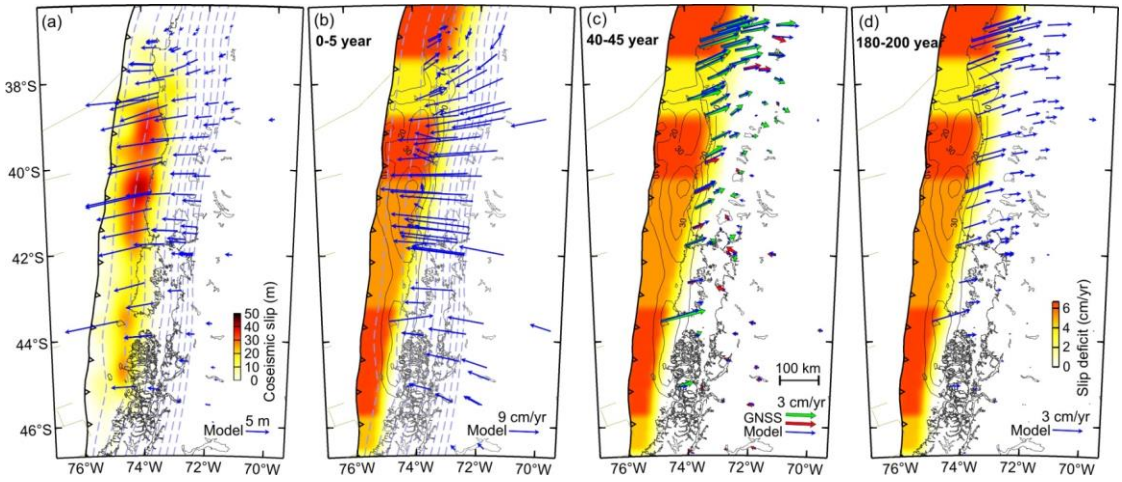

Figure 6.3. Coseismic and postseismic deformation of the 1960 M_w 9.5 Chile earthquake. Depth below sea level of the megathrust is contoured at 10 km intervals (light violet dashed lines). (a) Model predicted displacements by applying the coseismic slip distribution of Moreno et al. [2009] to our finite element mesh. Displacements are shown at modern GNSS sites which were nonexistent in 1960. (b), (c), and (d) Model predicted postseismic velocities over three different periods after the earthquake (labelled in each panel). Black contours (in m) show the same coseismic slip distribution as in (a. GNSS velocity data in (c) are based on campaign surveys between 1997 and 2009 from Wang et al. [2007] (red) and Moreno et al. [2011] (green). Slip deficit rates are allowed to vary in the strike direction to fit costal GNSS velocities.

The 1964 M_w 9.2 Alaska earthquake

Similar to the 1960 M_w 9.5 Chile earthquake, the 1964 M_w 9.2 Alaska earthquake (second largest instrumentally recorded earthquake) has a long rupture length, that extended 600-800 km from Prince William Sound along the Kenai Peninsula to Kodiak Island [Plafker, 1965; Plafker et al., 1994]. Published coseismic slip models for this event are different from one another [e.g. Ichinose et al., 2007; Holdahal and Sauber, 1994; Johnson et al., 1996], and it is difficult to fit geodetic observations when applying these slip distributions to our finite element model. Therefore we develop our own coseismic slip model. For modelling postseismic deformation, it is the net coseismic slip that is important. Details of the dynamic rupture process [e.g. Kanamori et al., 1970; Christensen and Beck, 1994] are less important, but the determination of three separate pulses in the earthquake source time function in seismological studies provides guidance for us to understand the patchiness of the rupture, assuming that each of the three pulses corresponds to an area of large slip (Figure 6.4a) [e.g., Christensen and Beck, 1994; Ichinose et al., 2007].

The Alaska earthquake occurred long before the age of GNSS. Geodetic observations that can help infer coseismic deformation are precise leveling and tide level change data for vertical displacements [Plafker, 1965] and triangulation surveying data for horizontal displacements (Figure 6.4a) [Snay et al., 1987]. Using these data as constraints, we construct a coseismic slip distribution consisting of three overlapping elliptical patches (Figure 6.4a), as explained in section 6.2.3, with a constant rake of 100º. The resultant coseismic deformation model captures the basic pattern of the observed deformation (Figure 6.4a), such as the > 2 m subsidence on the Kenai Peninsula and Kodiak Island [Plafker, 1965] and the ~10 m seaward displacements near the Prince William Sound [Snay et al., 1987]. We do not attempt to fit the data more precisely. These data have greater uncertainties compared to modern GNSS observations. In particular, because the post-earthquake campaign surveys were conducted a few months to a few years after the earthquake, the observed displacements must have included some postseismic

deformation. Also, for simplicity, we neglect the possible slip of a splay fault near Montage Island [Plafker, 1965; Holdahal and Sauber, 1994].

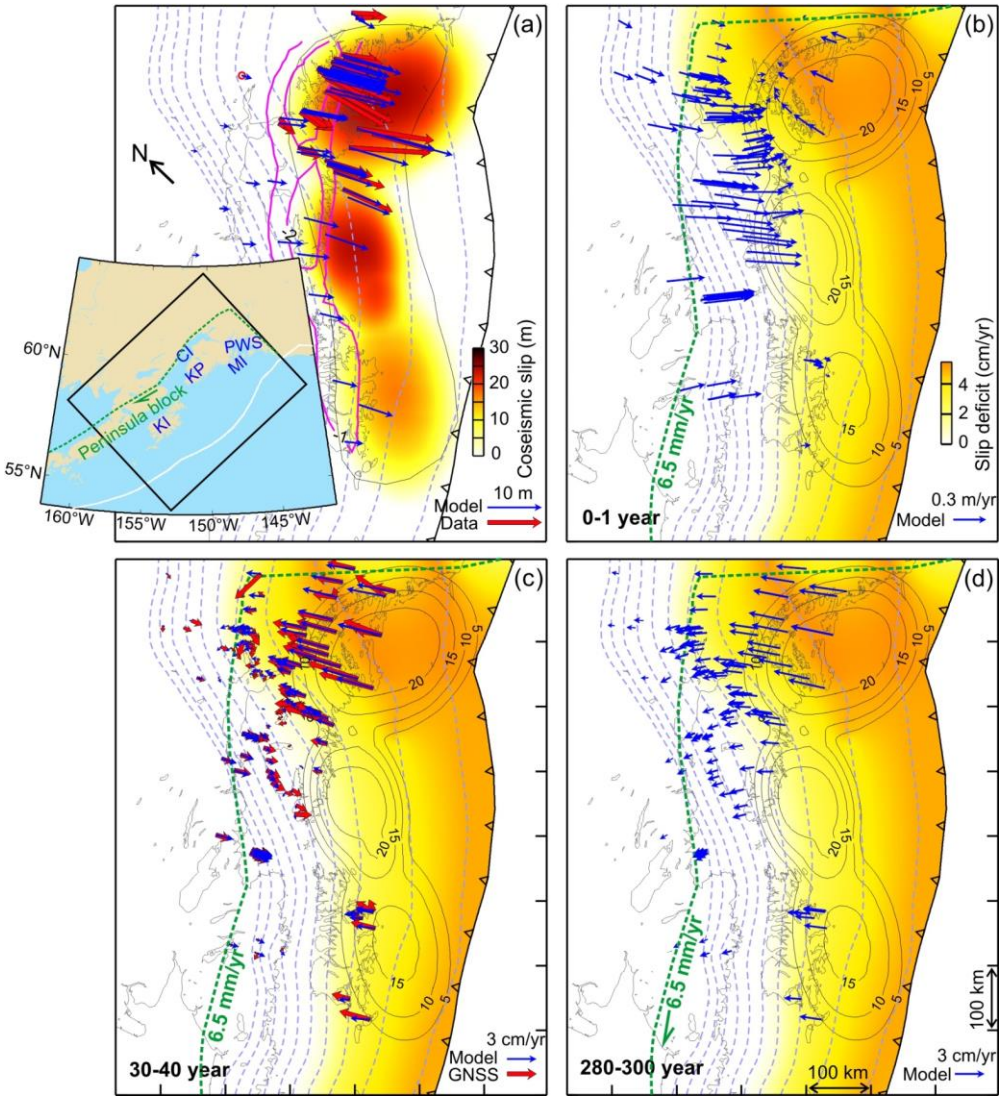

Figure 6.4. Coseismic and postseismic deformation of the 1964 M_w 9.2 Alaska earthquake. Depth below sea level of the megathrust is contoured at 10 km intervals (light violet dashed lines). (a) Coseismic horizontal displacements based on triangulation survey [Snay et al., 1987] and model predicted displacements using the shown slip distribution. Purple contours (in m) show the model predicted vertical displacements. Black line encompasses the rupture area [Plafker et al., 1994] inferred from precise leveling and tidal elevation data [Plafker et al., 1965]. (b), (c), and (d) Model predicted postseismic velocities over three different periods as labelled in each panel. Black contours (in m) show the same coseismic slip distribution as in (a). GNSS velocity data

between 1992 and 2004 [Li et al., 2016] are shown in (c). Along-strike variations in the slip deficit rate are based on Li et al. [2016]. To account for the motion of the Peninsula block (see Inset) [Li et al., 2016], a constant velocity of 6.5 mm/year in the strike direction has been added to GNSS sites located in it. Inset: Box outlines map area shown in the rest of the figure. PWS: Prince William Sound; MI: Montage Island; CI: Cook Inlet; KP: Kenai Peninsula; KI: Kodiak Island.

About 30-50 years after the earthquake, GPS velocities show opposing motion between sites on the southeast coasts of the Kenai Peninsula and Kodiak Island and other sites further inland (Figure 6.4c) [Freymueller et al., 2008; Li et al., 2016]. This opposing-motion pattern sustained over the period (~20 years) of GPS observations, although the occurrence of a couple of slow slip events beneath the Cook Inlet at depths of 40-60 km during this period affected the details of the deformation pattern [Li et al., 2016, and references therein]. In a previous study, Suito and Freymueller [2009] employed long-lasting afterslip and viscoelastic relaxation in a 3-D Cartesian finite element model of Maxwell rheology to explain the seaward motion of the inland GPS sites. They then used an elastic model to obtain a megathrust locking distribution after removing the modelled postseismic signals from observed GPS velocities.

Our model differs from Suito and Freymueller [2009] mainly in the spherical-Earth geometry and the inclusion of viscoelasticity in modelling fault locking (see Section 6.2.3). Although we use a bi-viscous mantle rheology, to be consistent with all our other models, GPS observations 30-50 years after the Alaska earthquake do not help constrain the transient viscosity. With the thicknesses of both elastic plates set at 30 km, the preferred steady-state viscosity of the mantle wedge is 7×10^{18} Pa s (Table 6.2). Our tests suggest that lower or higher viscosity values may not correctly depict the location of the GPS-observed dividing boundary of the opposing motion. According to this model, the dividing boundary passed through the 175-km reference location around 25-35 years after the earthquake.

The 2011 M_w 9.0 Tohoku-oki earthquake

Different from the1964 M_w 9.2 Alaska and the 1960 M_w 9.5 Chile earthquakes, coseismic and postseismic deformation of the 2011 M_w 9.0 Tohoku-oki earthquake is very well recorded, thanks to the dense geodetic network in Japan including seafloor GPS sites in and around the rupture area and many other types of observations. These observations have provided important information for us to understand the coseismic rupture and short-term postseismic deformation following this earthquake [e.g. Iinuma et al., 2012; Sun et al., 2014; Sun et al., 2017; Freed et al., 2017]. For a review of lessons learned from observed crustal deformation associated with the Tohoku-oki earthquake, the reader is referred to Wang et al. [2017] and references therein.

We expand the finite element model of our previous work [Sun et al., 2014; Sun and Wang, 2015] to predict future crustal deformation of the Japan Trench subduction zone over the next few hundred years. Model results for the coseismic deformation (Figures 6.5a) are identical to those in Sun et al. [2014] and Sun and Wang [2015]. Results for the short-term (0-1 years) postseismic deformation differ slightly from those in the two previous publications because of some fine adjustment of the afterslip distribution in this work. The along-strike variations of the locking state of the megathrust are assigned to fit the GNSS observations, but there are some uncertainties in the degree of locking in the creeping segments [Wang et al., 2017]. Assuming the locking pattern stays unchanged, predicted GPS site velocities averaged over time intervals of 30-40 years and 180-200 years after the earthquake are shown in Figures 6.5c and 6.5d, respectively. The time when the dividing boundary of opposing motion will pass through the 175-km reference location is predicted to be about 15-20 years, a time between the frames shown in Figures 6.5b and 6.5c.

The relatively low viscosities used in our Tohoku-oki model (Table 6.2), as compared to the values used for other subductions [Wang et al., 2012 and this work], may reflect site-specific processes affecting the thermal state and structural features. But the lower values could also be due to the inability of the Burgers body adopted by our model in describing what might be a more complex mantle rheology of the actual Earth. It is quite possible that deformation over the first 5 years after the earthquake is still in the

transient phase and the actual steady-state mantle viscosity that controls the longer-term (decades to centuries) deformation should be higher. This is a subject deserving further research.

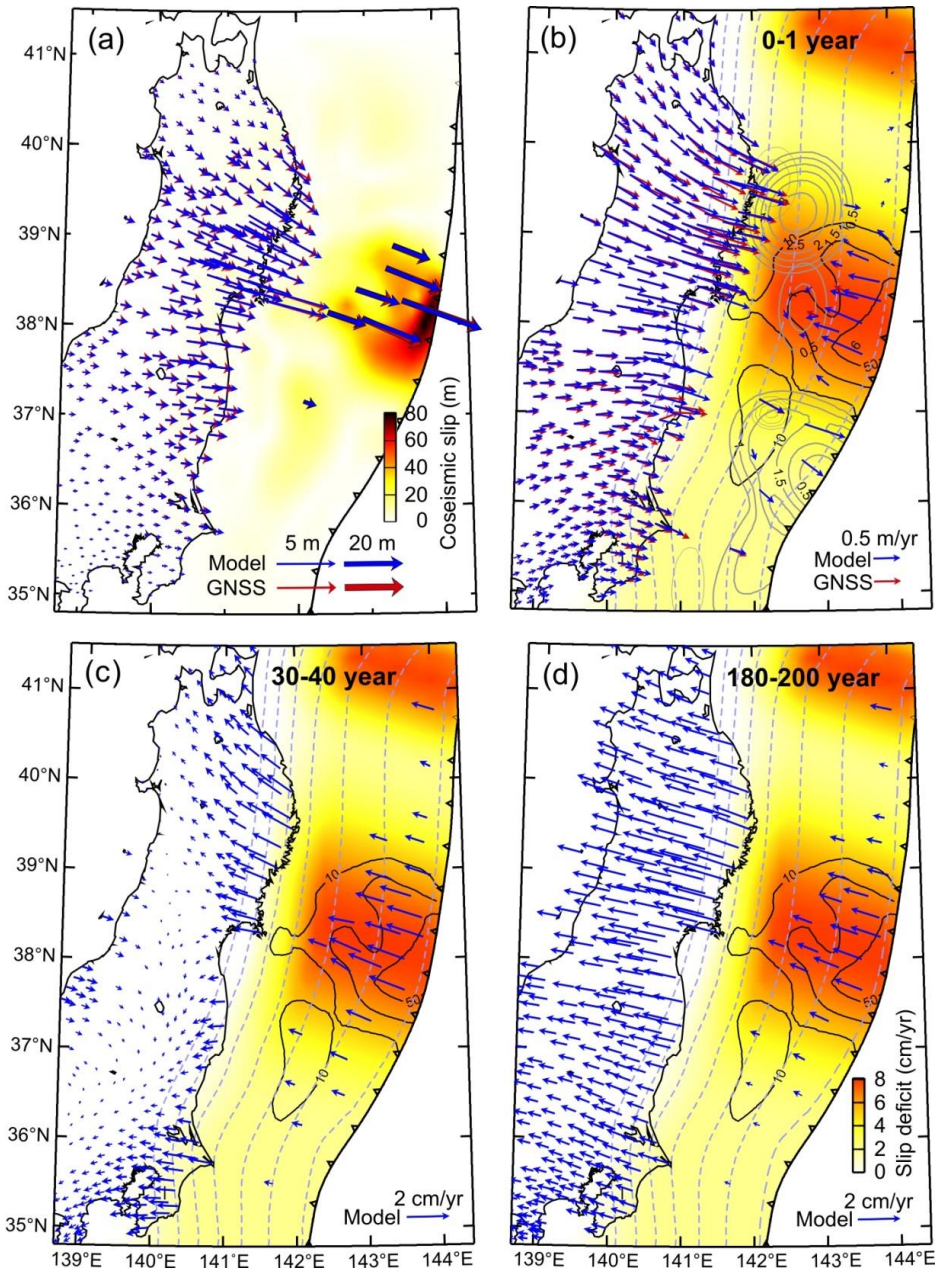

Figure 6.5. Coseismic and postseismic deformation of the 2011 M_w 9.0 Tohoku-oki earthquake. Depth below sea level of the megathrust is contoured at 10 km intervals (light violet dashed lines). (a) Coseismic horizontal displacements of land [Ozawa et al., 2011] and seafloor [Sato et al., 2011; Kido et al., 2011] GNSS sites and model predicted

displacements using the slip distribution of Iinuma et al. [2012] scaled by 0.92. (b), (c), and (d) Model predicted postseismic velocities over three different periods after the earthquake as labelled in each panel. Black contours show the same coseismic slip distribution as in (a) in m. Grey contours (in m) in (b) show afterslip distribution [Wang et al., 2017]. Land and seafloor GNSS velocity data over 0-1 year [Ozawa et al., 2012; Watanabe et al., 2014; Sun et al., 2014] are shown in (b). Slip deficit rates assigned to our model are modified from the locking distributions of Suwa et al. [2006] and Hashimoto et al. [2009].

6.2.5. $8.5 \leq M_w < 9$ subduction earthquakes

In this section, we discuss the postseismic deformation of the only two M_w 8.5-8.9 subduction earthquakes in the modern GNSS era, the 2005 M_w 8.6 Nias and 2010 M_w 8.8 Maule earthquakes. We will show that the dividing boundary of opposing motion after these two earthquakes migrated landward much faster than after the $M_w \geq 9$ events.

The 2010 M_w 8.8 Maule earthquake

The 2010 M_w 8.8 Maule earthquake is a well observed event. The part of the Chile subduction fault that ruptured during this earthquake, located just north of the 1960 M_w 9.5 rupture, had long been identified as a seismic gap. The previous great earthquake of a similar size occurred in 1835. Therefore, a large number of GPS sites were installed there before the earthquake by various research groups [Moreno et al., 2010; Vigny et al., 2011; Lorito et al., 2011; Lin et al., 2013], providing records of crustal deformation in both the coseismic and short-term postseismic phases. Also, the relatively shorter trench-coast distance (~100 km), compared to that of Japan Trench (> 200 km), allows the coseismic slip distribution of the Maule earthquake to be reasonably well determined with land-based GNSS observations in the absence of seafloor measurements, except the most near-trench area.

Published rupture models of the Maule earthquake share similar features [Delouis et al., 2010; Moreno et al., 2012; Vigny et al., 2011; Lay et al., 2010; Lorito et al., 2011]: a single elongated rupture area of ~450 km long and ~100 km wide, a major slip patch

north of the epicentre with more than 15 m slip, and another one or two patches to the south with up to ~10 m slip (Figure 6.6a). In this work, we directly use the coseismic slip model of Moreno et al. [2012] (Figure 6.6a). This model was derived by inverting GPS, InSAR, and land-level changes data using Green's functions derived from a spherical-Earth finite-element model that includes actual subduction zone geometries, in many ways similar to our model.

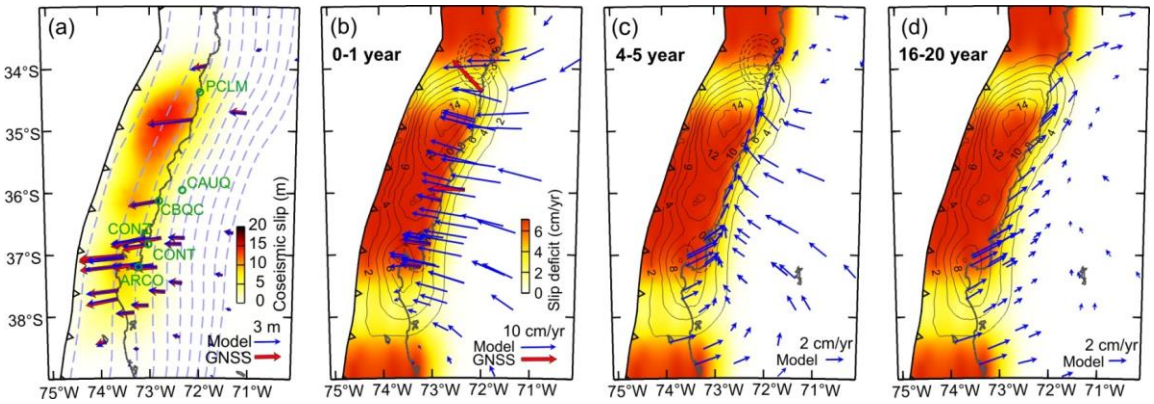

Figure 6.6. Coseismic and postseismic deformation of the 2010 M_w 8.8 Maule earthquake. (a) Coseismic horizontal GNSS displacements [e.g., Moreno et al., 2012] and model predicted displacements by applying the coseismic slip distribution of Moreno et al. [2012] to our finite element mesh. Depth below sea level of the megathrust is contoured at 10 km intervals (light violet dashed lines). Name-labelled green circles show the locations of the GNSS sites of which the observed and modelled time series are shown in Figure 6.7. (b), (c), and (d) Postseismic velocities over three different periods (as labelled) predicted by our model constrained by the GNSS time series shown in Figure 6.7. Black solid contours (in m) show the same coseismic slip distribution as in (a). Black dashed contours (every 0.5 m) show cumulative afterslip over 4.5 years. Observed GNSS velocities at some sites over 0-1 year are shown in (b). Along-strike variations in the slip deficit rate are based on Chileh et al. [2008] and Moreno et al. [2010].

Several studies have been conducted to investigate the postseismic deformation of the Maule earthquake, with some of them employing elastic models to study the effect of afterslip only [Bedford et al., 2013; Lin et al., 2013] and others including mantle viscoelasticity [Bedford et al., 2016; Klein et al., 2016; Li et al., 2017]. Klein et al. [2016]

used a finite element model of Burgers rheology, but did not include the effect of subduction fault relocking, as the long-term steady-state interseismic trend was removed from the GNSS data. Bedford et al. [2016] used a finite element model of Maxwell rheology including the locking effect. Their model can explain an observed change in the motion direction of coastal GPS sites from trenchward (westward) to northerly, as affected by the slightly oblique subduction of the Nazca Plate [DeMets et al., 2010]. Li et al. [2017] used a finite element model of Maxwell rheology with a heterogeneous viscosity distribution in the arc and backarc mantle to explain the postseismic uplift of the arc region.

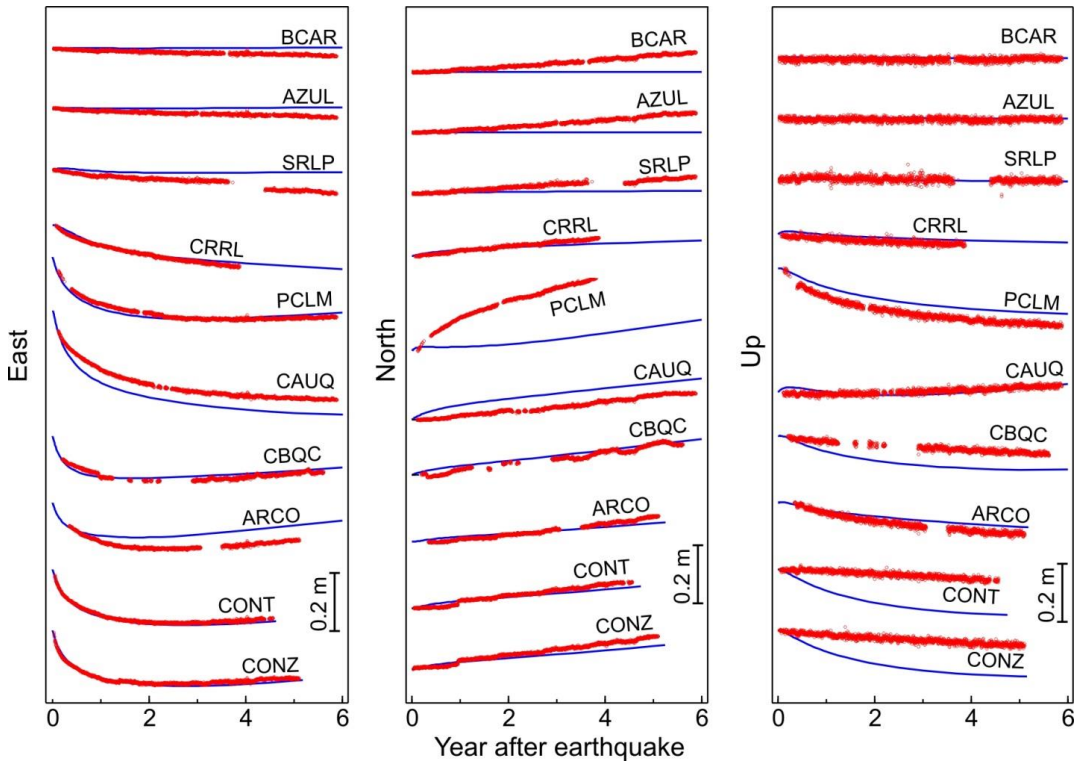

Figure 6.7. Observed (red) and modelled (blue) displacement time series after the 2010 M_w 8.8 Maule earthquake (t=0) at selected GNSS sites. Motion reversal in the east (trenchward) component (similar to site B in Figure 6.1c) has occurred at some coastal sites. Sites BCAR (58.301º W, 37.761º S), AZUL (59.881º W, 36.767º S), SRLP (64.280º W, 36.622º S), and CRRL (68.354º W, 36.153º S) are outside of the map area of Figure 6.6, with > 400 km distances from the trench. Locations of the other sites are shown in Figure 6.6a.

Our new model is similar to that of Bedford et al. [2016] but with a Burgers rheology (Table 6.2), more appropriate for modelling short-term postseismic deformation. The presence of the low-value transient viscosity results in less afterslip. Our model predicted postseismic GPS velocities for three time windows are shown in Figures 6.6b-6.6d. Observed and modelled time series for a few coastal and inland GPS sites are shown in Figure 6.7. The subset of GPS data shown in Figure 6.7 is adequate in representing the general evolution of the deformation. A group of GPS sites (ARCO, CONT, CONZ, CBQC, and PCLM) that cover a wide range along the coast reversed their direction of motion from seaward to landward within the first few years (Figure 6.7), causing the pattern of opposing motion to emerge on land (Figures 6.6c and 6.6d). Averaged along strike, the dividing boundary of opposing motion is predicted by our model to go through the 175-km reference location about 13-14 years after the earthquake.

The 2005 M_w 8.6 Nias earthquake

The 2005 M_w 8.6 Nias earthquake ruptured a ~350 km segment of the Sunda megathrust offshore northern Sumatra, abutting the coseismic slip area of the 2004 M_w 9.2 Sumatra earthquake to the north [Briggs et al., 2006]. GPS observations from forearc islands at relatively short distances from the trench (~60 km) provide important constraints for the coseismic slip [e.g., Briggs et al., 2006; Konca et al., 2007]. Published rupture models share similar features: buried slip that did not breach the trench, two major slip patches on both sides of the epicentre in the strike direction, and maximum slip larger than 10 m in the southern patch (Figure 6.8a). In this work, we use the coseismic slip model of Konca et al. [2007] that was obtained by jointly inverting teleseismic data, GPS displacements, and vertical displacements inferred from coral records of relative sea level change [Briggs et al., 2006]. When mapping slip vectors from Konca et al.'s [2007] planar fault to our curved fault, we need to scale up their slip values by a factor of 1.3 in order to fit GPS observations.

The forearc GPS observations yield important information also on the postseismic deformation in the near field. Large trenchward displacement (0.8 m) of the forearc site LHWA occurred over the first 9 months after the earthquake. Using an elastic model, Hsu et al. [2006] inferred > 1 m afterslip over this period updip of the rupture zone. Sun and Wang [2015] used a 2-D finite element model that incorporated Burgers rheology to demonstrate that the amount of the shallow afterslip could be even greater (> 2 m) when mantle viscoelasticity is considered. The lack of coseismic slip with the presence of large afterslip is understood to imply a velocity-strengthening behaviour of the shallowest portion of the megathrust [Wang and Hu, 2006].

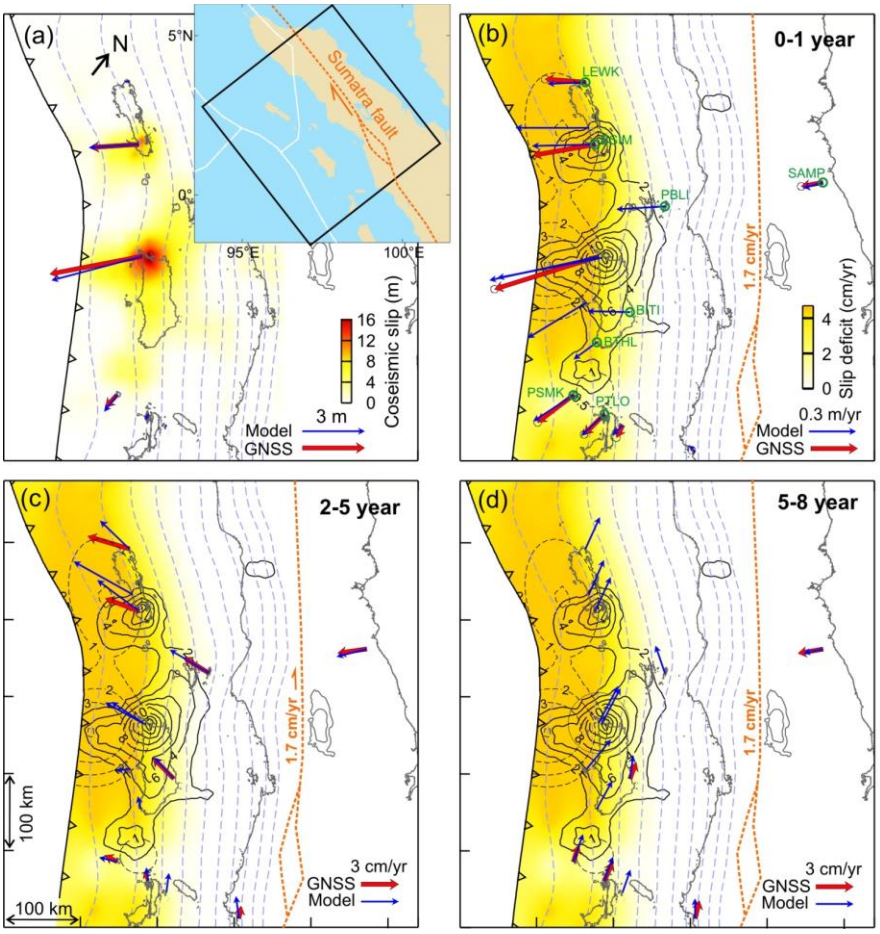

Figure 6.8. Coseismic and postseismic deformation of the 2005 M_w 8.6 Nias earthquake. Depth below sea level of the megathrust is contoured at 10 km intervals (light violet dashed lines). (a) Coseismic horizontal GNSS displacements [e.g., Briggs et al., 2006] and model predicted displacements using the coseismic slip distribution of Konca et al.

[2007] scaled up by a factor of 1.3. (b), (c), and (d) Observed and model predicted postseismic velocities over three different periods after the earthquake as labelled. Black solid contours (in m) show the same coseismic slip distribution as in (a). Black dashed contours (in m) show cumulative afterslip over 7.5 years. Slip deficit rates assigned to our model are based on Chileh et al. [2008] and Prawirodirdjo et al. [2010]. A constant velocity of 1.7 cm/year in the strike direction has been added to forearc GNSS sites, to account for the right-lateral motion of the strike-slip Sumatra fault (see Inset). Name-labelled green circles in Figure 6.8b show the locations of the GNSS sites of which the observed and modelled time series are shown in Figure 6.9. Error ellipses of GNSS velocities in 0-1 year represent standard error (derived in this work). Errors are larger for later periods but difficult to quantify, due partly to deformation associated with numerous M_w 6-7.8 earthquakes in this region [Feng et al., 2015]. Inset shows the map area of this figure and location of the Sumatra fault.

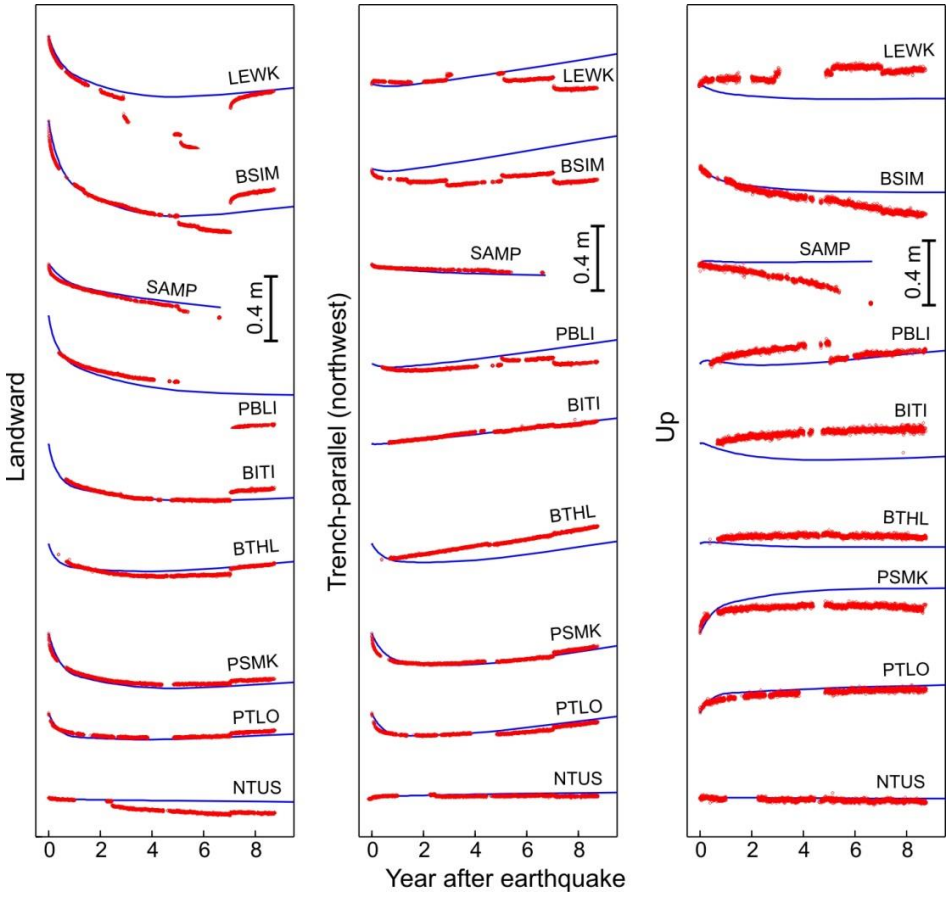

Figure 6.9. Observed (red) [Feng et al., 2015] and modelled (blue) displacement time series after the 2005 M_w 8.6 Nias earthquake (t=0) at GNSS sites shown in Figure 6.8b. and site NTUS (103.68º E, 1.35º N) located > 700 km from the earthquake rupture area (not shown in Figure 6.8b).

In this work, we use GPS observations over a longer period [Feng et al., 2015] to study the effects of viscoelastic relaxation, shallow afterslip, and subduction fault relocking. Our model parameters are shown in Table 6.2. The results suggest a fast continuing seaward motion of the forearc region due to the shallow afterslip immediately after the earthquake (Figure 6.8b). The afterslip diminishes rapidly with time, leading to quick slowing down of the seaward motion of forearc GPS sites (Figure 6.8c). Within 3-5 years, the locking of the subduction fault causes motion reversal of the forearc GPS sites, similar to the Maule example, while the inland site SAMP is still moving seaward (Figures 6.8c and 6.9). Averaged along strike, the dividing boundary of opposing motion went through the 175-km reference location in our model about 8-10 years after the earthquake.

To account for the right-lateral motion of the strike-slip Sumatra Fault (Figure 6.8), we have added a constant velocity (1.7 cm/year) in the strike direction to the forearc "sliver" seaward of this fault [Bradley et al., 2016]. This results in a rather good fit to the strike-parallel component of GPS time series (Figure 6.9 middle panel). A similar method in dealing with strike-parallel forearc sliver motion was used by Wang et al. [2007] in studying the postseismic deformation of the 1960 M_w 9.5 earthquake.

6.2.6. M_w < 8.5 subduction earthquakes

In this section, we discuss the postseismic deformation of five M_w 8-8.5 subduction earthquakes for which relevant geodetic observations are available. We will show that these earthquakes are followed by rather short-lived (one to a few years) opposing motion. The dividing boundary of the opposing motion sweeps through the geodetic network very fast. Therefore, observing the short-lived opposing motion with campaign-style measurements requires frequent occupation of campaign sites within a limited time window.

In assigning the coseismic slip distributions of these "small-size" (M_w 8-8.5) earthquakes, we use a simple elliptical slip patch (Section 6.2.3) and a constant slip rake, except for the 2007 M_w 8.0 Pisco earthquake for which we directly apply a published rupture model.

The 1995 M_w 8.0 Antofagasta Earthquake

The 1995 Antofagasta M_w 8.0 earthquake ruptured a ~150 km segment of the central Chile subduction fault, about 1000 km north of the 2010 M_w 8.8 Maule rupture (Section 6.2.5). The rupture of this earthquake terminated to the north before breaking into a seismic gap where an M_w ~9 earthquake occurred in 1877 [Delouis et al., 1997]. Published rupture models of this earthquake that were obtained using seismic, campaign GPS, and InSAR data [Delouis et al., 1997; Ruegg et al., 1996; Chlieh et al., 2004] suggest a single slip patch. The coseismic deformation predicted using an elliptical patch in our finite element model agrees with the campaign GPS data very well (Figure 6.10a) [Ruegg et al., 1996; Klotz et al., 1999; Chlieh et al., 2004].

Although only campaign observations were available to provide snapshots of crustal deformation for this earthquake [Klotz et al., 2001; Khazaradze and Klotz; 2003], the broad spatial coverage of the measurements helps to demonstrate clearly how quickly the dividing boundary of opposing motion must have migrated landward through the network (Figure 6.10). With primary parameters given in Table 6.2, we construct a continuous deformation history constrained by these campaign data (Figure 6.10). In this model, the dividing boundary went through the 175-km reference location as quickly as 0.5-1 years after the earthquake.

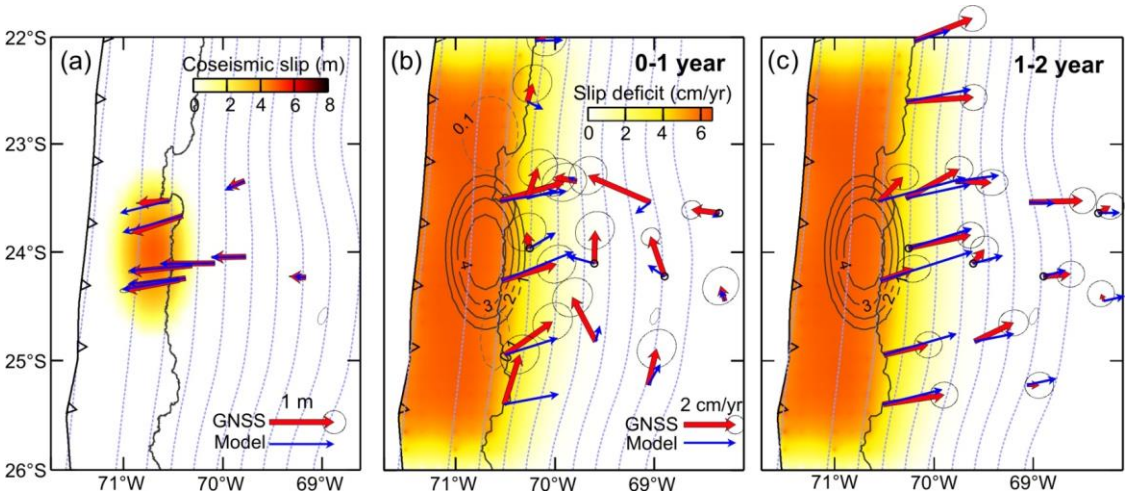

Figure 6.10. Coseismic and postseismic deformation of the 1995 M_w 8.0 Antofagasta earthquake. Depth below sea level of the megathrust is contoured at 10 km intervals (light violet dashed lines). (a) Coseismic horizontal displacements based on campaign GNSS surveys [e.g., Chileh et al., 2004] and model predicted displacements using the shown slip distribution. (b) and (c) Observed postseismic velocities based on campaign GNSS surveys [Klotz et al., 2001; Khazaradze and Klotz, 2003] and model prediction over the first two years after the earthquake. Black solid contours (in m) show the same coseismic slip distribution as in (a). Grey dashed ellipses in (b) encompass areas of > 0.1 m afterslip over the first year. Slip deficit rates are based on Chileh et al. [2011]. Error ellipses for the GNSS observations are from the original publications.

The 2007 M_w 8.0 Pisco Earthquale

The 2007 Pisco M_w 8.0 earthquake ruptured a part of the central Peru subduction zone, with a rupture length similar to 1995 Antofagasta. The rupture terminated to the south where the Nazca ridge is subducting [Sladen et al., 2010; Remy et al., 2016]. There were no campaign or continuous GNSS measurements prior to the earthquake, but five continuous GPS sites were installed ~20 days after the earthquake to record postseismic deformation (Figure 6.11) [Perfettini et al., 2010; Remy et al., 2016]. We apply to our finite element model the rupture model that Remy et al. [2016] derived by inverting InSAR data. The rupture model of Sladen et al. [2010] based on joint inversion of InSAR, teleseismic, and tsunami data shows a similar slip distribution.

All the available GPS sites quickly stopped moving seaward or changed their direction to landward (Figures 6.11). The continuous GPS monitoring clearly shows how the motion changed with time (Figure 6.12). With parameter values shown in Table 6.2, our postseismic deformation model can reproduce the main pattern of these observations. In this model, the dividing boundary of opposing motion went through the 175-km reference location around 1-1.5 years after the earthquake. The quick motion reversal suggests a rapid resumption of megathrust locking. Yet along-strike variations in the degree of locking affect the exact timing of the reversal of specific sites. For example, compared to site JUAN, the more southerly site GUAD, located even slightly closer to the rupture zone, reversed its motion slightly more slowly (Figure 6.12). Because of the lower degree of locking in the south, where the Nazca ridge is subducting [Villegas-Lanza et al., 2016; Wang and Bilek, 2014], it takes a little longer for the locking effect to overshadow the effect of viscoelastic relaxation.

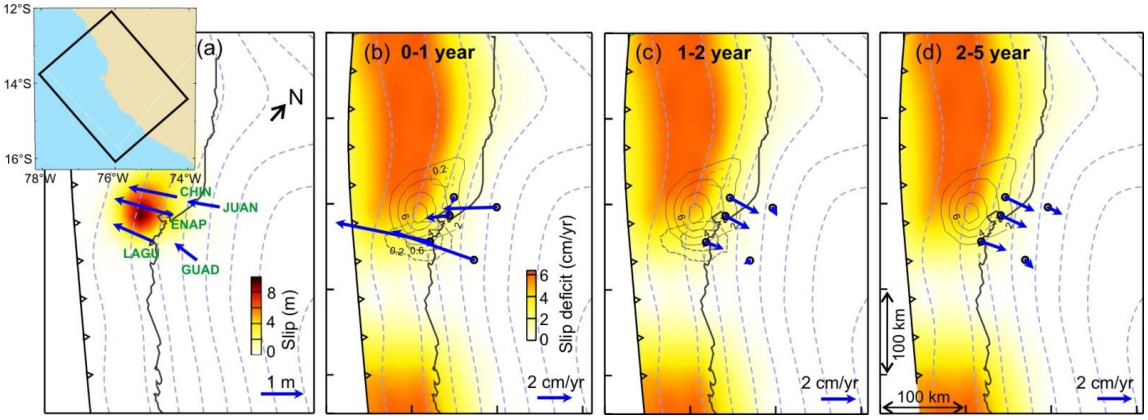

Figure 6.11. Model-predicted coseismic and postseismic deformation of the 2007 M_w 8.0 Pisco earthquake. Depth below sea level of the megathrust is contoured at 10 km intervals (light violet dashed lines). (a) Coseismic displacements predicted with the slip model of Remy et al. [2016]. The five GNSS stations were installed ~20 days after the earthquake, and their time series (Figure 6.12) were used to constrain our model. (b), (c) and (d) Postseismic velocities over three different periods after the earthquake as labelled. Grey solid contours (in m) show the same coseismic slip distribution as in (a). Grey dashed contours show the 2-year cumulative afterslip in m. Along-strike variations in the slip deficit rate are based on Villegas-Lanza et al. [2016] and Chileh et al. [2011]. Inset shows the location and orientation of the map area in this figure.

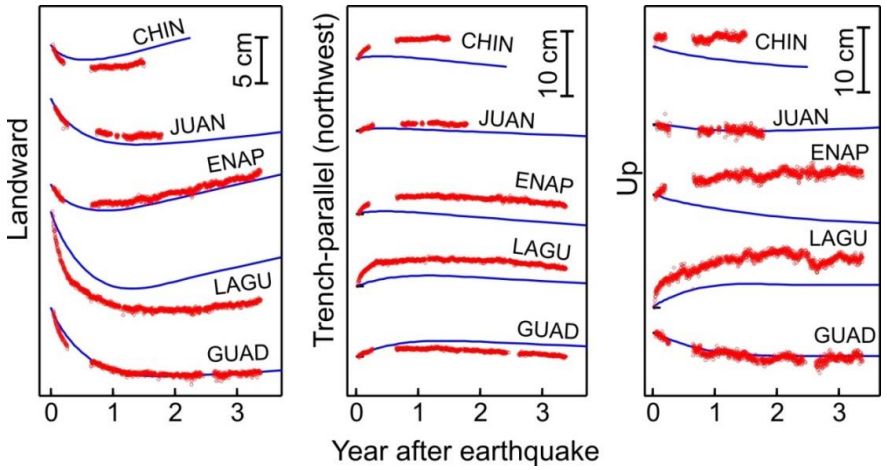

Figure 6.12. Observed (red) [Remy et al., 2016] and modelled (blue) displacement time series after the 2007 M_w 8.0 Pisco earthquake (t=0) at the GNSS sites shown in Figure 6.11a.

The 1995 M_w 8.0 Jalisco Earthquake

The 1995 M_w 8.0 Jalisco earthquake ruptured a ~150 km long segment along the northernmost part of the Mexico subduction zone, where the very young (< 10 Ma) Rivera Plate is subducting beneath the North American Plate at a rate of ~2-3 cm/year [DeMets and Wilson, 1997; DeMets and Traylen, 2000]. More than ten campaign GPS sites were surveyed in the Jalisco area and further inland before the 1995 earthquake, and another ~10 sites were established shortly after the earthquake. Most of these sites were occupied about 5-6 times over the first four years after the earthquake [Hutton et al., 2001], providing information on the spatiotemporal evolution of the postseismic deformation. In addition to these campaign sites, a continuous GPS site (COLI) located ~40 km from the coast and slightly south of the rupture area (Figure 6.13a) provides important information on the temporal variation of the crustal deformation [Márquez Azúa et al., 2002]. In a previous study, Márquez Azúa et al. [2002] employed an elastic dislocation model [Okada, 1985] and viscoelastic and poroelastic finite element models to explain the observed motion of COLI. In their work, the effect of megathrust locking was modelled using the elastic model.

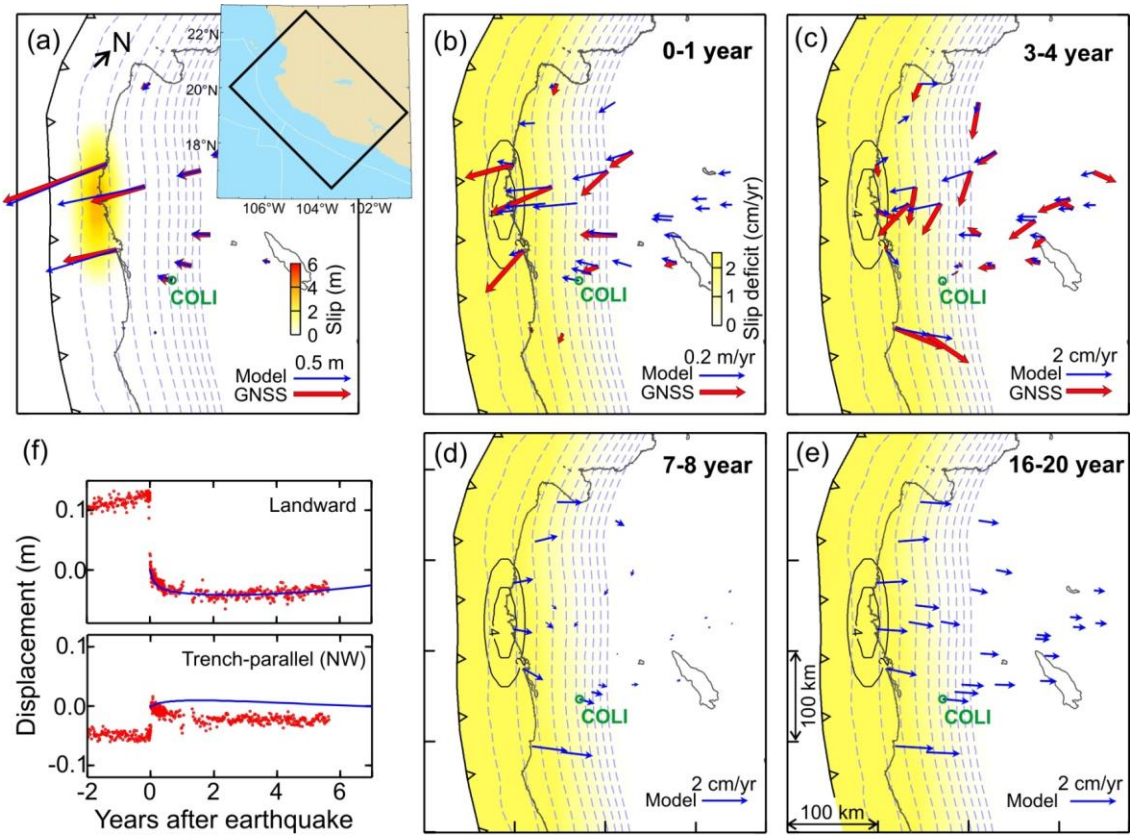

Figure 6.13. Coseismic and postseismic deformation of the 1995 M_w 8.0 Jalisco earthquake. Depth below sea level of the megathrust is contoured at 10 km intervals (light violet dashed lines). (a) Observed [Melbourne et al., 1997] and model predicted horizontal coseismic displacements using the shown slip distribution. COLI (green circle) was the only continuous GNSS site. (b), (c), (d), and (e) Model-predicted postseismic velocities over four different periods after the earthquake as labelled. GNSS velocities based on campaign surveys [Hutton et al., 2001] are shown where available. Solid contours (in m) show the same coseismic slip distribution as in (a). (f) Observed [Azua et al., 2002] (red) and modelled (blue) horizontal displacements of COLI before and after the Jalisco earthquake (t=0). Inset in (a) shows the location and orientation of the map area in this figure.

Our model parameters are given in Table 6.2, and results are shown in Figure 6.13 in comparison with available GPS data. Three to four years after the earthquake, most of the sites are still observed and modelled to be moving seaward, except along the coast (Figure 6.13). The landward migration of the dividing boundary of opposing motion is thus slower than that of the Antofagasta or Pisco earthquake (the preceding two sub-

sections), despite the identical M_w. This is obviously the consequence of a very slow subduction rate at this margin, Similar to the effect of the lower degree of megathrust locking as discussed in the preceding sub-section, a slower subduction rate means less contribution from fault locking. Therefore, if the effects of relaxation and afterslip are similar for these earthquakes of equal size, it should take longer for the locking effect to become fully dominant at Jalisco. In our model, the dividing boundary went through the 175-km reference location 7-8 years after the Jalisco earthquake.

The 2003 M_w 8.1 Tokachi-oki Earthquake

The 2003 M_w 8.1 Tokachi-oki earthquake ruptured a ~100 km long segment along the southern Kuril trench subduction zone (Figure 6.14). Paleoseismic and historical records suggest that this part of the subduction fault has produced a number of M_w 8-9 earthquakes. The most recent M_w 8 earthquake before the 2003 rupture occurred in 1952 [Hirata et al., 2003], and a much greater event that ruptured at least a 300 km long segment along the strike occurred ~350 years ago [Nanayama et al., 2003; Sawai et al., 2004].

Similar to the 2011 M_w 9.0 Tohoku-oki earthquake (Section 6.2.4), the Tokachi-oki earthquake is a well observed event. Two ocean-bottom pressure gauges offshore [Baba et al., 2006] provide important information for studying postseismic deformation in the near field. Many rupture models were obtained by various groups using different datasets, including GPS and high-rate GPS data [Ozawa et al., 2004; Miura et al., 2004; Miyazaki et al., 2004; Nishimura, 2011], seismic waves [Yagi, 2004; Yamanaka and Kikuchi, 2003], tsunami waveforms [Hirata et al., 2004; Tanioka et al., 2004], or by joint inversion of more than one types of data [Koketsu et al., 2004; Romano et al., 2010]. Most of these published rupture models suggest a single slip patch at relatively large depths (30-45 km). Using a nearly circular patch, our finite element model predicts coseismic deformation in good agreement with the GPS data (Figure 6.14a).

Several studies have been conducted on the postseismic deformation of the Tokachi-oki earthquake, with most of them focused on afterslip in an assumed purely elastic Earth

[Ozawa et al., 2004; Miyazaki et al., 2004; Baba et al., 2006; Sato et al., 2010]. They generally suggest substantial afterslip updip of the coseismic slip area, the most direct geodetic evidence being a > 20 cm uplift recorded by two ocean-bottom pressure gauges seaward of the rupture [Baba et al., 2006]. Itoh and Nishimura [2016] employed a layered-Earth model (without a slab) of Maxwell rheology to study the effects of both afterslip and viscoelastic relaxation but did not consider the effect of megathrust locking.

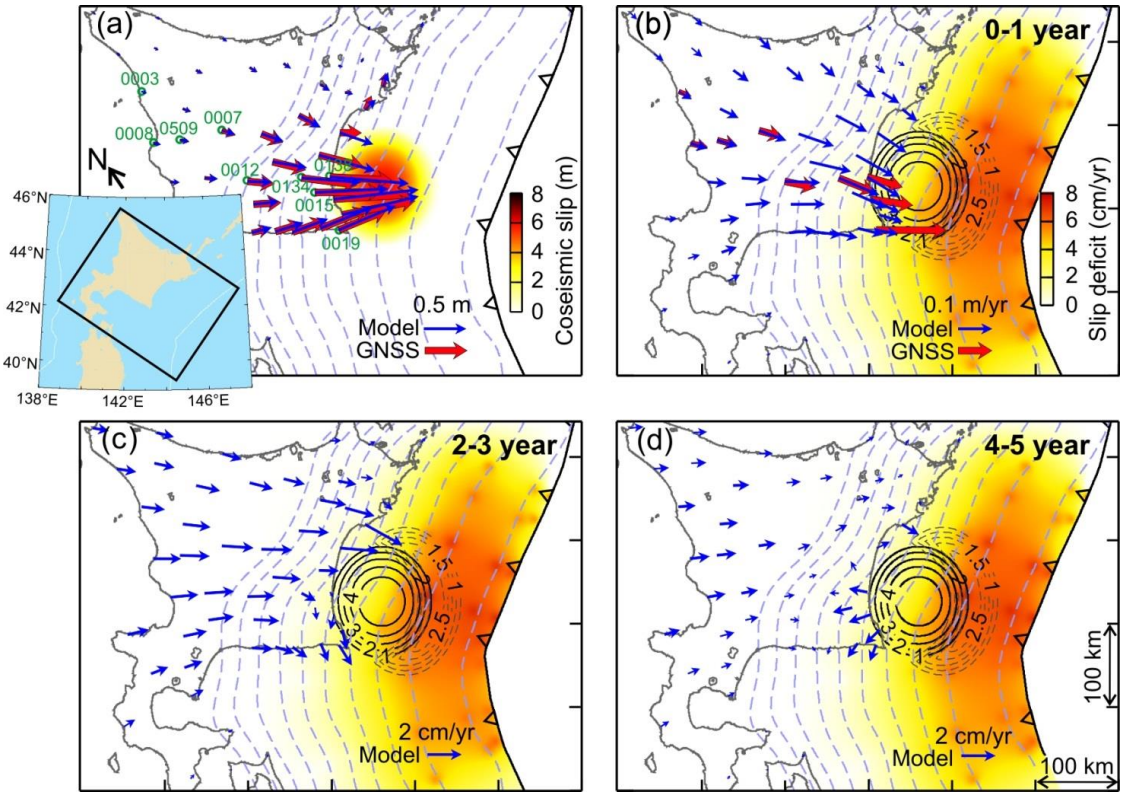

Figure 6.14. Coseismic and postseismic deformation of the 2003 M_w 8.1 Tokachi-oki earthquake. Depth below sea level of the megathrust is contoured at 10 km intervals (light violet dashed lines). (a) Observed [e.g., Larson and Miyazaki, 2008] and model predicted horizontal coseismic displacements using the shown slip distribution. Observed and modelled time series at the labelled sites will be shown in Figure 6.15. Observe postseismic velocities at these sites are shown in (b). (b), (c), and (d) Postseismic velocities over three different periods after the earthquake as labelled. Solid contours (in m) show the same coseismic slip distribution as in (a). Grey dashed contours show cumulative afterslip over 12 years in m. The slip deficit rates assigned to our model are based on Suwa et al. [2006] and Hashimoto et al. [2009]. Inset in (a) shows the location and orientation of the map area in this figure.

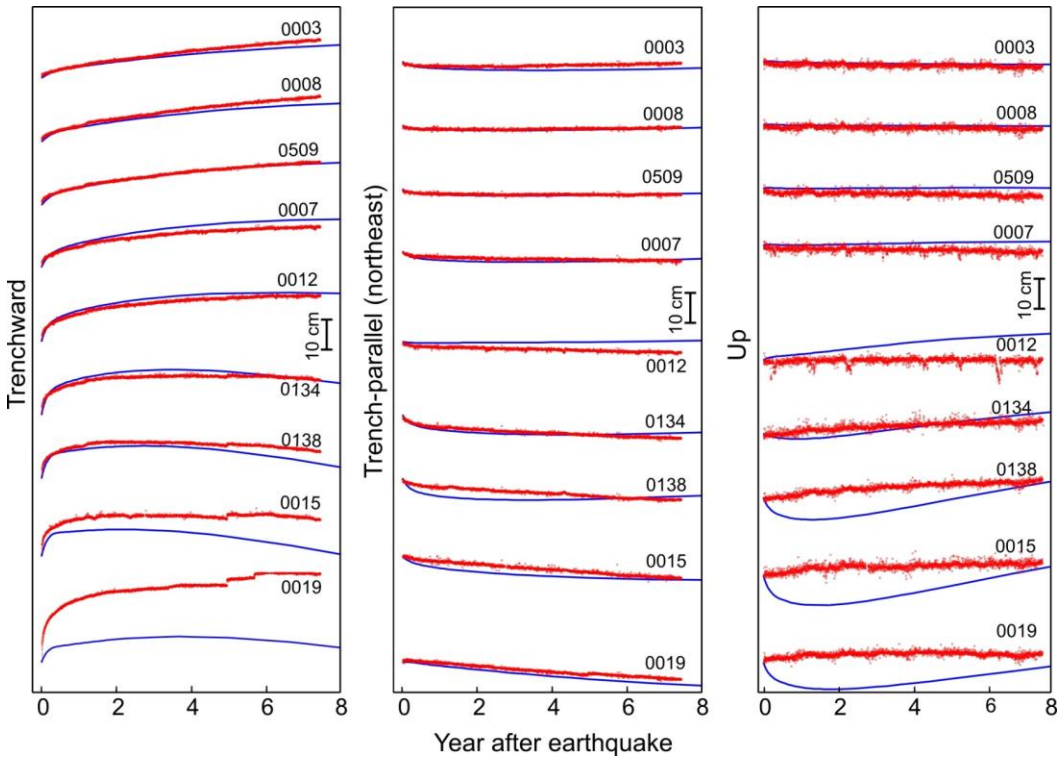

Figure 6.15. Observed (red) [Itoh and Nishimura, 2016] and modelled (blue) displacement time series after the 2003 M_w 8.1 Tokachi-oki earthquake (t=0) at GNSS sites shown and labelled in Figure 6.14a. Observed displacements after the 2011 M_w 9.0 Tohoku-oki earthquake (t ~7.5 years) are not shown.

We use a 3-D model including a slab, and the viscosity values are given in Table 6.2. In terms of the large and sustained afterslip updip of the rupture area, our model results agree with previous studies (Figure 6.14). Right after the earthquake, because of the large depth of the rupture, the dividing boundary of the viscoelastic opposing motion should be in the coastal area, above the downdip termination of the rupture. In other words, viscoelastic relaxation alone would cause landward motion of some the coastal GPS sites right after the earthquake (model tests not shown here; seen also Itoh and Nishimura [2016]). To explain the actually observed continuing seaward motion of the coastal sites, a large amount of afterslip updip of the rupture is required. Although the shallow afterslip amounts to larger than 2.5 m over ~10 years in our model, it still underestimates the seaward motion of GPS sites 0019 and 0015 southwest of the rupture zone, especially

during the first year after the earthquake (Figure 6.15). This implies an even greater local afterslip or other local processes near the southern edge of the rupture, which is not considered in our study.

Due to viscoelastic relaxation and the long-lasting shallow afterslip, GPS sites farther than 100 km from the rupture zone had been smoothly moving seaward until being interrupted by the 2011 M_w 9.0 Tohoku-oki earthquake. Closer to the rupture and near the coast, after an initial continuing seaward motion over the first 2-3 years as controlled primarily by the dominant effect of shallow afterslip, GPS sites reversed their motion direction (Figure 6.15). That is, the dividing boundary went through the 175-km reference location 2-3 years after the earthquake. Opposing motion was seen on Hokkaido 3-7 years after the Tokachi-oki earthquake, before the occurrence of the 2011 Tohoku-oki earthquake ~400 km to the south (Section 6.2.4). .

The 2001 M_w 8.4 Peru Earthquake

The 2001 M_w 8.4 Peru earthquake ruptured a ~200 km long segment along the southern portion of the Peru subduction zone (Figure 6.16), where a great M_w 8.8-9 earthquake had ruptured a longer segment extending farther south in 1868 [Bilek and Ruff, 2002; Comte and Pardo, 1991]. Seismological studies using surface waves [e.g., Bilek and Ruff, 2002] and teleseismic body waves [e.g., Giovanni et al., 2002; Bilek and Ruff, 2002] indicate two major pulses of moment release. Estimates of coseismic slip based on the seismic moment suggest a slip of 5 m if averaged over the aftershock area and greater slip of > 8 m in the area of concentrated moment release [Bilek and Ruff, 2002].

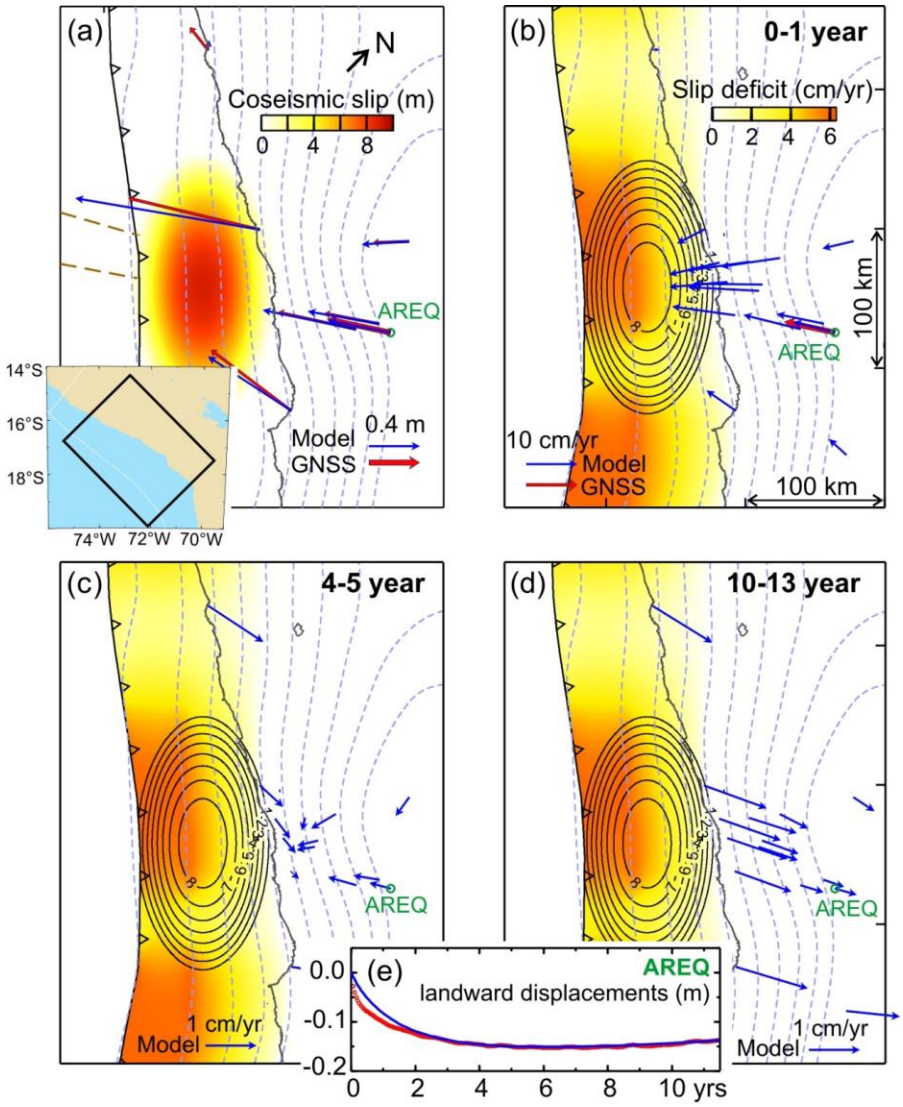

Figure 6.16. Coseismic and postseismic deformation of the 2001 M_w 8.4 Peru earthquake. Depth below sea level of the megathrust is contoured at 10 km intervals (light violet dashed lines). AREQ (green circle) was the only continuous GNSS site in operation. (a) Observed [e.g., Perfettini et al., 2005; Chileh et al., 2011] and model predicted horizontal coseismic displacements using the shown slip distribution. (b), (c), and (d) Model predicted postseismic velocities over three different periods after the earthquake as labelled. Solid contours (in m) show the same coseismic slip distribution as in (a). Along-strike variations in the slip deficit rate are based on Chileh et al. [2011] and Villegas-Lanza et al. [2016]. (e) Observed [Bevis and Brown, 2014] and modelled postseismic landward displacements of AREQ. Inset in (a) shows the location and orientation of the map area in this figure.

In contrast with the heterogeneity of the rupture as suggested by the multiple pulses of moment release, coseismic slip models derived by inverting GPS and InSAR data generally show a smoother slip distribution [e.g. Pritchard et al., 2007; Chlieh et al., 2011]. All the GPS sites that provide coseismic displacement values are campaign sites, except AREQ [Pritchard et al., 2007; Ruegg et al., 2001]. Using an elliptical rupture patch, our finite element model predicts the basic pattern of the observed GPS displacements (Figure 6.16a). The observed displacements must have included some postseismic deformation, because the campaign sites were not reoccupied until weeks to months after the earthquake. For our purpose of studying the longer-term evolution of the postseismic deformation, including some initial afterslip in the coseismic slip does not cause large errors.

Various models have been proposed to explain the postseismic time series of AREQ, the only continuous site in operation, located 225 km from the Peru trench and landward of the main slip area [Bevis and Brown, 2014]. Melbourne et al. [2002] attributed the continuing seaward motion of the site to afterslip downdip of the rupture area. Perfettini et al. [2005] used a 1-D semi-analytical model that includes an afterslip zone and a viscous ductile shear zone along the downdip extension of the seismogenic plate interface. Hergert and Heidbach [2006] used a 2-D finite element model that includes non-linear Maxwell rheology for the lower crust. No 3-D models that consider the effects of both viscoelastic relaxation and megathrust relocking have been published.

The primary parameters of our postseismic deformation model for this earthquake are given in Table 6.2. Model results are shown in Figure 6.16, with the predicted time series for AREQ compared with its GPS records. The model well explains the gradual motion reversal of AREQ ~6-7 years after the Peru earthquake (Figure 6.16e), although it does not precisely fit the earliest part of the AREQ displacements. The observed faster deformation in the first month than the model prediction could be due to some afterslip that is not included in our model or a more complex transient rheology than considered here. In this model, the dividing boundary of opposing motion went through the 175-km reference location 4-5 years after the earthquake.

6.2.7. Discussion and Conclusions

Using the 175-km reference location defined in Section 6.2.3, we compare in Figure 6.17 the results of all the earthquakes studied in this work. As described in the modelling strategy sub-section (Section 6.2.3), our models constrained by available geodetic observations depict a spatiotemporally continuous postseismic deformation history for each earthquake. From this modelled history, we obtain the time when the dividing boundary of the opposing motion passes through the reference location. Figure 6.17 shows this "reference time" for all the earthquakes as a function of earthquake magnitude.

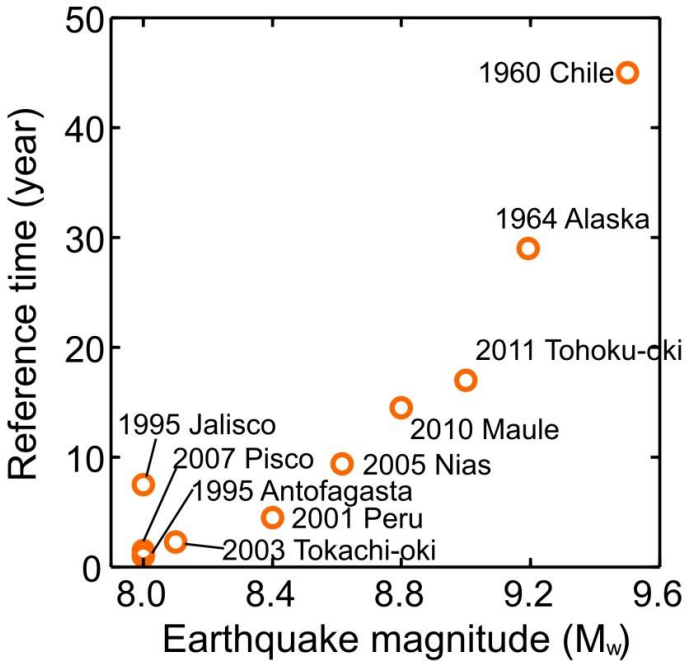

Figure 6.17. The "reference time" for each earthquake when the landward migrating dividing boundary of opposing motion passes through the reference location 175 km from the trench (see Discussions) against the earthquake magnitude M_w.

For different earthquakes, the geodetic constraints have different spatial and/or temporal coverages. An ideal situation of a dense network of continuous GNSS sites evenly distributed over a broad region and covering a long enough time span is rare. When continuous GNSS observations are few or not available, frequent campaign-mode measurements are very useful. For the M_w 8.0 Antofagasta, M_w 8.0 Jalisco, M_w 9.2

Alaska, and M_w 9.5 Chile earthquakes, most or all of the data were collected in campaign surveys. Frequent occupations of sites after the Antofagasta earthquake helped to define the fast evolving deformation at different sites. The more stable GNSS velocities observed at Alaska and Chile represent a certain stage of their earthquake deformation cycle. For Jalisco, our model is constrained mainly by campaign data, but a sole continuous record helps to improve the model's prediction of the time-dependence of the postseismic deformation. Similarly, data from a single continuous GNSS site provide critical model constraints for the M_w 8.4 Peru earthquake. For the M_w 8.0 Pisco, M_w 8.1 Tokachi-oki, M_w 8.6 Nias, M_w 8.8 Maule, and M_w 9.0 Tohoku-oki earthquakes, a greater number of continuous GNSS sites are available, but either the spatial coverage or the time span of the measurements is limited. For example, the five sites for Pisco are less than 100 km apart and form a spatially confined cluster. Sites for the Nias earthquakes are almost all located on forearc islands with less than 100 km from the trench. GNSS observations for the Tohoku-oki and Maule earthquakes are dense and continuous, but it is still too early for them to observe the dividing boundary of the opposing motion pass through the reference location.

Nonetheless, a comparison of the model results for the ten earthquakes indicates a clear trend: In general, the greater the earthquake, the longer time it takes for the dividing boundary of opposing motion to reach the 175-km reference location. This longer reference time reflects a slower migration of the dividing boundary and hence a longer duration of the opposing motion itself. For great earthquakes that feature a compact rupture area but huge slip such as M_w 9.0 Tohoku-oki, the long duration of the opposing motion is mainly because of the large stress perturbation induced by the rupture. For great earthquakes that feature a long rupture in the strike direction but locally less slip, such as M_w 9.2 Sumatra, the long duration is mainly because of the less efficient postseismic viscoelastic stress relaxation, with the viscous mantle flow tending to be more confined to the dip direction.

Besides the primary control by earthquake size, the reference times of the individual examples also reflect the effects of other site-specific factors. Examples follow.

- The larger reference time of the Jalisco earthquake, compared to other M_w 8.0 earthquakes, is more strongly influenced by plate kinematics. Here, the slower subduction of the oceanic plate leads to a smaller contribution by fault relocking to postseismic deformation, slowing down the evolution of the opposing motion.
- Similarly, less complete locking of segments of a subduction fault, in comparison to their neighbouring fully locked segments, also lead to a slower evolution. When the effects of heterogeneous locking is averaged along strike, such as for the 1964 Alaska and 1960 Chile earthquakes, the overall reference time is smaller than what would be obtained with uniform full locking.
- Although the reference time of the 2003 Tokachi-oki earthquake fits the trend in Figure 6.17, afterslip has a more dominant effect in this example than viscoelastic relaxation. In this case, because of the large depth of the earthquake rupture, the dividing boundary of the viscoelastic opposing motion immediately after the earthquake would be located near the coast. It is the large afterslip updip of the rupture zone that caused continuing seaward motion of the coastal GNSS sites over the first 2-3 years. Similarly, the large shallow afterslip following the Nias earthquake caused continuing seaward motion of forearc GNSS sites over the first ~5 years, offseting the effect of viscoelastic relaxation [Sun and Wang, 2015].

The Tokachi-oki example illustrates a major shortcoming of defining the reference location using a distance from the trench. This definition fails to take into consideration complications in fault geometry and slip distribution. In particular, the dip of the subduction fault and the downdip extension of the earthquake rupture are potentially important in controlling postseismic deformation but not represented by this reference distance. However, currently we do not have a better alternative to compare these earthquakes in a simple manner. We will continue to investigate the effects of these factors in our future studies.

Our postseismic deformation models generally require the use of similar mantle viscosity values for earthquakes that occur in the same or adjacent subduction zones. Margins located very far from each other may require more different viscosity values. A transient viscosity of $1\text{-}2\times10^{18}$ Pa s and steady-state viscosity of $3\text{-}5\times10^{18}$ Pa s are

preferred for the Chile and Peru subduction zones for all the M_w 8.0-8.8 earthquakes. In comparison, transient and steady-state viscosities smaller by a factor of 2-5 are preferred for the Japan and Kuril subduction zones. In addition, it is worth reiterating that the Burgers rheology employed in our models may not always be adequate in representing the potentially more complex upper mantle rheology. It is possible that the observed deformation following some of the recent great earthquakes is still in the transient phase but has been modelled to be already in the steady state. More geodetic observations over longer periods will lead to a deeper understanding of the rheology of the Earth.

Chapter 7. Conclusions

This Ph.D. project includes studies on two topics: slip behaviour of the shallowest portion of subduction megathrusts and postseismic deformation following great subduction earthquakes. The project's main scientific contributions are summarized as follows.

Studying the shallow megathrust behaviour is of great importance to understanding tsunami generation, but land-based geophysical observations provide very limited information for the shallow part of the fault which is located far offshore. The first topic of the Ph.D. project is focused on using deformation observations directly from the trench area to study shallow fault behaviour. Here two distinctly different types of trench-breaching slip have been documented using the examples of the 2011 M_w 9.0 Tohoku-oki and 2012 M_w 7.6 Costa Rica earthquakes. These examples in a way bracket a possibly wide range of slip modes of shallow megathrusts.

During the 2011 M_w 9.0 Tohoku-oki earthquake, large coseismic slip breached the trench (Chapter 2). By modelling high-resolution cross-trench bathymetry differences before and after the earthquake, we inferred > 60 m slip at the trench and a 5 m increase of the slip over the most seaward 40 km. The inferred slip distribution suggests a moderate degree of net weakening of the shallow fault during the earthquake. Scenarios of dramatic coseismic strengthening or weakening of the shallow megathrust, which would have led to much greater decrease or increase of slip towards the trench, respectively, can be excluded.

The 2012 M_w 7.6 Costa Rica earthquake shows a very different behaviour of the shallow megathrust (Chapter 3) from Tohoku-oki. Seafloor and sub-seafloor fluid pressure measurements at the trench and GNSS observations on land provide constraints to both coseismic and postseismic fault slip models over a wide spatial range in the dip

direction. According to the observations and model results, the coseismic slip was limited to the hypocentral area beneath the coast and did not breach the trench. Instead, aseismic afterslip occurred updip of the rupture and breached the trench. Similar temporal characteristics of the seafloor pressure records at the trench and GNSS time series on land indicate a broad spatial extent of the afterslip that caused concurrent postseismic deformation offshore and onshore.

In studying postseismic deformation immediately following great subduction earthquakes, the asymmetry of megathrust rupture is a key issue of interest (Chapters 4 and 5). The asymmetry, that is, a much larger coseismic seaward motion of the hanging wall than landward motion of the foot wall, results from the stiffness contrast of the two sides of the megathrust due to the shallow fault dip and the presence of a free surface. The asymmetry generates greater incremental tensile stresses in the upper plate landward of the rupture than in the incoming plate seaward of the rupture. After the earthquake, viscoelastic relaxation of the asymmetric stresses causes the land and trench areas to move in opposite, opposing directions. Seafloor GNSS measurements after the 2011 M_w 9.0 Tohoku-oki earthquake for the first time directly observed landward motion of the trench area immediately following a great subduction earthquake (see Figure 4.1) and provided unambiguous evidence for the dominance of viscoelastic relaxation in short-term (weeks to years) postseismic deformation.

Modelling studies presented in this dissertation show that the immediate opposing motion should be common to great subduction earthquakes and is affected by multiple factors, including mantle viscosity, earthquake size, coseismic slip distribution in the downdip direction, thicknesses of the slab and upper plate, and along-strike rupture length (Section 5.2.4). For earthquakes smaller than about M_w 8.0, the viscoelastic deformation is small and may be difficult to observe. Because the greatest tension in the upper plate generated by the earthquake is above the downdip termination of the rupture, downdip slip distribution controls the location of the dividing boundary of the opposing motion immediately after the earthquake.

When using geodetic observations to determine afterslip for $M_w \geq 8$ earthquakes, it is important to consider the effect of viscoelastic relaxation and the consequent opposing

motion. Neglecting this effect would lead to an under-estimate of shallow afterslip updip of the rupture and over-estimate of deep afterslip downdip of the rupture. With the same data, the shallow afterslip following the 2005 M_w 8.6 Nias earthquake estimated in this dissertation using a viscoelastic model (Chapters 5 and 6) is larger than what was inferred using an elastic model [Hsu et al., 2006] by a factor of ~1.5. The deep afterslip following the 2010 M_w 8.8 Maule and 2011 M_w 9.0 Tohoku-oki earthquakes estimated in this dissertation using viscoelastic models (Chapters 4 and 6) is much smaller than in any published elastic models [e.g., Bedford et al., 2013; Ozawa et al., 2012]. For earthquakes of M_w ~7.5 or smaller, afterslip determined using a purely elastic model, such as for the 2012 M_w 7.6 Costa Rica earthquake in Chapter 3 of this dissertation, is of adequate accuracy.

The evolution of postseismic deformation is governed by a common geodynamic process as has been previously demonstrated using $M_w \geq 9$ subduction earthquakes [Wang et al., 2012]. In this study, we have explored how the common governing process leads to different evolution histories for earthquakes of different sizes (Chapter 6). During postseismic deformation, as the effects of viscoelastic stress relaxation and afterslip decay with time, the effect of megathrust relocking becomes increasingly dominant. The strengthening locking effect causes the dividing boundary of opposing motion to migrate away from the rupture, eventually leading to wholesale landward motion of the surface.

Given the same mantle rheology, the "speed" of the deformation evolution toward the eventual wholesale landward motion depends mainly on earthquake size. Larger earthquakes generate greater coseismic stress perturbations, and they typically have longer along-strike rupture lengths which cause the flow of mantle material accompanying viscoelastic relaxation to be more confined to the dip direction. Both factors lead to longer-lived viscoelastic relaxation and consequently longer-lasting seaward motion of the inland area. The landward migration of the dividing boundary of opposing motion is hence slower, that is, it takes longer for the dividing boundary to pass by a reference location of given distance from the trench. In this dissertation, the reference location used to define this "reference time" is set at a distance of 175 km from

the trench. Using ten $8.0 \leq M_w \leq 9.5$ earthquakes comparatively studied in this dissertation, a positive correlation between earthquake size and the "reference time" is obtained (see Figure 6.17). As end-member examples, the 1960 M_w 9.5 Chile earthquake shows a "reference time" at least 40 times that of the 1995 M_w 8.0 Antofagasta earthquake.

GNSS observations of the ten earthquakes studied in Chapter 6 allow us to constrain mantle viscosities of multiple subduction zones. For segments of the same subduction zone or for adjacent subduction zones, the inferred viscosity values are very similar. For example, for all the studied earthquakes in the Chile and Peru margins since 1995, transient viscosities of $1\text{-}2\times10^{18}$ Pa s and steady-state viscosities of $3\text{-}5\times10^{18}$ Pa s are preferred. However, these steady-state viscosities are lower than the value (2×10^{19} Pa s) preferred for the 1960 M_w 9.5 Chile earthquake in the same margin. It is possible that deformation following the more recent earthquakes has not yet fully entered the steady-state phase, although it has been modelled to be already in the steady state by our models of bi-viscous Burgers rheology. For subduction zones far from each other, somewhat different viscosity values are inferred. For example, in comparison to Chile and Peru, viscosity values preferred for the Japan and Kuril margins are lower by a factor of 2-5.

Bibliography

Ammon, C. J., T. Lay, H. Kanamori, and M. Cleveland (2011), A rupture model of the 2011 off the Pacific coast of Tohoku Earthquake, *Earth, Planets Space, 63*, 693–696, doi:10.5047/eps.2011.05.015.

Baba, T., K. Hirata, T. Hori, and H. Sakaguchi (2006), Offshore geodetic data conducive to the estimation of the afterslip distribution following the 2003 Tokachi-oki earthquake, *Earth and Planetary Science Letters, 241(1–2)*, 281–292, doi:10.1016/j.epsl.2005.10.019.

Bedford, J., and 12 coauthors (2013), A high-resolution, time-variable afterslip model for the 2010 Maule Mw=8.8, Chile megathrust earthquake, *Earth and Planetary Science Letters, 383*, 26–36, doi:10.1016/j.epsl.2013.09.020.

Bedford, J., M. Moreno, S. Li, O. Oncken, J. C. Baez, M. Bevis, O. Heidbach, and D. Lange (2016), Separating rapid relocking, afterslip, and viscoelastic relaxation: An application of the postseismic straightening method to the Maule 2010 cGPS, *Journal of Geophysical Research: Solid Earth, 121*, doi:10.1002/2016JB013093.

Bevis, M., and A. Brown (2014), Trajectory models and reference frames for crustal motion geodesy, *Journal of Geodesy, 88(3)*, 283–311,doi: 10.1007/s00190-013-0685-5.

Bilek, S. L., and L. J. Ruff (2002), Analysis of the 23 June 2001 M_w = 8.4 Peru underthrusting earthquake and its aftershocks, *Geophysical Research Letters, 29(20)*, 1960, doi:10.1029/2002GL015543.

Bletery, Q., A. Sladen, B. Delouis, M. Vallée, J.-M. Nocquet, L. Rolland, and J. Jiang (2014), A detailed source model for the Mw 9.0 Tohoku-Oki earthquake reconciling geodesy, seismology, and tsunami records, *Journal of Geophysical Research: Solid Earth, 119*, 7636–7653, doi:10.1002/2014JB011261.

Bradley, K. E., L. Feng, E. M. Hill, D. H. Natawidjaja, and K. Sieh (2016), Implications of the diffuse deformation of the Indian Ocean lithosphere for slip partitioning of oblique plate convergence in Sumatra, *Journal of Geophysical Research: Solid Earth, 121*, doi:10.1002/2016JB013549.

Briggs, R. W., and 13 coauthors (2006), Deformation and slip along the Sunda Megathrust in the great 2005 Nias-Simeulue earthquake, *Science, 311*, 1897–1901, doi:10.1126/science.1122602.

Brown, L., K. Wang, and T. Sun (2015), Static stress drop in the M_w 9 Tohoku-oki earthquake: Heterogeneous distribution and low average value, *Geophysical Research Letters, 42*, 10595–10600, doi:10.1002/2015GL066361.

Bürgmann, R., and G. Dresen (2008), Rheology of the lower crust and upper mantle: Evidence from rock mechanics, geodesy, and field observations, *Annual Review of Earth and Planetary Science, 36*, 531–567, doi:10.1146/annurev.earth.36.031207.124326.

Bürgmann, R., and D. Chadwell (2014), Seafloor geodesy, *Annual Review of Earth and Planetary Science, 42*, 509–534, doi:10.1146/annurev-earth-060313-054953.

Chester, M. F., and 15 coauthors (2013), Structure and composition of the plate-boundary slip zone for the 2011 Tohoku-oki earthquake, *Science, 342*, 1208–1211, doi:10.1126/science.1243719.

Chlieh, M., J. B. de Chabalier, J. C. Ruegg, R. Armijo, R. Dmowska, J. Campos, and K. L. Feigl (2004), Crustal deformation and fault slip during the seismic cycle in the North Chile subduction zone, from GPS and InSAR observations, *Geophysical Journal International, 158*, 695–711, doi:10.1111/j.1365-246X.2004.02326.x.

Chlieh, M., J. P. Avouac, K. Sieh, D. H. Natawidjaja, and J. Galetzka (2008), Heterogeneous coupling of the Sumatran megathrust constrained by geodetic and paleogeodetic measurements, *Journal of Geophysical Research, 113*, B05305, doi:10.1029/2007JB004981.

Chlieh, M., H. Perfettini, H. Tavera, J.-P. Avouac, D. Remy, J.-M. Nocquet, F. Rolandone, F. Bondoux, G. Gabalda, and S. Bonvalot (2011), Interseismic coupling and seismic potential along the Central Andes subduction zone, *Journal of Geophysical Research, 116*, B12405, doi:10.1029/2010JB008166.

Christensen, D. H., and S. L. Beck (1994), The rupture process and tectonic implications of the great 1964 Prince William Sound earthquake, *Pure and applied geophysics, 142(1)*, 29–53, doi:10.1007/BF00875967.

Comte, D., and M. Pardo (1991), Reappraisal of great historical earthquakes in the northern Chile and southern Peru seismic gaps, *Natural Hazards, 4(1)*, 23–44, doi:10.1007/BF00126557.

Davis, E. E., M. J. Malone, and the Expedition 328 Scientists and Engineers (2010), Cascadia subduction zone ACORK observatory, *Integrated Ocean Drilling Program Preliminary Report, 328*, 59 pp, doi:10.2204/iodp.pr.328.2010.

Davis, E. E., M. Heesemann, and K. Wang (2011), Evidence for episodic aseismic slip across the subduction seismogenic zone off Costa Rica: CORK borehole pressure observations at the subduction prism toe, *Earth and Planetary Science Letters, 306*, 299–305, doi:10.1016/j.epsl.2011.04.017.

Davis, E. E., and H. W. Villinger (2006), Transient formation fluid pressures and temperatures in the Costa Rica forearc prism and subducting oceanic basement: CORK monitoring at ODP Sites 1253 and 1255, *Earth and Planetary Science Letters, 245*, 232–244, doi:10.1016/j.epsl.2006.02.042.

Davis, E. E., H. W. Villinger, and T. Sun (2015), Slow and delayed deformation and uplift of the outermost subduction prism following ETS and seismogenic slip events beneath Nicoya Peninsula, Costa Rica, *Earth and Planetary Science Letters, 410*, 117–127, doi:10.1016/j.epsl.2014.11.015.

Delouis, B., and 10 coauthors (1997), The M_w = 8.0 Antofagasta (Northern Chile) Earthquake of 30 July 1995: a precursor to the end of the large 1877 gap, *Bulletin of the Seismological Society of America, 87(2)*, 427–445.

Delouis, B., J.-M. Nocquet, and M. Vallée (2010), Slip distribution of the February 27, 2010 Mw=8.8 Maule Earthquake, central Chile, from static and high-rate GPS, InSAR, and broadband teleseismic data, *Geophysical Research Letters, 37*, L17305, doi:10.1029/2010GL043899.

DeMets, C., and D. S. Wilson (1997), Relative motions of the Pacific, Rivera, North America, and Cocos plates since 0.78 Ma, *Journal of Geophysical Research, 102(B2*), 2789–2806, doi:10.1029/96JB03170.

DeMets, C., and S. Traylen (2000), Motion of the Rivera plate since 10 Ma relative to the Pacific and North American plates and the mantle, *Tectonophysics, 318*, 119–159, doi:10.1016/S0040-1951(99)00309-1.

DeMets, C., R. G. Gordon, and D. F. Argus (2010), Geologically current plate motions, *Geophysical Journal International, 181*, 1–80, doi:10.1111/j.1365-246X.2009.04491.x.

Di Toro, G., R. Han, T. Hirose, N. De Paola, S. Nielsen, K. Mizoguchi, F. Ferri, M. Cocco, and T. Shimamoto (2011), Fault lubrication during earthquakes, *Nature, 471*, 494–498, doi:10.1038/nature09838.

Diao, F., X. Xiong, R. Wang, Y. Zheng, T. R. Walter, H. Weng, and J. Li (2014), Overlapping post-seismic deformation processes: afterslip and viscoelastic relaxation following the 2011 Mw 9.0 Tohoku (Japan) earthquake, *Geophysical Journal International, 196(1)*, 218–229, doi:10.1093/gji/ggt376.

Dixon, T. H., Y. Jiang, R. Malservisi, R. McCaffrey, N. Voss, M. Protti, and V. González (2014), Earthquake and tsunami forecasts: Relation of slow slip events to subsequent earthquake rupture, *Proceedings of the National Academy Sciences, 111(48)*, 17039–17044, doi:10.1073/pnas.1412299111.

Dragert, H., and K. Wang (2011), Temporal evolution of an episodic tremor and slip event along the northern Cascadia margin, *Journal of Geophysical Research, 116*, B12406, doi:10.1029/2011JB008609.

Feng, L., A. V. Newman, M. Protti, V. González, Y. Jiang, and T. H. Dixon (2012), Active deformation near the Nicoya Peninsula, northwestern Costa Rica, between 1996 and 2010: Interseismic megathrust coupling, *Journal of Geophysical Research, 117*, B06407, doi:10.1029/2012JB009230.

Feng, L., E. M. Hill, P. Banerjee, I. Hermawan, L. L. H. Tsang, D. H. Natawidjaja, B. W. Suwargadi, and K. Sieh (2015), A unified GPS-based earthquake catalog for the Sumatran plate boundary between 2002 and 2013, *Journal of Geophysical Research: Solid Earth, 120*, 3566–3598, doi:10.1002/2014JB011661.

Fischer, K. M., H. A. Ford, D. L. Abt, and C. A. Rychert (2010), The Lithosphere-Asthenosphere Boundary, *Annual Review of Earth and Planetary Sciences, 38*, 551–575. doi:10.1146/annurev-earth-040809-152438.

Frankel, A. (2013), Rupture history of the 2011 M 9 Tohoku Japan earthquake determined from strong-motion and high-rate GPS recordings: subevents radiating energy in different frequency bands, *Bulletin of the Seismological Society of America, 103*, 1290–1306, doi:10.1785/0120120148.

Freed, A. M., A. Hashima, T. W. Becker, D. A. Okaya, H. Sato, and Y. Hatanaka (2017), Resolving depth-dependent subduction zone viscosity and afterslip from postseismic displacements following the 2011 Tohoku-oki, Japan earthquake, *Earth and Planetary Science Letters, 459*, 279–290, doi:10.1016/j.epsl.2016.11.040.

Freymueller, J. T., H. Woodard, S. C. Cohen, R. Cross, J. Elliott, C. F. Larsen, S. Hreinsdóttir, and C. Zweck (2008), Active deformation processes in Alaska, based on 15 years of GPS measurements, *Active Tectonics and Seismic Potential of Alaska, Geophysical Monograph Series, 179*, 1–42, doi: 10.1029/179GM02.

Fujii,Y., K. Satake, S. Sakai, M. Shinohara, and T. Kanazawa (2011), Tsunami source of the 2011 off the Pacific coast of Tohoku Earthquake, *Earth, Planets Space, 63*, 693–696, doi:10.5047/eps.2011.05.015.

Fujimoto, H. (2014), Seafloor geodetic approaches to subduction thrust earthquakes, *Monographs on Environment, Earth and Planets, 2(2)*, 23–63, doi:10.5047/meep.2014.00202.0023.

Fujiwara, T., S. Kodaira, T. No, Y. Kaiho, N. Takahashi, and Y. Kaneda (2011), The 2011 Tohoku-oki earthquake: displacement reaching the trench axis, *Science, 334*, 1240, doi:10.1126/science.1211554.

Fulton, P. M., and 11 coauthors (2013), Low coseismic friction on the Tohoku-oki fault determined from temperature measurements, *Science, 342*, 1214–1217, doi:10.1126/science.1243641.

Giovanni, M. K., S. L. Beck, and L. Wagner (2002), The June 23, 2001 Peru earthquake and the southern Peru subduction zone, *Geophysical Research Letters, 29(21)*, 2018, doi:10.1029/2002GL015774.

Gusman, A. R., Y. Tanioka, S. Sakai, and H. Tsushima (2012), Source model of the great 2011 Tohoku earthquake estimated from tsunami waveforms and crustal deformation data, *Earth and Planetary Science Letters, 341–344*, 234–242, doi:10.1016/j.epsl.2012.06.006.

Hashimoto, C., A. Noda, T. Sagiya, and M. Matsu'ura (2009), Interplate seismogenic zones along the Kuril-Japan trench inferred from GPS data inversion, *Nature Geoscience, 2*, 141–144, doi:10.1038/NGEO421.

Hayes, G. P. (2011), Rapid source characterization of the 03-11-2011 Mw 9.0 off the Pacific coast of Tohoku Earthquake, *Earth, Planets Space, 63*, 529–534, doi:10.5047/eps.2011.05.012.

Hayes, G. P., D. J. Wald, and R. L. Johnson (2012), Slab1.0: A three-dimensional model of global subduction zone geometries, *Journal of Geophysical Research, 117*, B01302, doi:10.1029/2011JB008524.

Hergert, T., and O. Heidbach (2006), New insights into the mechanism of postseismic stress relaxation exemplified by the 23 June 2001 M_w = 8.4 earthquake in southern Peru, *Geophysical Research Letters, 33*, L02307, doi:10.1029/2005GL024858.

Hill, E. M., and 14 coauthors (2012), The 2010 M_w 7.8 Mentawai earthquake: Very shallow source of a rare tsunami earthquake determined from tsunami field survey and near-field GPS data, *Journal of Geophysical Research, 117*, B06402, doi:10.1029/2012JB009159.

Hirata, K., E. Geist, K. Satake, Y. Tanioka, and S. Yamaki (2003), Slip distribution of the 1952 Tokachi-oki earthquake (M 8.1) along the Kuril Trench deduced from tsunami waveform inversion, *Journal of Geophysical Research, 108(B4)*, 2196, doi:10.1029/2002JB001976.

Holdahl, S. R., and J. Sauber (1994), Coseismic slip in the 1964 Prince William Sound earthquake: a new geodetic inversion, *Pure and applied geophysics, 142(1)*, 55–82, doi:10.1007/BF00875968.

Hooper, A., J. Pietrzak, W. Simons, H. Cui, R. Riva, M. Naeije, A. Terwisscha van Scheltinga, E. Schrama, G. Stelling, and A. Socquet (2013), Importance of horizontal seafloor motion on tsunami height for the 2011 Mw=9.0 Tohoku-Oki

earthquake, *Earth and Planetary Science Letters, 361*, 469–479, doi:10.1016/j.epsl.2012.11.013.

Hsu, Y.-J., M. Simons, J.-P. Avouac, J. Galetzka, K. Sieh, M. Chlieh, D. Natawidjaja, L. Prawirodirdjo, and Y. Bock (2006), Frictional afterslip following the 2005 Nias-Simeulue earthquake, Sumatra, *Science, 312*, 1921–1926, doi:10.1126/science.1126960.

Hu, Y., and K. Wang (2008), Coseismic strengthening of the shallow portion of the subduction fault and its effects on wedge taper, *Journal of Geophysical Research, 113*, B12411, doi:10.1029/2008JB005724.

Hu, Y., and K. Wang (2012), Spherical-Earth finite element model of short-term postseismic deformation following the 2004 Sumatra earthquake, *Journal of Geophysical Research, 117*, B05404, doi:10.1029/2012JB009153.

Hu, Y., R. Bürgmann, J. T. Freymueller, P. Banerjee, and K. Wang (2014), Contributions of poroelastic rebound and a weak volcanic arc to the postseismic deformation of the 2011 Tohoku earthquake, *Earth, Planets Space 66*:106, doi:10.1186/1880-5981-66-106.

Hu, Y., K. Wang, J. He, J. Klotz, and G. Khazaradze (2004), Three dimensional viscoelastic finite element model for post-seismic deformation of the great 1960 Chile earthquake, *Journal of Geophysical Research, 109*, B12403, doi:10.1029/2004JB003163.

Hutton, W., C. DeMets, O. Sánchez, G. Suárez, and J. Stock (2001), Slip kinematics and dynamics during and after the 1995 October 9 M_w=8.0 Colima-Jalisco earthquake, Mexico, from GPS geodetic constraints, *Geophysical Journal International, 146*, 637–658, doi:10.1046/j.1365-246X.2001.00472.x.

Ichinose, G., P. Somerville, H. K. Thio, R. Graves, and D. O'Connell (2007), Rupture process of the 1964 Prince William Sound, Alaska, earthquake from the combined inversion of seismic, tsunami, and geodetic data, *Journal of Geophysical Research, 112*, B07306, doi:10.1029/2006JB004728.

Ide, S., A. Baltary, and G. C. Beroza (2011), Shallow dynamic overshoot and energetic deep rupture in the 2011 Mw 9.0 Tohoku-Oki Earthquake, *Science, 332*, 1425–1429, doi:10.1126/science.1207020.

Iinuma, T., R. Hino, M. Kido, D. Inazu, Y. Osada, Y. Ito, M. Ohzono, H. Tsushima, S. Suzuki, H. Fujimoto, and S. Miura (2012), Coseismic slip distribution of the 2011 off the Pacific Coast of Tohoku Earthquake (M9.0) refined by means of seafloor geodetic data, *Journal of Geophysical Research, 117*, B07409, doi:10.1029/2012JB009186.

Ikari, M. J., J. Kameda, D. M. Saffer, and A. J. Kopf (2015), Strength characteristics of Japan Trench borehole samples in the high slip region of the 2011 Tohoku-Oki earthquake, *Earth and Planetary Science Letters, 412*, 35–41, doi:10.1016/j.epsl.2014.12.014.

Imakiire, T., and M. Koarai (2012), Wide-area land subsidence caused by "the 2011 off the Pacific Coast of Tohoku Earthquake", *Soils and Foundation, 52(5)*, 842–855, doi:10.1016/j.sandf.2012.11.007.

Ito, Y., T. Tsuji, Y. Osada, M. Kido, D. Inazu, Y. Hayashi, H. Tsushima, R. Hino, and H. Fujimoto (2011), Frontal wedge deformation near the source region of the 2011 Tohoku-Oki earthquake, *Geophysical Research Letters, 38*, L00G05, doi:10.1029/2011GL048355.

Itoh, Y., and T. Nishimura (2016), Characteristics of postseismic deformation following the 2003 Tokachi-oki earthquake and estimation of the viscoelastic structure in Hokkaido, northern Japan, *Earth, Planets and Space, 68:156*, doi:10.1186/s40623-016-0533-y.

Japan Coast Guard and Tohoku University (2013), Seafloor movements observed by seafloor geodetic observations after the 2011 off the Pacific coast of Tohoku earthquake, *Report of Coordinating Committee Earthquake Prediction, 90*, 3–4.

Jiang, Y., S. Wdowinshi, T. H. Dixon, M. Hackl, M. Protti, and V. Gonzalez (2012), Slow slip events in Costa Rica detected by continuous GPS observations, 2002-2011, *Geochemistry Geophysics Geosystems, 13*, Q04006, doi:10.1029/2012GC004058.

Jiang, Y., Z. Liu, E. E. Davis, S. Y. Schwartz, T. H. Dixon, N. Voss, R. Malservisi, and M. Protti (in revision), Strain release at the trench during shallow slip: The example of Nicoya Peninsula, Costa Rica, *Geophysical Research Letters*.

Johnson, J. M., K. Satake, S. R. Holdahl, and J. Sauber (1996), The 1964 Prince William Sound earthquake: Joint inversion of tsunami and geodetic data, *Journal of Geophysical Research, 101(B1)*, 523–532, doi:10.1029/95JB02806.

Kanamori, H. (1970), The Alaska Earthquake of 1964: Radiation of long-period surface waves and source mechanism, *Journal of Geophysical Research, 75(26)*, 5029–5040, doi:10.1029/JB075i026p05029.

Kanamori, H. (2014), The diversity of large earthquakes and its implications for hazard mitigation, *Annual Review of Earth and Planetary Sciences, 42*, 7–26, doi:10.1146/annurev-earth-060313-055034

Karato, S. (2010), Rheology of the Earth's mantle: A historical review, *Gondwana Research, 18*, 17-45, doi:10.1016/j.gr.2010.03.004.

Karato, S. (2012), On the origin of the asthenosphere, *Earth and Planetary Science Letters, 321*, 95–103. doi:10.1016/j.epsl.2012.01.001.

Kawakatsu, H., P. Kumar, Y. Takei, M. Shinohara, T. Kanazawa, E. Araki, and K. Suyehiro (2009), Seismic evidence for sharp lithosphere-asthenosphere boundaries of oceanic plates, *Science, 324*, 499–502. doi:10.1126/science.1169499.

Khazaradze, G., K. Wang, J. Klotz, Y. Hu, and J. He (2002), Prolonged post-seismic deformation of the 1960 great Chile earthquake and implications for mantle rheology, *Geophysical Research Letters, 29(22)*, 2050, doi:10.1029/2002GL015986.

Khazaradze, G., and J. Klotz (2003), Short- and long-term effects of GPS measured crustal deformation rates along the south central Andes, *Journal of Geophysical Research, 108(B6)*, 2289, doi:10.1029/2002JB001879.

Kido, M., H. Fujimoto, S. Miura, Y. Osada, K. Tsuka, and T. Tabei (2006), Seafloor displacement at Kumano-nada caused by the 2004 off Kii Pen-insula earthquakes, detected through repeated GPS/acoustic surveys, *Earth, Planets Space, 58(7)*, 911–915.

Kido, M., Y. Osada, and H. Fujimoto (2008), Temporal variation of sound speed in ocean: A comparison between GPS/acoustic and in situ measurements, *Earth, Planets Space, 60(3)*, 229–234.

Kido, M., Y. Osada, H. Fujimoto, R. Hino, and Y. Ito (2011), Trench-normal variation in observed seafloor displacements associated with the 2011 Tohoku-Oki earthquake, *Geophysical Research Letters, 38*, L24303, doi:10.1029/2011GL050057.

Kim, Y., G. A. Abers, J. Li, D. Christensen, J. Calkins, and S. Rondenay (2014), Alaska Megathrust 2: Imaging the megathrust zone and Yakutat/Pacific plate interface in the Alaska subduction zone, *Journal of Geophysical Research: Solid Earth, 119*, 1924–1941, doi:10.1002/2013JB010581.

Kirkpatrick, J. D., and 10 coauthors (2015), Structure and lithology of the Japan Trench subduction plate boundary fault, *Tectonics, 34*, 53–69, doi:10.1002/2014TC003695.

Kita, S., T. Okada, A. Hasegawa, J. Nakajima, and T. Matsuzawa (2010), Anomalous deepening of a seismic belt in the upper-plane of the double seismic zone in the Pacific slab, *Earth and Planetary Science Letters, 290(3–4)*, 415–426, doi:10.1016/j.epsl.2009.12.038.

Klein, E., L. Fleitout, C. Vigny, and J. D. Garaud (2016), Afterslip and viscoelastic relaxation model inferred from the large scale postseismic deformation following the 2010 M_w 8.8 Maule earthquake (Chile), *Geophysical Journal International, 205(3)*, 1455–1472, doi:10.1093/gji/ggw086.

Klotz, J., and 11 coauthors (1999), GPS-derived deformation of the Central Andes Including the 1995 Antofagasta M_w=8.0 Earthquake, *Pure and applied geophysics, 154*, 709–730, doi:10.1007/BF00875968.

Klotz, J., G. Khazaradze, D. Angermann, C. Reigber, R. Perdomo, and O. Cifuentes (2001), Earthquake cycle dominates contemporary crustal deformation in Central and Southern Andes, *Earth and Planetary Science Letters, 193*, 437–446, doi:10.1016/S0012-821X(01)00532-5.

Kodaira, S., T. No, Y. Nakamura, T. Fujiwara, Y. Kaiho, S. Miura, N. Takahashi, Y. Kaneda, and A. Taira (2012), Coseismic fault rupture at the trench axis during the 2011 Tohoku-oki earthquake, *Nature Geoscience, 5*, 646–650, doi:10.1038/ngeo1547.

Kogan, M. G., N. F. Vasilenko, D. I. Frolov, J. T. Freymueller, G. M. Steblov, A. S. Prytkov, and G. Ekström (2013), Rapid postseismic relaxation after the great 2006-2007 Kuril earthquakes from GPS observations in 2007–2011, *Journal of Geophysical Research, 118*, 3691–3706, doi:10.1002/jgrb.50245.

Koketsu, K., K. Hikima, S. Miyazaki, and S. Ide (2004), Joint inversion of strong motion and geodetic data for the source process of the 2003 Tokachi-oki, Hokkaido, earthquake, *Earth, Planets and Space,56(3)*, 329–334, doi:10.1186/BF03353060.

Konca, A. O., V. Hjorleifsdottir, T. A. Song, J.-P. Avouac, D. V. Helmberger, C. Ji, K. Sieh, R. Briggs, and A. Meltzner (2007), Rupture kinematics of the 2005 M_w 8.6 Nias-Simeulue earthquake from the joint inversion of seismic and geodetic data, *Bulletin of the Seismological Society of America, 97(1A)*, S307–S322, doi:10.1785/0120050632.

Konca, A. O., and 14 coauthors (2008), Partial rupture of a locked patch of the Sumatra megathrust during the 2007 earthquake sequence, *Nature, 456*, 631–635, doi:10.1038/nature07572.

Kopp, H. (2013), Invited review paper: The control of subduction zone structural complexity and geometry on margin segmentation and seismicity, *Tectonophysics, 589*, 1–16, doi:10.1016/j.tecto.2012.12.037.

Kubo, H., and Y. Kakehi (2013), Source process of the 2011 Tohoku earthquake estimated from the joint inversion of teleseismic body waves and geodetic data including seafloor observation data: Source model with enhanced reliability by using objectively determined inversion settings, *Bulletin of the Seismological Society of America, 103*, 1195–1220, doi:10.1785/0120120113.

Kubota, T., R. Hino, D. Inazu, T. Saito, T. Iinuma, S. Suzuki, Y. Ito, Y. Ohta, K. Suzuki (2012), Source models of M-7 class earthquakes in the rupture area of the 2011

Tohoku-Oki Earthquake by near-field tsunami modeling, Abstract T13B-2594 presented at 2012 Fall Meeting, AGU, San Francisco, Calif., 3–7 Dec.

Kyriakopoulos, C., T. Masterlark, S. Stramondo, M. Chini, and C. Bignami (2013), Coseismic slip distribution for the Mw 9 2011 Tohoku-Oki earthquake derived from 3-D FE modeling, *Journal of Geophysical Research: Solid Earth, 118*, 3837–3847, doi:10.1002/jgrb.50265.

LaBonte, A. L., K. M. Brown, and Y. Fialko (2009), Hydrologic detection and finite element modeling of a slow slip event in the Costa Rica prism toe, *Journal of Geophysical Research, 114*, B00A02, doi:10.1029/2008JB005806.

Lay, T., C. J. Ammon, H. Kanamori, K. D. Koper, O. Sufri, and A. R. Hutko (2010), Teleseismic inversion for rupture process of the 27 February 2010 Chile (M_w 8.8) earthquake, *Geophysical Research Letters, 37*, L13301, doi:10.1029/2010GL043379.

Lay, T., C. J. Ammon, H. Kanamori, L. Xue, and M. J. Kim (2011), Possible large near-trench slip during the 2011 Mw 9.0 off the Pacific coast of Tohoku earthquake, *Earth, Planets Space, 63*, 687–692, doi: 10.5047/eps.2011.05.033.

Lay, T. (2015), The surge of great earthquakes from 2004 to 2014, *Earth and Planetary Science Letters, 409*, 133–146, doi:10.1016/j.epsl.2014.10.047.

Lee, S.-J., B.-S. Huang, M. Ando, H.-C. Chiu, and J.-H. Wang (2011), Evidence of large scale repeating slip during the 2011 Tohoku-Oki earthquake, *Geophysical Research Letters, 38*, L19306, doi:10.1029/2011GL049580.

Li, J., G. A. Abers, Y. H. Kim, and D. Christensen (2013), Alaska megathrust 1: Seismicity 43 years after the great 1964 Alaska megathrust earthquake, *Journal of Geophysical Research: Solid Earth,* 118, 4861–4871, doi:10.1002/jgrb.50358.

Li, S., J. Freymueller, and R. McCaffrey (2016), Slow slip events and time-dependent variations in locking beneath Lower Cook Inlet of the Alaska-Aleutian subduction zone, *Journal of Geophysical Research: Solid Earth, 121*, doi:10.1002/2015JB012491.

Li, S., M. Moreno, J. Bedford, M. Rosenau, and O. Oncken (2015), Revisiting viscoelastic effects on interseismic deformation and locking degree: A case study of the Peru-North Chile subduction zone, *Journal of Geophysical Research: Solid Earth, 120*, 4522–4538, doi:10.1002/2015JB011903.

Li, S., M. Moreno, J. Bedford, M. Rosenau, O. Heidbach, D. Melnick, and O. Oncken (2017), Postseismic uplift of the Andes following the 2010 Maule earthquake: Implications for mantle rheology, *Geophysical Research Letters, 44*, 1768–1776, doi:10.1002/2016GL071995.

Lin, Y.-n. N., and 12 coauthors (2013), Coseismic and postseismic slip associated with the 2010 Maule Earthquake, Chile: Characterizing the Arauco Peninsula barrier effect, *Journal of Geophysical Research: Solid Earth, 118,* 3142–3159, doi:10.1002/jgrb.50207.

Lorito, S., F. Romano, S. Atzori, X. Tong, A. Avallone, J. McCloskey, M Cocco, E. Boschi, and A. Piatanesi (2011), Limited overlap between the seismic gap and coseismic slip of the great 2010 Chile earthquake, *Nature Geoscience, 4*, 173–177, doi:10.1038/NGEO1073.

Maeda, T., T. Furumura, S. Sakai, and M. Shinohara (2011), Significant tsunami observed at ocean-bottom pressure gauges during the 2011 off the Pacific coast of Tohoku Earthquake, *Earth, Planets Space, 63*, 803–808, doi:10.5047/eps.2011.06.005.

Maercklin, N., G. Festa, S. Colombelli, and A. Zollo (2012), Twin ruptures grew to build up the giant 2011 Tohoku, Japan, earthquake. *Scientific Reports, 2*, 709, doi:10.1038/srep00709.

Malservisi, R., and 10 coauthors (2015), Multiscale postseismic behavior on a megathrust: The 2012 Nicoya earthquake, Costa Rica, *Geochemistry Geophysics Geosystems, 16*, 1848–1864, doi:10.1002/2015GC005794.

Marone, C. J., C. H. Scholz, and R. Bilham (1991), On the mechanics of earthquake afterslip, *Journal of Geophysical Research, 96(B5)*, 8441–8452, doi:10.1029/91JB00275.

Márquez Azúa, B., C. Demets, and T. Masterlark (2002), Strong interseismic coupling, fault afterslip, and viscoelastic flow before and after the Oct. 9, 1995 Colima-Jalisco earthquake: Continuous GPS measurements from Colima, Mexico, *Geophysical Research Letters, 29(8),* 1281, doi:10.1029/2002GL014702.

Mavrommatis, A. P., P. Segall, and K. M. Johnson (2014), A decadal-scale deformation transient prior to the 2011 Mw 9.0 Tohoku-oki earthquake, *Geophysical Research Letters, 41*, doi:10.1002/2014GL060139.

McCaffrey, R., R. W. King, S. J. Payne, and M. Lancaster (2013), Active tectonics of northwestern U.S. inferred from GPS-derived surface velocities, *Journal of Geophysical Research: Solid Earth, 118*, 709–723, doi:10.1029/2012JB009473.

Melbourne, T. I., F. H. Webb, J. M. Stock, and C. Reigber (2002), Rapid postseismic transients in subduction zones from continuous GPS, *Journal of Geophysical Research, 107(B10)*, 2241, doi:10.1029/2001JB000555.

Melgar, D., and Y. Bock (2015), Kinematic earthquake source inversion and tsunami runup prediction with regional geophysical data, *Journal of Geophysical Research: Solid Earth, 120,* 3324–3349, doi:10.1002/2014JB011832.

Melosh, H. J., and A. Raefsky (1981), A simple and efficient method for introducing faults into finite element computations, *Bulletin of the Seismological Society of America, 71*, 1391–1400.

Minson, S. E., M. Simons, J. L. Beck, F. Ortega, J. Jiang, S. E. Owen, A. W. Moore, A. Inbal, and A. Sladen (2014), Bayesian inversion for finite fault earthquake source models-II: the 2011 great Tohoku-oki, Japan earthquake, *Geophysical Journal International, 198*, 922–940, doi:10.1093/gji/ggu170.

Miura, S., Y. Suwa, A. Hasegawa, and T. Nishimura (2004), The 2003 M8.0 Tokachi-Oki earthquake – How much has the great event paid back slip debts?, *Geophysical Research Letters, 31*, L05613, doi:10.1029/2003GL019021.

Miyazaki, S., K. M. Larson, K. Choi, K. Hikima, K. Koketsu, P. Bodin, J. Haase, G. Emore, and A. Yamagiwa (2004), Modeling the rupture process of the 2003 September 25 Tokachi-Oki (Hokkaido) earthquake using 1-Hz GPS data, *Geophysical Research Letters, 31*, L21603, doi:10.1029/2004GL021457.

Miyazaki, S., P. Segall, J. Fukuda, and T. Kato (2004), Space time distribution of afterslip following the 2003 Tokachi-oki earthquake: Implications for variations in fault zone frictional properties, *Geophysical Research Letters, 31*, L06623, doi:10.1029/2003GL019410.

Miyazaki, S., J. J. McGuire and P. Segall (2011), Seismic and aseismic fault slip before and during the 2011 off the Pacific coast of Tohoku earthquake, *Earth, Planets Space, 63(7)*, 637–642, doi:10.5047/eps.2011.07.001.

Mochizuki, K., T. Yamada, M. Shinohara, Y. Yamanaka, and T. Kanazawa (2008), Weak interplate coupling by seamounts and repeating M ~ 7 earthquakes, *Science, 321*, 1194-1197, doi:10.1126/science.1160250.

Moore, C., and D. Saffer (2001), Updip limit of the seismogenic zone beneath the accretionary prism of southwest Japan: An effect of diagenetic to low-grade metamorphic processes and increasing effective stress, *Geology, 29*, 183–186, doi:10.1130/0091-7613(2001)029<0183:ULOTSZ>2.0.CO;2.

Moreno, M., M. Rosenau, and O. Oncken (2010), 2010 Maule earthquake slip correlates with pre-seismic locking of Andean subduction zone, *Nature, 467*, 198–202, doi:10.1038/ nature09349.

Moreno, M., and 11 coauthors (2011), Heterogeneous plate locking in the South–Central Chile subduction zone: Building up the next great earthquake, *Earth and Planetary Science Letters, 305*, 413–424, doi: 10.1016/j.epsl.2011.03.025.

Moreno, M., and 19 coauthors (2012), Toward understanding tectonic control on the M_w 8.8 2010 Maule Chile earthquake, *Earth and Planetary Science Letters, 321–322*, 152–165, doi:10.1016/j.epsl.2012.01.006.

Mori, N., T. Takahashi, T. Yasuda, and H. Yanagisawa (2011), Survey of 2011 Tohoku earthquake tsunami inundation and run-up, *Geophysical Research Letters, 38*, L00G14, doi:10.1029/2011GL049210.

Morris, J. D., and Leg 205 Scientists and Engineers (2003), Proceeding Ocean Drilling Program, Initial Reports, vol. *205*., College Station, TX (Ocean Drilling Program), 611 pp, doi:10.2973/odp.proc.ir.205.2003.

Nakajima, J., and A. Hasegawa (2006), Anomalous low-velocity zone and linear alignment of seismicity along it in the subducted Pacific slab beneath Kanto, Japan: Reactivation of subducted fracture zone?, *Geophysical Research Letters, 33*, L16309, doi:10.1029/2006GL026773.

Nakamura, W., N. Uchida, and T. Matsuzawa (2016), Spatial distribution of the faulting types of small earthquakes around the 2011 Tohoku-oki earthquake: A comprehensive search using template events, *Journal of Geophysical Research: Solid Earth, 121*, 2591–2607, doi:10.1002/2015JB012584.

Nanayama, F., K. Satake, R. Furukawa, K. Shimokawa, B. F. Atwater, K. Shigeno, and S. Yamaki (2003), Unusually large earthquakes inferred from tsunami deposits along the Kuril trench, *Nature, 424*, 660–663, doi: 10.1038/nature01864.

Nishimura, T. (2011), Elucidation of interplate coupling based on geodetic data, *Journal of the Geodetic Society of Japan, 57(1)*, 1–14, doi:10.11366/sokuchi.57.1.(in Japanese)

Noda, H., and N. Lapusta (2013), Stable creeping fault segments can become destructive as a result of dynamic weakening, *Nature, 493*, 518–521, doi:10.1038/nature11703.

Noda, H. and T. Shimamoto (2012), Transient behavior and stability analyses of halite shear zones with an empirical rate-and-state friction to flow law, *Journal of Structural Geology, 38*, 234–242, doi:10.1016/j.jsg.2011.08.012.

Nykolaishen, L., H. Dragert, K. Wang, T. S. James, and M. Schmidt (2015), GPS Observations of Crustal Deformation Associated with the 2012 M_w 7.8 Haida Gwaii Earthquake, *Bulletin of the Seismological Society of America, 105*, 1241–1252, doi:10.1785/0120140177.

Obana, K., and 13 coauthors (2013), Aftershocks near the updip end of the 2011 Tohoku-Oki earthquake, *Earth and Planetary Science Letters, 382*, 111–116, doi:10.1016/j.epsl.2013.09.007.

Okada, Y. (1985), Surface deformation due to shear and tensile faults in a half-space, *Bulletin of the Seismological Society of America, 75*, 1135–1154.

Okada, Y. (1992), Internal deformation due to shear and tensile faults in a half-space, *Bulletin of the Seismological Society of America,* 82, 1018–1040.

Osada, Y., M. Kido, Y. Ito, Y. Ohta, R. Hino, and H. Fujimoto (2012), Seafloor crustal movement observed off Miyagi after the 2011 Tohoku Earthquake using GPS-Acoustic observation system, Abstract T13F-2693 presented 2012 Fall Meeting, AGU, San Francisco, Calf., 3–7 Dec.

Ozawa, S., M. Kaidzu, M. Murakami, T. Imakiire, and Y. Hatanaka (2004), Coseismic and postseismic crustal deformation after the M_w 8 Tokachi-oki earthquake in Japan, *Earth, Planets and Space, 57(7)*, 675–680, doi:10.1186/BF03352530.

Ozawa, S., T. Nishimura, H. Suito, T. Kobayashi, M. Tobita, and T. Imakiire (2011), Coseismic and postseismic slip of the 2011 magnitude-9 Tohoku-Oki earthquake, *Nature, 475*, 373–376, doi:10.1038/nature10227.

Ozawa, S., T. Nishimura, H. Munekane, H. Suito, T. Kobayashi, M. Tobita, and T. Imakiire (2012), Preceding, coseismic, and postseismic slips of the 2011 Tohoku earthquake, Japan, *Journal of Geophysical Research, 117*, B07404, doi:10.1029/2011JB009120.

Ozawa, T., and E. Fujita (2013), Local deformations around volcanoes associated with the 2011 off the Pacific coast of Tohoku earthquake, *Journal of Geophysical Research: Solid Earth, 118*, 390–405, doi:10.1029/2011JB009129.

Panet, I., F. Pollitz, V. Mikhailov, M. Diament, P. Banerjee, and K. Grijalva (2010), Upper mantle rheology from GRACE and GPS postseismic deformation after the 2004 Sumatra-Andaman earthquake, *Geochemistry Geophysics Geosystems, 11*, Q06008, doi:10.1029/2009GC002905.

Peltier, W. R. (1974), The impulse response of a Maxwell Earth, *Review of Geophysics and Space Physics, 12*, 649–668.

Peltier, W. R., P. Wu, and D. A. Yuen (1981), The viscosities of the Earth's mantle, in *Anelasticity in the Earth, Geodynamics Series*, vol. 4, edited by F. D. Stacey, M. S. Paterson, and A. Nicolas, pp. 59–77, AGU, Washington, D.C.

Perfettini, H., J.-P. Avouac, and J.-C. Ruegg (2005), Geodetic displacements and aftershocks following the 2001 M_w = 8.4 Peru earthquake: Implications for the

mechanics of the earthquake cycle along subduction zones, *Journal of Geophysical Research, 110,* B09404, doi:10.1029/2004JB003522.

Perfettini, H., and 10 coauthors (2010), Seismic and aseismic slip on the central Peru megathrust, *Nature, 465,* 78–81, doi:10.1038/nature09062.

Perfettini, H., and J. P. Avouac (2014), The seismic cycle in the area of the 2011 Mw 9.0 Tohoku-Oki earthquake, *Journal of Geophysical Research: Solid Earth, 119,* 4469–4515, doi:10.1002/2013JB010697.

Plafker, G. (1965), Tectonic deformation associated with the 1964 Alaska earthquake, *Science, 148(3678),* 1675–1687, doi: 10.1126/science.148.3678.1675.

Plafker, G., L. M. Gilpin, and J. C. Lahr (1994), Neotectonic map of Alaska, in Plafker, G., and H. C. Berg, eds., The Geology of Alaska: Boulder, Colorado, Geological Society of America, The Geology of North America, v. G-1, plate 12, 1 sheet with text, scale 1:2,500,000.

Pollitz, F. F., R. Bürgmann, and P. Banerjee (2006), Post-seismic relaxation following the great 2004 Sumatra-Andaman earthquake on a compressible self-gravitating Earth, *Geophysical Journal International, 167,* 397–420, doi:10.1111/j.1365-246X.2006.03018.x.

Pollitz, F. F., R. Bürgmann, and P. Banerjee (2011), Geodetic slip model of the 2011 M9.0 Tohoku earthquake, *Geophysical Research Letters, 38,* L00G08, doi:10.1029/2011GL048632.

Prawirodirdjo, L., R. McCaffrey, C. D. Chadwell, Y. Bock, and C. Subarya (2010), Geodetic observations of an earthquake cycle at the Sumatra subduction zone: Role of interseismic strain segmentation, *Journal of Geophysical Research, 115,* B03414, doi:10.1029/2008JB006139.

Pritchard, M. E., and M. Simons (2006), An aseismic slip pulse in northern Chile and along-strike variations in seismogenic behavior, *Journal of Geophysical Research, 111,* B08405, doi:10.1029/2006JB004258.

Pritchard, M. E., E. O. Norabuena, C. Ji, R. Boroschek, D. Comte, M. Simons, T. H. Dixon, and P. A. Rosen (2007), Geodetic, teleseismic, and strong motion constraints on slip from recent southern Peru subduction zone earthquakes, *Journal of Geophysical Research, 112,* B03307, doi:10.1029/2006JB004294.

Protti, M., V. Gonzalez, A. V. Newman, T. H. Dixon, S. Y. Schwartz, J. S. Marshall, L. Feng, J. I. Walter, R. Malservisi, and S. E. Owen (2014), Nicoya earthquake rupture anticipated by geodetic measurement of the locked plate interface, *Nature Geoscience, 7,* 117–121, doi:10.1038/ngeo2038.

Pulvirenti, F., S. Jin, and M. Aloisi (2014), An adjoint-based FEM optimization of coseismic displacements following the 2011 Tohoku earthquake: new insights for the limits of the upper plate rebound, *Physics of the Earth and Planetary Interiors, 237*, 25-39, doi:10.1016/j.pepi.2014.09.003.

Rebischung, P., J. Griffiths, J. Ray, R. Schmid, X. Collilieux, and B. Garayt (2012), IGS08: the IGS realization of ITRF2008, *GPS Solutions, 16(4)*, 483-494, doi:10.1007/s10291-011-0248-2.

Remy, D. , H. Perfettini, N. Cotte, J. P. Avouac, M. Chlieh, F. Bondoux, A. Sladen, H. Tavera, and A. Socquet (2016), Postseismic relocking of the subduction megathrust following the 2007 Pisco, Peru, earthquake, *Journal of Geophysical Research: Solid Earth, 121*, doi:10.1002/2015JB012417.

Romano, F., A. Piatanesi, S. Lorito, and K. Hirata (2010), Slip distribution of the 2003 Tokachi-oki M_w 8.1 earthquake from joint inversion of tsunami waveforms and geodetic data, *Journal of Geophysical Research, 115*, B11313, doi:10.1029/2009JB006665.

Romano, F., E. Trasatti, S. Lorito, C. Piromallo, A. Piatanesi, Y. Ito, D. zhao, K. Hirata, P. Lanucara, and M. Cocco (2014), Structural control on the Tohoku earthquake rupture process investigated by 3D FEM, tsunami and geodetic data, *Scientific Reports, 4*, 5631 (2014), doi:10.1038/srep05631.

Ruegg, J. C., and 14 coauthors (1996), The M_w=8.1 Antofagasta (North Chile) Earthquake of July 30, 1995: First results from teleseismic and geodetic data, *Geophysical Research Letters, 23(9)*, 917–920, doi:10.1029/96GL01026 .

Ruegg, J. C., M. Olcay, and D. Lazo (2001), Co-, post- and pre(?)-seismic displacements associated with the Mw 8.4 Southern Peru Earthquake of 23 June 2001 from continuous GPS measurements, *Seismological Research Letter, 72(6)*, 673–678, doi:10.1785/gssrl.72.6.673.

Rychert, C. A., and P. M. Shearer (2009), A global view of the lithosphere-asthenosphere boundary, *Science, 324*, 495–498. doi:10.1126/science.1169754.

Saffer, D.M., E. Araki, A. Kopf, L. Wallace, S. Toczko, E. Davis, and A. Roesner (2016), Repeating and triggered slow slip events in the near-trench region of the Nankai Trough detected by borehole observatories, Abstract T11F–01 (Fall Meeting, American Geophysical Union, San Francisco, 12-16 December, 2016); available at https://agu.confex.com/agu/fm16/meetingapp.cgi/Paper/183534.

Saito, T., Y. Ito, D. Inazu, and R. Hino (2011), Tsunami source of the 2011 Tohoku-Oki earthquake, Japan: Inversion analysis based on dispersive tsunami simulations, *Geophysical Research Letters, 38*, L00G19, doi:10.1029/2011GL049089.

Sato, K., T. Baba, T. Hori, M. Hyodo, and Y. Kaneda (2010), Afterslip distribution following the 2003 Tokachi-oki earthquake: An estimation based on the Green's functions for an inhomogeneous elastic space with subsurface structure, *Earth, Planets and Space,62(12)*, 923–932, doi:10.5047/eps.2010.11.007.

Sakamaki, T., A. Suzuki, E. Ohtani, H. Terasaki, S. Urakawa, Y. Katayama, K. Funakoshi, Y. Wang, J. W. Hernlund, and M. D. Ballmer (2013), Ponded melt at the boundary between the lithosphere and asthenosphere, *Nature Geoscience, 6*, 1041–1044, doi:10.1038/NGEO1982.

Satake, K., Y. Fujii, T. Harada, and Y. Namegaya (2013), Time and space distribution of coseismic slip of the 2011 Tohoku earthquake inferred from tsunami waveform data, *Bulletin of the Seismological Society of America, 103(2B)*, 1473–1492, doi:10.1785/0120120122.

Sato, M., T. Ishikawa, N. Ujihara, S. Yoshida, M. Fujita, M. Mochizuki, and A. Asada (2011), Displacement above the hypocenter of the 2011 Tohoku-Oki earthquake, *Science, 332*, 1395, doi:10.1126/science.1207401.

Sato, M., M. Fujita, Y. Matsumoto, T. Ishikawa, H. Saito, M. Mochizuki, and A. Asada (2013), Interplate coupling off northeastern Japan before the 2011 Tohoku-oki earthquake, inferred from seafloor geodetic data, *Journal of Geophysical Research, 118*, 3860–3869, doi:10.1002/jgrb.50275.

Satriano, C., V. Dionicio, H. Miyake, N. Uchida, J.-P. Vilotte, and P. Bernard (2014), Structural and thermal control of seismic activity and megathrust rupture dynamics in subduction zones: Lessons from the Mw 9.0, 2011 Tohoku earthquake, *Earth and Planetary Science Letters, 403*, 287–298, doi.org/10.1016/j.epsl.2014.06.037.

Savage, J. C. (1983), A dislocation model of strain accumulation and release at a subduction zone, *Journal of Geophysical Research, 88(B6)*, 4984–4996, doi:10.1029/JB088iB06p04984 .

Sawai, Y., K. Satake, T. Kamataki, H. Nasu, M. Shishikura, B. F. Atwater, B. P. Horton, H. M. Kelsey, T. Nagumo, and M. Yamaguchi (2004), Transient uplift after a 17th-century earthquake along the Kuril subduction zone, *Science, 306(5703)*, 1918–1920, doi:10.1126/science.1104895.

Schmerr, N. (2012), The gutenberg discontinuity: melt at the lithosphere-asthenosphere boundary, *Science, 335*, 1480–1483, doi:10.1126/science.1215433.

Scholz, C. H. (1998), Earthquakes and friction laws, *Nature, 391*, 37–42, doi:10.1038/34097.

Shao, G., J. Chen, and R. Archuleta (2012), Quality of earthquake source models constrained by teleseismic waves: using the 2011 M9 Tohoku-oki earthquake as an

example, Poster 93, Presented at Incorporated Research Institutions for Seismology Workshop, Boise, Idaho, June 13–15.

Silverii, F., D. Cheloni, N. D'Agostino, G. Selvaggi, and E. Boschi (2014), Post-seismic slip of the 2011 Tohoku-Oki earthquake from GPS observations: implications for depth-dependent properties of subduction megathrusts, *Geophysical Journal International, 198(1)*, 580–596, doi:10.1093/gji/ggu149.

Simons, M., and 14 coauthors (2011), The 2011 magnitude 9.0 Tohoku-Oki earthquake: Mosaicking the megathrust from seconds to centuries, *Science, 332*, 1421–1425, doi:10.1126/science.1206731.

Sladen, A., H. Tavera, M. Simons, J. P. Avouac, A. O. Konca, H. Perfettini, L. Audin, E. J. Fielding, F. Ortega, and R. Cavagnoud (2010), Source model of the 2007 M_w 8.0 Pisco, Peru earthquake: Implications for seismogenic behavior of subduction megathrusts, *Journal of Geophysical Research, 115*, B02405, doi:10.1029/2009JB006429.

Snay, R. A., M. W. Cline, and E. L. Timmerman (1987), Project REDEAM: Models for historical horizontal deformation, *Technical Report NOS 125 NGS 42*, National Geodetic Survey Subseries, NOAA, Silver Spring, Md.

Spiess, F. N. (1985), Suboceanic geodetic measurements, IEEE Transactions. *Geoscience and Remote Sensing, 23*, 502–510.

Suito, H., and J. T. Freymueller (2009), A viscoelastic and afterslip postseismic deformation model for the 1964 Alaska earthquake, *Journal of Geophysical Research, 114*, B11404, doi:10.1029/2008JB005954.

Sun, T., K. Wang, J. He, T. Iinuma, H. Fujimoto, M. Kido, and Y. Osada (2013), Viscoelastic landward motion of the trench area following a subduction Earthquake, Abstract G14A-08 presented at 2013 Fall Meeting, AGU, San Francisco, Calif., 9–13 Dec.

Sun, T., K. Wang, T. Iinuma, R. Hino, J. He, H. Fujimoto, M. Kido, Y. Osada, S. Miura, Y. Ohta, and Y. Hu (2014), Prevalence of viscoelastic relaxation after the 2011 Tohoku-oki earthquake, *Nature, 514*, 84–87, doi:10.1038/nature13778.

Sun, T. and K. Wang (2015), Viscoelastic relaxation following subduction earthquakes and its effects on afterslip determination, *Journal of Geophysical Research: Solid Earth, 120*, 1329–1344, doi:10.1002/2014JB011707.

Sun, T., K. Wang, T. Fujiwara, S. Kodaira, and J. He (2017), Large fault slip peaking at trench in the 2011 Tohoku-oki earthquake, *Nature Communications, 8*, 14044, doi:10.1038/ncomms14044.

Suwa, Y., S. Miura, A. Hasegawa, T. Sato, and K. Tachibana (2006), Interplate coupling beneath NE Japan inferred from three-dimensional displacement field, *Journal of Geophysical Research, 111*, B04402, doi:10.1029/2004JB003203.

Suzuki, W., S. Aoi, H. Sekiguchi, and T. Kunugi (2011), Rupture process of the 2011 Tohoku-Oki megathrust earthquake (M 9.0) inverted from strong motion data, *Geophysical Research Letters, 38*, L00G16, doi:10.1029/2011GL049136.

Tajima, F., J. Mori, and B. L. N. Kennett (2013), A review of the 2011 Tohoku-oki earthquake (Mw 9.0): Large-scale rupture across heterogeneous plate coupling, *Tectonophysics, 586*, 15–34, doi:10.1016/j.tecto.2012.09.014.

Tanioka, Y., K. Hirate, R. Hino, and T. Kanazawa (2004), Slip distribution of the 2003 Tokachi-oki earthquake estimated from tsunami waveform inversion, *Earth, Planets and Space, 56(3)*, 373–376, doi: 10.1186/BF03353067.

Tarantola, A., and B. Valette (1982), Generalized nonlinear inverse problem solved using the least squares criterion, *Reviews of Geophysics, 20*, 219–232, doi:10.1029/RG020i002p00219.

Trubienko, O., L. Fleitout, J.-D. Garaud, and C. Vigny (2013), Interpretation of interseismic deformations and the seismic cycle associated with large subduction earthquakes, *Tectonophysics, 589*, 126–141, doi:10.1016/j.tecto.2012.12.027.

Tsuji, T., K. Kawamura, T. Kanamatsu, T. Kasaya, K. Fujikura, Y. Ito, T. Tsuru, and M. Kinoshita (2013), Extension of continental crust by anelastic deformation during the 2011 Tohoku-oki earthquake: The role of extensional faulting in the generation of a great tsunami, *Earth and Planetary Science Letters, 364*, 44–58, doi:10.1016/j.epsl.2012.12.038.

Ujiie, K., and 10 coauthors (2013), Low coseismic shear stress on the Tohoku-oki megathrust determined from laboratory experiments, *Science, 342*, 1211–1214, doi:10.1126/science.1243485.

Vigny, C., and 29 coauthors (2011), The 2010 M_w 8.8 Maule megathrust earthquake of central Chile, monitored by GPS, *Science, 332*, 1417, doi:10.1126/science.1204132.

Villegas-Lanza, J. C., M. Chlieh, O. Cavalié, H. Tavera, P. Baby, J. Chire-Chira, and J.-M. Nocquet (2016), Active tectonics of Peru: Heterogeneous interseismic coupling along the Nazca megathrust, rigid motion of the Peruvian Sliver, and Subandean shortening accommodation, *Journal of Geophysical Research: Solid Earth, 121*, 7371–7394, doi:10.1002/2016JB013080.

Wada, I., and K. Wang (2009), Common depth of decoupling between the subducting slab and mantle wedge: Reconciling diversity and uniformity of subduction zones, *Geochemistry Geophysics Geosystems, 10*, Q10009, doi:10.1029/2009GC002570.

Wada, I., C. A. Rychert, and K. Wang (2011), Sharp thermal transition in the forearc mantle wedge as a consequence of nonlinear mantle wedge flow, *Geophysical Research Letters, 38*, L13308, doi:10.1029/2011GL047705.

Wallace, L. M., S. C. Webb, Y. Ito, K. Mochizuki, R. Hino, S. Henrys, S. Y. Schwartz, and A. F. Sheehan (2016), Slow slip near the trench at the Hikurangi subduction zone, New Zealand, *Science, 352(6286)*, 701–704, doi: 10.1126/science.aaf2349.

Wallace, L. M., 13 coauthors (2016), Near-field observations of an offshore M_w 6.0 earthquake from an integrated seafloor and subseafloor monitoring network at the Nankai Trough, southwest Japan, *Journal of Geophysical Research: Solid Earth, 121*, doi:10.1002/2016JB013417.

Wang, C., X. Ding, X. Shan, L. Zhang, and M. Jiang (2012), Slip distribution of the 2011 Tohoku earthquake derived from joint inversion of GPS, InSAR and seafloor GPS/acoustic measurements, *Journal of Asian Earth Sciences, 57*, 128–136, doi:10.1016/j.jseaes.2012.06.019.

Wang, K., J. He, H. Dragert, and T. S. James (2001), Three-dimensional viscoelastic interseismic deformation model for the Cascadia subduction zone, *Earth, Planets and Space, 53(4)*, 295–306, doi:10.1186/BF03352386.

Wang, K., R. Wells, S. Mazzotti, R. D. Hyndman, and T. Sagiya (2003), A revised dislocation model of interseismic deformation of the Cascadia subduction zone, *Journal of Geophysical Research, 108(B1)*, 2026, doi:10.1029/2001JB001227.

Wang, K., and Y. Hu (2006), Accretionary prisms in subduction earthquake cycles: The theory of dynamic Coulomb wedge, *Journal of Geophysical Research, 111*, B06410, doi:10.1029/2005JB004094.

Wang, K., Y. Hu, M. Bevis, E. Kendrick, R. Smalley Jr., R. B. Vargas, and E. Lauría (2007), Crustal motion in the zone of the 1960 Chile earthquake: Detangling earthquake-cycle deformation and forearc-sliver translation, *Geochemistry Geophysics Geosystems, 8*, Q10010, doi:10.1029/2007GC001721.

Wang, K., and J. He (2008), Effects of frictional behavior and geometry of subduction fault on coseismic seafloor deformation, *Bulletin of the Seismological Society of America*, *98*, 571–579, doi:10.1785/0120070097.

Wang, K., Y. Hu, and J. He (2012), Deformation cycles of subduction earthquakes in a viscoelastic Earth, *Nature, 484*, 327–332, doi:10.1038/nature11032.

Wang, K. (2013), Megathrust surprises, *Nature Geoscience, 6*, 11–12, doi:10.1038/ngeo1682.

Wang, K., and M. Kinoshita (2013), Dangers of Being Thin and Weak, *Science, 342*, 1178–1180, doi: 10.1126/science.1246518.

Wang, K., and S. L. Bilek (2014), Invited review paper: Fault creep caused by subduction of rough seafloor relief, *Tectonophysics, 610*, 1–24, doi:10.1016/j.tecto.2013.11.024.

Wang, K., and A. M. Tréhu (2016), Invited review paper: Some outstanding issues in the study of great megathrust earthquakes–The Cascadia example, *Journal of Geodynamics, 98*, 1–18, doi:10.1016/j.jog.2016.03.010.

Wang, K., T. Sun, L. Brown, R. Hino, T. Iinuma, S. Kodaira, T. Fujiwara (2017), Learning from crustal deformation associated with the M=9 2011 Tohoku-oki earthquake, submitted to *Geosphere*.

Wang, P.-L., S. E. Engelhart, K. Wang, A. D. Hawkes, B. P. Horton, A. R. Nelson, and R. C. Witter (2013), Heterogeneous rupture in the great Cascadia earthquake of 1700 inferred from coastal subsidence estimates, *Journal of Geophysical Research: Solid Earth, 118*, 2460–2473, doi:10.1002/jgrb.50101.

Wang, R., S. Parolai, M. Ge, M. Jin, T. R. Walter, and J. Zschau (2013), The 2011 Mw 9.0 Tohoku Earthquake: Comparison of GPS and Strong Motion Data, *Bulletin of the Seismological Society of America, 103*, 1336–1347, doi:10.1785/0120110264.

Watanabe, S., M. Sato, M. Fujita, T. Ishikawa, Y. Yokota, N. Ujihara, and A. Asada (2014), Evidence of viscoelastic deformation following the 2011 Tohoku-Oki earthquake revealed from seafloor geodetic observation, *Geophysical Research Letters, 41*, doi:10.1002/2014GL061134.

Wei, S., R. Graves, D. Helmberger, J.-P. Avouac, and J. Jiang (2012), Sources of shaking and flooding during the Tohoku-oki earthquake: A mixture of rupture styles, *Earth and Planetary Science Letters, 333–334*, 91–100, doi:10.1016/j.epsl.2012.04.006.

Wei, Y., A. V. Newman, G. P. Hayes, V. V. Titov, and L. Tang (2014), Tsunami forecast by joint inversion of real-time tsunami waveforms and seismic or GPS data: application to the Tohoku 2011 tsunami, *Pure and Applied Geophysics, 171*, 3281–3305, doi:10.1007/s00024-014-0777-z.

Yagi, Y. (2004), Source rupture process of the 2003 Tokachi-oki earthquake determined by joint inversion of teleseismic body wave and strong ground motion data, *Earth, Planets and Space, 56*, 311–316, doi:10.1186/BF03353057.

Yagi, Y., and Y. Fukahata (2011), Rupture process of the 2011 Tohoku-oki earthquake and absolute elastic strain release, *Geophysical Research Letters, 38*, L19307, doi:10.1029/2011GL048701.

Yamamoto, Y., R. Hino, and M. Shinohara (2011), Mantle wedge structure in the Miyagi Prefecture forearc region, central northeastern Japan arc, and its relation to corner-flow pattern and interplate coupling, *Journal of Geophysical Research, 116*, B10310, doi:10.1029/2011JB008470.

Yamanaka, Y., and M. Kikuchi (2003), Source process of the recurrent Tokachi-oki earthquake on September 26, 2003, inferred from teleseismic body waves, *Earth, Planets and Space, 55(12)*, e21–e24, doi:10.1186/BF03352479.

Yamazaki, Y., T. Lay, K. F. Cheung, H. Yue, and H. Kanamori (2011), Modeling near-field tsunami observations to improve finite-fault slip models for the 11 March 2011 Tohoku earthquake, *Geophysical Research Letters, 38*, L00G15, doi:10.1029/2011GL049130.

Yao, D., J. I. Walter, X. Meng, T. E. Hobbs, Z. Peng, A. V. Newman, S. Y. Schwartz, and M. Protti (2017), Detailed spatiotemporal evolution of microseismicity and repeating earthquakes following the 2012 Mw 7.6 Nicoya earthquake, *Journal of Geophysical Research: Solid Earth, 122*, doi:10.1002/2016JB013632.

Yokota, Y., K. Koketsu, Y. Fujii, K, Satake, S. Sakai, M. Shinohara, and T. Kanazawa (2011), Joint inversion of strong motion, teleseismic, geodetic, and tsunami datasets for the rupture process of the 2011 Tohoku earthquake, *Geophysical Research Letters, 38*, L00G21, doi:10.1029/2011GL050098.

Yoshida, Y., H. Ueno, D. Muto, and S. Aoki (2011), Source process of the 2011 Off the Pacific Coast of Tohoku Earthquake with the combination of teleseismic and strong motion data, *Earth, Planets Space, 63*, 565–568, doi:10.5047/eps.2011.05.011.

Yue, H., T. Lay, S. Y. Schwartz, L. Rivera, M. Protti, T. H. Dixon, S. Owen, and A. V. N (2013), The 5 September 2012 Nicoya, Costa Rica M_w 7.6 earthquake rupture process from joint inversion of high-rate GPS, strong-motion, and teleseismic P wave data and its relationship to adjacent plate boundary interface properties, *Journal of Geophysical Research: Solid Earth, 118*, 5453–5466, doi:10.1002/jgrb.50379.

Yue, H., and T. Lay (2013), Source rupture models for the Mw 9.0 2011 Tohoku earthquake from joint inversions of high-rate geodetic and seismic data, *Bulletin of the Seismological Society of America, 103(2b)*, 1242–1255, doi:10.1785/0120120119.

Zhao, D., Z. Wang, N. Umino, and A. Hasegawa (2009), Mapping the mantle wedge and interplate thrust zone of the northeast Japan arc, *Tectonophysics, 467*, 89–106.

Zhou, X., G. Cambiotti, W. Sun, and R. Sabadini (2014), The coseismic slip distribution of a shallow subduction fault constrained by prior information: the example of 2011

Tohoku (Mw 9.0) megathrust earthquake, *Geophysical Journal International, 199(2),* 981–995, doi: 10.1093/gji/ggu310.